

# Improvement to hydrocyclone used in separating particles from produced water in the oil and gas industry.

ADEWOYE, A.J.

2020

*The author of this thesis retains the right to be identified as such on any occasion in which content from this thesis is referenced or re-used. The licence under which this thesis is distributed applies to the text and any original images only – re-use of any third-party content must still be cleared with the original copyright holder.*



**ROBERT GORDON  
UNIVERSITY ABERDEEN**

# **Improvement to Hydrocyclone Used in Separating Particles from Produced Water in the Oil and Gas Industry**

---

Adebola Jumoke Adewoye

A thesis submitted in partial fulfilment of the requirements of the Robert Gordon University for the degree of Doctor of Philosophy.

June 2020



**Title of Research Project:**

**Improvement to Hydrocyclone Used in Separating  
Particles from Produced Water in the Oil and Gas  
Industry**

**Principal Supervisor: Dr. Mamdud Hossain**

Supervisor's details:

**Dr. Mamdud Hossain, Dr. Sheikh Islam and Dr. Aditya Karnik**

School of Engineering, Robert Gordon University, Schoolhill, AB10 1FR,  
Aberdeen, UK

## Acknowledgement

*'The end is never the end. It's always the beginning of something'*- I would like to express my profound gratitude to the following people for their tremendous contribution to my PhD journey during my stay at Robert Gordon University, Aberdeen.

I would like express my heartfelt gratitude to my principal supervisor **Dr Mamdud Hossain** and the member of supervisory team, Dr Sheikh Islam and Dr Aditya Karnik for their much-appreciated guidance and support throughout my PhD programme.

I am appreciative of the support of the entire staff for school of engineering, Robert Gordon University (RGU) Aberdeen. I am grateful for the support of the staff of Robert Gordon University library department for the sourcing of journals and book for me promptly as required. In addition, I will like to thank the member of the security for their support anytime I decide to work at odd hours. My most profound gratitude is to Dr. Ibiye Iyalla for his support during my programme, your words of encouragement are invaluable.

Finally, I cannot express my appreciation enough to my family; to my parents Mr & Mrs Abdul Rahaman Adewoye, my sibling Dr. Kayode Adewoye, Mojirola Airekholo, Olayiwola Adewoye, Adeola Adewoye. Words are not enough to describe your contribution to my work, your encouragement and support during this programme; I am tremendously grateful.

## **Dedication**

I dedicate this thesis to almighty God for being the provider of all needs. The Lord has indeed been faithful to me. This thesis is also dedicated to my late sister Motunrayo Muhammed. I have come to understand that time does not heal anything but acceptance heals everything.

## **Abstract**

Hydrocyclone is an equipment that is used to separate particles from produced water. This equipment can be used in different industries including oil and gas, water treatment, pharmaceutical among others. The hydrocyclone can effectively separate particles more than  $10\mu\text{m}$  but the efficiency is greatly reduced when the particle size is less than  $10\mu\text{m}$ . This research work was therefore aimed at improving the efficiency of small oil droplets (particle size of  $0\text{-}20\mu\text{m}$ ) separated in liquid-liquid hydrocyclone.

In order to achieve this, the use of micro particles was employed and magnetism was later induced into the system. The hydrocyclone with micro-doped oil is referred to as the micro-hydrocyclone while the hydrocyclone that include both with micro-doped oil and induced magnetism is referred to as magnetic hydrocyclone.

Computation fluid dynamics (CFD) was employed for the analysis of the fluid flow in the hydrocyclone; a review of the turbulence model shows that the Reynold stress model (RSM) and Large eddy simulation (LES) are the best turbulence models for the analysis. RSM was employed because of the reduced computational time when compared to the LES model. A pressure-based solver with transient time was used for the simulations. The discretization was done using SIMPLE for the pressure velocity coupling, QUICK was used for all other discretization.

The review of the turbulence model was done to evaluate the best RANS model for hydrocyclone simulation as a reduction in computational time would be greatly appreciated. Results of the eddy viscosity models with curvature correction terms and RSM model were compared to Hseih's experimental results. The fluid flow in liquid-liquid and solid-liquid hydrocyclones were analysed using different geometrical parts to establish that the geometrical parts cannot be used to effectively separate particles less than  $10\mu\text{m}$  as reviewed in the literature.

A comparison of the fluid flow in liquid-liquid and solid-liquid hydrocyclone was also reviewed using the same hydrocyclone geometry. The impact of microparticles and microparticles with magnetic induction on the separation oil-emulsion was compared to the conventional hydrocyclone, a review of the magnetic permeability, charge density, magnetic particle density and effect of flowrate was also performed.

From turbulence model analysis, it was concluded that RSM better predicts the flow in the hydrocyclone rather than the other RANS model evaluated. However, the use of the eddy viscosity model with curvature correction can also be used with a slight reduction in efficiency. While the eddy viscosity without curvature correction terms does not can be used to predict the anisotropy flow in the hydrocyclone.

The results of the micro-doping analysis show that the magnetic hydrocyclone can improve the efficiency of particles less than  $10\mu\text{m}$  by approximately 30% therefore the magnetic hydrocyclone is better used for particles of a size less than  $10\mu\text{m}$ . The micro-doped hydrocyclone however provides better efficiency of particle size between  $10\text{-}30\mu\text{m}$  while the conventional hydrocyclone is better used for a particle size greater than  $30\mu\text{m}$  at a higher flowrate. It was also concluded that the density difference caused by doping oil with magnetic particles is the most important factor influencing the separation.

Increasing the density of the microparticle increases the separation efficiency. For the split ratio, however, increasing from a density of  $2175\text{kg}/\text{m}^3$  to  $3175\text{kg}/\text{m}^3$  increases the split ratio after which a further increase of the density from  $3175\text{kg}/\text{m}^3$  to  $5175\text{kg}/\text{m}^3$  did not significantly affect the split ratio.

Decreasing the magnetic permeability increases the drag force, lift force and moment while hydrocyclones with lower permeability have a higher velocity profile than hydrocyclones with high permeability. The pressure and split ratio also decrease with increasing permeability. Finally, increasing the microparticle charge density increases separation. However, it decreases the split ratio although the difference is really small.

# Table of Contents

List of Figures .....	12
List of Tables.....	19
Nomenclature .....	20
1.0 Introduction .....	23
1.1 Research Motivation .....	23
1.2 Water Treatment Equipment for Fine Dispersed Emulsion .....	27
1.3 Research Aim and Objectives .....	33
<b>1.3.1 Aim</b> .....	33
<b>1.3.2 Objectives</b> .....	33
<b>1.3.3 Thesis Outline</b> .....	34
2.0 Literature Review .....	36
2.1 Hydrocyclone Velocity and Force Profile .....	36
2.2 Turbulence Models Used in Hydrocyclone Simulation .....	39
2.3 Effect of Geometrical Parameters in Hydrocyclone.....	42
<b>2.3.1 Overflow Section</b> .....	42
<b>2.3.2 Inlet Section</b> .....	44
<b>2.3.3 Underflow Diameter</b> .....	46
<b>2.3.4 Hydrocyclone Size</b> .....	47
<b>2.3.5 Cone Angle</b> .....	49
2.4 Magnetic Hydrocyclone.....	51
2.5 Magnetic Material .....	52
2.6 Magnetic particles .....	55
2.7 Thermoresponsive polymers.....	58
Summary of Chapter 2 .....	59
Chapter 3 Methodology .....	60
3.1 Modelling of separation of oil from produced water .....	60
3.2 Concept of Magnetic Particle Doping.....	61



3.3	Computational Fluid Dynamics.....	61
3.4	Multiphase Flow Modelling Methods .....	62
<b>3.4.1</b>	<b>Eulerian- Lagrangian model</b> .....	63
3.5	Governing Equations .....	65
<b>3.5.1</b>	<b>Continuity Equation</b> .....	65
3.6.	Turbulence Model .....	67
<b>3.6.1</b>	<b>Standard k-<math>\epsilon</math> model</b> .....	68
<b>3.6.2</b>	<b>Renormalization (RNG) k-<math>\epsilon</math> model</b> .....	68
<b>3.6.3</b>	<b>Realizable k-<math>\epsilon</math> model</b> .....	70
3.7	Transition SST model .....	71
<b>3.7.1</b>	<b>The intermittency transport equation is defined by equation 3.22 below</b> .....	72
<b>3.7.2</b>	<b>Equation for transition momentum thickness Reynold number is given by <math>Re_{\theta t}</math></b> .....	73
<b>3.7.3</b>	<b>Modification to improve separation induced transition</b> .....	74
<b>3.7.4</b>	<b>Empirical Correlations</b> .....	74
3.8	Reynolds Stress Model (RSM).....	75
3.9	Discrete Particle Model (DPM).....	76
3.10	Magnetohydrodynamic Model (MHD).....	79
3.11	Boundary Conditions .....	80
3.12	Computational Procedure.....	80
Chapter 4.....		83
4.0	Evaluation of Turbulence Models and Solution Validation.....	83
4.1	Turbulence Model .....	83
4.3	Model Setup .....	86
<b>4.3.1</b>	<b>Boundary Conditions</b> .....	87
<b>4.4</b>	<b>Grid Size/ Number</b> .....	88
4.5	Results and Discussion.....	89
<b>4.5.1</b>	<b>Mesh Independency test</b> .....	89
4.6	Turbulence Model Comparison Results and discussion of Results .....	91

4.6.1	<b>Tangential Velocity</b> .....	91
4.7	Summary of Turbulence Models and CFD Validation .....	108
5.0	Comparing the effect of hydrocyclone geometrical parameters on the separation of particles and flow of fluid parameters in hydrocyclone .....	110
5.1	The Cylindrical Diameter .....	112
5.2	Result and Discussion of results .....	113
5.2.1	<b>Turbulence Kinetic Energy</b> .....	113
5.2.2	<b>Tangential Velocity</b> .....	116
5.2.3	<b>Axial Velocity</b> .....	118
5.2.4	<b>Pressure Profile</b> .....	122
5.2.5	<b>Pressure Drop</b> .....	123
5.2.6	Particle Tracking .....	125
5.3	Vortex Finder Depth .....	128
5.3.1	<b>Results and Discussion of Results</b> .....	128
5.3.2	<b>Axial Velocity</b> .....	130
5.3.4	<b>Turbulence Kinetic Energy</b> .....	132
5.3.3	<b>Radial Velocity</b> .....	135
5.3.5	<b>Pressure</b> .....	136
5.3.1	<b>Tangential Velocity</b> .....	139
5.3.6	<b>Swirling Strength at the Vortex Core Region of the cyclone at level 0.01</b> .....	141
	<b>Swirling Strength of at Vortex core Region of the cyclone at swirl level of 0.01</b> .....	142
5.2.8	<b>Particle Tracking</b> .....	143
5.3	Spigot Section .....	145
5.3.4	<b>Axial Velocity</b> .....	145
5.3.5	<b>Radial Velocity</b> .....	146
5.3.5	<b>Turbulence Kinetic Energy</b> .....	148
5.3.6	<b>Swirling Strength of the cyclone at Level 0.01</b> .....	149
5.3.7	<b>Pressure Drop</b> .....	150

5.3.8	Particle Tracking .....	151
5.4	Comparison of the fluid flow in liquid-liquid and solid-liquid hydrocyclones .....	153
5.4.1	<b>Results and Discussion of Results</b> .....	154
5.4.2	<b>The Axial Velocity</b> .....	154
5.4.3	<b>Spigot Diameter</b> .....	156
5.4.4	<b>Vortex Finder</b> .....	156
5.4.3	<b>Tangential Velocity</b> .....	158
5.4.3	<b>Turbulence Kinetic Energy</b> .....	163
5.4.4	<b>Pressure Drop</b> .....	167
5.4.5	<b>Split Ratio</b> .....	169
5.5	Summary of Chapter .....	171
6.0	Use of Microparticles and a magnetically induced hydrocyclone in the separation of fine-dispersed oil emulsion .....	173
6.1	Solution Technique .....	175
6.1.1	<b>RSM Model</b> .....	175
6.1.2	<b>Discrete Phase Model</b> .....	175
6.1.3	<b>Magnetohydrodynamic Model (MhD)</b> .....	175
6.1.4	<b>Boundary Conditions and Solution methods</b> .....	176
6.1.5	<b>Operating Conditions</b> .....	177
6.2	Effect of Magnetic Particle on Oil-Water Separation Efficiency and Velocity Profile .....	178
6.2.1	<b>Efficiency</b> .....	178
6.2.2	<b>Pressure Drop</b> .....	180
6.2.3	<b>Split Ratio</b> .....	185
6.2.4	<b>Tangential Velocity</b> .....	186
6.2.4	<b>Axial Velocity</b> .....	191
6.2.6	<b>Radial Velocity</b> .....	192
6.3	Effect of Micro-Particle Permeability on Hydrocyclone Separation efficiency of Oil-Emulsion .....	196

6.3.1	Efficiency .....	197
6.3.2	<b>Forces in the Hydrocyclone</b> .....	198
6.3.3	<b>Velocity profiles at different magnetic permeability</b> .....	201
6.3.4	<b>Turbulence Kinetic Energy</b> .....	206
6.3.5	<b>Pressure Drop</b> .....	207
6.3.6	<b>Split Ratio at different magnetic permeability</b> .....	209
6.4	Effect of Micro-Particle Density on Hydrocyclone Separation efficiency of Oil-Emulsion Without the Use of MhD .....	209
6.4.1	<b>Efficiency</b> .....	210
6.4.2	<b>Split Ratio</b> .....	210
6.4.3	<b>Pressure</b> .....	211
6.4.4	<b>Velocity Distribution</b> .....	212
6.4.5	Turbulence Kinetic Energy .....	217
6.4.6	<b>Swirl Strength at Vortex Core Region</b> .....	219
6.5	Effect of Charge Density of Micro-particles in Magnetic Hydrocyclone Separation .....	220
6.5.1.	<b>Efficiency</b> .....	221
6.5.2	<b>Split Ratio</b> .....	222
6.5.3	<b>Velocity Profile</b> .....	223
6.5.4	<b>Turbulence Kinetic Energy</b> .....	224
6.5.5	<b>Swirl Strength at Vortex Core Region</b> .....	224
6.6	Summary of Chapter .....	227
7.0	Conclusion, Future Work and Recommendation .....	229
7.1	Conclusion .....	229
7.2	Future Work and Recommendations .....	231
	References .....	233

## List of Figures

Figure 1-1	Composition of Produced Water Generated in the Oil and Gas Industry
Figure 1-2	Produced Water Treatment Layout
Figure 1-3	Deoiling Hydrocyclone Separation
Figure 3-1	Doping of Oil droplet
Figure 3.2	Numerical process flow diagram
Figure 3-3	Grid arrangement
Figure 4-1	Hydrocyclone Geometry and Boundaries for Computational Domain
Figure 4-2	Hydrocyclone mesh with different number of elements and nodes
Figure 4-3	Comparison of tangential velocity produced the three meshes using RSM model to the experimental results
Figure 4-4	Comparison of axial velocity produced the three meshes using RSM model to the experimental results
Figure 4-5	Comparison of tangential velocity of k- $\epsilon$ models, SST model without curvature with RSM and experimental results
Figure 4-6	Comparison of tangential velocity of k- $\epsilon$ models, SST model with curvature with RSM and experimental results
Figure 4-7	Comparison of axial velocity of k- $\epsilon$ models, SST model without curvature with RSM and experimental results
Figure 4-8	Comparison of axial velocity of k- $\epsilon$ models, SST model with curvature with RSM and experimental results
Figure 4-9	Comparison of tangential velocity contours of k- $\epsilon$ models, SST model without curvature with RSM

Figure 4-10	Comparison of tangential velocity contours of k- $\epsilon$ models, SST model with curvature with RSM
Figure 4-11	Comparison of axial velocity contours of k- $\epsilon$ models, SST model without curvature with RSM
Figure 4-12	Comparison of axial velocity contours of k- $\epsilon$ models, SST model with curvature with RSM
Figure 4-13	Comparison of turbulent kinetic contours of k- $\epsilon$ models, SST model without curvature with RSM
Figure 4-14	Comparison of turbulent kinetic contours of k- $\epsilon$ models, SST model with curvature with RSM
Figure 4-15a	Turbulence model efficiency without curvature correction terms
Figure 4-15b	Turbulence model efficiency with curvature correction terms
Figure 4-16a	Turbulence models split ratio efficiency without curvature correction terms
Figure 4-16b	Turbulence model split ratio efficiency with curvature correction terms
Figure 4-17a	Turbulence model pressure drop without curvature correction terms
Figure 4-17b	Turbulence model pressure drop with curvature correction terms
Figure 4-18	Swirl strength at the vortex core region- without curvature correction terms
Figure 4-19	Swirl strength at the vortex core region- with curvature correction terms
Figure 5-1	Hydrocyclone Geometrical Parts
Figure 5-2	Turbulence Kinetic Energy contour plots
Figure 5-3	Turbulence Kinetic Energy at different cylindrical diameter
Figure 5-4a to b	Tangential velocity at the cylindrical and conical section

Figure 5-4c to e	Tangential velocity Contour at changing cylindrical sections
Figure 5-5a to b	Axial Velocity in the cylindrical and conical section
Figure 5-5c to e	Axial velocity Contours at changing cylindrical sections
Figure 5-6a to b	Radial Velocity in the cylindrical and conical section
Figure 5-6c to e	Radial velocity Contours at changing cylindrical sections
Figure 5-7a to b	Pressure in the cylindrical and conical section
Figure 5-7c to e	Pressure Contours at changing cylindrical sections
Figure 5-7f	Pressure drop in hydrocyclone with different cylindrical diameters
Fig 5-8a to c	Particle Tracking with different cylindrical diameters
Figure 5-9a to b	Tangential velocity at different vortex finder lengths
Figure 5-9c	Tangential Velocity Contour at different vortex finder lengths
Figure 5-10a to b	Axial velocity at different vortex finder lengths
Figure 5-10c to f	Axial Velocity Contour at different vortex finder lengths
Figure 5-11a to b	Radial velocity at different vortex finder lengths
Figure 5-11c to f	Radial Velocity Contour for different vortex finder lengths
Figure 5-12a to b	Turbulence kinetic energy for different vortex finder lengths
Figure 5-13a to c	Turbulence kinetic energy contour for different vortex finder lengths
Figure 5-14a to b	Pressure graph for different vortex finders
Figure 5-14c	Pressure drop for different vortex finders
Figure 15a to d:	Static pressure contour for different vortex finders
Figure 5-16 a to d	Swirl strength for different vortex finders
Figure 5-17a to d	Particle tracking for different vortex finders
Figure 5-18a to b	Tangential velocity for different spigot diameter in cylindrical and conical sections

- Figure 5-18c Forces Acting on Hydrocyclone
- Figure 5-18d to f Tangential velocity contour for different spigot sections
- Figure 5-19 a to b Axial velocity for different spigot sections
- Figure 5-20 a to c Axial velocity contour for different spigot sections
- Figure 5-21 a to b Radial velocity for different spigot sections
- Figure 5-22a to b Turbulence kinetic energy for different spigot sections
- Figure 5-23 Swirling Strength of the cyclone at Level 0.01
- Figure 5-23a Effect of Hydrocyclone Spigot Diameter on Pressure drop
- Figure 5-23b to d: Particle tracking for the different spigot sections
- Figure 5-24 Axial Velocity of Base (75mm) cyclone diameter, 50mm cyclone diameter, 7.5mm spigot diameter and 17.5mm Spigot diameter hydrocyclone
- Figure 5-25 Axial Velocity in 0mm, 10mm and 25mm Vortex finder for the solid-liquid and liquid-liquid hydrocyclone
- Figure 5-26 Tangential Velocity in Base cylindrical section (75mm), 50mm cylindrical section, 17.5mm spigot section
- Figure 5-27 Tangential Velocity in 0mm, 10mm and 25mm Vortex finder for solid-liquid and liquid-liquid hydrocyclone
- Figure 5-28 Radial Velocity in Base cylindrical section (75mm), 50mm cylindrical section, 17.5mm spigot section for the solid-liquid and liquid-liquid hydrocyclone
- Figure 5-29 Radial Velocity in 0mm, 10mm and 25mm Vortex finder for solid-liquid and liquid-liquid hydrocyclone
- Figure 5:30 Turbulence Kinetic Energy of Base, 50mm diameter and 17.5mm Spigot diameter hydrocyclone for solid-liquid and liquid-liquid hydrocyclone
- Figure 5-31 Turbulence Kinetic Energy in 0mm, 10mm and 25mm Vortex finder for the solid-liquid and liquid-liquid hydrocyclone



Figure 5-32	Comparison of the pressure drop for solid-liquid and liquid-liquid hydrocyclone at different geometrical parameters
Figure 5-33	Split ratio comparison for solid-liquid and liquid-liquid hydrocyclone at different geometrical parameters
Figure 6-1	Hydrocyclone geometrical parts
Figure 6-1a	Effect of Use of Micro-Particles and Induction of Magnetic field on Deoiling Hydrocyclone efficiency
Figure 6-2	Pressure drop between the inlet and overflow
Figure 6-2a to c	Effect of microparticles and magnetic induction on hydrocyclone split ratio at different mass flowrates
Figure 6-2d to f	Effect of concentration on split ratio for magnetic hydrocyclone, micro-doped hydrocyclone and conventional hydrocyclone
Figure 6-3a	Effect of microparticles and magnetic induction on the tangential velocity of hydrocyclone
Figure 6-3b	Effect of microparticles and magnetic induction on tangential velocity contours
Figure 6-3c	Effect of microparticles and magnetic induction on the axial velocity of a hydrocyclone
Figure 6-3d	Effect of microparticles and magnetic induction on the axial velocity contours
Figure 6-3e	Effect of microparticles and magnetic induction on the radial velocity of a hydrocyclone
Figure 6-4	Effect of magnet particle permeability on the efficiency of a magnetic hydrocyclone
Figure 6-5	Effect of magnetic particle on drag force
Figure 6-6	Effect of magnetic permeability on lift force
Figure 6-7	Effect of magnetic permeability on moment

Figure 6-8	Effect of magnetic permeability on hydrocyclone tangential velocity
Figure 6-8a	Effect of magnetic permeability on hydrocyclone tangential velocity- Contour plots
Figure 6-9	Effect of magnetic permeability on hydrocyclone Axial Velocity
Figure 6-9a	Effect of magnetic permeability on hydrocyclone Axial Velocity-Contour Plots
Figure 6-10	Effect of magnetic permeability on hydrocyclone Radial Velocity
Figure 6-11	Effect of magnetic permeability on hydrocyclone Turbulence Kinetic Energy
Figure 6-12	Effect of magnetic permeability on hydrocyclone Static Pressure
Figure 6-12a	Effect of magnetic permeability on hydrocyclone split ratio
Figure 6-13	Effect of magnetic density on hydrocyclone efficiency
Figure 6-14	Effect of magnetic density on hydrocyclone Split ratio
Figure 6-15	Effect of magnetic density on hydrocyclone Split ratio
Figure 6-16	Effect of magnetic density on hydrocyclone Tangential Velocity
Figure 6-17	Effect of magnetic density on hydrocyclone Tangential Velocity Contour Plots
Figure 6-18	Effect of magnetic density on hydrocyclone Axial Velocity Contour Plots
Figure 6-19	Effect of magnetic density on hydrocyclone Axial Velocity Contour Plots
Figure 6-20	Effect of magnetic density on hydrocyclone Radial Velocity
Figure 6-21	Effect of magnetic density on hydrocyclone Turbulence Kinetic Energy
Figure 6-22	Effect of magnetic density on hydrocyclone Turbulence Kinetic Energy Contour Plots

Figure 6-23	Effect of magnetic density on hydrocyclone Swirl Strength
Figure 6-24	Effect of charge density on hydrocyclone efficiency
Figure 6-25	Effect of charge density on hydrocyclone Split Ratio
Figure 6-26	Effect of charge density on hydrocyclone Velocities
Figure 6-27	Effect of charge density on hydrocyclone Turbulence Kinetic Energy
Figure 6-28	Effect of charge density on hydrocyclone Swirl Strength

## List of Tables

Table 1-1	Produced Water Treatment Equipment and oil droplet size separated
Table 1-2	Produced Water Treatment Equipment
Table 2-1	Currie Temperature of magnetic material
Table 3-1	The values of k- $\epsilon$ model constants
Table 3-2	Discretization table
Table 4-1	Hydrocyclone Geometry
Table 4-2	Fluid properties fed into hydrocyclone
Table 5-1	Properties of Fluid in hydrocyclone
Table 5-2	Different Cylindrical Dimensions Used
Table 5-3	Hydrocyclone with different Vortex Finder Dimensions
Table 5-4	The spigot geometries used in Spigot diameter analysis
Table 6-1	Hydrocyclone Geometry
Table 6-2	Magnetic permeability of different ferromagnetic materials
Table 6-3	Properties of Microparticle used for Density Analysis simulations
Table- 6-4	Magnetic particle properties at varying charge density

## Nomenclature

$C_1, C_2, C_\mu$	Coefficient in approximated turbulent transport equation
$C_D$	Drag Coefficient
$C_c$	Cunningham correction to strokes drag law
$C_{LS}$	Lift force coefficient
$C_{\gamma 1}, C_{\gamma 2}, C_{\gamma 3}$	Intermittency equation constant with value of 0.03, 50 and 0.5 respectively
$C_{e2}$	Constant
$d_p$	Particle diameter
$F_D$	Drag Force
$F_{length}$	Empirical correlation that controls the length of the transition region
$F_{onset}$	Transition onset trigger
$F_{turb}$	disabler of destruction or re-laminarization source in fully turbulent regime
$F_{\theta t}$	Blending function used to turn off the source term in the boundary layer and allow the transported scalar $\widetilde{Re_{\theta t}}$ to diffuse in from free stream
$F_{\theta t}$	Blending function
$F_{reattach}$	Function that disables the modification once the viscosity ratio is large enough to cause reattachment
$G_k$	Generation of turbulence kinetic energy due to mean velocity gradient
$G_b$	Generation of turbulence kinetic energy due to buoyancy
$i, j, k$	denotes Cartesian coordinate direction
$k$	Kinetic energy

$Pr_t$	Turbulence prandtl number
$P_{\gamma 1}$ and $E_{\gamma 1}$	Transition sources
$P_{\gamma 2}$ and $E_{\gamma 2}$	Destruction/re-laminarization sources.
$R_T$	Viscosity ratio
$Re_\nu$	Vorticity (strain-rate) Reynolds number
$R_y$	Wall-distance based turbulent Reynolds number
$Re$	Reynold number
$S$	Modulus of the mean rate of strain tensor
$S_{k\epsilon}, S_\epsilon$	User defined source terms
$S$	Mean strain rate
$S_{ij}$	Strain rate
$S$	Strain rate magnitude
$S_1$	Constant
$t$	time
$Tu$	Turbulence intensity
$U$	mean velocity
$U_P$	Mean velocity of the fluid at the near wall node P
$u, v$ and $w$	Velocities in the x, y and z direction
$V_t$	Terminal velocity
$Y_M$	Dilatation dissipation, this is normally neglected in an incompressible flow
$y$	Distance from the nearest wall
$y_P$	Distance from point p to the wall

$\rho_p$	Particle density
$\rho_L$	Liquid density
$\mu$	Viscosity
$\rho$	Density of fluid
$\mu_t$	Turbulence viscosity
$\varepsilon$	Dissipation energy
$\alpha$	Inverse prandtl number
$\mu_{t0}$	Turbulent viscosity calculated without swirl modification
$\Omega$	Swirl number evaluated
$\alpha_s$	Swirl constant
$\tilde{\Omega}_{ij}$	Rotation rate
$\Omega$	Vorticity magnitude
$\rho$	Density
$\gamma$	Intermittency factor
$\delta$	Boundary layer thickness
$\omega$	Dissipation
$\theta$	Momentum thickness
$\lambda$	Molecular mean free path
$\dot{\gamma}$	Fluid rate of deformation
$\mathcal{K}$	Von Karman constant (which is 0.4187)
$\mathcal{K}_p$	Turbulence kinetic energy at the near wall node P

# 1.0 Introduction

## **1.1 Research Motivation**

Produced water is a major by-product of oil and gas production with the estimated production rate expected to increase with the increase in well life. In 1999 it was estimated that over 210 million barrels of produced water are produced daily worldwide (Khatib and Verbeek, 2003) and in 2012 Igunmu (2012) noted that the daily production of produced water from oil and gas activities increased to approximately 250 million barrels per day. About 244 million tonnes of produced water was discharged into the sea in the year 2000 (Ekins, 2005) with an estimated dispersal oil of about 5768 tonnes while the rate of production of produced water in the UK increase by over 130% between 2011 and 2012 (TUV, 2013). UKCS reported that about 53 million m<sup>3</sup> of produced water was reinjected in 2017 while about 143 million m<sup>3</sup> (1.12 billion bbl) of produced water was discharged into the sea in 2017 along with about 2000 tonnes (2million Kg) of oil.

Some of the produced water was reinjected into the well. However, in the North sea the rate of reinjection is not very high, making the discharge of produced water into the sea very common in the North sea. Out of the 24.4 billion barrels of produced water produced in the USA in 2017, 37.9% was injected for disposal, 44% injected for enhanced oil recovery, 0.4% evaporated, 5.5% disposed via surface discharge, 9.9% disposed to offsite commercial disposal and 2.3% converted to other beneficial use. From this, it can be deduced that about 15.4% (3.76 billion bbl) of produced water was disposed to the environment in 2017 (USA alone). Although produced water is an inseparable part of the hydrocyclone recovery process; apart from the oil that it contains, it also includes other contaminants like dissolved formation minerals, production solids (including formation solids, waxes, asphaltenes, corrosion and scales products etc), radionuclides, chemical compounds (corrosion and hydrate inhibitors etc), dissolved gases etc (Ahmadun, 2009; Hansen 1994)



Produced water can undergo two types of treatment before disposal and these are the primary and the secondary treatments phases. The primary treatment phase involves separation of oil, water and solids while the secondary phase involves the removal of dissolved and other organic pollutants.

The oil in water exist in three different forms; dissolved, dispersed and free oil. According to OSPAR 2001/1, oil in water means the total hydrocarbon in water (free, dispersed or dissolved hydrocarbon)

Dissolved oil contains aromatic hydrocarbons (like benzene, ethyl-benzene, toluene and Xylene (BETX), naphthalene, phenanthrene, dibenzofluorene (NPD) and other polyaromatic hydrocarbons (PAHs)) and non-hydrocarbons like organic acids and phenols. The amount of dissolved oil in produced water varies from 100mg/l to 300000mg/l depending on the geological location and the age of the reservoir.

Dispersed oil contains aliphatic hydrocarbons with particle size ranging from 0.5-80µm, this is typically referred to as oil in water emulsion and can be stable for a significant period; therefore, separation of dispersed oil from produced water can be difficult depending of the particle size.

Free oil has a larger particle size ranging from 150µm and above; free oil can easily be seen floating on the surface of water. Produced water typically contains 0.1 to 10 volume percent of dispersed and dissolved hydrocarbons.

Before produced water can be disposed of, either into the sea or the environment, the oil in the water must to be reduced to an acceptable level stated by the regulatory bodies. The quantity of oil in water that can be disposed offshore into the sea differs between regions and countries (usually ranges from 15-30mg/l). In Europe, the OSPAR recommendation 2001/1 set a monthly average standard of 30mg/l for dispersed oil in produced water; the US Department of Energy set a monthly average standard of 29mg/l (EPA, 2015; Ahmadun, 2009), while in Nigeria, the Department of Petroleum Resources set the monthly standard of 30mg/l. The International Maritime Organisation published regulations which stated that 15mg/l of dispersed oil in water can be disposed offshore. The focus of the current studies will be on offshore disposal because onshore, 98% of produced water is reinjected for enhanced oil recovery and for disposal purposes while only 9% of offshore produced water was injected in the US in 2007 (Liang, 2018) while the remaining 91% was discharged offshore.

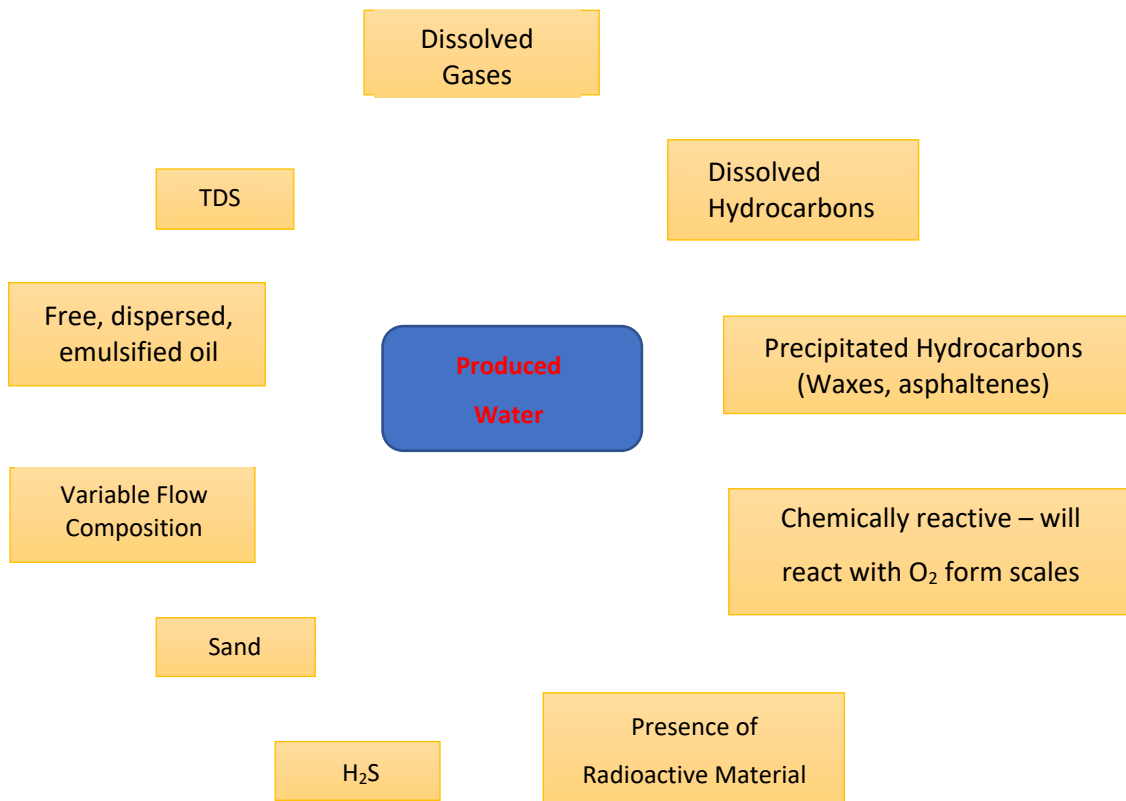


**Figure 1: Composition of Produced Water Generated in the Oil and Gas Industry**

**Table 1-1: Produced Water Treatment Equipment**

Process	Size of Hydrocarbon droplet removed (µm)	Oil inlet concentration (ppm)	Typical Specification Oil in effluent (ppm)
Skim Tanks	100-150	500-10,000	100-200
Coalescer	40	1000-4000	100-300
API Separator	100-150	Up to 20,000	50-100
Corrugated Plate Interceptor (CPI)	30-60	500-10,000	20-100
Hydrocyclone	10-15	Upto 5000	20-30

Induced Flootation	gas	5-10	Less than 500	15-50
Dissolved Flotation	Gas	2-5	Less than 500	10-40
Compact Unit	Flotation	2-5	Less than 500	5-15
Crushed Walnut		2	150-200	0
Dual media filter		2	Less than 30	0

To achieve the required quality of produced water for discharge, different equipment can be used depending on the droplet size (table 1). The tighter the oil in water emulsion, the more difficult and expensive it is to separate the oil from the water.

Dispersed emulsion can be classified into coarsely dispersed emulsions that contains droplets size more than 10 $\mu$ m; finely dispersed emulsion also known as secondary emulsion with particle size less than 10 $\mu$ m and are not easily separated from water. Factors that promote the formation of fine dispersed oil emulsion include increased turbulence, surface tension of the oil in water interface, viscosity of the oil, temperature and shearing of the oil droplet using mechanical equipment like pumps and choke valves

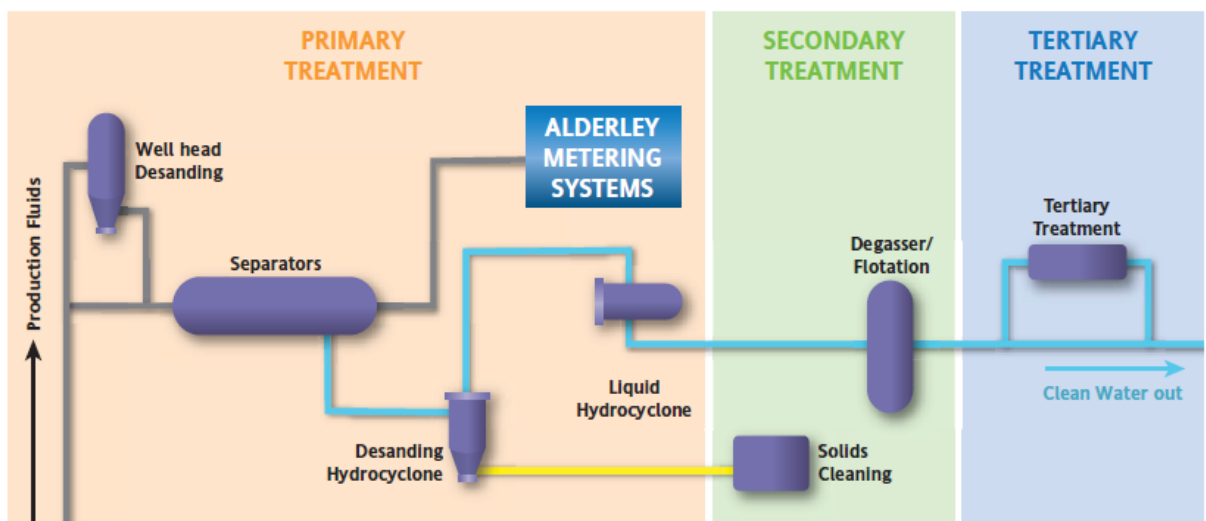


**Figure 1-2: Produced Water Treatment Layout**

Cleaning of fine emulsion requires the use of complex circuits consisting of several series of connected cleaning methods as shown in figure 2. The knowledge of how this finely dispersed oil can be separated easily and cheaply is imperative, based on the volume of produced water disposed into the sea every year.

## **1.2 Water Treatment Equipment for Fine Dispersed Emulsion**

There are three stages of treating produced water at the primary phase; primary, secondary and tertiary stages. Each stage tackles different pollutants with water becoming cleaner as it moves through the stages. The primary stage comprises of the use of API separator, skim tank, corrugated/parallel plate interceptor and hydrocyclone separator.

The secondary stage of produced water treatment includes the use of a flotation unit; induced gas flotation, dissolved gas flotation and compact flotation units. The last stage is the tertiary stage or polishing stage that involves the use of adsorption technology (crushed walnut and dual media filters etc), membrane technology and centrifuges. In oil and gas production, the hydrocyclone is mostly used to separate dispersed oil in water emulsion, and is the preferred option for the reasons in table 2 (the advantages and disadvantages of using each of this primary and secondary stage equipment). As can be seen in table 2, hydrocyclones are unable to separate fine dispersed emulsion (with particle less than 10µm) and are therefore unable to bring down the oil in water 15-30mg/l required by the regulatory bodies when the oil- water emulsion is tight (with very fine particles).

**Table 1-2: Produced Water Treatment Equipment**

	Principle	Advantages	Disadvantages
Skim Tank	Gravity Separation	Large surge capacity ensuring stable flow to downstream.  Large residence time and ensures solid separation	Large footprint area.  Occurrence of stagnant areas of fluid due to poor internal designs or build-up of solids.

API Separator	Gravity Separation	A simple design with large residence time that ensures solid separation.	<p>Old design, now replaced by corrugated plate interceptors</p> <p>Solids removal from the bottom is difficult and separated solids affect the separator efficiency</p> <p>Large footprint area</p> <p>Atmospheric Design- Cannot be used for PWRI</p> <p>Needs a degasser to be installed upstream</p>
Corrugated Plate Interceptor	Gravity Separation	<p>Corrugated plates enhance the degree of oil-water separation and therefore it requires significantly less space than a conventional API separator</p> <p>Atmospheric Design- Cannot be used for PWRI</p>	<p>Atmospheric Design- Cannot be used for PWRI</p> <p>Needs a degasser to be installed upstream</p>
Plate Coalescer (PPI, CPI and cross flows)	Coalescing and Gravity Separation	<p>No moving parts and simple control</p> <p>Little maintenance or attention required</p> <p>High efficiency at particle size more than 10microns</p> <p>Can handle high levels of oil in the produced water</p>	<p>Plates can be blocked with solids or fouling hydrocarbons. Cannot effectively separate fluid with high viscosity</p>

		Capable of handling relatively large oil content fluctuations	
Hydrocyclone	Centrifugal Force	<p>Compact in design, small footprint compared to other oil- water separation equipment.</p> <p>High separation efficiency of 10-15<math>\mu</math>m</p> <p>Flexibility for volume change/ high volume flowrate.</p> <p>Versatile application</p> <p>No downtime for recovery or maintenance</p> <p>Operates at a wide range of temperatures and pressures</p> <p>Insensitive to platform motion</p> <p>Hydrocyclone can be used where there is restraint in power supply as this equipment does not require the use of any outside energy expect for the energy used by the recirculating pumps where required</p>	<p>Difficult to separate particles of similar densities</p> <p>Energy requirement to pressurise Inlet is high</p> <p>Inability to handle viscous flow</p> <p>Extremely high velocities cause abrasive wear</p> <p>Hydrocyclones cannot produce completely dry underflow</p> <p>Inefficient in separating particles less than 10<math>\mu</math>m</p> <p>Used when an appreciative amount of free gas is not present</p>

		Brings down oil in water to 15-30ppm required by the different regulatory bodies	
Induced Gas Floatation	Froth Floatation	<p>Low CAPEX</p> <p>Shear forces required to generate the micron sized gas bubbles reduced the size of the oil droplets which adverse effect on the overall efficiency.</p> <p>Accepts high inlet concentration, relatively insensitive to changes in oil droplet size</p> <p>Requires steady flow for effective operation</p>	<p>Normally requires de-oiling chemical to be dosed upstream to optimize performance</p> <p>High OPEX</p> <p>Adversely affected by platform motion</p> <p>Cannot be used when there is restraint in power supply</p>
Dissolved Gas Floatation	Froth Floatation	<p>The method of producing bubbles is relatively gentle. The absence of High Shear Forces helps better separation.</p>	<p>Moving parts and associated maintenance requirements</p> <p>De-oiling chemicals normally dosed upstream to optimize performance</p> <p>Gas solubility decreases with increasing temperature which can make the technology less effective at higher operating temperatures</p> <p>Adversely affected by platform motion</p>

			Cannot be used when there is restraint in power supply
Compact Flootation Unit	Froth Flootation and Cyclonic Effect	Residence times in CFU's are significantly lower than traditional IGF systems, with residence times of 1 minute being typical, compared to 4 minutes for IGF systems.  Significantly smaller and lighter than conventional IGF  Excellent turndown	Requires deoiling chemical to be dosed upstream to optimize performance  Sensitive to vessel motion Adversely affected by platform motion  Cannot be used when there is restraint in power supply
Crushed Nut Filter / Dual Media Filter	Hydrophillic Nature of Crushed Nut Shells	High quality water effluent  Very efficient for IW  Removes TSS in addition to OiW  The crushed nut shells have an affinity to hold the oil particles and the suspended particles	The backwash mechanism is high on energy and maintenance  Erosional issues due to abrasive nature of media  Large and heavy equipment.

At present to separate finely dispersed oil from water, the use of flotation units are employed which are more expensive to build and operate, have a large foot print, are not quite suitable for offshore as it can be adversely affected by platform motion and requires use of de-oiling chemical upstream of the equipment to optimize performance. Therefore, the optimisation of the hydrocyclone to separate these fine particles will be a welcome development in the industry.

Hydrocyclones also referred to as cyclones, are mechanical separation devices originally designed to promote solid-liquid separation and are frequently used in



mining, pharmaceutical, and chemical industries etc to separate solid particles from liquid media; further research performed in Southampton University (in the 1970s and 1980s) led to the design and commercialisation of a liquid- liquid hydrocyclone (Thew, 1986).

The hydrocyclone operates by fluid entering the cyclone tangentially via the inlet opening into the cylindrical section creating a swirling flow (vortex). The swirling flow (vortex) generates a high centrifugal force required to separate the particles from produced water thus a heavier fluid fraction spin to the wall of the cyclone whereas the lighter fluid fraction migrates towards the core of the cyclone. The swirling movement causes the flow pattern in the hydrocyclone to contain a spiral within another spiral with the inner spiral moving upwards while the outer spiral moves downwards thus creating a forced vortex at the area close to the axis and free-like vortex at the outer wall. The outer vortex moves downward to the underflow while the inner vortex flow moves in the reverse direction to the overflow.

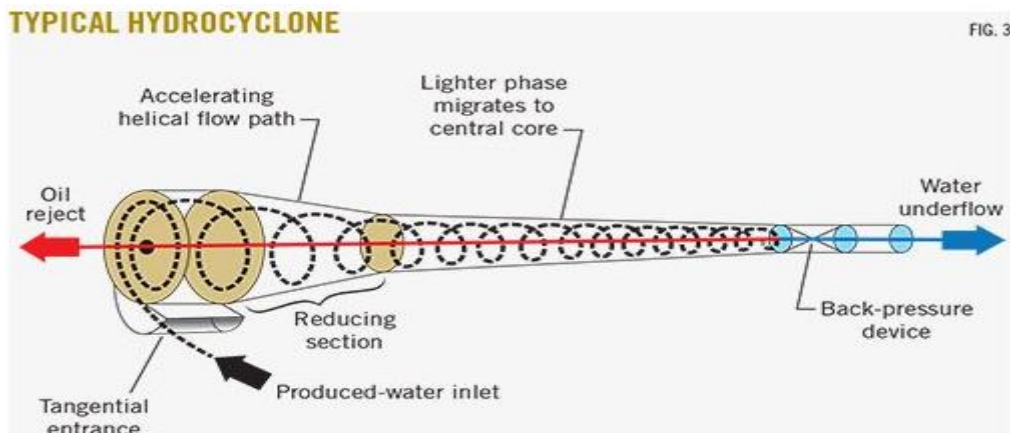


**Figure 1-3: Doiling Hydrocyclone Separation**  
Koleshwar S. et al, 2012

The ability of the hydrocyclone to separate particles is governed by Stokes law and the ease of separation is directly proportional to the particle diameter, the density difference with the particle and the liquid phase and inversely proportional to the viscosity of the continuous liquid phase.

$$V_t = \frac{gd_p^2(\rho_p - \rho_L)}{18\mu}$$

Where  $V_t$ - terminal velocity,  $d_p$  -particle diameter,  $\rho_p$ - particle density,  $\rho_L$ - liquid density and  $\mu$ - viscosity.

Hydrocyclone separation efficiency reduces when the particle size is less than 20 $\mu\text{m}$  and below (Jiang, 2019; Tang, 2016). Many research works have been carried out on the improvement of hydrocyclone separation efficiency, but none have been able to efficiently separate particles less than 10 $\mu\text{m}$ . This research has investigated how a hydrocyclone can be used to separate fine dispersed oil from produced water in order to reduce the cost of treating produced water, maximise space where there are space constraints and generally be versatile equipment for offshore produced water treatment irrespective of the location and weather condition.

### **1.3 Research Aim and Objectives**

This section presents the overall aim and objectives of this research

#### **1.3.1 Aim**

The overall aim of the PhD research work is to develop a novel method of improving hydrocyclone effectiveness to separate fine dispersed oil from produced water and fine solid particles from liquid stream by establishing design parameters through Computational Fluid Dynamics simulation.

#### **1.3.2 Objectives**

Specific objectives of the PhD are:

To establish numerical approaches and multiphase models that can be used for simulating separation oil -water in the hydrocyclone to predict the effect of flow conditions influencing the separation of oil and water.

To establish the accuracy of CFD predictions by comparing simulation results against published experimental data in predicting flow and separation of oil particles from water in the hydrocyclone.

To establish the performance of the hydrocyclone separator by investigating the effect of hydrocyclone geometrical parameters in the separation of oil from produced water with attention to the inlet diameter, spigot diameter, vortex finder diameter and cylindrical section.

To establish the effect of using micro-particles in optimising the separation efficiency of fine oil particles from produced water in a hydrocyclone

To establish the concept of a magnetically induced hydrocyclone with micro-particles in comparison with conventional hydrocyclone in separating fine dispersed oil from water and sand particles from water of less than 10 micron.

### **1.3.3 Thesis Outline**

Chapter 1 introduces the background of the problem identified in produced water treatment and the present study concerns. It provides an overview of the research motivation which details the significance of the present study; and the study aim and objectives.

Chapter 2 reviews the literature relating to the research investigation on the treatment of oil emulsion in the oil and gas industry and most especially using a hydrocyclone, numerical analysis of flow in a hydrocyclone, the effect of geometry on hydrocyclone separation, the chemistry behind the use of micro-particles in a hydrocyclone, the effect of concentration, flowrate in a hydrocyclone and the forces acting in a hydrocyclone. The chapter concludes with a discussion of reducing the relevant of efficiently separating fine dispersed oil emulsion using a hydrocyclone and the relevance to the industry.

Chapter 3 evaluates the methodology used in optimising the efficiency of the hydrocyclone for fine-dispersed oil emulsion. It describes the computational fluid dynamics methods for multiphase flows with a detailed description of the numerical equations and closure models in a hydrocyclone. It also briefly looks at the methodology of using applying microparticles in hydrocyclones.

Chapter 4 describes the numerical solution procedures, the mathematical equations for the multiphase flow and all the procedures used to obtain realistic results in hydrocyclone simulation. This chapter also covers details of mesh independence and validation of the numerical framework prediction of flow in hydrocyclone.

Chapter 5 presents the results of the numerical prediction of the effect of different geometrical parts of the hydrocyclone and how these geometrical parts affect the separation efficiency of the hydrocyclone.

Chapter 6 presents the result of the numerical analysis of the use of the micro particle and magnetically induced hydrocyclone in the separation of fine-dispersed oil emulsion and its effect on separation efficiency, particle size distribution, turbulence of flow, and pressure and forces acting in the hydrocyclone. This chapter will also look at the use of microparticles and the magnetically induced hydrocyclone in the separation of fine sand particles and its effect on separation efficiency, particle size distribution, turbulence of flow, pressure and forces acting in the hydrocyclone.

Chapter 7 presents the conclusion drawn from the findings of the present study and the recommendations for future work

## **2.0 Literature Review**

### **2.1 Hydrocyclone Velocity and Force Profile**

The velocity of fluid entering the cyclone is in three components; tangential, axial and radial. The tangential velocity acts perpendicular to the wall, the radial velocity towards the centre while axial velocity acts towards the longitudinal axis of the cyclone, the axial component is negative (downward) close to the wall in the cone section and positive upward near the core increasing towards the spigot (underflow).

The tangential velocity generates centrifugal force which separates the higher density particles from the lower density particles. The radial velocity on the other hand has a magnitude smaller than the axial or tangential velocity and is directed towards the centre of the cyclone and increases towards the apex thus moving the lighter density particles to the overflow while the larger density particles are moved to the wall of the cyclone thus causing separation

Afolabi (2012) in his dissertation explained the effect of tangential, radial and axial velocity in a hydrocyclone. It was stated that the tangential velocity component is the main velocity component that affects the swirling flow field and its interaction with strong shear in the radial direction produces centrifugal forces that determine particle separation. Afolabi's (2012) explanation of the velocities in the hydrocyclone was similar to the conclusion of other researchers (Fisher, 2002; Cilliers, 2011). However, none of these researchers analysed the detailed forces in the cyclone.

The direction of particle motion/separation in solid-liquid is affected by the total forces acting on the particle (Ji, 2016; Zhang, 2017) and these forces are drag, centrifugal and pressure gradient. The centrifugal force is outward with positive values while the drag and pressure gradient forces are inward and have negative values (Ji, 2016; Salimi, 2011; Afolabi, 2012; Ciller 2002). Other types of force

that can act on particles are mass force, Saffman lift force, magnus force and Basset force; these forces are considered to have a minimum effect on particle separation.

According to Saidi (2012), in liquid-liquid hydrocyclone, separation of large droplets starts from the cylindrical part of the hydrocyclone; by reducing the size of droplets the location of separation is shifted towards the underflow (in the conical section) of the hydrocyclone. However, the separation of solid from liquid takes place in the conical section of the hydrocyclone (Ji, 2016).

Saidi (2012) stated that because the density difference between the continuous and the dispersed phase is small in a liquid-liquid hydrocyclone; in addition to the drag force acting on the hydrocyclone, the pressure gradient, virtual mass force should be also considered in analysing the forces in a liquid-liquid hydrocyclone. The drag force coefficient in liquid droplets was also stated to be different from that of solid particles. The drag force causes the oil at the core region of the hydrocyclone to be trapped in the reverse flow taking fluid to the vortex finder of the hydrocyclone (Al-Kayiem, 2014).

Studies have shown that the two main forces (centrifugal force and drag force) acting in a hydrocyclone are influenced by the particle size distribution (Song, 2016; Zhang, 2017); however, others like Zhang (2017) considered the pressure gradient force significant enough to be mentioned. Both small and large particles are influenced by the drag force but in different directions.

The large particles are mostly influenced by the outward drag which pushes the particles away from the rotating reference frame. The centrifugal force on the otherhand is a fictitious force peculiar to a particle moving on a circular path, it has the same magnitude and dimensions as the force that keeps the particles on its circular path but points in the opposite direction. Therefore, can be defined as the outward inertial force apparent as the axis of rotation passes through the coordinate system's origin, the centrifugal force is directed radially outwards from the axis.

For the small particles, the inward drag force is predominant and therefore these particles tend to move to the central zone of the cyclone. The outwards drag gradually decrease with increase in particle size thus the influence of centrifugal force minimal as particles are not been through out of the rotation axis.

The performance of hydrocyclones are often determined by evaluating the separation efficiency, split ratio and can also be implied by evaluating the pressure drop. The separation efficiency is defined as the ratio of concentration of the impurity removed in the hydrocyclone to the impurity feed into the hydrocyclone at the inlet. The separation efficiency of hydrocyclone is mostly affected by the centrifugal effect generated by the rotational liquid flow (Hwang, 2008). Hence, efficiency is greatly affected by the particle or droplet diameter, the composition of the liquid and the inlet velocity of the fluid.

Using computational analysis, the efficiency is calculated using equation stated by Azimian (2015)

$$\eta = \frac{w_{p,inlet} - w_{p,overflow}}{w_{p,inlet}} \times 100\% \quad 2-1$$

Where the  $w_{p,inlet}$  and  $w_{p,overflow}$  is the percentage by weight of particle at the inlet and overflow section respectively.

According to Wang (2006), increasing the inlet velocity or decreasing the particle/water ratio can improve the separation efficiency in a hydrocyclone with smaller particles mostly affected by these changes. In a conventional hydrocyclone, the separation efficiency of the hydrocyclone increases with increase in particle size and a typical hydrocyclone efficiency curve is illustrated in Mokni, (2019) Wei, (2017); Yang, (2010). The hydrocyclone efficiency curve shows the probability of particle or droplet reporting to the underflow or overflow respectively.

Yang (2010) evaluated the separation efficiency in a solid-liquid hydrocyclone using a two cone hydrocyclone and the result showed that as the particle size increases from 5 $\mu$ m to 35 $\mu$ m, the separation efficiency increases from less than 10% to 100%.

Larger particles produced better separation in the hydrocyclone thus the larger the particle in the hydrocyclone the more efficient the separation (Liu, 2016; Tang, 2018). As the particle size increases, the number of particles reporting to the overflow section of the cyclone decreases indicating better classification/ separation of the bigger particles (Tang, 2018; Shojaeefard, 2006; Cui, 2017).

The split ratio can be defined as the ratio of the volume of overflow to the volume of flow of inlet; the split ratio reflects the situation of flow distribution in the hydrocyclone. Increase in split ratio in oil-water hydrocyclone means more water will be separated out from the underflow outlet of the hydrocyclone. However, when the split ratio is relatively small, more water will be separated out from the oil outlet (overflow section) thus the split ratio can indicate the overall performance of the hydrocyclone. It can therefore be concluded that improving the split ratio or optimisation of split ratio can contribute to improving the separation performance of the hydrocyclone.

## **2.2 Turbulence Models Used in Hydrocyclone Simulation**

In the early days of hydrocyclone invention, experimental studies were the only way of evaluating fluid flow in hydrocyclone (Kelsall, 1952; Ohasi and Maeda, 1958; Bradley, 1965; Svarovsky, 1965; Mendronho, 1984; Rietema, 1961). Fluid flow in hydrocyclone was first successfully predicted numerically by Pericleous in 1986 using a Prandtl mixing length model and asymmetry assumptions. In recent years numerical simulations used in determining the flow in a hydrocyclone have improved with the use of incompressible Navier-stokes equations with suitable turbulence models.

The same model used for numerical evaluation of a solid- liquid hydrocyclone was seen to be good for liquid-liquid and other forms of cyclones (Jiang 2019; Zhang 2019; Jiang 2019; Zhao , 2019; Huixin , 2017; Yumeng 2017; Shalaby , 2015; Al-Kayiem, 2019). This is because the principle of separation in a hydrocyclone is the same irrespective of the particle type been separated. A review of different turbulence models used for analysing flow in a hydrocyclone were seen in the literature with the models producing different results, thus making the choice of a turbulence model used in hydrocyclone simulation an important parameter that needs to be reviewed in order to achieve the best result through computational analysis. With increasing use of computation analysis in evaluating flow in hydrocyclone, different developed turbulence models have been used to evaluate the flow in a hydrocyclone. Some of the turbulence models evaluated in the past are the algebraic stress model, k- $\epsilon$  models, Reynold stress model (RSM) and Large Eddy Simulation (LES).



Hargreaves (1990) used the Algebraic stress model with 2D cylindrical coordinate systems to model flow in a deoiling Hydrocyclone, ignoring particle/particle interaction, coalescence and slippage while in 1994 the Dyakowski simulation assumed the flow in the hydrocyclone as axi-symmetrical and solved a two-dimensional equation using the  $k-\epsilon$  model. All these authors' claims were acceptable results when compared to experimental data. To evaluate how these turbulence models perform against each other, comparison of the turbulence models was evaluated.

Delgadillo (2004) compared the use of the renormalisation group (RNG)  $k-\epsilon$  model with RSM and LES in the modelling of the air core in a hydrocyclone and found that LES simulation produces more accurate results when compared to experimental results than the  $k-\epsilon$  RNG or RSM models. This is because LES captures the dynamics of large vortex structures without any modelling assumptions, therefore allowing accurate prediction of the velocity profile. It was however noted that the predictions of LES when compared to experimental results were weaker at the walls where molecular viscosity has a significant effect. LES was also seen to work well when the concentration of the particles is low.

Narasimha (2007) also modelled aircore in hydrocyclone using RSM and LES. The result showed that RSM is in good agreement with velocity measurements (axial, tangential and radial) while LES provides additional accuracy in predicting the velocity profiles or the grade efficiency of the hydrocyclone. Other studies have also produced similar results (Slack, 2000; Delgadillo, 2005 and 2009; Brennan, 2006; Brennan, 2007; Narasimha, 2007).

Shalaby (2015) used the  $k-\epsilon$ , RSM and LES models to evaluate the turbulent flow in a hydrocyclone. The results were evaluated by comparing the velocities profile of the models with the experimental result. According to Shalaby (2015), LES predicts the tangential and axial velocities better than the RSM and  $k-\epsilon$  models. For the  $k-\epsilon$  model, the maximum tangential velocity was seen to be maximum at the wall of the cyclone in contrary to a zero tangential velocity when experimentally measured. The result considered the  $k-\epsilon$  model weak as this does not properly model velocity profile and flow phenomena in the hydrocyclone.

Jafari (2017) compared the use of SST with curvature correction,  $k-\epsilon$ , SSG RSM and LES models. According to the study, the velocity distribution in the near wall

region and in the shear region between downward flow near the wall and upward flow near the centreline are the most challenging features of modellers. Jafari (2017) concluded that all models considered agree with the experimental tangential velocity and the width of the vortex core well except for the k- $\epsilon$  model. The k- $\epsilon$  model predicted the vortex core to be too wide and thus had the problem of predicting the location of the peak tangential velocity, also it failed to reproduce the mean axial velocity. He concluded by pointing out that RSM shows it could work with coarse grids and required less computation time compared to SST and LES models.

Saidi (2011) compared the use of the k- $\epsilon$  model with LES in a deoiling hydrocyclone and concluded that the results of k- $\epsilon$  models have high numerical diffusivity while LES gives better prediction of the flow when compared to the experimental results. Saidi (2011) et al also attributed the better separation efficiency seen in the simulation to better axial velocity and horizontal pressure gradient in LES simulation. From the above review, RSM and LES are well validated for predicting the flow in a hydrocyclone compared to other forms of RANS equations.

The turbulence model is seen to affect all the fluid flow parameters (Jafari, 2017; Shalaby, 2015; Saidi, 2011) and therefore affects the separation efficiency of the Hydrocyclone. The geometrical parameters of the cyclone itself and the operational parameters can influence the separation of particles and the overall fluid flow in the Hydrocyclone

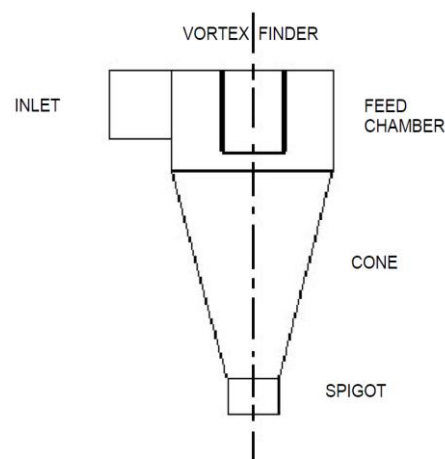


**Figure 2-1: Hydrocyclone Geometrical Parts**

## **2.3 Effect of Geometrical Parameters in Hydrocyclone**

### **2.3.1 Overflow Section**

The influence of the vortex finder on the Hydrocyclone has been reviewed by many researchers. According to Belaidi and Thew (2003), the geometry of the overflow/vortex finder of a hydrocyclone is an important parameter in the separation and control process. Over the last couple of years researchers have used two different variables to express the vortex finder; use of the ratio of vortex finder diameter to underflow diameter and the use of the ratio of vortex finder length to Hydrocyclone length.

In the earlier years of Hydrocyclone design the ratio of vortex finder to underflow diameter were considered as a geometrical variable to be used in evaluating the separation Hydrocyclone. Concha F. 1996 evaluated the air core diameter (in rope and spray discharge conditions) using the ratio of vortex finder to underflow diameter and according to the research the ratio of underflow to vortex finder diameters separate from the region of rope and spray discharge. Moder (1952), Kelsall (1953), Rietema (1961), Svarovsky (1984) all used the ratio of vortex finder to underflow diameter to evaluate separation in the Hydrocyclone.

Shah's (2006) experimental studies on the development of water split however show that use of the ratio of underflow to vortex finder in evaluating Hydrocyclone separation is misleading because the ratio of underflow to vortex finder diameter can be kept constant by changing the dimensions of the spigot and vortex finder and their effect is bound to be different. The result of the experimental studies also reflects that the effect of vortex finder diameter and underflow diameter on Hydrocyclone separation are dissimilar thus suggesting that the underflow orifice and vortex finder should be considered as independent variables when evaluating the separation in the Hydrocyclone. Other researchers who have carried out similar studies on are Ghodrat (2014) and Long Ni (2018) among others.

Generally, the use of the ratio of the vortex finder to cylindrical length is an acceptable way of evaluating the effect of the vortex finder in a Hydrocyclone. Farias (2011) reviewed the influence of the vortex finder on the separation efficiency of a conventional deoiling hydrocyclone and found that increasing the

overflow diameter (vortex finder) increases the separation of all the phases but equally observed the presence of sand and water at the overflow of the cyclone which otherwise decreases the separation efficiency of the deoiling Hydrocyclone. In the work of Ghodrati (2013), the separation efficiency of particles increases with the decrease in vortex finder diameter (using a vortex finder diameter ranging from 25mm to 75mm)

Vieira L.G, 2013 looked at the effect of overflow diameter in an unconventional Hydrocyclone and his result corresponds to Farias. It was found that the overflow diameter is inversely related to the underflow to through put ratio and therefore is an influence on the separation efficiency. The result showed that decreasing the overflow diameter by 45% increases the underflow through put by about 175% and the overall efficiency by 10.5% and recommends the use of a smaller overflow diameter for the separation of fine particles. However, for concentrated suspensions; larger values of overflow diameter will be beneficial. Zhao (2014) correlated this with findings of a smaller overflow diameter giving a better efficiency.

Martinez (2008) is one of the researchers who investigated the effect of the vortex finder's length in a solid-liquid hydrocyclone. Martinez found that use of the vortex finder prevents the re-entrainment of particles in the overflow stream; the particles were rather made to flow downward by the outside wall. He further suggested that increasing the length of the vortex finder will give the particles more time to enter the underflow stream. However, if the vortex finder gets to the conical section, some sand particles might get into the overflow stream thus decreasing the separation efficiency of the cyclone.

The Martinez analysis found that the separation efficiency of the hydrocyclone is maximized when the vortex finder length is 10% of the total length. Patra (2017) performed a similar analysis on a conventional hydrocyclone and found that the efficiency of the hydrocyclone is maximised when the vortex finder length is 12% of the total length of the cyclone.

Tian (2019) computationally simulated the effect of vortex finder length ranging from 0 to twice the cylindrical section and found that with a vortex finder length less than the cylindrical length, the separation efficiency and the of the cyclone increases with the length of the vortex finder which is consistent with the result of many others (Hsu (2010); He (2013); Long Ni (2017)). But as the vortex finder length becomes longer than the cylindrical section the separation efficiency first decreases because of the cylindrical-conical section interface and further increases causing the separation efficiency to increase by up to 100% with a very poor split ratio (split ratio becomes inversely proportional to the length of the vortex finder) resulting in reduced efficiency.

### **2.3.2 Inlet Section**

Vieira (2011) performed experimental and numerical analysis on a hydrocyclone with different geometries and the result shows the effect of different parts of the hydrocyclone on the efficiency. Numerical studies performed showed that increase in inlet diameter ( $D_i$ ) resulted in a lower Euler number ( $Eu$ ) and therefore the pressure drops in the cyclone, increase in the centrifugal force in the cyclone and the overall efficiency of the cyclone is also increased.

TANG (2016) reviewed the effect of inlet configuration on solid-liquid hydrocyclone efficiency. It was observed from the simulation analysis that an increase in inlet diameter at constant flow rate decreases the split ratio of the cyclone and the magnitude of the axial velocity increases with an increase in the inlet diameter. However, it was concluded that the inlet diameter affects the separation efficiency in two ways. For a particle size less than  $20\mu\text{m}$ , no significant effect was seen on the grade efficiency but for a particle size greater than  $20\mu\text{m}$  a significant change in grade efficiency was observed with a decrease of inlet diameter; this is also one of the conclusions of Jiangang (2014) .

Elsayed (2010) studied the effect of cyclone dimensions (width and height) on the separation efficiency of a liquid-liquid hydrocyclone. It was observed that increasing the cyclone inlet dimensions decreases pressure drop, increases the cyclone cut off diameter, the vortex strength decreases and the overall efficiency decreases. It was seen that the highest value of decrease in static pressure was

observed with increasing inlet height while the tangential velocity maintained the Rankine profile of typical hydrocyclone. The highest value decrease in tangential velocity was observed with an increase of the inlet width, thus better separation was expected with a decreasing width of the cyclone inlet. In all, Elsayed (2010) concluded that changing the inlet width is more significant than changing the inlet height and the optimum ratio of inlet width to inlet height is between 0.5 and 0.7. Erikli (2015) numerically simulated the effect of inlet diameter on liquid-liquid hydrocyclone and found that a decrease in inlet diameter increases the flow speed and pressure loss increases in the cyclone and consequently separation efficiency increases. The effect of inlet diameter in a conventional deoiling and desanding hydrocyclone are different, thus a generally comparison of the effect of geometrical parameters on liquid-liquid and solid-liquid hydrocyclone is required.

Osei (2016) reviewed the use of inlet diameter as well as the use of single and dual inlet in a deoiling hydrocyclone. The result shows that a smaller dimensioned hydrocyclone of 30mm inlet width outperforms the 60mm inlet hydrocyclone, the comparison was done by evaluating the total pressure at the core of the cyclone with a 30mm width inlet being found to have a higher core pressure than a 60mm width inlet and the same trend of 30mm outperforming a 60mm width inlet was observed in a dual inlet hydrocyclone. Increased pressure at the core means more of the oil rich fraction concentrated at the core will be pushed to the vortex finder although this is just one of the contributors to the performance of the Hydrocyclone.

The dual inlet hydrocyclone is not very commonly used and is mostly seen in liquid-liquid, gas-liquid hydrocyclones but is not seen in any solid-liquid hydrocyclone reviewed. Osei (2016), compared the 30mm inlet diameter in a single inlet cyclone to the 30mm inlet diameter double inlet and observed that the 30mm single inlet hydrocyclone outperforms the 30mm dual inlet counterpart which is quite contrary to the work of other researchers.

Al-Kayiem (2019) compared the use of a dual inlet in a deoiling hydrocyclone to a single inlet hydrocyclone and found that the separation efficiency in a dual inlet outperforms the single inlet. This is attributed to the occurrence of many recirculation regions in the single inlet hydrocyclone with some spreading over

large areas while the dual inlet cyclone has virtually no recirculation zone. The occurrence of the recirculation was said to affect the segregation of the oil and water droplets as some oil droplets in the recirculation zone have an increased residence time but hardly go through classification in the hydrocyclone thus escaping unclassified so reducing the separation efficiency of the cyclone.

Sathish (2007), Lim (2003), Yan Yang (2017) among others all agreed with the fact that the separation efficiency of the hydrocyclone inlet increases with the use of a double inlet hydrocyclone compared with the single inlet hydrocyclone. The use of a dual hydrocyclone is an area that has not been properly explored and can be looked at in the future

### **2.3.3 Underflow Diameter**

The underflow diameter is usually adjusted to overcome the variable operational conditions of the feed flow to achieve the desired result thus using an orifice at the underflow section of the cyclone. Long Ni (2019) revealed that most commercial hydrocyclones apart from specialised hydrocyclone have variable underflow diameters, this is because correct adjustment of the underflow diameter is important for separation. From the experimental and numerical simulation conducted by Long Ni (2019), it was concluded that for optimum separation to be achieved, correct adjustment of the underflow diameter is critical and therefore it is very difficult to predict underflow pipe diameter.

Different operational parameters used with the underflow diameter in evaluating the effect of hydrocyclone underflow diameter have produced different results. The hydrocyclone must be designed with suitable appropriate underflow orifice diameter to achieve the desired separation efficiency. There have been several recommendations on what the orifice diameter should be over the years. Bradley (1965) recommended that the ratio of underflow diameter to the cylindrical diameter should be between 1:10 while Silva (2015) recommended a ratio of 1:6 for optimal efficiency and 1:12 to produce thick underflow (dewater solids). Arterburn reported that the underflow orifice must be large enough to prevent plugging of the exit of the cyclone and recommended an underflow orifice size of 10-35% of the hydrocyclone cylindrical diameter.

Ghodrat (2013) looked at the effect of feed concentration and underflow diameter in a hydrocyclone and reveals that the effect of underflow diameter is more pronounced when the feed concentration is high with particle separation cut size decreasing with increasing spigot diameter and it was shown that zero cut size (no separation) is achievable when the underflow diameter is large enough. Therefore, it can be deduced that a smaller micron particle less than 20 $\mu$ m will be difficult to separate using a larger underflow diameter. The result of Long Ni (2016) is similar to this where it was reported that as the underflow diameter increases, the separation efficiency reduces.

Freitas (2009) results show bigger underflow diameter lower efficiency, this agrees with what can be obtained in the industry as the Weir cyclone operating manual (2008) stated that a decrease in spigot(underflow) diameter will increase the underflow density and improve efficiency. While Mousavian (2008) explained this further by saying increasing the underflow diameter increases the downward axial velocity which in turn causes coarse particles to be trapped in the upward stream which then go to the overflow. Other researchers with similar results are Silva (2015), and Saengchan (2009).

According to Zhang (2019), the underflow diameter affects the air core diameter in the hydrocyclone, as the diameter of the underflow diameter increases the air core diameter was seen to increase. This was associated with the increased quantity of air that enters the cyclone as the underflow orifice diameter increases. The motion of air in the cyclone also changes as the underflow diameter increases. Rakesh (2014) studies show that as the underflow diameter increases, the low-pressure area occupied by air becomes bigger resulting in more pressure drop in the central zone of the hydrocyclone. The variation of air with inlet pressure is not pronounced with a larger underflow diameter.

### **2.3.4 Hydrocyclone Size**

Both the hydrocyclone diameter and length affect the separation performance of the hydrocyclone. The cylindrical diameter is generally referred to as the hydrocyclone size/diameter, that is a 10mm hydrocyclone is a hydrocyclone in which the width of the cylindrical section is 10mm. A larger hydrocyclone is less



effective in separating smaller particle size while the longer the cylindrical section is the less effective it is to separate particles from produced water.

Hoffman (2001) performed experimental and numerical simulation on the effect of cyclone length and found that cyclone efficiency improves with increased length but at an optimal length the efficiency will start to decrease. The optimal length to diameter ratio of 5.65 was said to be the peak, after which further increase in length decreases the separation efficiency of the hydrocyclone. The result of the simulation work also shows that the pressure-drop decreases with increasing length after the optimum length was achieved; which is consistent with the finding of Saengchan (2019), Vieira (2001), and Lakhbir (2015)

Lakhbir (2015) breaks the effect cyclone length further by looking at the effect of increasing the hydrocyclone cylindrical length and the result showed that increasing the cylindrical length by up to 5.5 times the cyclone diameter increased the pressure drop by about about 34%, while the efficiency was increased by about 9.5%. But increasing the cone length by about 6.5 times the cyclone diameter resulted in an increase of about 29% in pressure drop and the efficiency increased by 11% thus showing that increasing the length of the conical section can yield better results than than increasing the length of the cylindrical section of the hydrocyclone.

Saengchan (2019) reviewed the relation between the ratio of the cylindrical-conical length section on the separation performance of the hydrocyclone. The result of the experimental work performed at different ratios varying from 0.00-0.14 shows that a cylindrical-conical ratio of 0.11 yielded better separation than other ratios considering the changes in the cylindrical-conical ratio affecting the pressure drop in the hydrocyclone. Saengchan (2019) investigated the effect of different cyclone diameters in Hydrocyclone separation from the perspective of the connection between the cyclone length and the cyclone diameter.

The diameter of the cylindrical section is the main variable affecting the size of particle that can be separated; the size of commercial hydrocyclone ranges from 10mm to 2.5m (Cilliers, 2000). Separation takes place when a bigger cyclone is used for a smaller size particle. The problem is that a low amount of these particles

will be separated using a large cyclone. Endres (2012) used a 20mm hydrocyclone to separate solid particles from produced water; particles less than 20µm were separated through the process of recirculation of the overflow for about 120 minutes while 10mm hydrocyclone was used by Neesse (2014). Neesse (2014). results also show the separation of sub-micron solids from liquid using the recirculation through the process of optimising pressure and temperature of the inlet feed. Grady (2003) looked at the use of a 10mm cyclone in a deoiling hydrocyclone system. However, the result of the simulation only revealed the flow field difference when compared to a 76mm hydrocyclone. Wen-ching (2003) however, noted that the use of a small hydrocyclone can lead to the problem of particle bouncing and rebounding from the wall of the cyclone and recommended that cyclone size should be increased over a typical diameter dimension to counter this effect.

### **2.3.5 Cone Angle**

According to Cilliers (2000), the cone angle for classification of a hydrocyclone should be between 15-30 degrees, with smaller angles for fine cut sizes and larger angles for coarser cut sizes. This agrees with Svavosky (2000) who stated that at narrow angles, flow is suppressed, and this makes a cyclone more efficient in separating fine particles/droplets.

Vieira (2001) established that a larger cone angle led to reduction in efficiency as this aids the dragging of more particles to the overflow stream. This was linked to increasing radial velocity which resulted in higher radial force dragging particles towards the cyclone centre. Saidi (2013) collaborated in the work of other researchers with the result of the simulations run for a liquid-liquid hydrocyclone, showing that the enlarged cone angle increases tangential velocity and pressure gradient but reduces the separation efficiency of the cyclone. It was also noted that efficiency reduction was due to reduction of oil droplet residence time.

Minghu (2011) evaluated the effect of cone angle on pressure drop in a hydrocyclone and found that increasing the cone angle decreases the pressure in the cyclone. While this is not pronounced when the cone angle is already large, the effect is seen more when the cone angle is increased from a relatively small

angle to a larger one. Since the pressure drop is relatively proportional to the separation taking place in the cyclone, an increase in pressure drop (larger cone) thus leads to increased separation. However, when the optimal pressure drop is achieved, a further increase will result in decrease in separation efficiency.

Other work on the geometry of hydrocyclone includes the incorporation of other parts into the cyclone or changing the shape of the hydrocyclone parts to improve efficiency. Junxiang (2019) proposed the used arc inlet and convex cone and the result of the experiment and simulation shows the separation efficiency of the particle increasing from 0.849 to 0.956 (84.9% to 95.6%) but the efficiency of the separated fine particles was seen to reduce.

Yang (2019) changed the cylindrical part of the cyclone to tapered and conical shapes respectively and evaluated this against a conventional hydrocyclone. The result of the numerical analysis showed cut sizes of 13.05 $\mu\text{m}$ , 11.25 $\mu\text{m}$ , and 17.95 $\mu\text{m}$  were obtained when conventional, tapered and conical hydrocyclone were used respectively with a recovery rate of fine particles at 23.56%, 22.17% and 29.29%.

Junxiang (2019) also changed the shape of the hydrocyclone cylindrical section to a conical one. This was called a conical design, particles size ranging from 0.2 $\mu\text{m}$  to 70 $\mu\text{m}$  were fed into the cyclone. The results show micron particle classification with a demarcation of 5 $\mu\text{m}$  was accomplished with classification sharpness improving from 0.833 to 0.938. However, the efficiency of particles less than 10 $\mu\text{m}$  was not up to 20%.

Motin (2017) studied the effect of parabolic and hyperbolic wall profiles of the hydrocyclone swirl chamber and separation. The result shows that for an oil concentration of about 1%, the separation improved by 16.5% and 25% when hyperbolic and parabolic designs without tail were used compared with the conventional hydrocyclone. The comparison of the hyperbolic and parabolic design with tail to the conventional hydrocyclone shows an improvement of about 17% and 33% respectively. Vakamalla (2017) reviewed the use of some conical designs for high throughput and finer cut size separation and his result revealed that the cut size of the cyclone reviewed was improved to 8-13 $\mu\text{m}$  when compared to the conventional hydrocyclone with a cut size of 16 $\mu\text{m}$

Geometry is one factor that affects the separation efficiency/cut size of a hydrocyclone but most of the journals reviewed for geometry have one thing in common, the droplet sizes considered when geometry has been optimised were between 10-30 $\mu\text{m}$  and use of 10mm can improve the cut size to less than 10 $\mu\text{m}$  with poor separation efficiency. Therefore, changes in geometrical dimension alone can be said to have a great effect on large particle separation and little effect on finer particles.

## **2.4                      *Magnetic Hydrocyclone***

Siadaty (2017) used a new approach of separating fine particles (gas) of 2-4 $\mu\text{m}$  from solids using a hydrocyclone. The separation efficiency was improved by applying an external magnetic field, where the centrifugal force separates the large particles and magnetic force is used to separate the finer particles. The research shows that a magnetic field can be used to improve separation of the cyclone for ferromagnetic particles and non-ferromagnetic materials coated with ferromagnetic materials. Siadaty stated that in the absence of a magnetic field the drag force is the main force acting on the smaller particles and the effect of other forces like pressure gradient, Brownian, gravity etc are negligible. The Siadaty analysis of drag force in the cyclone complements the work of Zhang discussed earlier. The Saidaty result shows that for gas-solid separation; the separation efficiency of 2 $\mu\text{m}$  and 4 $\mu\text{m}$  was 82.96% and 97.78% respectively without the use of a magnetic field, while applying the magnetic field increases the separation efficiency to 91.11% and 100% respectively.

This is not the first time magnetic hydrocyclones have been used; the magnetic cyclone was first developed in the late sixties with the aim of providing an additional external force to supplement gravitational and centrifugal forces that cause classification and separation of solid-liquid (Rowson, 2003). In 1983 and 1985, Watson and Fricker proposed ways of separating particles from a cyclone using a magnetic field. In the Watson design the magnetic force is induced at the wall of the cyclone while in Fricker's design the magnetic force is applied at the centre of the cyclone.

Other researchers have also performed different experimental work on the use of a magnetic field to enhance the separation of metallic particles, this can be seen in the work of Premaratne et al (2003) and Fan (2016). Fan (2016) in his research fed a coal sample mixed with dense medium suspension into a cyclone and found that the magnetic field decreased separation density and this was caused by the downward flow of magnetite due to axial magnetic force.

Lin Liu (2019) was able to improve the separation efficiency of a deoiling hydrocyclone using a modified hydrocyclone shape and the application of magnetic force force at the centre of the cyclone. An improvement of 13.2% was achieved when compared to a conventional hydrocyclone. The question that arises from this type of design is, how easy will it be to have a magnet at the centre of a 4", 2" or 1" hydrocyclone and in an industrial setting where this cyclone is located in a vessel and how applicable is this principle? It is almost impractical to use where there are over 50 cyclones in a vessel (as is seen in the oil and gas industry) though this method can be used for a single large cyclone. Also, Lin Liu (2019) did not specify the cut size that was improved by this work.

Therefore, this study will employ the innovative use of the Watson magnetic hydrocyclone design to solve the problem of separating fine particles from produced water with the use of ferromagnetic microparticles.

## **2.5 Magnetic Material**

The magnetic materials are classified into three main different types depending on their interaction with an external magnetic field: the diamagnetic, paramagnetic, ferromagnetic; others are antiferromagnetic and ferrimagnetic materials.

Diamagnetism is a form of non-permanent magnet whose magnetism only persists in the presence of an external magnetic field; the magnitude of the magnetism is very small and is in the opposite direction to the external field thus weakly repelled by an external magnetic field. Under a uniform magnetic field the magnetism tends to move from the stronger to the weaker part of the field. The relative permeability of diamagnetic material is less than one and their magnetic susceptibility is negative (range of  $-10^{-5}$ ). This type of magnetism is mostly observed when other forms of magnetism are absent (Marghussian, 2015). Examples of diamagnetic materials are water, bismuth, mercury, silver, diamond, copper etc

Paramagnetism are magnetic materials that are weakly magnetised in the same direction as the magnetic field but possess no net macroscopic magnetization in the absence of an external magnetic field. The magnetism moves from the weaker to the stronger part of the magnetic field and the orientation of the magnetic moment is aligned in the presence of the magnetic field. The relative permeability is more than one and the magnetic susceptibility is between  $10^{-3}$  and  $10^{-6}$ . Examples of paramagnetic materials are aluminium, platinum, manganese, chromium, sodium, calcium, lithium etc.

Ferromagnetic material retains its magnetism after a magnet has been removed and is strongly magnetised under the influence of a magnetic field. When the applied magnetic field is removed, a part of the induced domain may be aligned making ferromagnetic material act like a permanent magnet. However, when these materials are heated above the Curie number it becomes a paramagnetic material. Ferromagnetic materials have a magnetic permeability as high as  $10^6$ . The most common ferromagnetic materials are those that contain iron, cobalt and nickel but other elements such as dysprosium and gadolinium and compounds such as chromium oxide and manganese bismide also demonstrate ferromagnetic properties

**Table 2-1: Currie Temperature of magnetic material**

Material	Curie Temperature (K)	Material	Curie Temperature (K)
Fe	1043	Fe <sub>2</sub> O <sub>3</sub>	948
Co	1388	CrO <sub>2</sub>	386
Ni	627	MnOFe <sub>2</sub> O <sub>3</sub>	573
Gd	292	FeOFe <sub>2</sub> O <sub>3</sub>	858
Dy	88	NiOFe <sub>2</sub> O <sub>3</sub>	858
MnAs	318	CuOFe <sub>2</sub> O <sub>3</sub>	728
MnBi	630	MgOFe <sub>2</sub> O <sub>3</sub>	713

Ferrimagnetism and anti-ferromagnetism; ferrimagnetism occurs when the magnetic moment of the magnet sublattices are unequal thus resulting in net moment. When the moments are equal and ordering occurs at the Neel

temperature in an antiparallel alignment to give zero net magnetization then it is referred to as Anti-ferromagnetism.

Magnetic materials relevant to this study are ferrimagnetic and ferromagnetic material. Both ferrimagnetic and ferromagnetic materials are similar; with the exception of equal magnetic moment in ferromagnetic material; other properties like the Curie temperature, spontaneous behaviour under the influence of a magnet, hysteresis and remanence are all the same. Most ferrimagnetic materials are oxides of iron and a typical sample of ferrimagnetic material is magnetite ( $\text{Fe}_3\text{O}_4$  and  $\text{Fe}_2\text{O}_3$ ).

Blaney (2007) revealed through electron probe analysis that as the size of the magnetite decreases, the concentration of oxygen in the magnetite decreases, thus decreasing the ion valence bond which supports greater ferrous ion presence. This consequently leads to a decrease in the spontaneous resistance of the magnetization thus an increase in magnetization is observed. The Blaney review also shows that magnetization in a magnetite (nano, micro or bulk) varies along the particle diameter with a high magnitude within the particle and a lower magnitude near the surface, therefore as the particle diameter is decreased the surface effect will ultimately affect the saturation magnetization. However, Thapa (2004) showed that the positive effect of decreasing magnetite size is limited to 10nm after which a further decrease will cause a decrease in saturation magnetization. In summary, the induced magnetic field is higher in a nano-scaled magnitude than that of a bulk magnetite when an external magnetic field is applied.

Not only is the property of nano-scale magnetite different from bulk magnetite, it also differs from the micron size particles. Generally, nano-scale magnetite is approximately one billion times smaller (by volume) than micron scale magnetite. Rivas-Sanchez (2008) experimental studies show that the magnetic susceptibility of a nano particle (2-14nm) is about 13% while that of micron-sized particle is less than 4.5% or higher (0.2-56 $\mu\text{m}$ ). The result of the experiment also reveals that the coercivity of micro particles of a size between 5.6 $\mu\text{m}$ -10 $\mu\text{m}$  is 2.8mT-3.927mT while coercivity of finer particles between 10-0.2 $\mu\text{m}$  increases from 5.15mT-11.09mT.

There are several methods that can be used to synthesise nanoparticles including magnetite and these include precipitation, polyol process, sonochemical synthesis, microemulsion and coprecipitation method, however this study will not be looking at the synthesis of nanoparticles.

## **2.6                      *Magnetic particles***

Magnetic nanoparticles are mostly oxides of ferromagnetic material. Magnetic nanoparticles are a class of nanoparticle material that can be manipulated using magnetic fields. The benefit of using magnetic nanoparticles includes quick movement of the particle in the direction of the external magnetic force, the fact that the surface can be modified to suit the contaminant to be removed, low cost and high efficiency can be obtained. Magnetic nanoparticles like  $\text{Fe}_3\text{O}_4$ ,  $\text{Fe}_2\text{O}_3$ , etc are form of nano-absorbent material while nanomaterials such as  $\text{ZnO}$ ,  $\text{TiO}_2$ ,  $\text{ZnO-CeO}_2$  etc are nanophotocatalyst material (Kumar, 2016). In oil water treatment, the nano-absorbent materials are mostly used, the magnetic nano-particles used ( $\text{Fe}_3\text{O}_4$ ,  $\text{Fe}_2\text{O}_3$ ,) act as a magnetic seeding agent that forms flocs with other suspended particles to be removed.

Of all the magnetic nanoparticles, the iron oxide nanoparticle (IONPs) is the most widely used and the most interesting as it possesses the additional property of magnetism. Once a ferrite particle is smaller than 128nm, it becomes superparamagnetic (An-Hui Lu,2007) which prevents self-agglomeration and thus can be used directly as nanoadsorbents or as the core component of core-shell structures, where the IONPs function as a magnetic separation material while the shell provides the desired functionality for pollutant adsorption. Nano-particles bigger than 128nm give rise to the difficulty of agglomeration of the nanoparticles due to Van der Waals forces. To overcome this difficulty of particles agglomerating, the nanoparticles are coated with polymeric material or surfactants (Opoku ,2017). A polymer-based nanostructure is not used in a hydrocyclone because of the possible breakage of the polymer coated nanoparticle in turbulence.

Boisson (2017) mentioned that the polymer used in water treatment is dependent on the water composition (thus the type of polymer used in oil-water emulsion is



different from the polymer required to separate sand), dewatering equipment (mechanical effect can break the polymer structure, therefore the type of polymer chosen to be used must be able to withstand the mechanical effect taking place in the equipment, for example in a centrifuge a structured polymer will be better than a linear one). Another factor that determines the type of polymer to be used is the availability of water for polymer preparation. In cases where a powder polymer is used then it will have to be dissolved in water before use and if there is insufficient water in the field then this will not be possible. This assertion was validated by Muhamad (2017) who was able to create a polymer nanostructure using high speed centrifugal force. Rather than breaking the polymer structure, the centrifugal force strengthened the polymer, showing that breakage of polymer in turbulence is dependent on the type of polymer used. Woodfield (2002) was also able to successfully separate flocculant using hydrocyclone, while according to the study of Plitt (1968) on hydrocyclone thickening with flocculation, flocs can be formed which can resist the shear force in a hydrocyclone. Therefore, flocs created as a result of the polymers addition to nanoparticles can be separated from the hydrocyclone without breakage.

Shao (2019) used polyvinylpyrrolidone (PVP) as a polymer to coat nanoparticles for the separation of oil emulsion from water. The result of the experiment showed that the introduction of PVP in a solvothermal process could significantly increase the demulsification efficiency of the magnetic nano-particles with demulsification efficiency decreasing with a decreasing concentration of the PVP and that the recovered magnetic nanoparticles (MNPs) could be used up to 5 cycles under acidic and neutral conditions.

Mirshahghassemi (2017) reviewed the application of high gradient magnetic separation for oil concentration using polymer-coated magnetic nanoparticles (NP). Mirshahghassemi used polyvinylpyrrolidone (PVP) coated magnetic nanoparticles (NP) with a high gradient magnetic separation technique for the rapid removal of oil from water mixtures in a continuous flow system and the result showed that an increasing magnetic field and inserting wool significantly increased oil and NP removal efficiencies. Atta (2017) in his research used liquid based on 1-allyl-3-methylimidazolium oleate to cap and stabilize the magnetite used for cleaning oil from water. An-Hui Lu (2007) listed polymers that can be used with

magnetic nano particles as polypyrrole, polyaniline, polyalkylcyanoarylates, polymethylidene malonate and polyesters such as polylactic acid, poly glycolic acid poly( $\epsilon$ -capro-lactone) and their copolymers.

Although polymer coated nanoparticles are increasingly used in wastewater treatment, the ease of separating these polymers from the liquid separated will pose a challenge thus the use of thermoresponsive polymers.

In a patent developed by Riele (2014) for Shell Petroleum, ferromagnetic nanoparticles were used to separate liquid-liquid by mixing the emulsion with ferromagnetic nanoparticles coated with thermoresponsive polymers with tunable lower critical solution temperatures (LCST). Exerting a magnetic field on the mixture of fluids and LCST polymer coated nanoparticles, induced LCST polymer coated nanoparticles to migrate and thereby separated the fluid adsorbed to the LCST polymer coated nanoparticles. After the emulsion separation, a change in temperature releases these nanoparticles from the extracted fluid and these particles can be reused for another cycle of separation.

While many authors have investigated the use of polymer to coat nanoparticle used for water treatment, others have just used the magnetic particle or nanoparticle alone. Juan (2017) used magnetic graphene oxide nanosheet for rapid efficient demulsification of oil in water emulsion, the separated oil was floated, and water removed. While Hatamie (2016) evaluated the use of nano-ferrofluid as a coagulant for surface water treatment, the use of the nano fluid was seen to effective in removing more than 90% of  $\text{Cd}^{2+}$ ,  $\text{Co}^{2+}$ ,  $\text{Mn}^{2+}$ ,  $\text{Fe}^{2+}$ ,  $\text{Pb}^{2+}$ ,  $\text{Zn}^{2+}$ ,  $\text{Ni}^{2+}$ , and  $\text{Cu}^{2+}$ , with the turbidity of the water decreasing by about 90% and equally performing as an excellent antibacterial removing 98% of fecal coliform bacteria, 97% of coliform bacteria and 60% of chemical oxygen demand (COD).

As can be seen from the review above, different authors have used different polymers in wastewater treatment, therefore it is imperative to know the exact type of polymer that is ideal for the separation of oil from water. This not only prevents agglomeration of the nanoparticles but at the same time enhances the deposition of the oil on the surface of the nanoparticle. The use of polymer on micro or nano-scale magnetic material modifies the resistivity of the material from the insulator realm to a semiconductor regime (Balney, 2007).

Based on the nature of the oil and gas industry and water industry, the nano particles must be able to adhere to the particles being separated from the produced water, thus the polymer that is required should be hydrophobic in nature. The polymer should also be resistible to turbulence in the hydrocyclone and easily detached from the separated particles (whether liquid or solid). Studies have shown that thermo-responsive polymers can be easily detachable.

## **2.7 Thermoresponsive polymers**

Responsive polymers are polymeric materials that fall into the smart material category, which show reversible transition in properties such as shape, solubility, surface characteristics, and molecular assembly in response to a stimulus (Teotia,2015). This stimulus could be temperature, magnetic field, electrical charges, light, biological and chemical stimuli etc. When the polymer response is to temperature it is called thermo-responsive polymer. Although extensively used in the pharmaceutical/biomedical industry, it has recently been used in oil- water emulsion treatment (Riele, 2014)

There are two different types of thermo-responsive material based on their phase transition when subjected to heat; lower critical solution temperature (LCST) and upper critical solution temperature (UCST). Polymers that becomes insoluble upon heating are LCST polymers while polymers that are soluble upon heating are UCST. Examples of LCST include N-isopropylacrylamide (NIPAM), N,N-diethylacrylamide(DEAM), methyl vinyl ether(MVE), N-vinylcaprolactam(NVCI) and their polymers, while examples of UCST are acrylic acid (AAc) and acrylamide (AAm). Among the LCST, polymer of NIPAM (PNIPAM) is considered as the gold standard of thermo-responsive polymer (Lutz,2006). The type of thermoresponsive polymer to be used depends on the temperature of the oil-water emulsion.

## ***Summary of Chapter 2***

The effect of hydrocyclone parts (cyclone diameter, vortex finder, spigot section and cone angle) on the separation efficiency, pressure drop, and the flow parameters were discussed. It was established that optimising hydrocyclone parts alone is not sufficient for the separation of particles less than 10 $\mu\text{m}$  in hydrocyclone.

The use of magnetic particles in the separation of oil emulsion was also shown. It was established that magnetic nanoparticles can be used to separate nano and micro sized oil droplets from water. The use of magnetic particles in the separation of oil emulsion in a hydrocyclone has however not been evaluated.

Therefore, in this current study it will be assumed that a thermo-responsive polymer will be added to the iron oxide magnetic particle (magnetite). The purpose of this innovative study is to numerically investigate the integration of magnetic particles into the oil water emulsion separation using a magnetically induced hydrocyclone (Watson design) with the aim of improving the separation efficiency of particles less than 20 $\mu\text{m}$  using a hydrocyclone.

The numerical investigation has provided further understanding of the usability of the magnetic hydrocyclone in oil separation. It also predicts the fluid flow regime process in separating small droplets of oil in a magnetic hydrocyclone. The separation efficiency of the magnetic hydrocyclone was reviewed with that of conventional hydrocyclone and analyses of changes found were discussed. The CFD approach used offered to provide more insight into the flow and forces in the magnetic hydrocyclone flow that might be difficult to measure experimentally.

### ***3.1 Modelling of separation of oil from produced water***

A hydrocyclone is effective equipment to use for separating particles from produced water. However, its separation efficiency decreases with a decrease in the particle size and it is generally known that particles less than 10 $\mu$ m cannot be efficiently separated from produced water using a hydrocyclone. In this study, an innovative way of separating oil droplets less than 10 $\mu$ m using a hydrocyclone was evaluated. This innovative approach to oil-water separation in a hydrocyclone incorporates the use of magnetic particles by way of doping the oil droplets with a magnetic particle (micron sized).

The magnetic particle is assumed to be coated with a suitable polymer. The addition of polymer or surfactants make magnetic particles oleophilic and hydrophobic in nature. This polymer coated magnetic particles are added to the produced water which causes the attraction of oil to the surface of ferromagnetic material. The magnetic particles not only induce magnetism into the fluid but also increase the density of oil for better separation. This study has focused on the complexity of inducing magnetism in a hydrocyclone for the separation of polymer coated ferromagnetically doped oil (PCFDO) from produced water. This was evaluated using computational fluid dynamics (CFD).

Certain preparation was assumed to have been made prior to feeding the hydrocyclone with PCFDO emulsion, the assumption ranges from the properties of the magnetite and polymer to be used and the preparation of the mixture of magnetite and polymer.

### **3.2 Concept of Magnetic Particle Doping**

Ferromagnetic particles (magnetite) with the properties stated below have been used (Walid, 2017; Zhdanov, 2015; Vella. 2012):

Properties of Magnetite

Density	5175kg/m <sup>3</sup>
Magnetic permeability	2.5 to 16 h/m
Electrical conductivity	10000 S/m
Charge density	7.02c/m <sup>3</sup>

The addition of polymer or surfactants makes magnetic particles oleophilic and hydrophobic in nature. The coated magnetite was added to the oil- water emulsion via gentle agitation prior to being fed into the hydrocyclone.

A three-dimensional transient state simulation has been run to predict the effect of doping oil droplets with polymer magnetic particles and how the introduction of magnetic field can improve the separation process of oil droplets with focus on a particle size less than 10µm.

### **3.3 Computational Fluid Dynamics**

Computational fluid dynamics (CFD) is the numerical analysis that enables the prediction of fluid flow, heat transfer, and related phenomena often referred to as a numerical experiment in a virtual laboratory. CFD is used in many industries including water treatment, food processing, marine engineering, automotive, aerodynamics and turbine design among others. This methodology is considered because it:

- Provides faster results (used when faster result is required)
- Can be used in the early stages of design
- Reduces risk involved in carrying out experimental work
- Is very cheap compared to experimental work
- Can be used to evaluate fluid flow that an experiment might not be able to deduce
- Analyses complex problems involving fluid-fluid, fluid-solid or fluid-gas interaction

The prediction of fluid flow in CFD is based on conservation laws governing the flow and is defined in terms of flow geometry, the physical properties of the fluid,

and the boundary and initial condition of the flow field (Howard H., 2004). However, a suitable numerical method needs to be applied for the solution of the conservation law. In these studies, CFD Ansys Fluent 18.2 was used to evaluate the following

- Validation of the experimental results with model results in order to make appropriate assumptions for the simulations work
- Investigation of the separation process of discrete phase particles from produced water
- Investigation of the influence of particle size, flowrate and concentration of fluid flow
- Parametric study of the comparison of the influence of geometrical parameter in liquid-liquid and solid-liquid separation
- Investigation of the influence of magnetic particles in oil- water separation
- Analysis of the effect of magnetic induction on PCFDO hydrocyclone flow through.

This chapter sheds light on the governing equations for modelling the flow of oil in produced water including the polymer coated ferromagnetically doped oil (PCFDO) in produced water under the influence of magnetic field. The procedure for solving the numerical equation was presented, the modelling parameter (including fluid properties, geometry, mesh) and boundary conditions were provided.

### **3.4            *Multiphase Flow Modelling Methods***

The fluid flowing in a hydrocyclone is classified as multiphase flow because there are at least two physical states of matter that exist (liquid-liquid, solid-liquid, solid-gas etc) and the flow is equally anisotropic (highly random and chaotic). In anisotropic turbulence flow, the flow is dominated by large eddies (object shape and dimension) and small eddies; the small-scale eddies become smaller as the fluctuation increases with an increase in the Reynold number. This makes the computing requirement for flow with a high Reynold number huge and modelling of such flow difficult. Studies have shown that not all turbulence models can be used to evaluate this sort of complex anisotropic flow in a hydrocyclone with many of these models producing inaccurate solutions to the conservation equations.

There are two approaches to modelling a multiphase flow; the Eulerian- Lagrangian model and the Eulerian- Eulerian model. In the Eulerian- Eulerian model; particles (including droplets, bubbles) are dispersed in a continuous fluid phase and these dispersed particles act as a continuum phase. The different phases are treated mathematically as interpenetrating continua. Therefore, individual particles cannot be tracked. The volume of one phase cannot be occupied by the other phase with the volume fractions assumed to be assumed to be a continuous function of space and time and their sum equals one (Wei Chen,2016).

Eulerian – Lagrangian tracks the movement of individual droplets, bubbles or particles through the continuum fluid phases to model the overall behaviour of the fluid flow. To evaluate the separation of particles in a hydrocyclone, a known quantity of particles to be separated from the produced water was imputed into the inlet as a dispersed phase and the amount of these particles coming out of the hydrocyclone overflow and underflow were noted. In order to be able to evaluate the quantity of particles coming out of the overflow and underflow as compared to the quantity at the inlet of the hydrocyclone, the particles need to be tracked, thus the use of the Eulerian- Lagrangian model in this study.

### **3.4.1 Eulerian- Lagrangian model**

In the Eulerian- Lagrangian approach the fluid phase is treated as the continuum phase by solving time averaged Navier-Stokes equations. However, the dispersed phase is solved by tracking the number of particles, bubbles or droplets through the calculated flow field (Fluent Manual, 2006). This model captures the interaction between the oil droplets and fluid. The dispersed phase particles trajectories are computed discretely at intervals in the fluid phase calculation. Therefore, detailing the behaviour of the particle motion simplifies the knowledge of the physical phenomenon shown in the solution of Newtonian equations of Lagrangian coordinates and conservation equations for the continuum phase.

Generally, the dispersed phase is assumed to have a low volume (less than 10%) when compared to the continuum phase although a high mass loading is acceptable. The particles of the dispersed phase are also assumed to be spherical



in shape. In produced water separation, the oil or sand to be separated are the dispersed phase while the continuum phase is the water phase. The principle of separating either oil or sand are different. With oil-water separation, the oil is discharged at the overflow section of the cyclone, while in solid-water separation, sand is discharged at the underflow section of the hydrocyclone. An important factor causing separation in the hydrocyclone is the density differential between the separating particles and the produced water. In a hydrocyclone, the particle motion behaviour is modelled by evaluating the forces acting on the dispersed phase.

The Lagrangian discrete phase model is adopted in this study because of its ability to track particles as a group and most especially because it is the recommended model for tracking liquid droplets like oil. The discrete element method is more appropriate for tracking solid particles. Using the Lagrangian model, the continuum and discrete phase can be coupled together. This allows the exchange of momentum and energy between the two phases (continuum and discrete) and the type of coupling used depends on the particle loading as this affects the degree of interaction between the phases. The interaction between the continuum and the discrete phase can be divided into three categories one-way coupling, two-way coupling and four-way coupling.

One-way coupling is centred on the prediction of the discrete phase flow field based on the fixed continuous phase, that is the discrete phase has no influence on the continuum phase. However, the continuum phase influences the discrete phase via drag and turbulence. This is normally used when particle loading is extremely low. Two-way coupling on the other hand captures the influence of the continuum phase on the discrete phase via drag and turbulence and the influence of the discrete phase on the continuum phase via reduction in mean momentum and turbulence. Two-way loading is usually used for intermediate particle loading. When the particle loading is high, in addition to the two-way coupling the pressure velocity stresses due to the particles are also evaluated and this is called four way coupling and only the Eulerian model can be used with this type of particle coupling method (Fluent manual, 2006). In this research, because particle loading is expected to be less than 10% in a hydrocyclone, the two way coupling approach was used.

With the coupling of the discrete phase with the continuum phase, the trajectories of the discrete particles can be in escaped, incomplete, trapped, evaporated or aborted form.

In fluent, particles are considered to have escaped if the trajectories terminate at the flow boundary for which the escape is set. When particle trajectories exceed the maximum allowable time step then it is declared incomplete. A trapped particle on the other hand has its trajectory terminated at the boundary for which the trap is set. When particle trajectories evaporate in the domain it is declared evaporated, and lastly an aborted particle is a particle that fails to complete due to numerical or round-off reasons.

### **3.5 Governing Equations**

The governing equations for the Eulerian- Lagrangian approach include the transport equations and the closure models. The mass and momentum conservation equation for two phase incompressible fluid (solid-liquid or liquid-liquid) are derived based on the description in Versteeg (2007), Fluent manual (2006), Blazek (2015) and Mazhar (2016) and are based on the principle of conservation of mass, momentum and energy (known as the Navier Stokes equation). The conservation of flow quantity means the total variation of flow in a volume and is the result of the total volume being transported across the boundary of any internal or external forces or sources acting on the volume, Blazek (2015). In the Eulerian- Lagrangian approach the mass and momentum conservation equation is given as follows:

#### **3.5.1 Continuity Equation**

Continuity Equation

The rate at which mass enter a system is equal to the mass out of the system plus the accumulated mass in the system. For unsteady three-dimensional incompressible fluid, density of fluid remains constant and the continuity equation is given by equation 3.1

$$\frac{\partial \rho_m}{\partial t} + \frac{\partial (\rho_m u_{mi})}{\partial x_i} = 0 \quad (3.1)$$

## Momentum Equation

The change of momentum of a fluid particle equals the sum of the forces on the particle (Newton Second Law). Therefore, the rate of increase of the momentum per unit volume is given by equation 3.2

$$\frac{\partial(\rho_m u_{mi})}{\partial t} + \frac{\partial(\rho_m u_{mi} u_{mj})}{\partial x_j} = -\frac{\partial P}{\partial x_i} + \frac{\partial P_s}{\partial x_i} + \frac{\partial \tau_{mij}}{\partial x_j} + \frac{\partial(-\rho_m \overline{u'_{mi} u'_{mj}})}{\partial x_j} + \frac{\partial}{\partial x_j} \left( \sum_{k=1}^n \rho_k u_{dr,ki} u_{dr,kj} \right) + g \rho_m \quad (3.2)$$

Where  $\rho_m$ ,  $u_m$ ,  $\tau_m$  and  $P_s$  are density, velocity, viscous stress and pressure of total discrete phase respectively. These equations are based on momentum theory under the assumption that flow is steady, incompressible, and the fluid is homogenous and viscous. The viscous stress ( $\tau_m$ ) and drift velocity are given by equation 3.2a and 3.2b respectively

$$\tau_{mjj} = \mu_m \left( \frac{\partial u_{mj}}{\partial x_i} + \frac{\partial u_{mi}}{\partial x_j} \right) \quad (3.2a)$$

$$u_{dr,ki} = \frac{(\rho_k - \rho_m) d_k^2}{18 \mu_w f} a_{ki} - \frac{4 \eta_t}{3} \left( \frac{\bar{v} \alpha_k}{\alpha_k} - \frac{\bar{v} \alpha_w}{\alpha_w} \right) - \sum_{k=1}^n \left( \frac{\alpha_k \rho_k u_{wk,i}}{\rho_m} \right) \quad (3.2b)$$

$\mu_m$  and  $\alpha_w$  are the viscosity and volume fraction of the continuous phase while  $\alpha_k$ ,  $\rho_k$ ,  $a_k$ ,  $d_k$  are volume fraction, density, acceleration and diameter of the discrete phase.  $u_{wk,i}$  is the velocity of the continuous phase relative to the discrete phase and  $\eta_t$  is the turbulent diffusivity. Figure 3-1 shows the coordinate of the hydrocyclone.

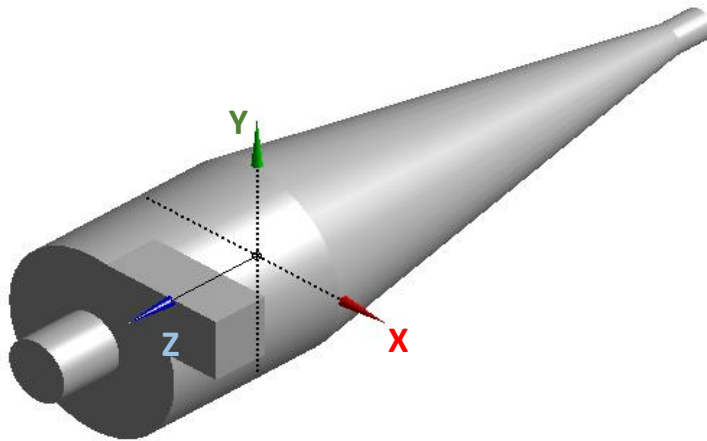


**Figure 3-1: Hydrocyclone Coordinate Sketch**

### **3.6. Turbulence Model**

The instantaneous fluid flow as a function of time in a hydrocyclone can be solved directly by using direct numerical simulation, DNS (defined as the complete three-dimensional and time dependent solution of the Navier-Stokes equation) or resolving the flow into small and large scale fluctuation by using large eddy simulation LES. However, both methods are computationally expensive as it takes more time to run these simulations. Studies have shown (Narasimha, 2007; Dejoan, 2007; Jafari, 2017) that numerical simulation carried out using the Reynold average Navier- Stokes (RANS) equations are computationally less expensive compared to DNS and LES and produced acceptable results even with coarser mesh structure and large time steps in the numerical simulation. Out of the RANS equations available, the RSM model is the most elaborate type of turbulence model that is recommended for modelling anisotropic flow (fluent manual, 2006).

The transport and closure models used in the modelling of fluid flow in hydrocyclone are very important because separation is based on the direction of movement of fluid particles in a hydrocyclone. The particle movement is dependent on how the flow turbulence is being modelled. The turbulence model not only affects how particles are separated but also the size of the particle.

Different turbulence models have been used over the years for the simulation of flow in a hydrocyclone, out of which are the RANS models (the most widely used of this RANS model is the  $k-\epsilon$  models and RSM models), Large Eddy Model (LES) and Direct Numerical simulation ((DNS). The comparison of the use of some of the RANS models ( $k-\epsilon$  models, transition SST and RSM) in hydrocyclone simulation is evaluated in the next chapter.

The  $k-\epsilon$  models resolve average turbulence stresses through modelling their own transport equations, while in the RSM model, each turbulence stress is resolved individually with anisotropy of turbulence having a dominant effect on the mean flow. All  $k-\epsilon$  models have similar transport equations for the turbulence kinetic energy ( $k$ ) and rate of dissipation ( $\epsilon$ ) but tend to differ in the method used for calculating turbulent viscosity.

### 3.6.1 Standard k-ε model

This model assumed flow to be isotropic and thus considers average and time scales.

The transport equation for the standard k-ε two equation model is given by equations 3.3 and 3.4 (Launder and Spalding, 1974)

$$\frac{D\varepsilon}{Dt} = \frac{1}{\rho} \frac{\partial}{\partial x_k} \left[ \frac{\mu_t}{\sigma_\varepsilon} \frac{\partial \varepsilon}{\partial x_k} \right] + \frac{C_1 \mu_t}{\rho} \frac{\varepsilon}{k} \left( \frac{\partial U_i}{\partial x_k} + \frac{\partial U_k}{\partial x_i} \right) \frac{\partial U_i}{\partial x_k} - C_2 \frac{\varepsilon^2}{k} \quad (3.3)$$

$$\frac{Dk}{Dt} = \frac{1}{\rho} \frac{\partial}{\partial x_k} \left[ \frac{\mu_t}{\sigma_k} \frac{\partial k}{\partial x_k} \right] + \frac{\mu_t}{\rho} \left( \frac{\partial U_i}{\partial x_k} + \frac{\partial U_k}{\partial x_i} \right) \frac{\partial U_i}{\partial x_k} - \varepsilon \quad (3.4)$$

In the standard k-ε model,  $\mu_t$  which is the turbulence viscosity is calculated using equation 3.5

$$\mu_t = \rho C_\mu \frac{k^2}{\varepsilon} \quad (3.5)$$

Where  $k$ - kinetic energy,  $\varepsilon$ -dissipation,  $t$  – time, subscript I, j, k denotes Cartesian coordinate direction,  $C_1$ ,  $C_2$ ,  $C_\mu$  are coefficient in the approximated turbulent transport equation and the value of these constants are given in table 3.1 below

Table 3-1: The values of k-ε model constants				
$C_\mu$	$C_1$	$C_2$	$\sigma_k$	$\sigma_\varepsilon$
0.09	1.44	1.92	1.0	1.3

### 3.6.2 Renormalization (RNG) k-ε model

RNG k-ε model is based on a theory that takes into consideration the prediction of swirl flow and strain rate variation. It is also capable of making the model more versatile than the standard k-ε model.

The transport equation is shown in equation 3.6 and 3.7 below

$$\frac{\partial(\rho k)}{\partial t} + \frac{\partial(\rho k u_i)}{\partial x_i} = \frac{\partial}{\partial x_j} \left( \sigma_k \mu_{eff} \frac{\partial k}{\partial x_j} \right) + G_k + G_b - \rho \varepsilon - Y_M + S_k \quad (3.6)$$

$$\frac{\partial(\rho\varepsilon)}{\partial t} + \frac{\partial(\rho\varepsilon u_i)}{\partial x_i} = \frac{\partial}{\partial x_j} \left( \sigma_k \mu_{eff} \frac{\partial \varepsilon}{\partial x_j} \right) + C_{1\varepsilon} \frac{\varepsilon}{k} (G_k + C_{3\varepsilon} G_b) - C_{2\varepsilon} \rho \frac{\varepsilon^2}{k} - R_\varepsilon + S_\varepsilon \quad (3.7)$$

$G_k, G_b, Y_M$  are solved using the same equation in standard k- $\varepsilon$  models but the turbulence prandtl number ( $Pr_t$ ) is calculated differently in the RNG model.

$$Pr_t = \frac{1}{\alpha} \quad (3.8)$$

$G_k$  Generation of turbulence kinetic energy due to mean velocity gradient, it is modelled the same as for RNG and realisable models

$$G_k = \mu_t S^2 \quad (3.9)$$

$S$  Modulus of the mean rate of strain tensor

$G_b$  Generation of turbulence kinetic energy due to buoyancy

$$G_b = \beta g_i \frac{\mu_t}{Pr_t} \frac{\partial T}{\partial x_i} \quad (3.10)$$

$Y_M$  Dilatation dissipation, this is normally neglected in an incompressible flow

$$Y_M = 2\rho\varepsilon M_t^2 \quad (3.11)$$

$\rho$  Density of the fluid

$\alpha$  Inverse prandtl number

$S_k, S_\varepsilon$  user defined source terms

### RNG Viscosity Modification

Effective turbulence viscosity allows the RNG model to handle a low Reynold number and near wall flows. The effective viscosity can either be calculated using equation 3.12 below or equation 3.5 above for low and high Reynold number respectively.

$$d \left( \frac{\rho^2 k}{\sqrt{\varepsilon \mu}} \right) = 1.72 \frac{\hat{v}}{\sqrt{\hat{v}^3 - 1 + C_v}} d\hat{v} \quad (3.12)$$

$\hat{v} = \frac{\mu_{eff}}{\mu}$  and  $C_v$  is assumed to be 100

The flow in the hydrocyclone is high turbulence flow, therefore equation (3.5) above is applicable.

#### RNG Swirl Modification

To account for the swirl in turbulence flow, equation 3.13 below was introduced into the model. Swirl modification is used for three dimensional, axisymmetric swirling flows.

$$\mu_t = \mu_{t0} f\left(\alpha_s, \Omega, \frac{k}{\epsilon}\right) \quad (3.13)$$

$\mu_{t0}$  This is the value of turbulent viscosity calculated without swirl modification using equation 3.5 or 3.12

$\Omega$  Swirl number

$\alpha_s$  Swirl constant that assumes different values depending on whether the flow is swirl dominated or only mildly swirling. The default of 0.07 is for mild swirl while it is recommended that a high value can be used for a strong swirl flow.

#### Addition to Dissipation Equation

The significant difference between the RNG k- $\epsilon$  model and the standard k- $\epsilon$  model is the introduction of  $R_\epsilon$  terms in the dissipation equation.

$$R_\epsilon = \frac{c_\mu \rho \eta^3 \left(1 - \frac{\eta}{\eta_0}\right) \epsilon^2}{1 + \beta \eta^3} \frac{1}{k} \quad (3.14)$$

With the modifications above, the RNG model is considered suitable for turbulence with low/high swirl as well as low or high Reynold number flows.

### 3.6.3 Realizable k- $\epsilon$ model

This model can produce better results for rotational flows, boundary layers under adverse pressure gradient, flow involving separation and recirculation because it fulfils some mathematical constraints on Reynold stresses that are consistent with the physics of turbulence flow.

The model differs from the standard k-ε model as it includes new equations for the turbulent viscosity and has a new transport equation for the dissipation rate (ε) shown in 3.15 and 3.16: add original reference.

$$\frac{\partial(\rho k)}{\partial t} + \frac{\partial(\rho k u_i)}{\partial x_i} = \frac{\partial}{\partial x_j} \left[ \left( \mu + \frac{\mu_t}{\sigma_k} \right) \frac{\partial k}{\partial x_j} \right] + G_k + G_b - \rho \varepsilon - Y_M + S_k \quad (3.15)$$

$$\frac{\partial(\rho \varepsilon)}{\partial t} + \frac{\partial(\rho \varepsilon u_i)}{\partial x_i} = \frac{\partial}{\partial x_j} \left[ \left( \mu + \frac{\mu_t}{\sigma_\varepsilon} \right) \frac{\partial \varepsilon}{\partial x_j} \right] + \rho C_1 S_\varepsilon - \rho C_2 \frac{\varepsilon^2}{k + \sqrt{v \varepsilon}} + C_{1\varepsilon} \frac{\varepsilon}{k} C_{3\varepsilon} G_b + S_\varepsilon \quad (3.16)$$

Where

$$C_1 = \max \left[ 0.43, \frac{\eta}{\eta + 5} \right] \quad (3.17)$$

$$\eta = S \frac{k}{\varepsilon} \quad (3.18)$$

$$S = \sqrt{2 S_{ij} S_{ij}} \quad (3.19)$$

$S_{ij}$  Strain rate

### New Turbulence Viscosity Equation

In the realizable k-ε model, the turbulence viscosity (eddy viscosity) is calculated based on equation 3.5; however, the value of  $C_\mu$  is calculated using equation 3.20. A viscosity constant of 0.09 is used for an inertial sublayer in an equilibrium boundary layer and 0.05 can be used in a strong homogenous shear flow.

$$C_\mu = \frac{1}{A_0 + A_s \frac{k U^*}{\varepsilon}} \quad (3.20)$$

$$U^* \equiv \sqrt{S_{ij} S_{ij} + \tilde{\Omega}_{ij} \tilde{\Omega}_{ij}} \quad (3.21)$$

$A_0$  and  $A_s$  are model constants given as 4.04 and  $A_s = \sqrt{6 \cos \theta}$

$\tilde{\Omega}_{ij}$  Rotation rate

## 3.7 Transition SST model

This model looks at the important effect of the laminar-turbulence transition, it covers standard bypass transition as well as flows in low free-stream turbulence



environments. The model coupled two transport equations, one for intermittency and the other for transition onset in terms of momentum thickness, Reynold number in addition to SST's of k- $\omega$  equations.

The transition SST model is divided into five sections

- The formulation of the intermittency transport equation used to trigger transition onset
- Transport equation for transition momentum thickness Reynold number
- Modification used to improve the predictions for separated flow transition
- Correlation overview that needs to be used with the model
- Coupling of transition model with SST model

### 3.7.1 The intermittency transport equation is defined by equation 3.22 below

$$\frac{\partial(\rho\gamma)}{\partial t} + \frac{\partial(\rho U_j \gamma)}{\partial x_j} = P_{\gamma 1} - E_{\gamma 1} + P_{\gamma 2} - E_{\gamma 2} + \frac{\partial}{\partial x_j} \left[ \left( \mu + \frac{\mu_t}{\sigma_\gamma} \right) \frac{\partial \gamma}{\partial x_j} \right] \quad (3.22)$$

The transition sources are defined by equation below

$$P_{\gamma 1} = 2F_{length} \rho S [\gamma F_{onset}]^{c_{\gamma 3}} \quad (3.23)$$

$$E_{\gamma 1} = P_{\gamma 1} \gamma \quad (3.24)$$

$$P_{\gamma 2} = (2C_{\gamma 1}) \rho \Omega \gamma F_{turb} \quad (3.25)$$

$$E_{\gamma 2} = C_{\gamma 2} P_{\gamma 2} \gamma \quad (3.26)$$

$P_{\gamma 1}$  and  $E_{\gamma 1}$  Transition sources

$P_{\gamma 2}$  and  $E_{\gamma 2}$  Destruction/re-laminarization sources.

$\Omega$  Vorticity magnitude

$S$  Strain rate magnitude

$F_{length}$  Empirical correlation that controls the length of the transition region

$F_{onset}$  Transition onset trigger

$F_{turb}$  disabler of destruction or re-laminarization source in fully turbulent regime

$\rho$	Density
$\gamma$	Intermittency factor
$C_{\gamma 1}, C_{\gamma 2}, C_{\gamma 3}$	Intermittency equation constant with value of 0.03, 50 and 0.5 respectively
$R_T$	Viscosity ratio
$Re_v$	Vorticity (strain-rate) Reynolds number

The transition onset is controlled by equation below

$$F_{onset1} = \frac{Re_v}{2.193Re_{\theta c}} \quad (3.26a)$$

$$F_{onset2} = \min[\max(F_{onset1}, F_{onset1}^4), 2.0] \quad (3.27)$$

$$F_{onset3} = \max\left(1 - \left(\frac{R_T}{2.5}\right)^3, 0\right) \quad (3.28)$$

$$F_{onset} = \max(F_{onset2} - F_{onset3}, 0) \quad (3.29)$$

$$F_{turb} = e^{-\left(\frac{R_T}{4}\right)^4} \quad (3.30)$$

Where  $Re_v = \frac{\rho y^2}{\mu}$  (3.31)

$$R_T = \frac{\rho k}{\mu \omega} \quad (3.32)$$

### 3.7.2 Equation for transition momentum thickness Reynold number is given by $(\widetilde{Re}_{\theta t})$

$$\frac{\partial(\rho \widetilde{Re}_{\theta t})}{\partial t} + \frac{\partial(\rho U_j \widetilde{Re}_{\theta t})}{\partial x_j} = P_{\theta t} + \frac{\partial}{\partial x_j} \left[ \sigma_{\theta t} (\mu + \mu_t) \frac{\partial \widetilde{Re}_{\theta t}}{\partial x_j} \right] \quad (3.33)$$

$P_{\theta t}$  transition momentum thickness source term and is defined by

$$P_{\theta t} = C_{\theta t} \frac{\rho}{t} (Re_{\theta t} - \widetilde{Re}_{\theta t}) (1.0 - F_{\theta t}) \quad (3.34)$$

$t$  is time scale given by

$$t = \frac{500\mu}{\rho U^2} \quad (3.35)$$

$F_{\theta t}$  blending function used to turn off the source term in the boundary layer and allow the transported scalar  $\widetilde{Re_{\theta t}}$  to diffuse in from free stream

$F_{\theta t}$  zero in free stream and one in boundary layer

$$F_{\theta t} = \min \left( \max \left( F_{wake} e^{(y/\delta)^4}, 1.0 \left( \frac{\gamma - 1/C_{e2}}{1 - 1/C_{e2}} \right)^2 \right), 1.0 \right) \quad (3.36)$$

$$F_{wake} = e^{-\left(\frac{Re_{\omega}}{1 \times 10^5}\right)} \quad (3.37)$$

$$Re_{\omega} = \frac{\rho \omega y^2}{\mu} \quad (3.38)$$

$F_{wake}$  inactivate blending function in the wake region

$$\delta = \frac{50\Omega y}{U} \delta_{BL} \quad \delta_{BL} = \frac{15}{2} \theta_{BL} \quad \theta_{BL} = \frac{\widetilde{Re_{\theta t}} \mu}{\rho U}$$

$\delta$  boundary layer thickness

$\mu$  Viscosity

$y$  distance from the nearest wall

$\omega$  Dissipation

$C_{e2}$  Constant

### 3.7.3 Modification to improve separation induced transition

$$\gamma_{sep} = \min \left( S_1 \max \left[ 0, \left( \frac{Re_{\nu}}{3.235 Re_{\theta c}} \right) - 1 \right] F_{reattach}, 2 \right) F_{\theta t} \quad (3.39)$$

$$F_{reattach} = e^{-\left(\frac{R_T}{20}\right)^4} \quad (3.40)$$

$$\gamma_{sep} = \max(\gamma, \gamma_{sep}) \quad (3.41)$$

$S_1$  constant given as 2

$F_{\theta t}$  blending function

$F_{reattach}$  disables the modification once the viscosity ratio is large enough to cause reattachment.

### 3.7.4 Empirical Correlations

$$Re_{\theta t} = f(Tu, \lambda_{\theta}) \quad (3.42)$$

$$F_{length} = f(\overline{Re_{\theta t}}) \quad (3.43)$$

$$Re_{\theta c} = f(\overline{Re_{\theta c}}) \quad (3.44)$$

$$Tu = \frac{100\sqrt{2k/3}}{U} \quad (3.45)$$

$$\lambda_{\theta} = \frac{\rho\theta^2}{\mu} \frac{dU}{ds} \quad (3.46)$$

$Tu$  turbulence intensity

$\theta$  momentum thickness

$k$  turbulent kinetic energy

$U$  mean velocity

$R_y$  wall-distance based turbulent Reynolds number

**The transition model is coupled with SST k- $\omega$  using equation 3.47**

$$\frac{\partial}{\partial t}(\rho k) + \frac{\partial}{\partial x_j}(\rho u_j k) = \widetilde{P}_k - \widetilde{D}_k + \frac{\partial}{\partial x_j} \left( (\mu + \sigma_k \mu_t) \frac{\partial k}{\partial x_j} \right) \quad (3.47)$$

$$\widetilde{P}_k = \gamma_{eff} P_k \quad (3.48)$$

$$\widetilde{D}_k = \min(\max(\gamma_{eff}, 0.1), 1.0) D_k \quad (3.49)$$

$$R_y = \frac{\rho y \sqrt{k}}{\mu} \quad (3.50)$$

$$F_3 = e^{-\left(\frac{R_y}{120}\right)^3} \quad (3.51)$$

$$F_t = \max(F_{1orig}, F_3) \quad (3.52)$$

Where  $P_k$  and  $D_k$  are production and destruction terms in the SST model while  $F_{1orig}$  is the SST blending function

$F_{1orig}$  is the original blending function from the SST turbulence model

### **3.8 Reynolds Stress Model (RSM)**

The Reynolds Stress Model uses seven equations to solve the transport equation of stresses in addition to the equation for dissipation rate. It accounts for the effect

of swirl, curvature, rotation and changes in strain more rigorously than any other RANS equation models. RSM is a seven-equation model which is used for calculating transport Reynold stresses, these equations are given below.

$$\frac{DR_{ij}}{Dt} = \frac{\delta R_{ij}}{\delta t} + C_{ij} = -D_{T,ij} + D_{L,ij} - P_{ij} - G_{ij} + \emptyset_{ij} + \varepsilon_{ij} + F_{ij} \quad (3.53)$$

Where

$$\frac{\delta R_{ij}}{\delta t} = \frac{\partial}{\partial t} (\rho \overline{u'_i u'_j}) \quad \text{Local time derivative} \quad (3.54)$$

$$C_{ij} = \frac{\partial}{\partial x_k} (\rho u_k \overline{u'_i u'_j}) \quad \text{Convection} \quad (3.55)$$

$$D_{T,ij} = \frac{\partial}{\partial x_k} [\rho \overline{u'_i u'_j u'_k} + P'(\delta_{kj} u'_i + \delta_{ik} u'_j)] \quad \text{Turbulence Diffusion} \quad (3.56)$$

$$D_{L,ij} = \frac{\partial}{\partial x_k} [\mu \frac{\partial}{\partial x_k} (\overline{u'_i u'_j})] \quad \text{Molecular Diffusion} \quad (3.57)$$

$$P_{ij} = \rho (\overline{u'_i u'_k} \frac{\partial u_j}{\partial x_k} + \overline{u'_j u'_k} \frac{\partial u_i}{\partial x_k}) \quad \text{Stress Production} \quad (3.58)$$

$$G_{ij} = \rho \beta (g_i \overline{u'_j \theta} + g_j \overline{u'_i \theta}) \quad \text{Buoyancy production} \quad (3.59)$$

$$\emptyset_{ij} = P' \overline{(\frac{\partial u'_j}{\partial x_j} + \frac{\partial u'_i}{\partial x_i})} \quad \text{Pressure Strain} \quad (3.60)$$

$$\varepsilon_{ij} = -2\mu \overline{\frac{\partial u'_i}{\partial x_k} \frac{\partial u'_j}{\partial x_k}} \quad \text{Rate of dissipation} \quad (3.61)$$

$$F_{ij} = -2\rho \Omega_k (\overline{u'_j u'_m} \epsilon_{ikm} + u'_i u'_m \epsilon_{jkm}) \quad \text{Production by system rotation} \quad (3.62)$$

### 3.9 Discrete Particle Model (DPM)

DPM was used to model the discrete phase in the fluid flowing in the hydrocyclone, this model is used for dilute medium density particle concentration in flows. The acceleration of the particles/ physical equation used for discrete phase calculation is given by Newton's second law

$$\frac{d}{dt} u_p = \sum f_p \quad (3.63)$$

$$\frac{d}{dt} u_p = F_D(u - u_p) + \frac{g_x(\rho_p - \rho)}{\rho_p} + F_x \quad (3.64)$$

Where  $F_x$  is the additional particle forces that can be important to the flow, these forces include virtual mass force, Saffman lift force, pressure gradient force, magnus force and Basset force. All these forces are neglected in the simulations apart from the lift force to evaluate the size of the force against the drag force.

$$F_D(u - u_p) \quad \text{Drag force per unit mass}$$

### Drag Force $F_D$

Drag force is a resistance force resulting from the motion of a particle through a fluid, it acts in parallel to the flow direction. Drag force is based on the velocity difference between particles and fluid and is expressed by equation 3.65 below

$$F_D = \frac{18\mu}{\rho_p d_p^2} \frac{C_D R_e}{24} \quad (3.65)$$

For sub-micron particles

$$F_D = \frac{18\mu}{\rho_p d_p^2 C_c} \quad (3.66)$$

$$R_e = \frac{\rho d_p |u_p - u|}{\mu} \quad (3.67)$$

$u$  = fluid phase velocity

$u_p$  = Particle velocity

$\mu$  = Molecular Viscosity

$\rho$  = Density of Fluid

$\rho_p$  = Density of Particle

$d_p$  = Particle Diameter

$R_e$  = Reynold number

$C_D$  = Drag Coefficient

$C_c$  = Cunningham correction to strokes drag law path

$\lambda$  = Molecular mean free path

$$C_c = 1 + \frac{2\lambda}{d_p} \left( 1.257 + 0.4e^{\left( \frac{1.1d_p}{2\lambda} \right)} \right) \quad (3.68)$$

### Lift Force

Generally, the flow of fluid around a particle introduces a force on the particle, lift force is the component of this force that is perpendicular to the flow direction. Lift force acts in an upward direction to oppose the force of gravity and can also act in any direction at right angles to the flow. Lift force is produced in a fluid when the velocity gradient is induced by pressure distribution on a particle.

$$F_s = \frac{9.69}{\pi d_p \rho_p} \left( \frac{\mu \rho}{\dot{\gamma}} \right)^{\frac{1}{2}} C_{LS} (u - u_p) \quad (3.69)$$

$\dot{\gamma}$  is the fluid rate of deformation, and  $C_{LS}$  is the lift force coefficient,  $u_p$  is the particle velocity and  $u$  fluid viscosity.

### Virtual Mass Force

The virtual force is the force required to accelerate the continuous phase in the immediate environment of the droplet or particle being considered. This force is significant when the density of fluid is greater than the density of the particle. The force is given by

$$F_x = \frac{1}{2} \frac{\rho}{\rho_p} \frac{d}{dt} (u - u_p) \quad (3.70)$$

### Pressure Gradient force

The pressure gradient force occurs as a result of the difference in the pressure across the surfaces. This force accelerates particles because of the irregular distribution of hydraulic pressure on the surface of particles, resulting in local fluid pressure gradient around the particles. The strength of the pressure gradient force can be changed by reducing the distance of the pressure change. The pressure gradient force is given by equation 3.71 below

$$F_p = \frac{m_f}{\rho} \bar{\nabla} p \quad (3.71)$$

### Saffman Lift Force

The Saffman force occurs due to the local flow velocity gradient and this is usually due to near wall shear. It can also be described as the force produced in a fluid when the velocity gradient is induced by pressure distribution on a particle.

$$F_s = \frac{9.69}{\pi d_p \rho_p} \left( \frac{\mu \rho}{\dot{\gamma}} \right)^{\frac{1}{2}} C_{LS} (u - u_p) \quad (3.72)$$

$\dot{\gamma}$  is the fluid rate of deformation, and  $C_{LS}$  is the lift force coefficient,  $u_p$  is the particle velocity and  $u$  fluid viscosity.

### Basset Force

This is the force resulting from the delay a particle undergoes when moving in a viscous fluid, this force produce an unstable boundary layer around the practice as

velocity changes with time. The Basset term accounts for the viscous effect and addresses the delay in boundary layer development as the relative velocity changes with time. The force is given by the equation below.

$$F_B = \frac{9}{d_p \rho_p} \sqrt{\frac{\rho \mu}{\pi} \int_{t_0}^t \frac{(d_u/d_\tau) - du_p/d\tau}{\sqrt{t-\tau}} d\tau} \quad (3.73)$$

### **Magnus Force**

This is the force due to the rotation of particles. The pressure difference between the particle sides produces velocity difference because of the rotational motion thus producing the force. The force is given by the equation below

$$F_m = \frac{1}{2} \rho (u - u_p)^2 C_L \frac{A d^2}{4} \quad (3.74)$$

$C_L$  is lift force coefficient

A is area and d the diameter of particle.

## **3.10 Magnetohydrodynamic Model (MHD)**

To evaluate the effect of magnetic induction on PCFDO a magnetic field needs to be introduced into the system and this is done in fluent with the introduction of the Magnetohydrodynamic Model (MHD). MHD studies magnetic properties and the behaviour of electrically conducting fluids; governing equation for MHD are fluid dynamics and the Maxwell equation. MHD equations describe the motion of a conducting fluid interacting with a magnetic field. The electrically conductive fluid is usually the discrete phase; thus, oil droplets are the conductive fluid used in this study. The solutions of the equations of MHD is constrained by set of conservation law below

For a conductive fluid, the Magnetic induction equation is shown in equation 3.75 below

$$\frac{\partial B}{\partial t} = \nabla (u \cdot B) - \nabla (\eta \nabla B) \quad (3.75)$$

where  $\eta = \frac{1}{\mu \sigma}$

$B$  =Magnetic Field in Tesla



$u$  = Fluid velocity Field

$\mu$ =Magnetic Permeability

$\eta$  =Magnetic Diffusivity

$\nabla$ = Operator referred to as grad, nabla, or delta

$\sigma$  =conductivity of fluid

Fluid carrying current density in a magnetic field experience Lorentz force ( $F_m$ ) per unit volume and this is given by equation 3.76

$$F_m = -\nabla \left( \frac{B^2}{2\mu} \right) + \frac{1}{\mu} B \cdot \nabla B \quad (3.76)$$

### **3.11 Boundary Conditions**

The boundary conditions include the inlet, outlets and wall boundaries in the computational domains. A velocity inlet was used as the inlet boundary condition because the flow velocity at the inlet of the hydrocyclone is not known and the pressure changes to the value required for the velocity distribution.

The outlets were set to outlet vent boundaries because it is assumed that the oil and water were discharged at atmospheric conditions (with this assumption the outlet vent and the pressure outlet boundary condition produced the same results). The wall was set to the wall boundary condition.

### **3.12 Computational Procedure**

The computational domain geometry and grid were produced with the ansys design modeller and ansys ICEM (integrated computer engineering and manufacturing software) respectively with 386318 hexahedral structured cells and 396357 nodes. The grid is a discrete representation of the geometric domain in which the problem is solved and divides the solution domain into a finite number of sub-domains called elements. A grid sensitivity test was done with 592,000 cells which showed that the size of the grid is enough to give an acceptable accurate result. The simulations took between 400000 and 750,000 iterations and converge in approximately 2 months (using a computer with 4GB RAM and processor of 4 core) but with an improved system, the convergence time was reduced to 2-3 weeks for the two-phase simulations run (using computer with 32GB RAM and 16 core processor).

The discretization was done using the finite volume method, pressure-based solver, and transient time with a timestep of 0.0001 secs. The convergence criteria were set to fluent default of  $10^{-3}$ , these convergence criteria were considered sufficient for research work (Hugo A., 2014). These convergence criteria are important from the accuracy and efficiency point of view.

The discrete values of the scalar are stored in the cell centres, on the surface convection terms are required for the discrete values and must be interpolated from the cell centre values. This is accomplished by using an upwind scheme. The upwind scheme used in the simulation for the geometrical analysis were as follows; pressure velocity coupling. The post processing was done using fluent, CFD post and Microsoft Excel and the process flow diagram for solving the numerical equation is shown below.

**Table 3-2: Discretization table**

	Chapter 5	Chapter 4 and 6
Pressure velocity coupling scheme	SIMPLE	SIMPLE
Spatial discretization	Least square cell based	Least square cell based
Pressure	Standard	Standard
Momentum	Second order upwind	QUICK
Turbulent kinetic energy	Second order upwind	QUICK
Turbulent dissipation energy	Second order upwind	QUICK
Reynold stresses	Second order upwind	QUICK
Transient formulation	First order implicit	First order implicit

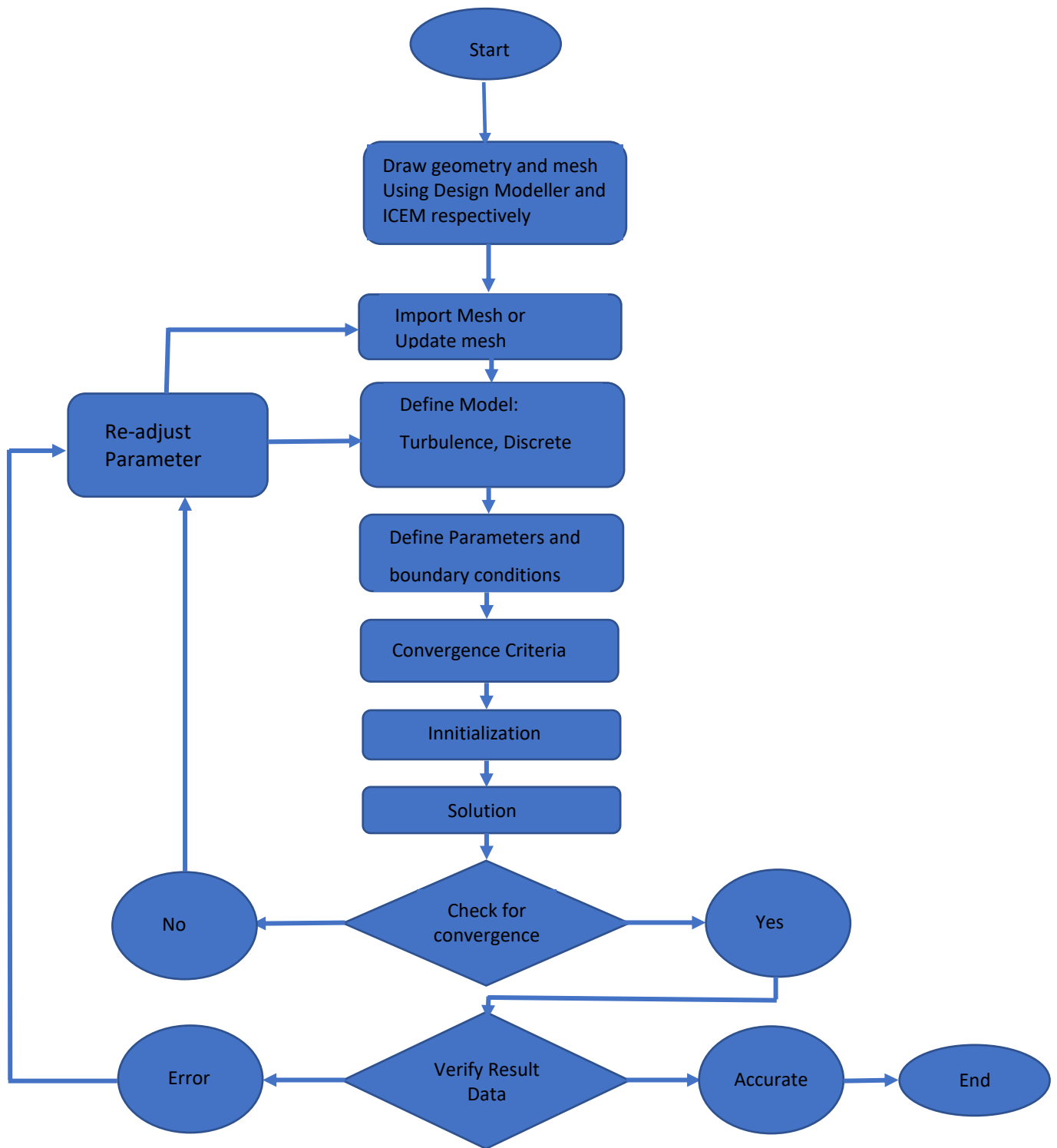


**Figure 3-3 Numerical process flow diagram.**

## Chapter 4

### **4.0 Evaluation of Turbulence Models and Solution Validation**

RSM and LES are well known for producing acceptable results for hydrocyclone simulation but are computationally expensive (Delgadillo, 2004; Narasimha, 2007; Saidi, 2011; Shalaby 2015; Jafari, 2017). Recently, development of many variants of k- $\epsilon$  models consider streamline curvatures, wall boundary layers and stress transport and so it is imperative to evaluate the use of these k- $\epsilon$  models and the transition SST model. The chapter is therefore aimed to:

- Present the solution procedure of the Eulerian- Lagrangian multiphase model and validate the study of the model predictions.
- Ascertain if any of the different variants of the k- $\epsilon$  models are good enough and where and when it can be used for hydrocyclone simulation as any two-equation model will reduce the computational time significantly.
- Compare the modelling of flow in hydrocyclone using standard eddy viscosity models and eddy viscosity with the introduction of curvature correction terms to ascertain the influence of curvature correction terms on each of the eddy viscosity models and on hydrocyclone modelling.

The validation process involves comparing the results of the numerical models investigated with published experimental results. The same geometry and fluid properties used in the experimental work were used in the numerical analysis. The experimental work performed by Hsieh and Rajamani (1986) was used for the validation.

#### **4.1 Turbulence Model**

The turbulence model is a computational procedure used to close the system of mean flow equations. In engineering the effect of the turbulence model on mean flow is very important. Large eddies in turbulence flow interact and extract energy

from the mean flow while the smaller eddies extract energy from the large eddies and weakly from the mean flow thus the kinetic energy in the turbulence flow cascades from the larger eddies to the smallest eddies.

Dissipation of energy is a result of energy loss associated with turbulence flow during the cascading progress. The viscosity dictates the smallest scale of motion that can occur in turbulence flow therefore the evaluation of the viscous stress is important in turbulence flow. The structure of large eddies is highly directional (anisotropic) due to strong interaction with the mean flow while the small eddies are non-directional (isotropic). The way the small eddies is being evaluated makes the difference in the turbulence models. The flow in the hydrocyclone is considered anisotropy.

The finite volume discretization method in CFD solver 18.1 was used to numerically solve the multiphase flow governing equations and closure models. The flow in the cyclone is considered turbulence therefore the specific closure equations and modelling approaches for continuous and dispersed flow phase stress and interfacial momentum transfer were investigated.

In fluent there are three different  $k-\varepsilon$  multiphase models, these models include standard  $k-\varepsilon$  (STD  $k-\varepsilon$ ), renormalization  $k-\varepsilon$  (RNG  $k-\varepsilon$ ) and realizable  $k-\varepsilon$ . All these models have similar transport equations for the turbulence kinetic energy ( $k$ ) and rate of dissipation ( $\varepsilon$ ) but tend to differ in the method used for calculating turbulent viscosity, the turbulence prandtl number governing the turbulent diffusion of  $k-\varepsilon$  and how terms in rate of diffusion are being generated and destroyed. The transition shear stress model (SST) combines the near wall region of  $k-\omega$  model with the free stream independency of the  $k-\varepsilon$  model to predict the onset and the amount of flow separation under high adverse pressure gradients. The eddy viscosity modification in the transition SST model is only applicable at the near wall while the original  $k-\omega$  formulation is used for the remaining part of the flow (Menter, 1994).

There are several drawbacks with  $k-\varepsilon$  models and transition SST model when they predict complex strain fields and significant body forces. In cases like this, the second moment closure model also known as the Reynold stress model (RSM) is preferred. The RSM provides the exact Reynolds stress transport equation that can account for the directional effect of the Reynolds stress field, it accounts for swirl,

curvature, rotation and changes in strain more rigorously than any other RANS equation models.

The numerical models investigated in the present study are standard  $k-\epsilon$ , renormalization  $k-\epsilon$ , realizable  $k-\epsilon$  models, transition SST model (eddy viscosity models) and the Reynolds Stress Model for continuous (liquid) and dispersed (solid) flow turbulence. The first set of simulations involve the use of eddy viscosity models without incorporating curvature while the second sets of simulations involve the use of the eddy viscosity models with the use of curvature correction terms.

## 4.2 Hydrocyclone Geometry

The hydrocyclone operates based on the principle of centrifugal force; the fluid enters the cyclone tangentially via the inlet into the cylindrical section generating a swirl flow which create the centrifugal force needed to separate the solid particles from produced water by moving particles denser than produced water to the wall of the cyclone and the less dense particles to the centre core region of the cyclone. The denser particles move to the wall of the cyclone and are discharged via the underflow/spigot section while the lighter particles at the core region of the cyclone are discharged via the overflow/vortex finder; the hydrocyclone has two outlets, the spigot/underflow and the overflow/vortex finder. The geometry used for the model analysis is shown in table 4-1 below

**Table 4-1: Hydrocyclone Geometry**

Parameter	Symbol	Size
Diameter of the cyclone body	$D_c$	75mm
Size of Inlet	$D_i$	22.16mm x 22.16mm
Diameter of the vortex finder	$D_o$	25mm
Insertion depth of the vortex finder	$L_v$	50mm
Length of the cylindrical part	$L_c$	75mm
Cone Angle	$A$	20°
Diameter of the spigot	$D_u$	12.5mm

### 4.3 **Model Setup**

The model was set using a pressure-based solver with an absolute velocity formulation for the transient flow field. Gravity was activated with gravitational acceleration set to  $9.81\text{m/s}^2$  in the vertical axis, to account for the effect of gravity on the cyclone. The continuous and discrete phase was water and  $\text{CaCO}_3$  respectively.  $\text{CaCO}_3$  was released from the inlet into the continuous phase as an inert particle with uniform diameter distribution. The properties of the water and  $\text{CaCO}_3$  used can be seen in table 4-2 below

**Table 4-2: Properties of fluid fed into Hydrocyclone**

<b>Property</b>	<b>Water</b>	<b>CaCO<sub>3</sub></b>
Density (kg/m <sup>3</sup> )	998.2	2800
Viscosity (kg/m-s)	0.001003	-
Thermal Conductivity (W/m-K)	0.6	2.5
Molecular Weight (Kg/mol)	18.0152	100.09
Reference Temperature (K)	298	298
Specific Heat (C <sub>p</sub> ) J/Kg-K	4182	856
Velocity (m/s)	2.5	2.5
Concentration (%) (Vol/Vol)	98.14	1.86

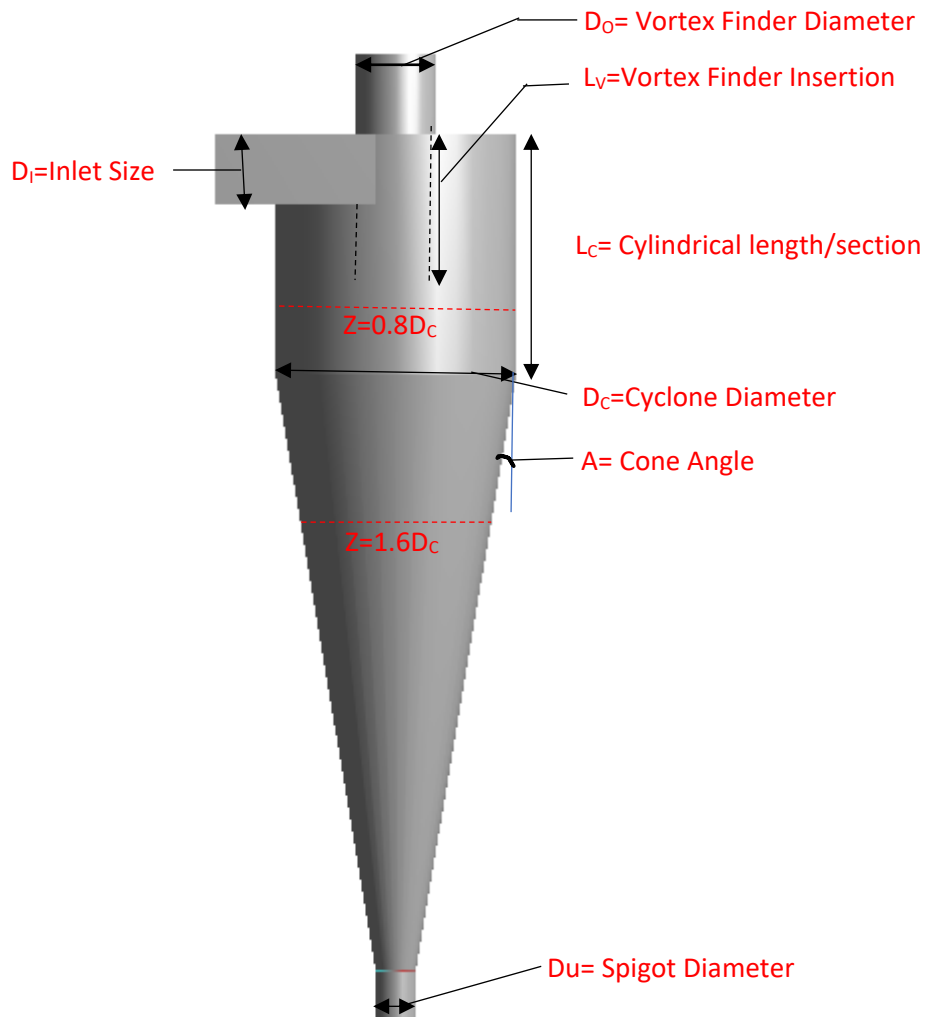


**Figure 4-1: Hydrocyclone Geometry and Boundaries for the Computational Domain**

### 4.3.1 Boundary Conditions

Boundary conditions are required for all computational domains as this helps to constrain the flow in order to establish the uniqueness of each flow and direct the motion. In the current study, inlet, outlet and wall boundaries are in the hydrocyclone computational domain. Figure 4A above shows the boundary considered in this computational domain.

#### **Inlet and Outlet Boundaries**



A velocity inlet boundary condition was used and velocities of both continuous and discrete phases were specified with the assumption of a no-slip shear condition between the fluids. The total flow rate of the injection was calculated based on a concentration of 1.86% as specified in Hsieh's experiment seen in the calculation below.

The discrete phase mass flowrate was specified when the particle was injected at the inlet, the inlet discrete phase boundary condition was equally set to escape.

Calculating the actual mass flowrate (M)

$$\begin{aligned} m &= \text{density} \times \text{velocity} \times \text{area} \times \text{concentration of particle} \\ &= 2800 \times 2.5 \times 0.00055268 \times 0.0186 \\ &= 0.0719 \text{ kg/s} \end{aligned}$$

There are two outlets in the hydrocyclone and these outlets are tagged outlet 1 (vortex finder) and outlet 2 (spigot). An outlet vent boundary condition was used for both outlets on the hydrocyclone because the cyclone is to be exposed to the atmosphere (therefore back pressure is not considered); zero barg was specified as the pressure on both outlets. Outlet-1 (vortex finder) discrete phase boundary condition was set to trap while outlet-2 (spigot) discrete phase boundary condition was set to escape.

#### **4.4 Grid Size/ Number**

The hydrocyclone was meshed using ICEM-CFD. For the mesh independence test, three different meshes were used. Mesh-1 has 300318 elements and 300357 nodes while mesh-2 has 406506 elements and 396357 nodes and mesh-3 has 581312 elements and 566064 nodes. Mesh 1 has a larger grid size than mesh 2 and 3 with mesh 3 having the smallest sized mesh (finer mesh) . The meshes are shown in figure 4-2 below.

Based on the above setup, simulations were run with the different meshes to evaluate the best mesh for the numerical simulations and establish the mesh independency of the simulations.

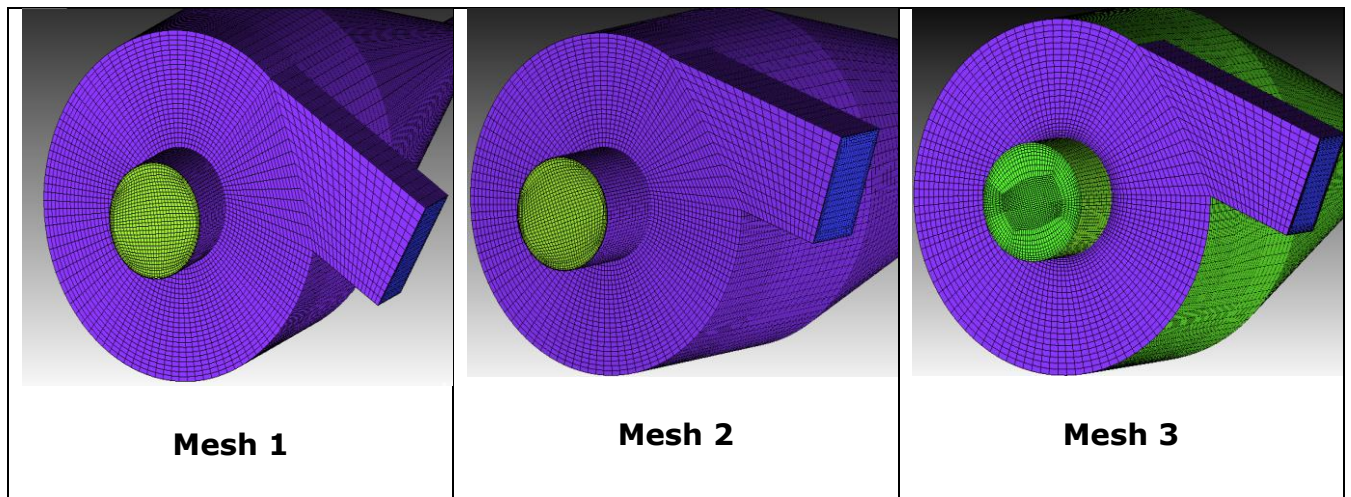


**Figure 4-2: Hydrocyclone Meshes with different number of elements and nodes**

## **4.5 Results and Discussion**

### **4.5.1 Mesh Independency test**

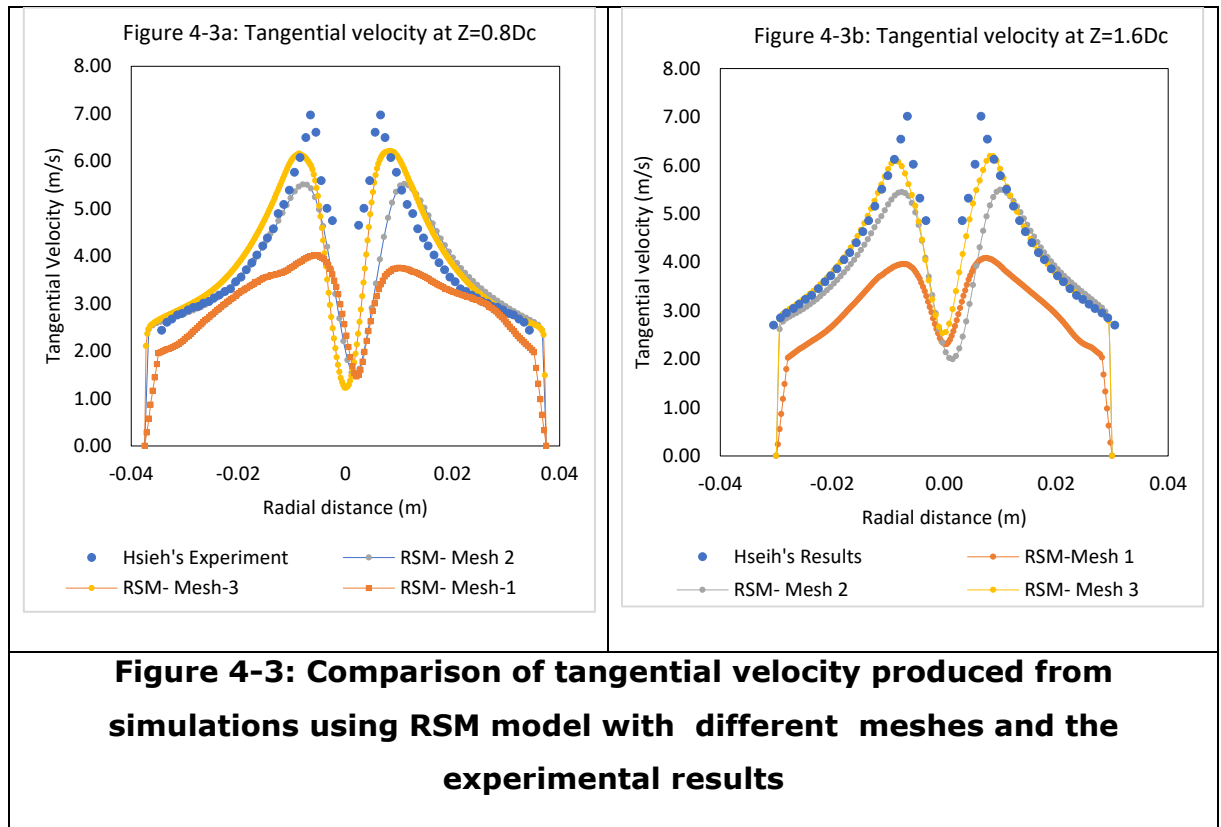
#### **Tangential velocity**

The flow in a hydrocyclone is mainly influenced by the tangential velocity component of the hydrocyclone thus making tangential velocity an important performance index of the hydrocyclone (Jiang, 2019; Liu. 2019). Therefore, one of the factors to consider in evaluating grid influence on simulation precision is tangential velocity. The tangential velocity profile results when taken at point  $Z=0.8D_C$ , this falls within the cylindrical section (above the vortex finder) and at point  $Z=1.6D_C$  which falls in the conical section of the cyclone (below the vortex finder).

Figure 4-3 compares the tangential velocities of the RSM model to the experiment results using the three types of mesh element and nodes being reviewed. From Figure 4-3, it can be seen that the tangential velocity result of mesh 3 corroborates well with the experimental result rather than with the other two meshes; while mesh two result is better than the result of mesh one. Also, the change in tangential velocity from mesh 1 to mesh 2 was quite significant. However, when the mesh size was increased from mesh 2 to mesh 3, the tangential velocity change was very small (not significant) indicating that mesh independency has been

reached and a further increase will further have little or no effect of the velocity profile (Jiang, 2019; Liu, 2019).

The similarity of mesh 3-tangential velocity result to the experimental results proves that the RSM model with mesh 3 is good enough for the simulation analysis. Mesh one and mesh two can be used for the analysis of flow in a hydrocyclone. However, the result will not be as accurate as with mesh 3 when compared to the experimental data.

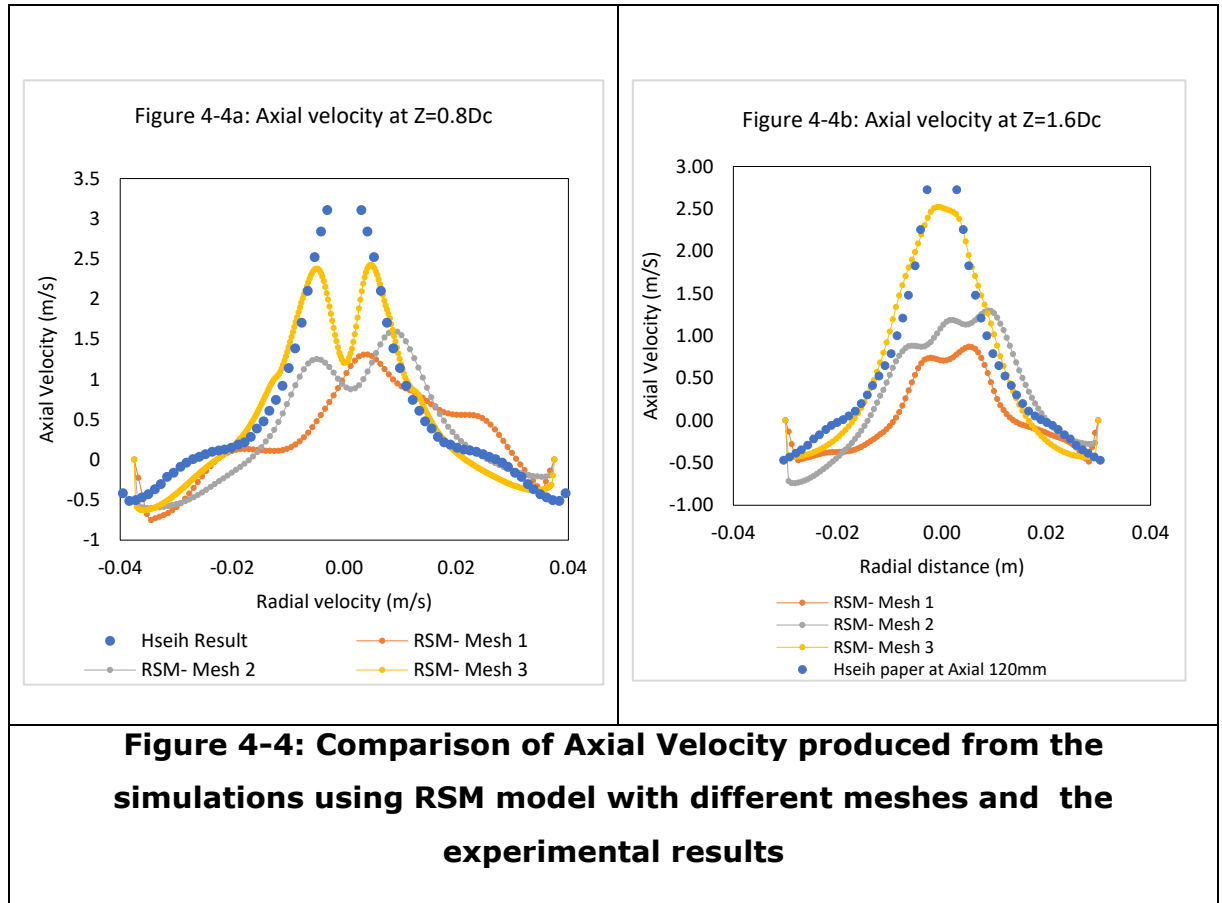


### Axial Velocity

Axial velocity predicts the longitudinal movement of fluid along the axial direction of flow. The axial velocity profile of mesh 3 is very close to that of the experiment result. This depicts that mesh 3 better predicts the flow in the hydrocyclone rather than the other two meshes considered; confirming that the use of a larger number of cells leads to a more accurate solution (Martins, 2014).

Both the axial velocity profiles (mesh 3) in the cylindrical section and in the conical show a good corroboration with the experimental data confirming that this mesh/grid is good enough for the prediction of flow in this hydrocyclone geometry.

Mesh 3 having velocity profile results similar/close to the experimental result affirms the use of computation fluid dynamics for hydrocyclone simulation, most importantly justifying the use of mesh-3; although mesh 2 and 3 can be used, but the accuracy will be reduced.



## 4.6 Turbulence Model Comparison Results and discussion of Results

### 4.6.1 Tangential Velocity

Out of the three-dimensional velocities in the hydrocyclone, tangential velocity is the most important as it determines the centrifugal force that leads to separation in the hydrocyclone and as a result the tangential velocity has the highest value among the three velocities. Figure 4.5 compares the tangential velocity of k-ε

models without curvature, transition-SST model without curvature, RSM and experimental results.

Figure 4-5 shows that the tangential profile of the RSM model is the closest to the experimental profile out of all the RANS equations under consideration. This is because only the RSM can be used to accurately model anisotropy flow by directly solving all components of Reynold stress tensor (Bianco, 2016). The RSM tangential velocity increases from the outer radius to the inner radius and a sharp decrease close to the core of the cyclone; which is the trend seen in the experimental result.

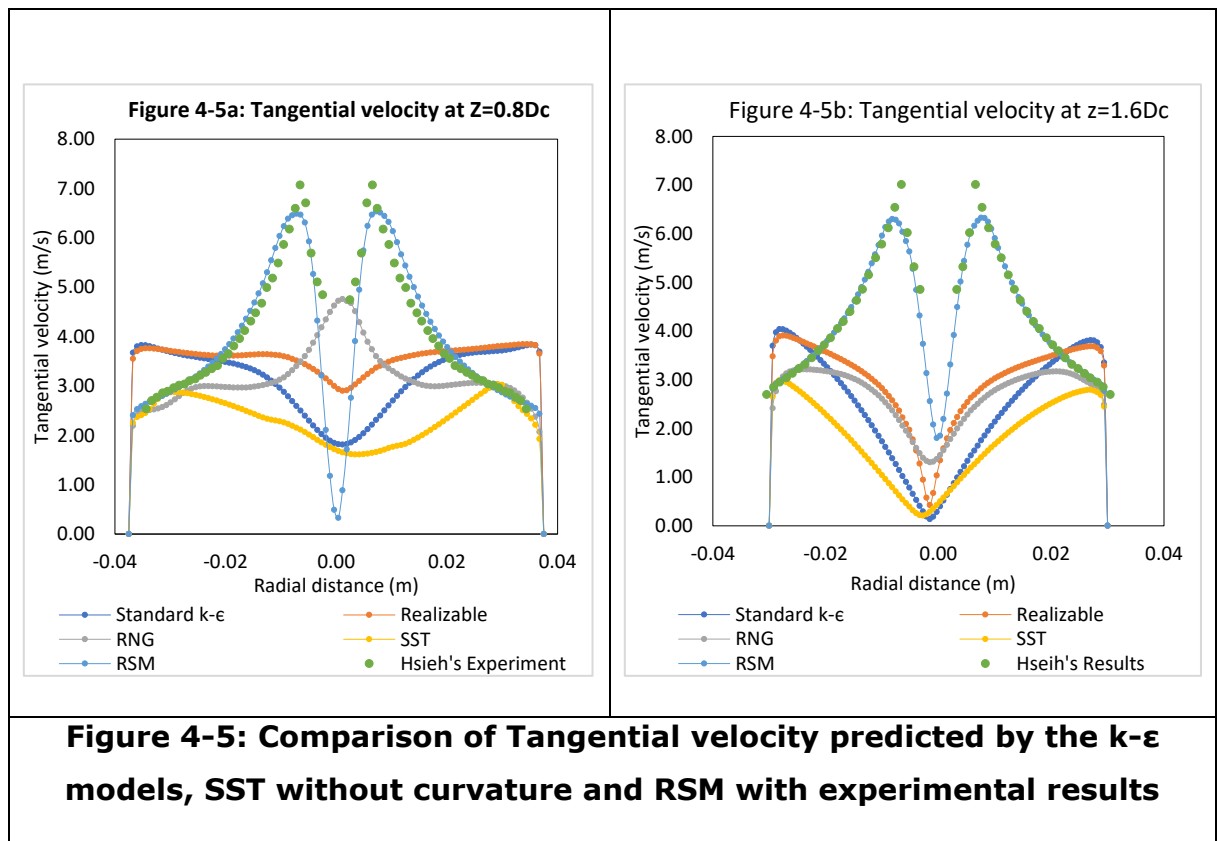
It can also be seen from figure 4-5 that the velocity profiles of  $k-\epsilon$  models and the SST model are different from the RSM and the experimental result with decreasing tangential velocity from the outer region to the inner region of the cyclone. This is because the  $k-\epsilon$  models are not suitable for resolving flows near the walls; at the wall or close to the wall of the hydrocyclone, viscous forces are dominant over the turbulence forces, therefore dampening turbulence near the wall (Davis, 2012). This reveals that eddy viscosity models cannot adequately represent the interaction between body forces and turbulence (Leschziner, 1992). The results also convey that irrespective of the modifications on eddy viscosity models at standard ansys fluent condition, eddy viscosity models are unable to evaluate the turbulence flow in a hydrocyclone. The behaviour of the  $k-\epsilon$  models' and SST models (eddy viscosity models) in the prediction of tangential velocity flow in the hydrocyclone can also be attributed to the assumption of isotropy by the models, which does not make provision for the strong curvature/buoyancy- induced enhancement on normal stress anisotropy to be captured (Leschziner, 1992) in hydrocyclone flow.

Figure 4-5 shows that the prediction of the flow in the SST model was almost the same as the prediction by  $k-\epsilon$  models, this is because the SST model is designed to account for near wall accuracy and for adverse pressure gradient in-flows (Eduardo, 2014; Menter, 1994; Cheng, 2009). The standard transition SST does not account for the strong anisotropy flow in the hydrocyclone thus there is a result similar to  $k-\epsilon$  models in the hydrocyclone

With the introduction of curvature correction terms into the  $k-\epsilon$  models and SST, the modelling of the flow in the hydrocyclone greatly improved as shown in figure

4-6. The Curvature Correction (CC) of each of the models better match the RSM model and the experimental model compared to the models with CC (Elliot, 2012).

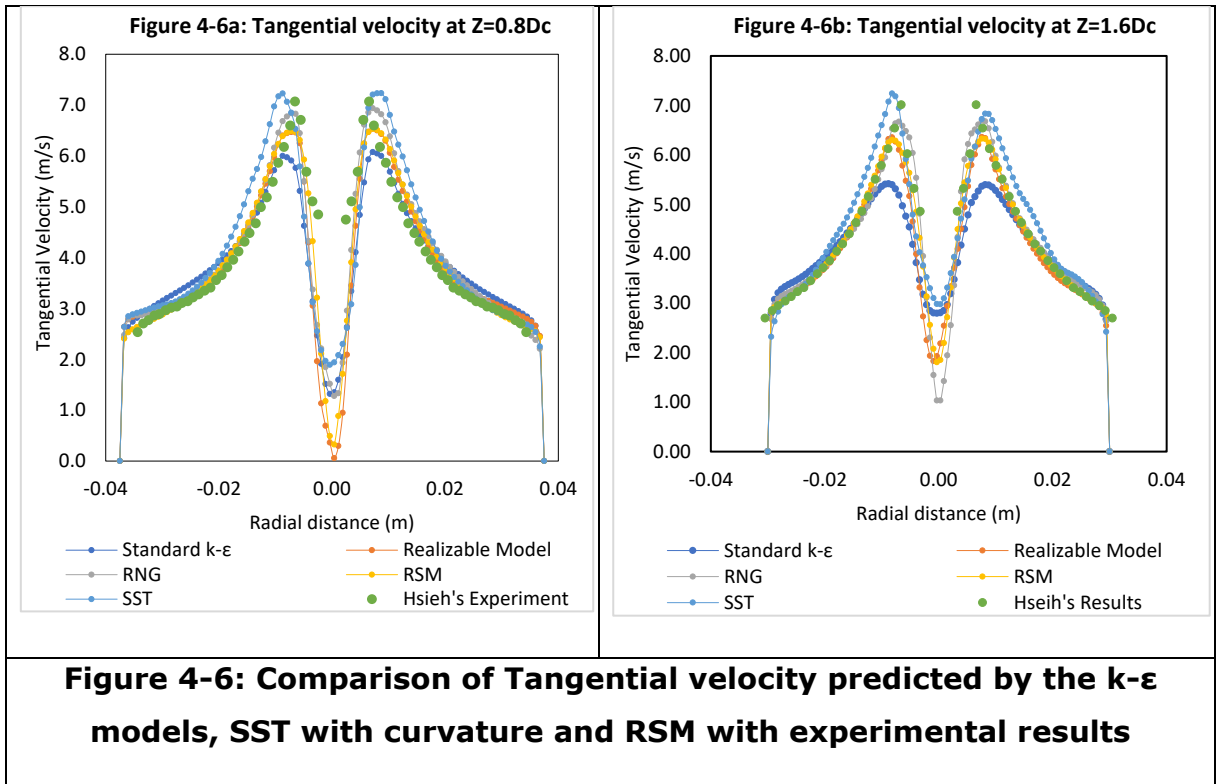
In k-ε models and SST, the incorporation of curvature made it possible to account for the rotation/ swirl of flow in hydrocyclone. The eddy viscosity in these models without CC is accounted for by the eddy viscosity equation below, where  $C_\mu = 1$  (approximately). This means the turbulence kinetic energy has no explicit presence in the rotational flow thus is less sensitive to rotational effect (Arolla, 2014).



In standard eddy viscosity models, the production terms do not contain streamline curvature therefore, the model does not respond to streamline curvature.

$$V_T = \frac{C_\mu k}{\omega} \quad (4-1)$$

According to Bradshaw (1973), the curvature correction provides an extra strain to the principal strain in the eddy viscosity standard model. The direction of the curvature in this flow can be described as concave in nature as it shows an increase in the turbulence quantities (Patel, 1997; Elliot, 2012). On a concave surface, the angular momentum increases with increasing radial distance from the centre of the hydrocyclone (Zhu, 2013)



From figure 4-6, it can be seen that the RSM model corroborates the experimental result better than all other RANS models. This shows that irrespective of the modification provided on other RANS equations, the RSM model is better in predicting in the turbulence in hydrocyclone than the other models.

#### 4.6.2.2 Axial Velocity

Figure 4-7 shows the axial velocity for k-ε models, SST without curvature with the RSM and the experimental data. It can be seen from figure 4-8 that the RSM model best predicts the experimental result than the other RANS equation evaluated. The deviation of SST and k-ε models from the experiment result is wide and the shape of the graph is equally different showing that the k-ε models and SST models do not properly predict the axial velocity flow in the hydrocyclone (Meng, 2019; Stephens, 2009; Bhaskar, 2007; Delgadillo, 2005). The axial velocity determines the separation zone of the cyclone, it acts along the longitudinal axis of the cyclone. It can be seen from figure 4-7 that axial velocity is in two parts; at a positive radial distance it can be seen that axial velocity decreases to zero value and when that radial distance is negative the

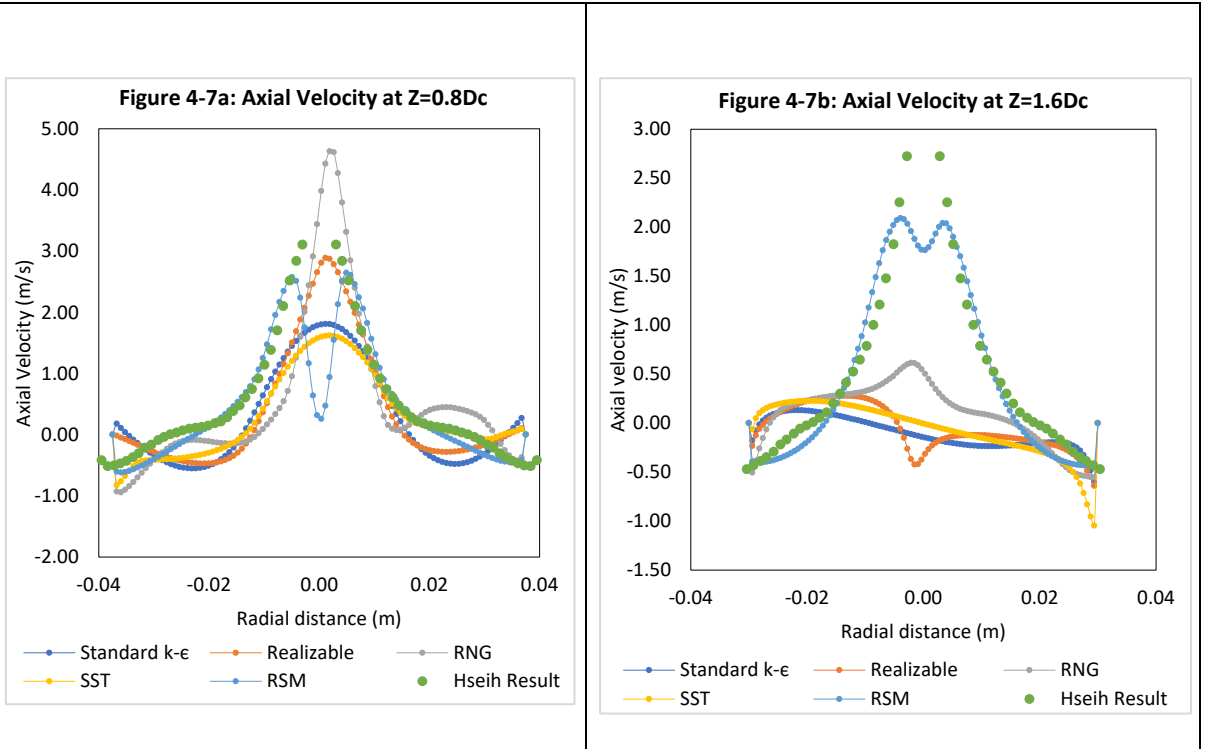


**Figure 4-7: Comparison of Axial velocity predicted by the k-ε models, SST without curvature and RSM with experimental results**

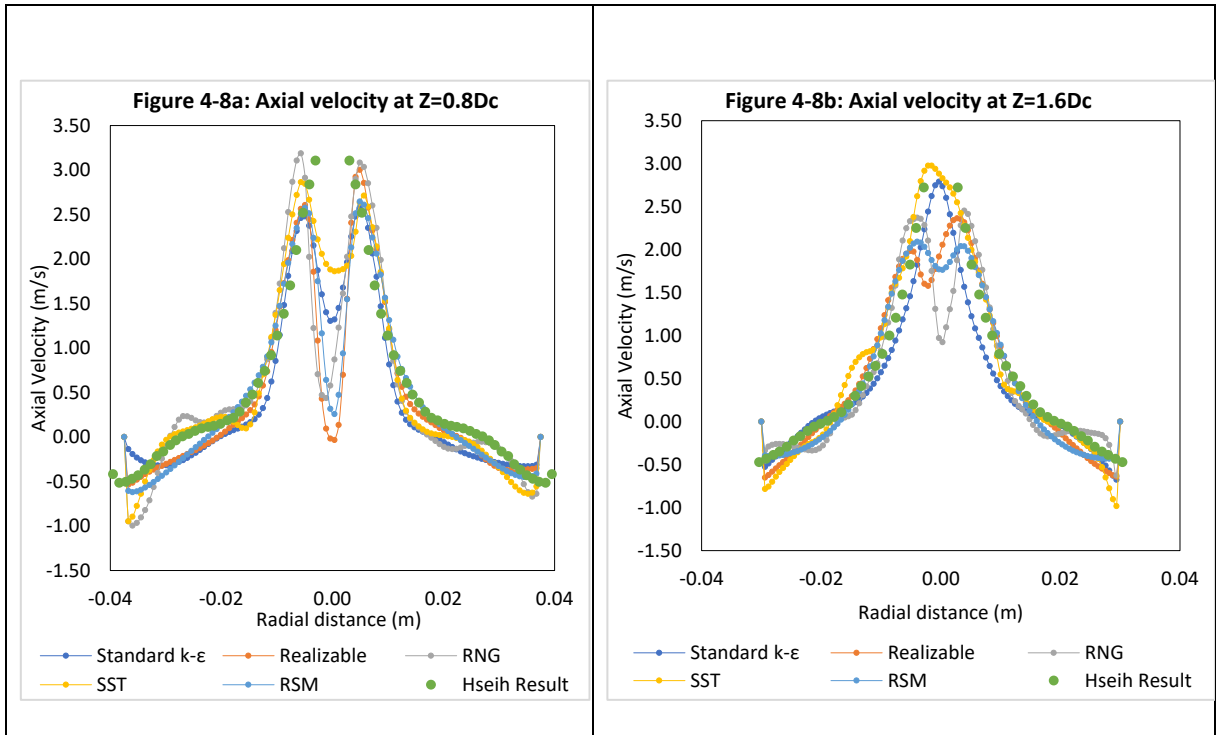


**Figure 4-8: Comparison of Axial velocity predicted by the k-ε models, SST with curvature and RSM with experimental results**



axial velocity decreases from the core to the wall. The area between these two is the core where flow reversal takes place. All  $k-\epsilon$  models and the SST model present a solid body rotation rather than a combined vortex and therefore give an unrealistic distribution of axial velocities, thus the core of the cyclone was not properly modelled using any of the  $k-\epsilon$  models.

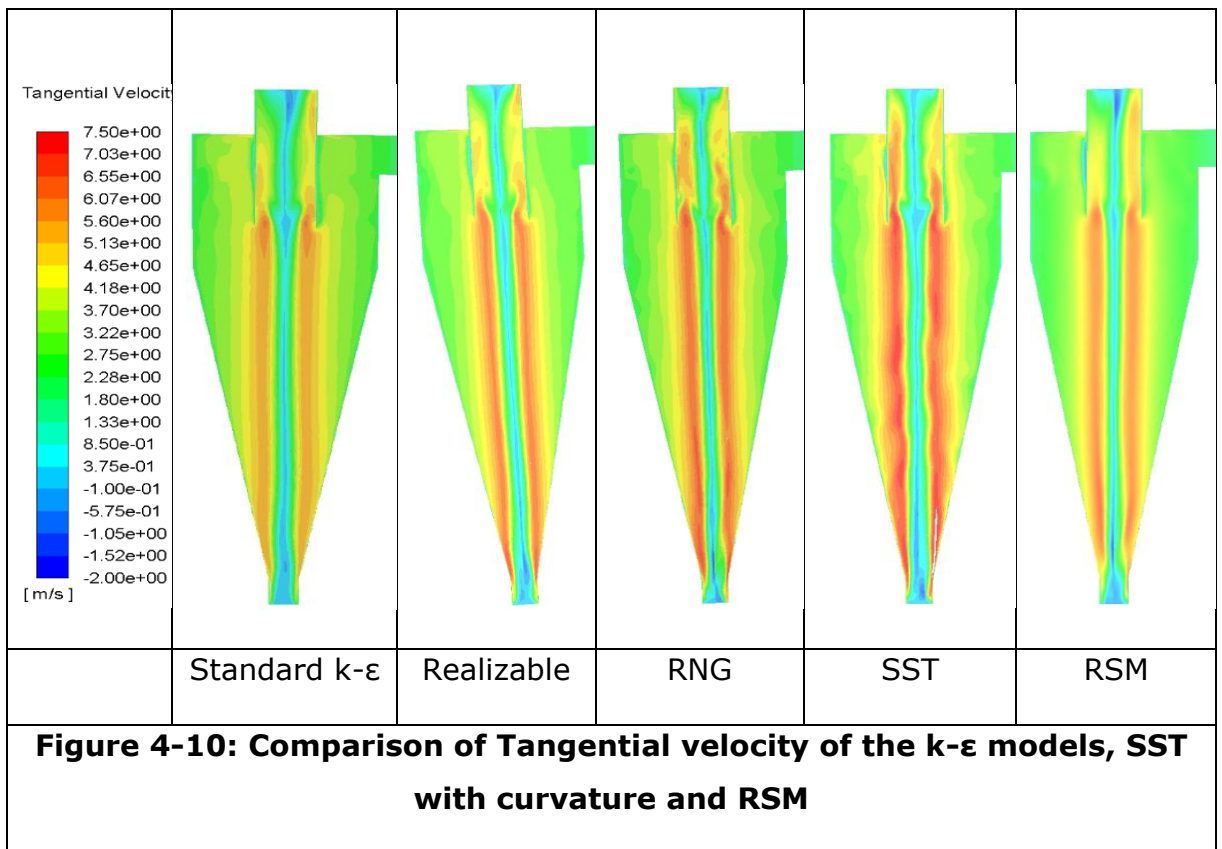
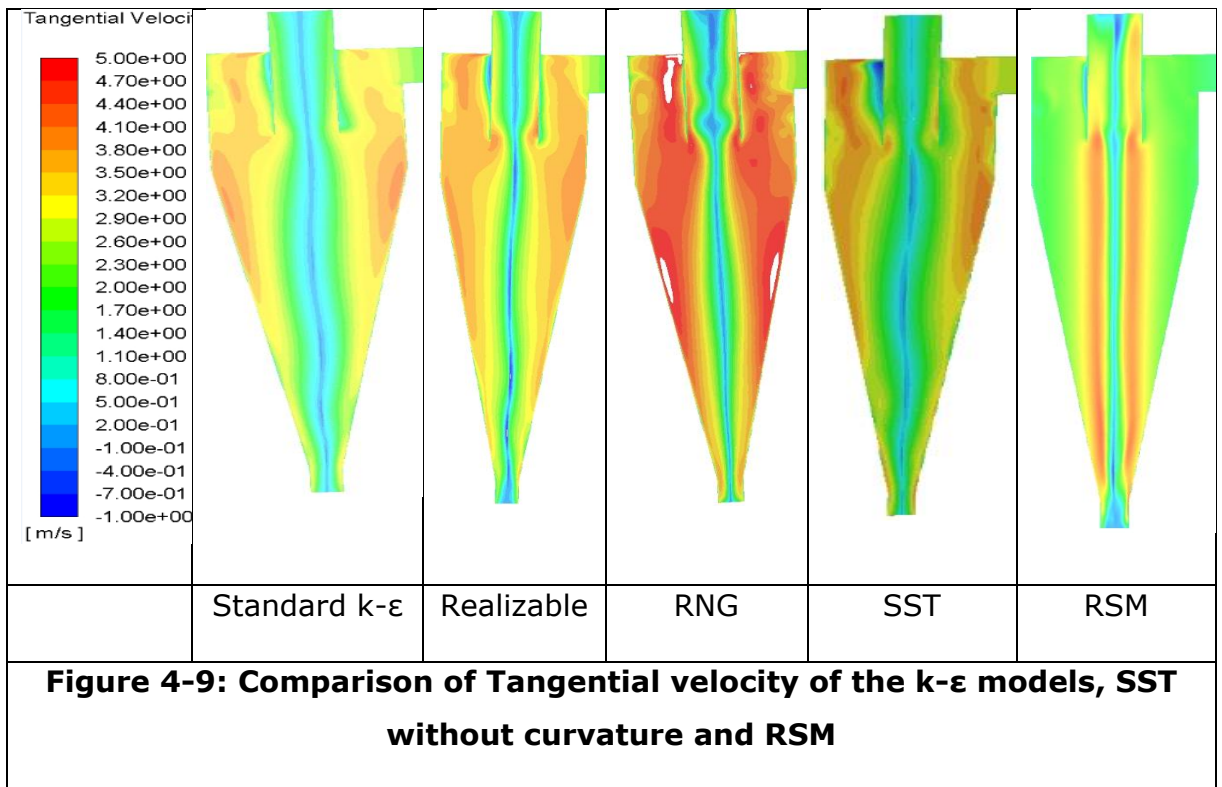
Figure 4-8 is the chart of the  $k-\epsilon$  models with curvature correction, SST model with curvature correction, RSM and experiment. It can be seen that the introduction of the curvature correction factor changes the behaviour of the flow in the hydrocyclone as the  $k-\epsilon$  models and the SST model results are closer to the RSM and experiment results (Stephens, 2019). Although the RSM model still better predicts the experimental results, the result of the  $k-\epsilon$  models and SST model with curvature can also be used for the prediction of hydrocyclone flow. The results of the  $k-\epsilon$  models and SST model are however not as accurate as the result of the RSM model.

#### **4.6.2.3 Tangential Velocity Contour**

Figure 4-9 and 4-10 show the comparison of the standard, realizable, RNG and SST tangential velocity contour without and with curvature correction respectively. It can be seen that the velocity contour of the RNG and SST are more pronounced/higher in the hydrocyclone without and with the curvature correction factor respectively.

Figure 4-9 reflects that the eddy viscosity models cannot properly model the turbulence in a hydrocyclone with highest velocity seen at or around the wall of the cyclone (velocity of a properly modelled turbulence will decrease towards the wall). This is because  $k-\epsilon$  models & SST generate high turbulence kinetic energy and assumes that the flow in the hydrocyclone is isotropic as against anisotropy flow in the hydrocyclone.

However, figure 4-10 includes the use of curvature correction, a great improvement in the models were seen. The contour plots reflect a typical hydrocyclone Rankine flow with forced vortex around the core region of the cyclone and free vortex towards the wall of the cyclone. The difference in the contour plot in figure 4-10 can be attributed to the modification in RNG, realizable and SST model equations which changes the time average product of the fluctuating velocity components (Gao, 2012).



The difference in the velocity contour in figure 4-9 can be attributed to the use of different eddy viscosity in evaluating Reynold stresses. In addition to eddy viscosity changes, the high tangential velocity seen in the RNG model (without curvature) can also be credited to the additional dissipation production rate in the RNG equation, this additional dissipation rate was meant to account for the effect of anisotropic in turbulence flow (Sukoriansky, 2003). The realizable k-ε model has a new transport equation for the dissipation rate derived from the transport of mean square vorticity fluctuation.

The eddy viscosity used for calculating the Reynold stresses differs for each of the eddy viscosity models used. In the standard k-ε model and RNG k-ε model at a high Reynold number (high Reynold is seen in the hydrocyclone), the coefficient of eddy viscosity  $C_\mu$  is calculated by equation 4-2, however in realizable model  $C_\mu$  is calculated by equation 4-3.  $C_\mu$  in the realizable model account for the mean strain and rotation rates, the angular velocity of the system rotation and the turbulence fields. The eddy viscosity of SST on the other hand is calculated using equation 4-4

$$\mu_t = \rho C_\mu \frac{k^2}{\varepsilon} \quad (4-2)$$

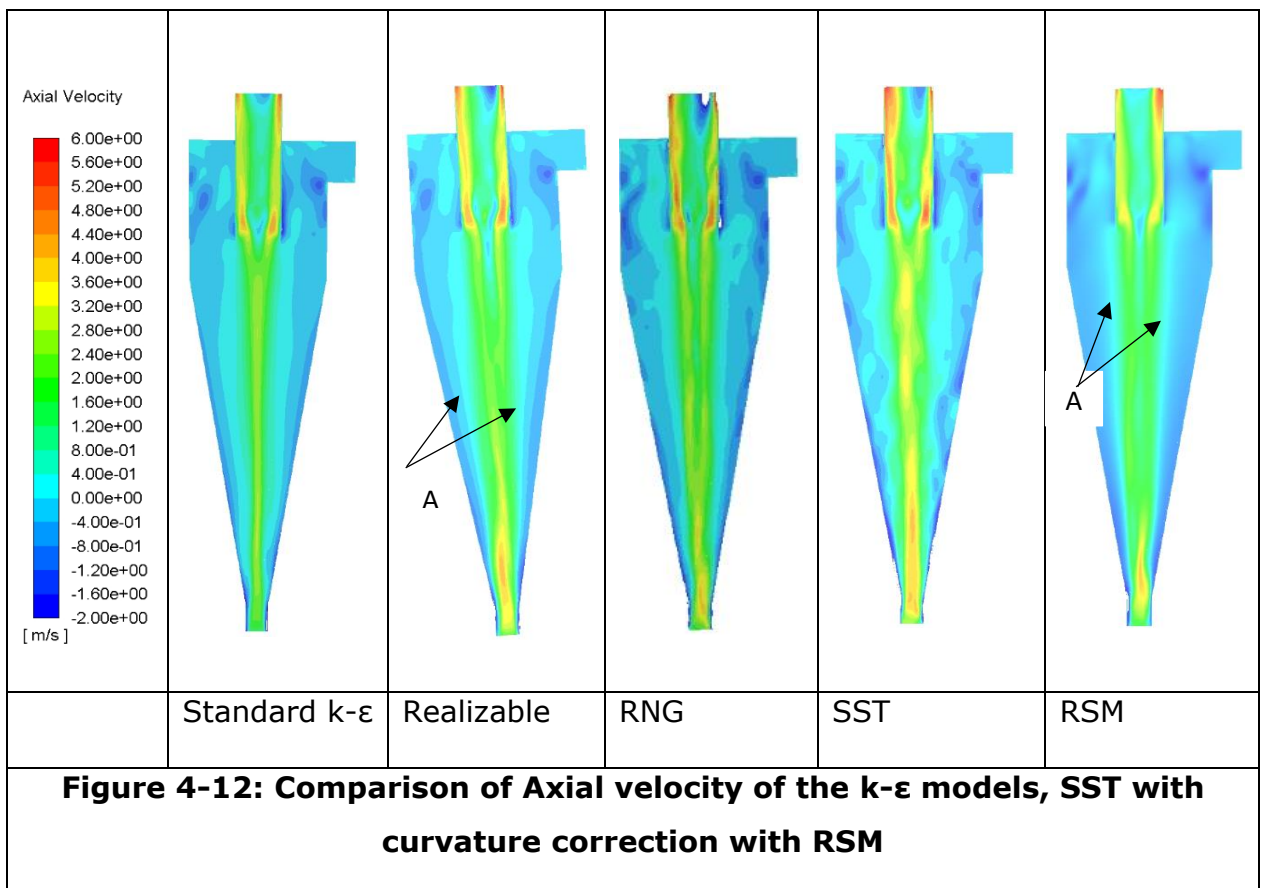
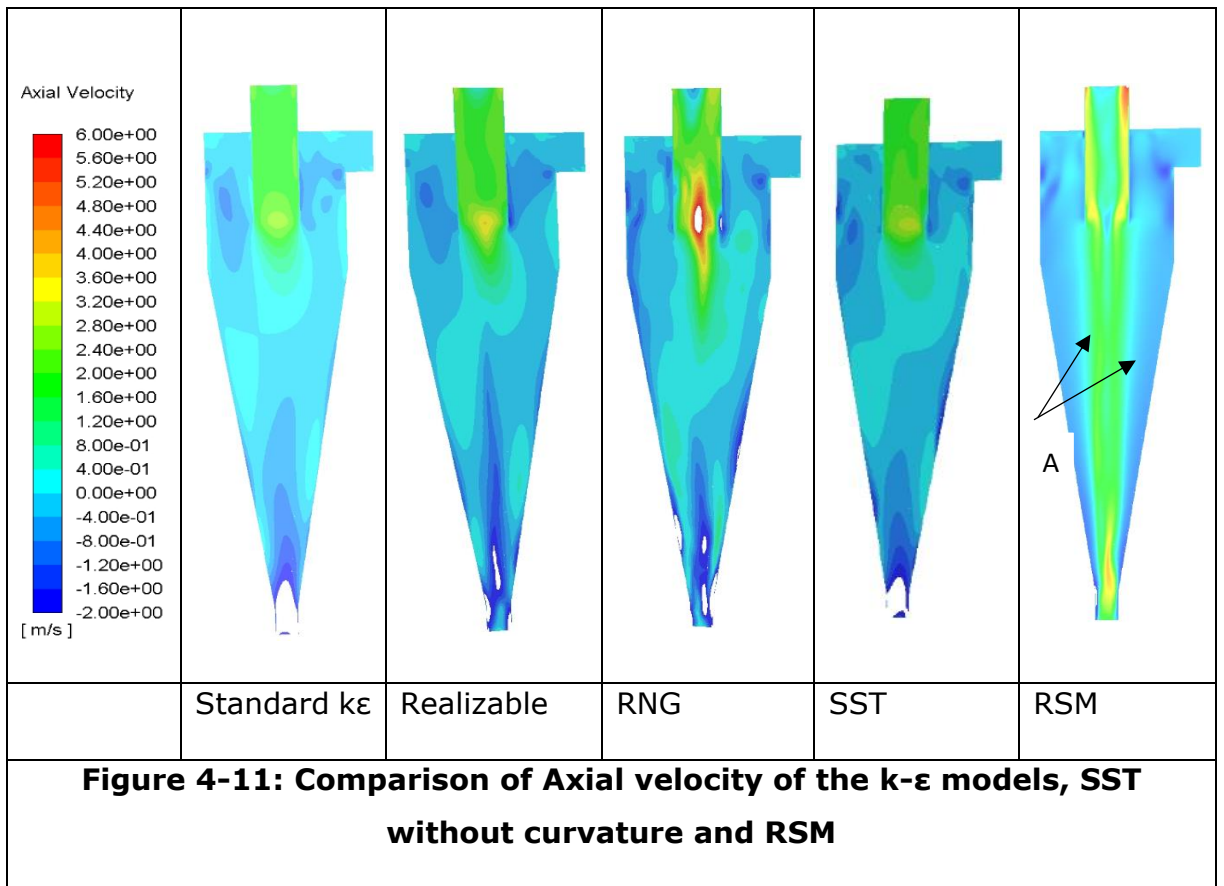
$$C_\mu = \frac{1}{A_0 + A_S \frac{kU^*}{\varepsilon}} \quad (4-3)$$

$$V_t = \frac{a_1 k}{\max(a_1 \omega; \Omega F_2)} \quad (4-4)$$

#### 4.6.2.4 Axial Velocity Contour

Figure 4-11 is the axial velocity contour of k-ε models and SST without curvature correction, the locus of zero vertical velocity (A) was not clearly def

ined on the contour plots when compared to the RSM. This is because of the isotropic assumption in eddy viscosity models, meaning only one scalar velocity fluctuation is modelled. This assumption is impracticable for swirling turbulent flows and this would suggest that k- ε models are unsuitable for modelling turbulence in a hydrocyclone (Saqr, 2009; Dalz, 2015).



The axial velocity takes fluid to the overflow or the underflow section of the cyclone, therefore the LVZZ (A) runs along the longitudinal section of the cyclone as shown on the RSM contour plot. The shortness to non-appearance of the LVZZ seen in figure 4-11 reveals that there is a short circuiting of flow in the cyclone (leading to unclear direction of flow) with the use of eddy viscosity models (Saqr, 2009). The SST on the other hand, modifies the boundary conditions; however, the result in figure 4-11 does not show a significant change in the boundary flow when compared to the other two-equation models. Hence, it can be concluded that the flow in the hydrocyclone is fully turbulent at the boundary layer resulting in the transition SST model switching to standard  $k-\omega$  models thus not properly modelling the flow at the boundary.

Figure 4-12 shows a well-developed LZVV in the flow, this indicates that the use of curvature correction can model the flow in the hydrocyclone. The realizable model profiles match the RSM model contour more than the other models with similar LZVV. This also confirms that the use of curvature correction in the two equation models can be used in the modelling of the flow in the hydrocyclone and this can help the computational time used in modelling flow in a hydrocyclone.

#### **4.6.2.5 Turbulence Kinetic Energy**

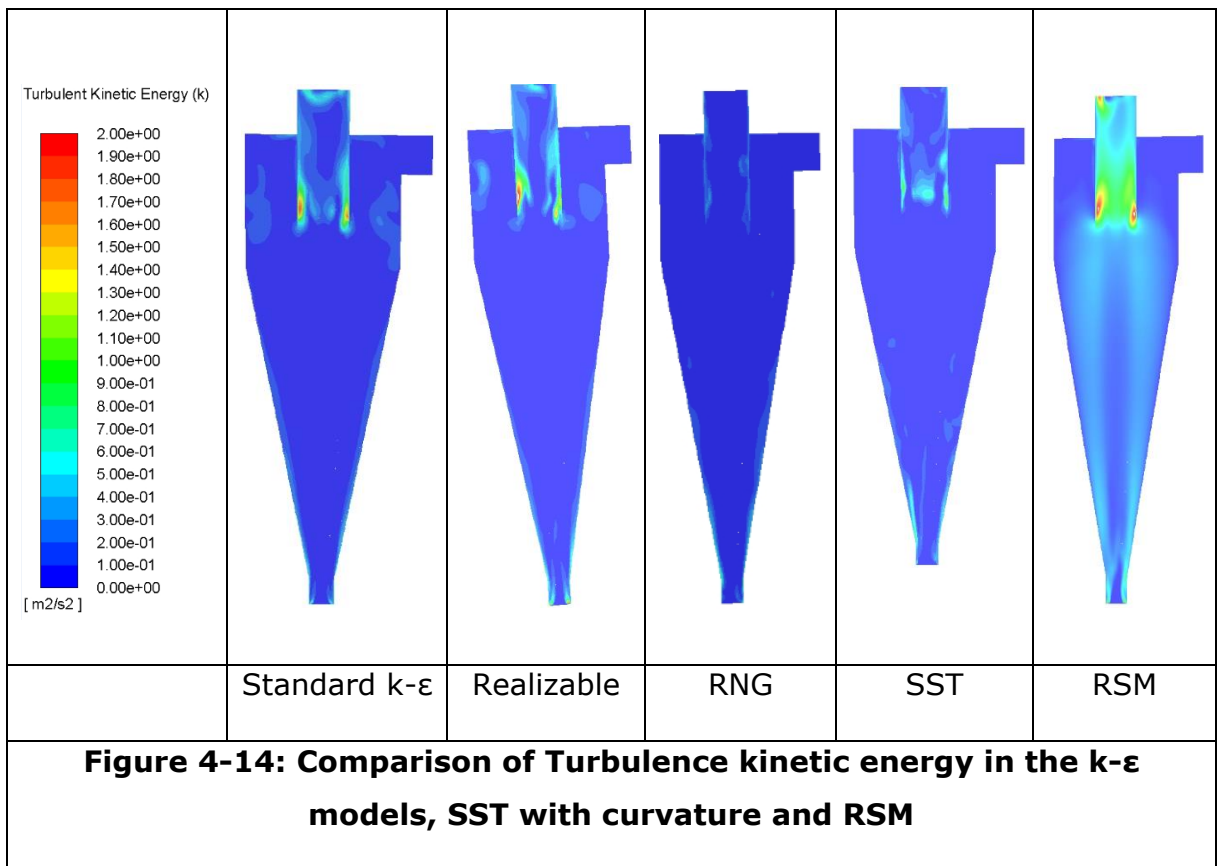
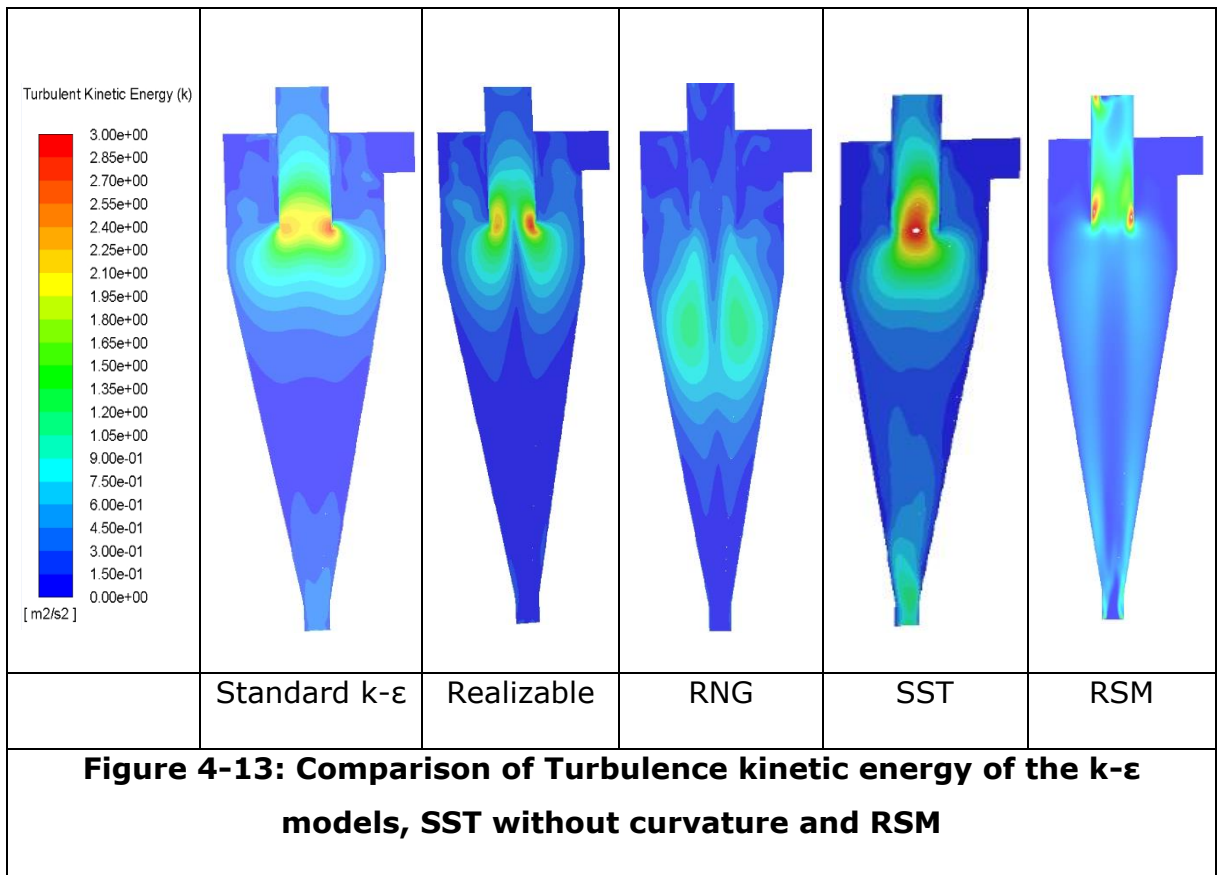
The flow in a hydrocyclone is characterised by a strong swirl flow with strong streamline curvature. Turbulence kinetic energy (TKE) represents the strength of the swirl flow; turbulence kinetic energy is also the mean kinetic energy per unit mass associated with eddies in turbulence flow. It is normally characterised by root mean square (RMS) velocity fluctuations. Large eddies derive energy from the mean flow and energy is transferred from the large eddy to small eddies. In the smallest eddies the turbulence energy is converted to internal energy by viscous dissipation. Fairly uniform turbulence kinetic energy can be seen in the RSM contour plot (figure 4-13) along the body of the cyclone thus showing uniform distribution of the Reynold stress in the flow thus a better resolution of flow. This is because the RSM resolves directly all components of the Reynold stress tensor (Bianco, 2016) and does not use eddy viscosity for its resolution.

The turbulence kinetic energy of the eddy viscosity models can be seen to be unevenly distributed and especially high along the vortex finder. This is because the conventional eddy viscosity model used a boussinesq eddy viscosity

assumption; the transport equation used is a factor affecting the modelling result from standard  $k-\epsilon$  models (figure 4-13). Modification to the RNG and realizable  $k-\epsilon$  models transport equations accommodate a large rate of flow deformation (Jiyuan Tu, 2013), thus a reduction in the turbulence kinetic energy seen in the RNG and realizable model contour when compared to the standard  $k-\epsilon$  model. The transition SST model is used to model accurate near wall functions in adverse pressure gradient flow (Menter, 2006). The eddy viscosity modification in the transition SST model is only applicable at the near wall while the original  $k-\omega$  formulation is used for the remaining part of the flow (Menter, 1994) thus high turbulence kinetic energy is seen in the vortex finder of the cyclone. It can be concluded that the conventional eddy viscosity models cannot predict the effect of strong streamlines curvatures in a cyclone (Alahmadi, 2016)

Figure 4-14 is the contour plot for the  $k-\epsilon$  models with curvature correction, SST with curvature correction and the RSM model. The application of curvature correction to  $k-\epsilon$  models and the SST model significantly reduce the turbulence kinetic energy in the hydrocyclone. This is because in a rotating body modelled by conventional eddy viscosity models like  $k-\epsilon$  models and SST models, the eddy viscosity coefficient is approximately one. Therefore, without implementation of curvature correction, the production term of turbulence kinetic energy is not precise hence the turbulence kinetic energy will not be sensitive to rotational effect (Arolla, 2014). In curvature correction, a modification is introduced into the turbulence production term to compute the Reynold stresses which account for the rotational effect thus there is an overall reduction of the turbulence kinetic energy as seen on the contour plot (figure 4-14).





#### 4.6.2.6 Separation Efficiency

The hydrocyclone uses centrifugal force to separate particles to the wall of the cyclone. This centrifugal is generated from the swirl flow in the hydrocyclone, making fluid flow an important component for separation thus making the turbulence model used in hydrocyclone modelling very important.

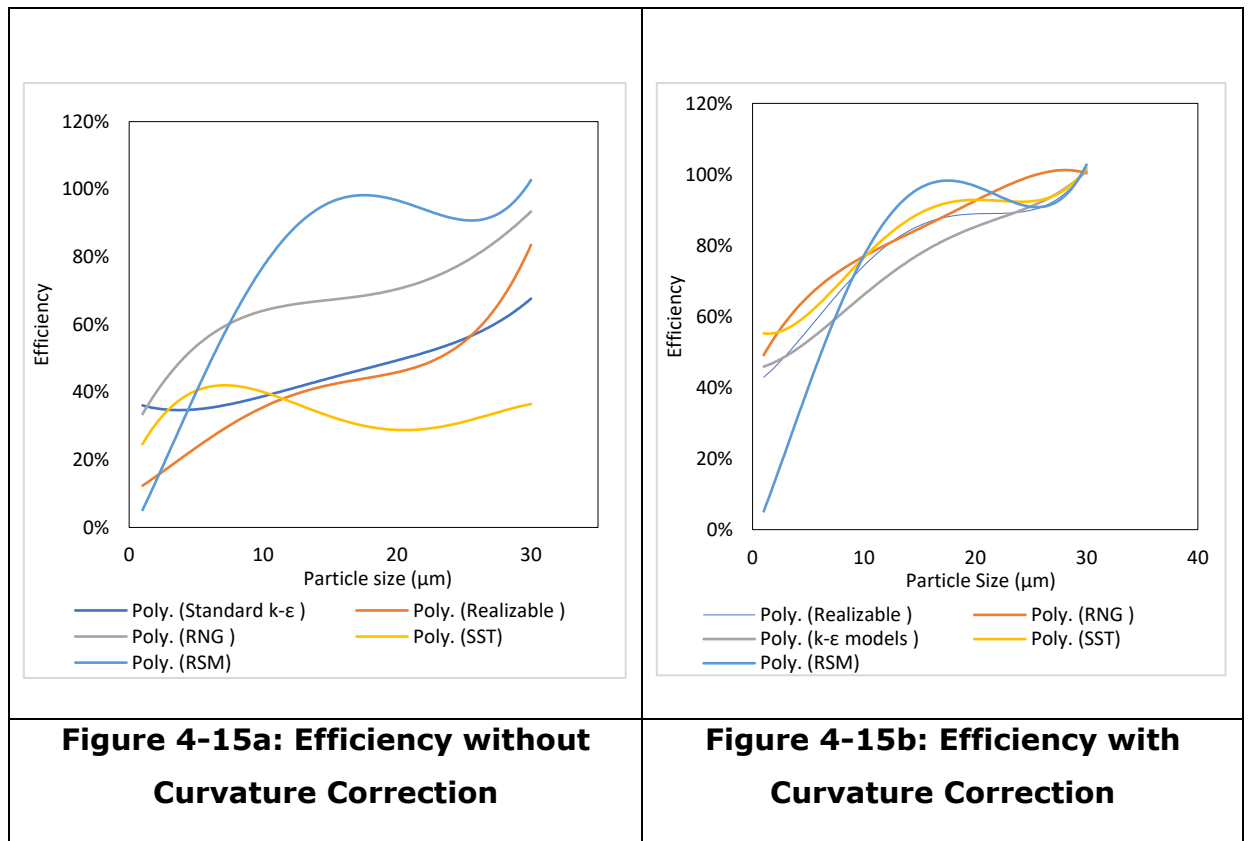


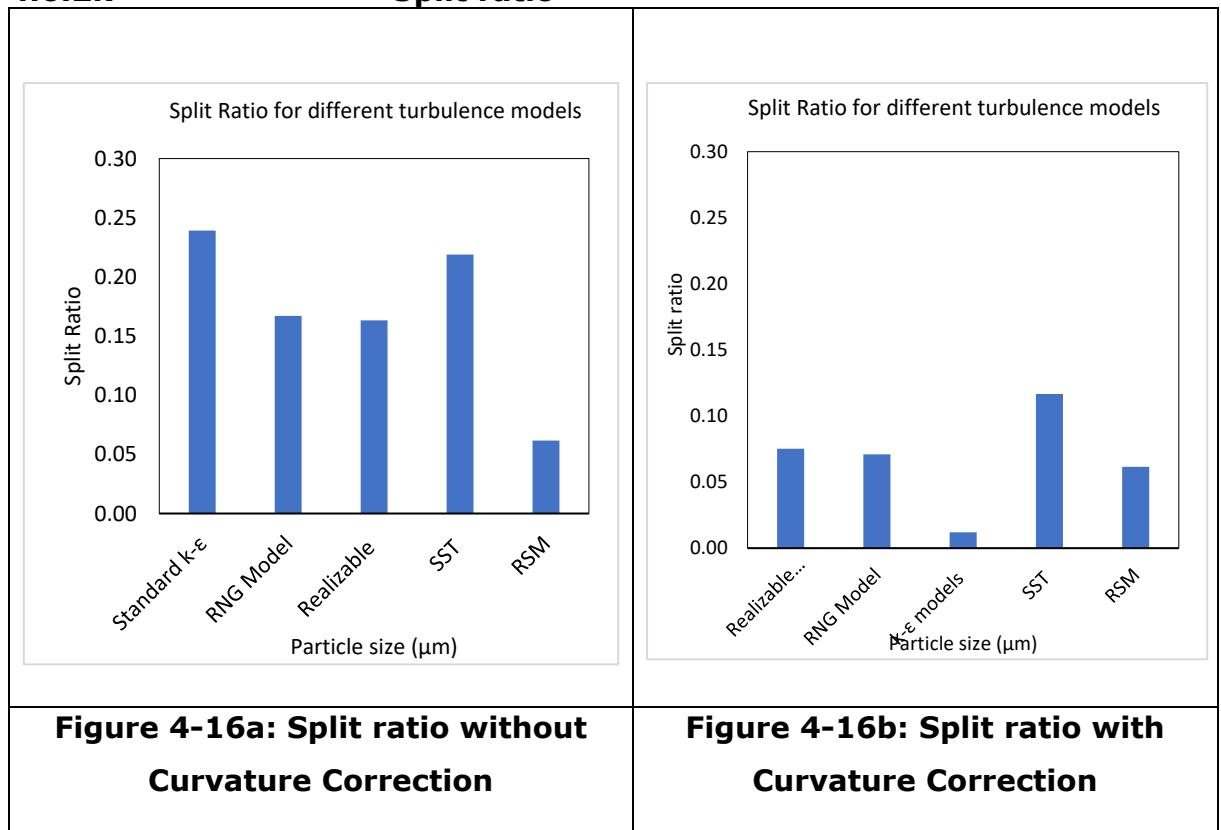
Figure 4-15a shows the separation efficiency curve for the turbulence models under review (standard  $k-\epsilon$  model, realizable  $k-\epsilon$  model, renormalization  $k-\epsilon$  model, transition SST and RSM) without curvature. It can be seen that the RSM model efficiency curve is the best compared to the literature (Mokni, 2019; Wei, 2017; Yang, 2010). This further confirms the superiority of the RSM model in modelling anisotropy turbulence flow. With the use of conventional eddy viscosity models without curvature correction terms, the efficiency curve of RNG is better than the standard  $k-\epsilon$  model. Standard  $k-\epsilon$  model efficiency outperforms both the realizable and transition SST model.

Figure 4-15b shows the separation efficiency for the turbulence model with the use of curvature correction terms. It can be seen that the gap between the efficiency



of the RSM and other models closed up with the introduction of curvature correction term into the simulations. The RSM provides better efficiency than other models while the efficiency of the eddy viscosity models can be ranked from best to worse as follows: SST, RNG, realizable and standard k-ε model.

#### 4.6.2.7 Split ratio



The split ratio is an important factor that predicts the separation of particles from produced water. The split ratio gives us the idea of the percentage of the flow that will be seen at the overflow and the underflow sections and is often described in terms of the percentage of flow expected in the discrete section of the cyclone. In this section the split ratio is define as the ratio of the of underflow mass flowrate to the inlet mass flowrate

$$Split\ ratio = \frac{U_{underflow}}{U_{inlet}}$$

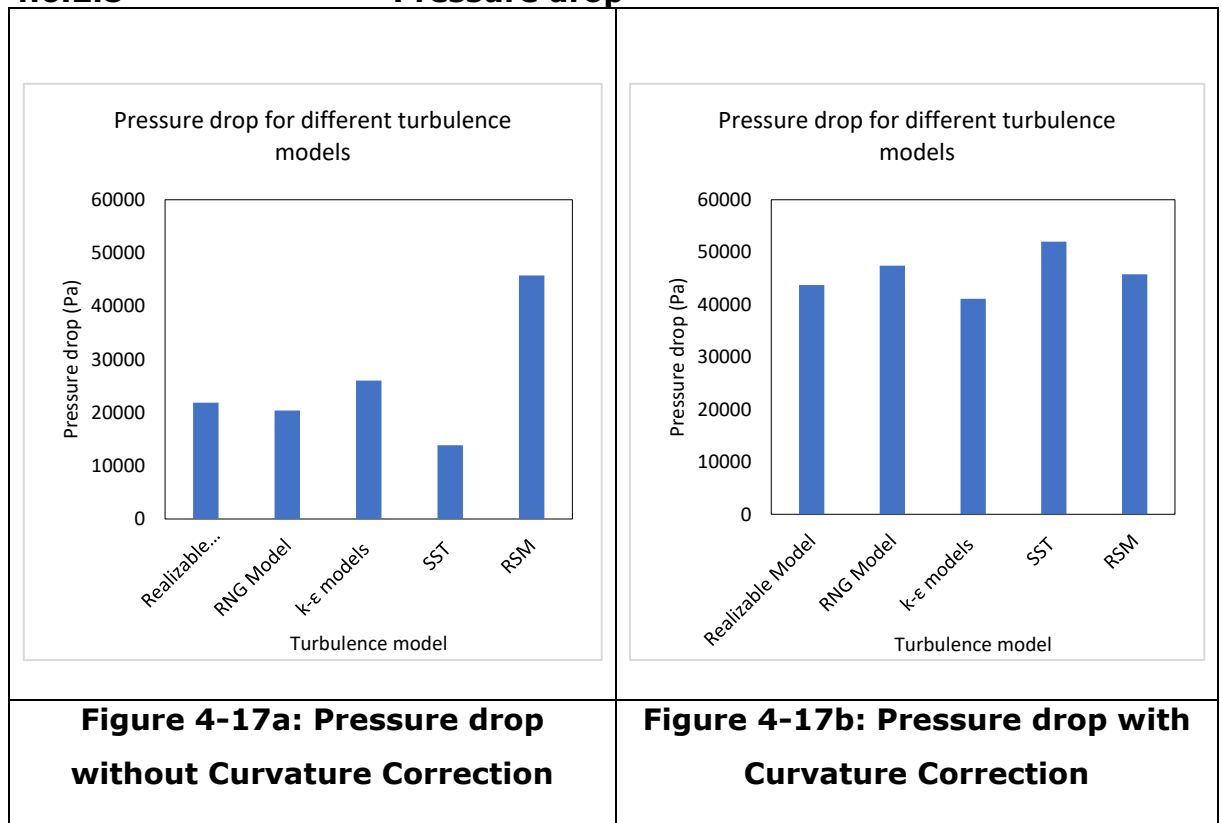
Figure 4-16 is the chart of the split ratio of the turbulence models taken between the inlet and the underflow section of the cyclone. Underflow was used as the reference because the higher density particles (CaCO<sub>3</sub>) are expected to report to

the underflow section while the lower density particle (water) will report to the overflow of the cyclone. Split ratio reflects the percentage of the inlet fluid going to the underflow.

It can be seen that more of the fluid reports to the underflow section of the cyclone with the use of the standard k-ε model and the smallest split ratio was seen in the RSM. This is contrary to the literature which states that increasing split ratio is expected to lead to an increase in efficiency (Yuan, 2015; Jian-Feng, 2016). This is because the comparison split ratio should be considered when analysing flow with same turbulence model rather than flow analysis with different turbulence models. Flow in turbulence models is reviewed using different equations thus leading to different split ratios and cannot be directly related to the overall performance of the hydrocyclone.

Comparing the split ratio of each of the models (i.e with and without curvature correction terms), it can be seen that the split ratio of the model without curvature is higher than the split ratio of the same model with curvature correction terms for all the eddy viscosity turbulence models.

#### 4.6.2.8 Pressure drop

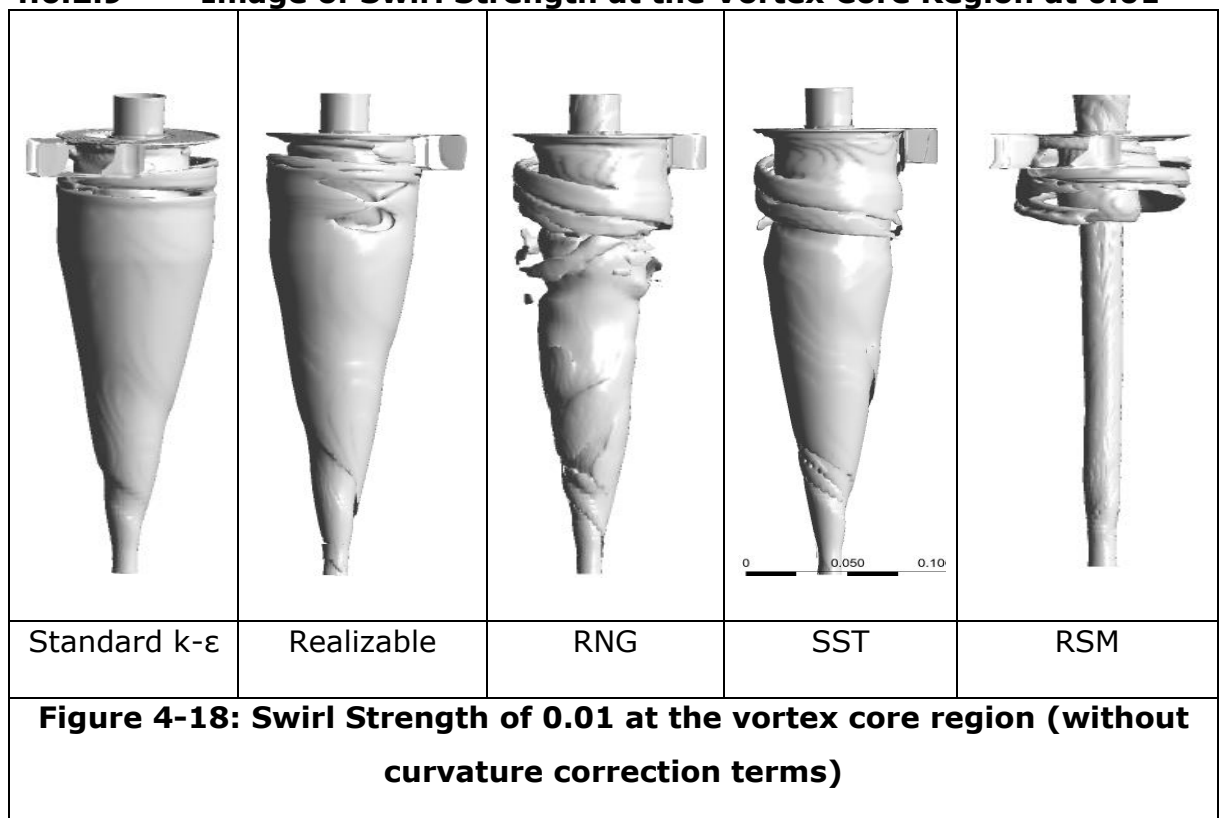


From figure 4-17a, the pressure drop in the RSM model is higher than that of the eddy viscosity models. This means that use of RSM model to predict flow in a hydrocyclone led to more energy loss, the higher the energy loss is said to lead to greater separation efficiency (Priestman, 2006).

Studies have also shown that increasing pressure drop increases the separation efficiency (Bicalho, 2012) until an optima pressure drop is attained after which a further increase will cause a decrease in the efficiency of the hydrocyclone. The huge difference between the pressure drop of eddy viscosity and the RSM shows that the equations solved for the turbulence model affect the energy required for the simulation. RSM pressure drop can be linked to the direct resolution of the Reynold stress tensors.

The pressure drop of the standard eddy viscosity models are considerably smaller compared to the eddy viscosity model with curvature correction where the pressure drop was seen to increase considerably indicating that the production terms introduced into via curvature correction terms required more energy to generate a swirl flow than when conventional/ standard eddy viscosity models are used.

**4.6.2.9 Image of Swirl Strength at the Vortex Core Region at 0.01**

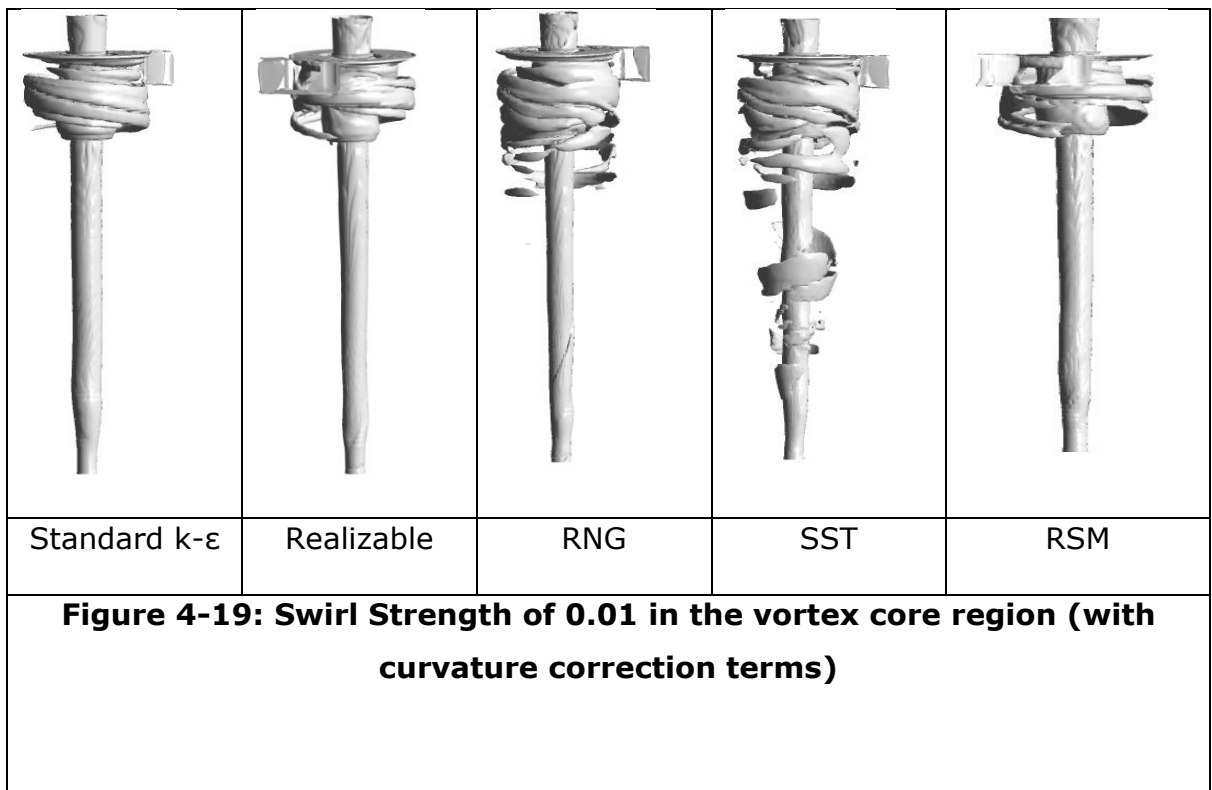


Swirling strength is an effective vortex indicator in wall turbulence, vortex size increases inversely with the threshold used for growing the vortex region from background turbulence (Chen, 2018). The swirling strength criterion has been proven to be effective and efficient in wall turbulence

The appropriate model to be used for any analysis depends on the swirl strength that is to be encountered, for weak to moderate swirl, standard  $k-\epsilon$  model, realizable  $k-\epsilon$  model and RNG can be used (Fluent 2016, Mulu, 2015). However, with high swirl strength the RSM model is the most appropriate RANS equation to be used. From figure 4-19, it can be seen that little to no-vortices/ flow pattern appear on the chart of the standard  $k-\epsilon$  model, realizable  $k-\epsilon$  model and SST model plot, this indicates low flow separation as the vortices promote flow separation as fluid is transported (Rosenfeld, 1995; Johnson, 1989).

Swirl effect modification on the RNG enhances the swirl flow thus the swirl effect that can be seen on the RNG model. The SST on the other hand combines the near wall region of the  $k-\omega$  model with the free stream independency of a  $k-\epsilon$  model to predict the onset and the amount of flow separation under high adverse pressure gradients, thus having little effect of the swirl in the flow. A realizable model does not include swirl effect and changes to the viscosity constant and the production term in the dissipation equation has little effect of the swirl thus the slight change in the model compared to the standard  $k-\epsilon$  model. The RSM accounts for the effect of streamline curvature, swirl, rapid changes in strain and anisotropy of turbulence stress, therefore, is able to account for the accurate flow pattern and vortices of the flow in the hydrocyclone (Mulu, 2015).

Figure 4-19 is the swirl strength around the vortex core when the curvature correction term was introduced to the eddy viscosity models. This is used to modify the turbulence production terms in the eddy viscosity models' equations. The flow pattern of the models improves with more pronounced vortices and is also similar to the RSM model flow pattern. The RNG and transition SST plot differs lightly because the RNG and transition SST already include swirl effect and therefore the use of curvature correction should be with caution (Fluent, 2016)



#### **4.7 Summary of Turbulence Models and CFD Validation**

This chapter evaluates the mesh independency of the result of the hydrocyclone fluid flow analysis using three different meshes. It also confirms the competency of the use of computation fluid analysis in hydrocele simulation. The appropriate RANS turbulence model was also evaluated by comparing the results of eddy viscosity models (standard k- $\epsilon$  models, realizable k- $\epsilon$  models, Renormalization k- $\epsilon$  models, transition shear stress transport equation) to the experiment and RSM model results. The influence curvature correction term to the eddy viscosity models were also reviewed and compared to the experimental and RSM model results.

The mesh independency analysis reveals that with the use of mesh-3, no significant change of result will be experienced due to mesh size and that computational fluid dynamics can accurately predict the flow in hydrocyclone.

The turbulence model analysis result shows that the RSM model performs better than the eddy viscosity models with and without curvature correction terms.

The use of curvature correction terms in eddy viscosity models was also seen to improve the fluid flow and separation of particles in the hydrocyclone. Without the

use of curvature correction terms, conventional RNG model performance was better than the standard, realizable  $k$ - $\epsilon$  models and transition SST model. With the use curvature correction terms, RNG and transition SST results are closer to that of RSM and the experimental result than the realizable and standard  $k$ - $\epsilon$  models.

It can therefore be concluded that for a good accurate result, the RSM is the best model among the models analysed. However, for a preliminary analysis any of the eddy viscosity models can be used with the incorporation of curvature correction terms with emphasis on the SST and RNG models.

## **5.0 Comparing the effect of hydrocyclone geometrical parameters on the separation of particles and flow of fluid parameters in hydrocyclone**

The geometry is one of the main determinants of the effectiveness and efficiency of the hydrocyclone, thus improvement to the hydrocyclone can be achieved by adjusting the geometrical parameters. This chapter investigates the effect of various geometry parameters on particle separation and fluid flow in the hydrocyclone. A detailed understanding of the flow structure is essential for proper design, design modifications, and improving the efficiency and effectiveness of the hydrocyclone. The use of computational studies to evaluate hydrocyclone flow is generally limited to low particle concentration and simplified geometry of the hydrocyclone (Motsamai, 2015). The drivers of modelling hydrocyclone flow behaviour are the complex flow structure, interaction between particles and the formation of air-core for hydrocyclone open to the atmosphere. Previous studies of hydrocyclone have shown that a 3D model (Motsamai, 2015) better analyses the flow field in the hydrocyclone and the accuracy of the hydrocyclone model since the flow inside the hydrocyclone is a three-dimensional swirling flow restricted to cylindrical and conical geometry. Therefore, a 3D model was used for the simulation analysis carried out in this chapter.

The hydrocyclone geometrical dimensions were changed around a reference geometry; in this chapter, the reference geometry has been referred to as the base geometry. The same flowrate/flow parameters were used for all the simulations. The properties of the water and CaCO<sub>3</sub> used can be seen in table 5-1 below.

**Table 5-1: Properties of Fluid in hydrocyclone**

Property	Water	CaCO <sub>3</sub>
Density (kg/m <sup>3</sup> )	998.2	2800
Viscosity (kg/m-s)	0.001003	-
Thermal Conductivity (W/m-K)	0.6	2.5
Molecular Weight (kg/mol)	18.0152	100.09
Reference Temperature (K)	298	298
Specific Heat (C <sub>p</sub> ) J/Kg-K	4182	856
Velocity (m/s)	2.5	2.5
Concentration (%) (Vol/Vol)	98.14	1.86

The simulation models were set using a pressure-based solver with absolute velocity formulation for the transient flow field. The gravity was activated with gravitational acceleration set to  $9.81\text{m/s}^2$  in the vertical axis to account for the effect of gravity on the cyclone. Water was used as the continuous phase while CaCO<sub>3</sub> was the discrete phase (solid). The CaCO<sub>3</sub> was released from the inlet into the continuous phase as an inert particle with uniform diameter distribution. The same boundary conditions and solver control used in chapter 4 were used in this chapter while the mesh of about 580000 elements was used for all the simulations.

In this study, the RSM model was used to evaluate the turbulence in the cyclone while the DPM model evaluates the particle behaviour. It was observed that a large number of iterations were required to stabilize the solution. The outlets were exposed to the atmosphere, therefore giving a region of low pressure along the axis of the cyclone

Usually, the flow inside a hydrocyclone is a Rankine vortex (Jordan Ko, 2006; Yaojun, 2000; Bing Liu, 2019) with a combination of two vortices which are the forced vortex also known as body rigid rotation and the free vortex known as a potential vortex. In the forced vortex the tangential velocity is proportional to the radius of the cylindrical section of the hydrocyclone while in the free vortex the tangential velocity is inversely proportional to the hydrocyclone cylindrical section. How the various geometrical parts affect the generation of the free and forced



vortex and properties of fluid flowing in the hydrocyclone are critically reviewed in this chapter.

## **5.1 The Cylindrical Diameter**

The hydrocyclone cylindrical diameter is often referred to as the hydrocyclone diameter or hydrocyclone size which can be from 10mm to 2.5m depending on the cut size required for hydrocyclone separation. Small cut size usually results in the use of smaller diameter hydrocyclone and larger cut size requires the use of larger diameter hydrocyclone. Therefore, reducing the hydrocyclone diameter is important for improving the separation of smaller particles from the produced water. The effect of the cylindrical section on pressure, turbulence kinetic energy, velocities and swirl in the hydrocyclone were evaluated.

Three cylindrical geometries were considered for the hydrocyclone diameter evaluation, the base geometric which is 75mm cylindrical geometry, 35mm and 50mm hydrocyclone diameter.

Table 5-2: Different Cylindrical Dimension Used

Parameter	Symbol	35mm	50mm	Base (75mm)
Diameter of the cyclone body (mm)	Dc	35	50	75
Size of Inlet (mm)	Di	22.16 x 22.16	22.16 x 22.16	22.16 x 22.16
Diameter of the vortex finder (mm)	Do	12.5	25	25
Insertion depth of the vortex finder (mm)	Lv	12.5	50	50
Length of the cylindrical part (mm)	Lc	75	75	75
Cone Angle (°)	A	20°	20°	20°
Diameter of the spigot (mm)	Du	12.5	12.5	12.5

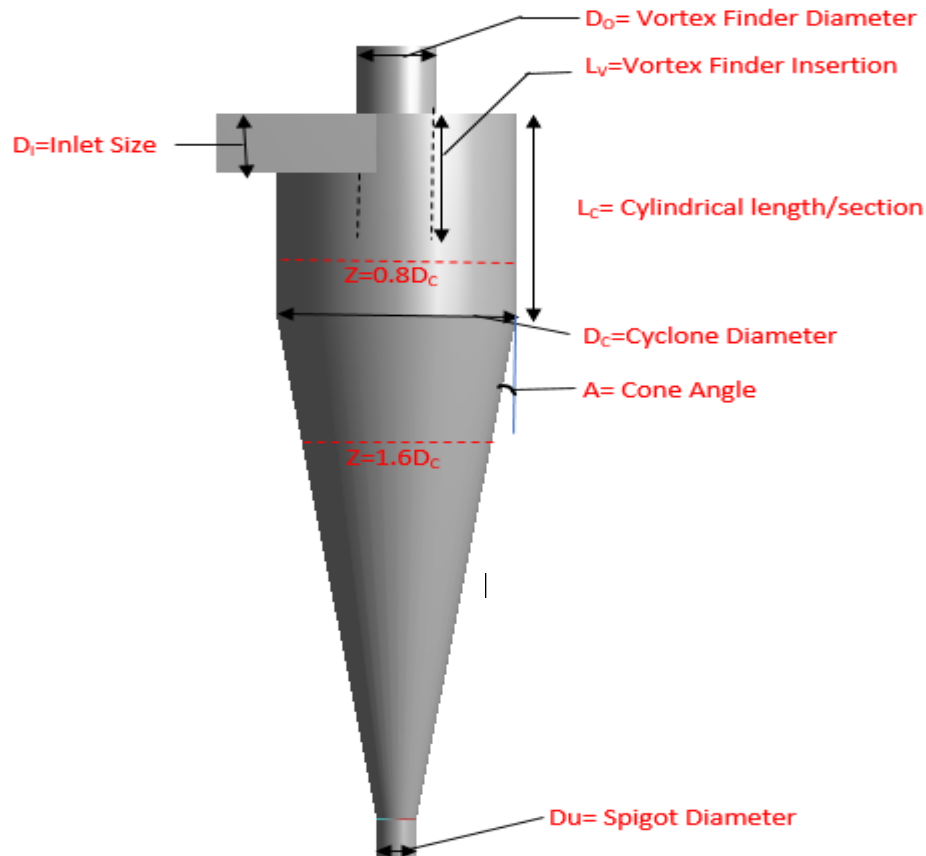


**Figure 5-1: Hydrocyclone Geometrical Parts**

## **5.2 Result and Discussion of results**

### **5.2.1 Turbulence Kinetic Energy**

The turbulence in a cyclone is an important factor in determining the structure of flow and the motion of particles in the cyclone. There are not many experimental results on the turbulence in a cyclone because it is difficult to measure the pulsating velocities in the cyclone thus the analysis in the section will be based on existing theories and literature. Figure 5a is the contour of the turbulence kinetic energy for the cylindrical diameter being evaluated. It can be seen that highest turbulence kinetic energy is at the lower end of the vortex finder where the flow turns and the velocity gradient is very large (Matvienko, 2004). The turbulence is carried from the lower end of the vortex finder by convection and gradually decays towards the lower parts of the hydrocyclone. Figure 5a also shows that the turbulence is also high at the lower end of the hydrocyclone towards the spigot

section, this is as a result of the resistance to flow due to the diameter of the spigot leading to more resistance in flow and consequently increasing interparticle collisions which increase turbulence and friction within this area of the cyclone (Cavex, 2016).

The turbulence kinetic energy of a 50mm hydrocyclone has higher turbulence at the lower end of the vortex finder than the 35mm and the 75mm hydrocyclone because the turbulence flow is not well distributed in the hydrocyclone as is the case of the 35mm and 75mm hydrocyclone. Based on the distribution of the turbulence kinetic energy flow in the hydrocyclone, the efficiency of the hydrocyclone can be predicted with the most evenly distributed turbulence kinetic energy giving better efficiency than the others; turbulence dispersion has been found to have a great effect particle separation; Zaman, 2016. Therefore, the separation efficiency of the 35mm and 75mm hydrocyclone are expected to outperform the efficiency of the 50mm hydrocyclone.

Figure 5b gives a better insight into how the turbulence kinetic energy changes from the cylindrical to the conical section of the hydrocyclone. The 50mm cylindrical cyclone was seen to have a very high turbulence kinetic energy in the cylindrical section and across the radial distance of the hydrocyclone when compared to the 35mm and the 75mm hydrocyclone. This can be attributed to the ratio of the hydrocyclone diameter to the vortex finder diameter. A 50mm hydrocyclone with a 25mm diameter vortex finder is considered too large for the cyclone diameter, as there is an optimum ratio of the inlet head diameter, vortex finder and spigot diameter to the hydrocyclone diameter (Kumar, 2018). Decreasing the vortex finder diameter to 12.5mm as the hydrocyclone cylindrical diameter is almost halved (35mm) was seen to improve hydrocyclone performance, this is consistent with the experimental result of Elsayed, 2013. The turbulence kinetic energy in the conical section tends to behave differently with increasing cylindrical size yielding higher turbulence kinetic energy. This is because the size of the conical section remains constant for the three hydrocyclones.

It is, therefore, safe to conclude that increasing the cylindrical diameter of the hydrocyclone increases the turbulence kinetic energy in the hydrocyclone especially in the conical section of the hydrocyclone. In the cylindrical section,

however, this turbulence kinetic energy depends on the ratio of the cyclone diameter to the vortex finder diameter.

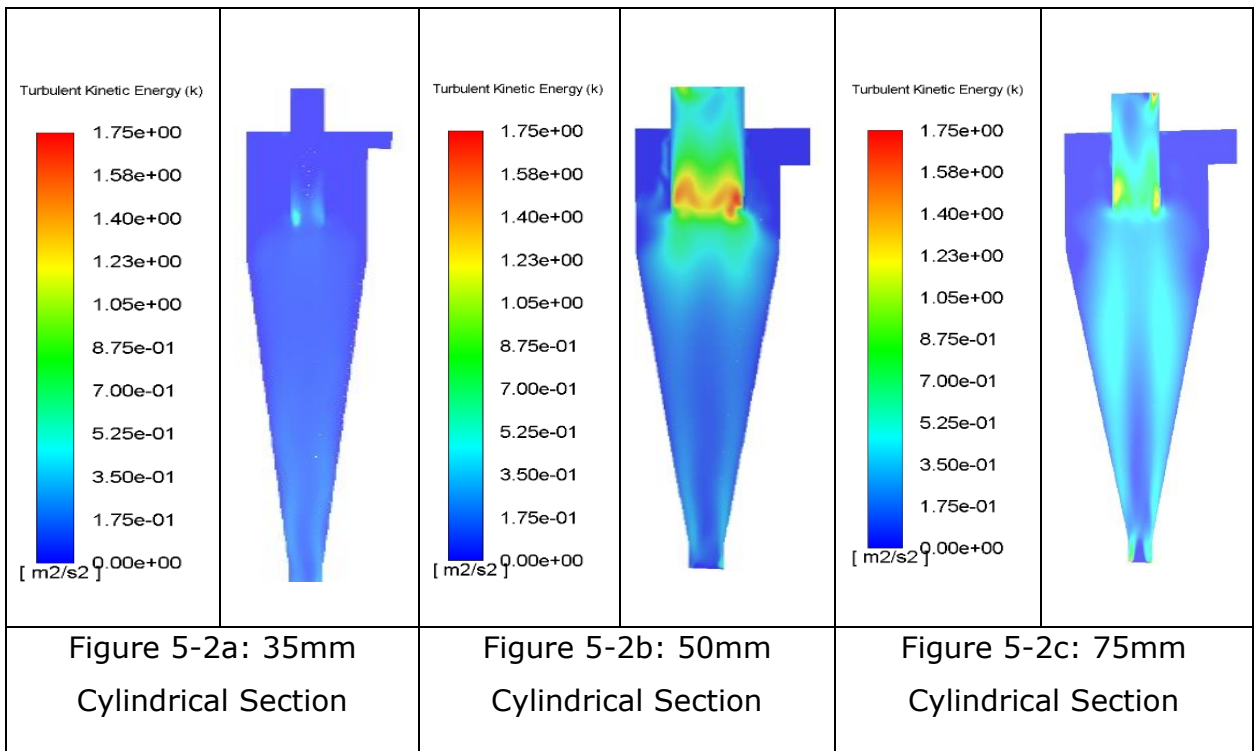


**Figure 5-2: Turbulence Kinetic Energy contour plots**

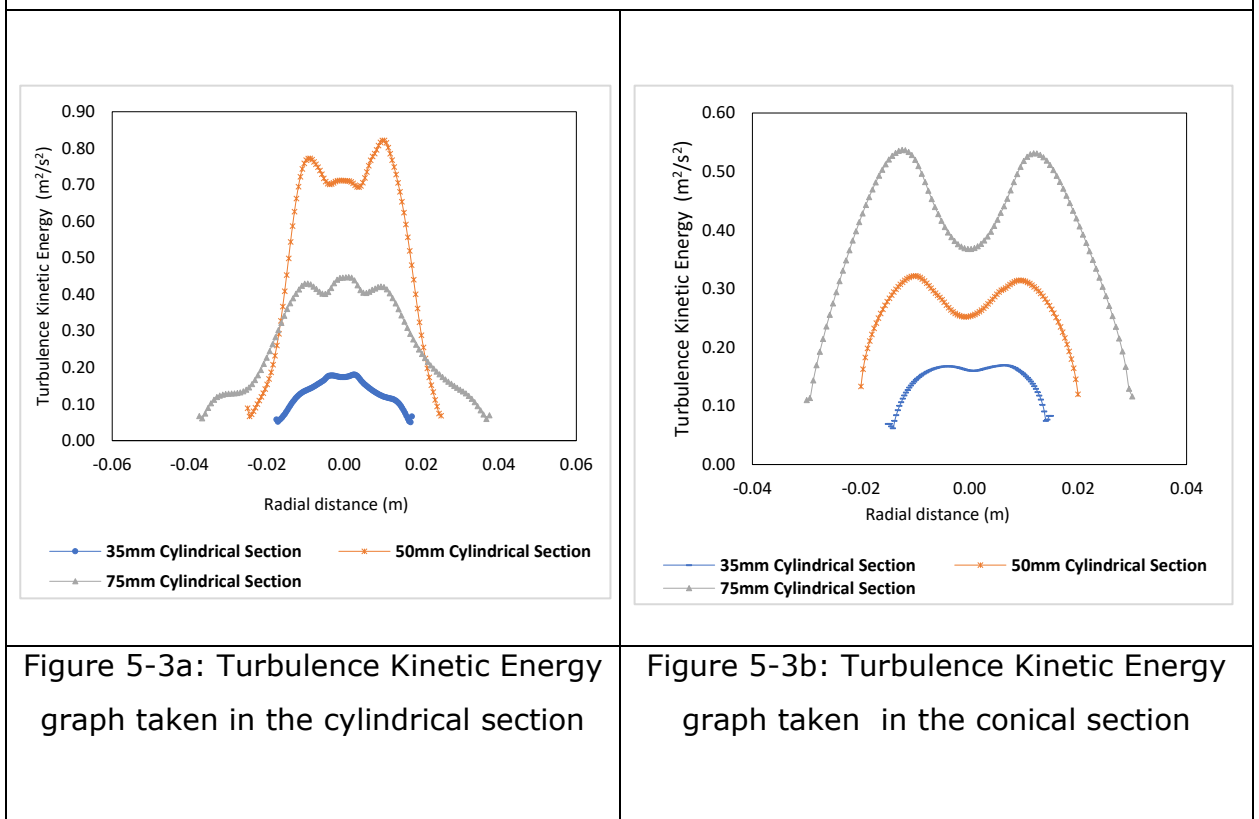


**Figure 5-3 Turbulence Kinetic Energy at different cylindrical diameters**

## 5.2.2 Tangential Velocity

According to Jiang L. (2019), tangential velocity directly determines the strength of the centrifugal force which is the driving force for phase separation and a very important factor in evaluating hydrocyclone performance. The centrifugal force acting on a particle (p) with density ( $\rho_p$ ) moving with a velocity at radius r and tangential velocity  $U_{\theta p}$  is given by the equation 1 below

$$F_c = (\rho_p - \rho_l) \frac{\pi d_p^3}{6} \frac{U_{\theta p}^2}{r} \quad (1)$$

Therefore, it can be said that the centrifugal force is directly proportional to the tangential velocity. In a hydrocyclone, a higher centrifugal force leads to better separation. The flow field in figure 5-4 shows the expected forced/free combination of Rankine type of vortex which is expected in a hydrocyclone. However, the change in tangential velocity distribution along the axial length (cylindrical and conical section) is minimal with the velocity in the cylindrical section, not more than 0.5m/s velocity in the conical section.

An increase in cyclone diameter is seen to have a direct impact on the hydrocyclone tangential velocity as the tangential velocity decreases with the decreasing cyclone diameter. Studies have (Jiang, 2019) shown that higher tangential velocity improves the separation of particles in a control volume, but this analysis is only valid for cyclones with similar body size (Ghodrat, 2013). The current studies reveal that increasing the cyclone diameter increases the tangential velocity (Chaware, 2017; Ghodrat, 2013). Chaware, 2017 revealed that tangential velocity in a pipe with turbulence flow increases with the distance from the centre of the pipe. This is attributed to the intensity of the swirl increasing with the cyclone cylindrical diameter which is influenced by the Reynold number (the Reynold number is proportional to the cyclone diameter) if the flow is not fully developed. This can also be explained using the concept of the circulation in axisymmetric swirling flow of an incompressible fluid which is given by equation 2 below with the latter being the most likely.

$$\Gamma \equiv \iint_S (\Omega \times n) dS = 2\pi r v_t \quad (2)$$

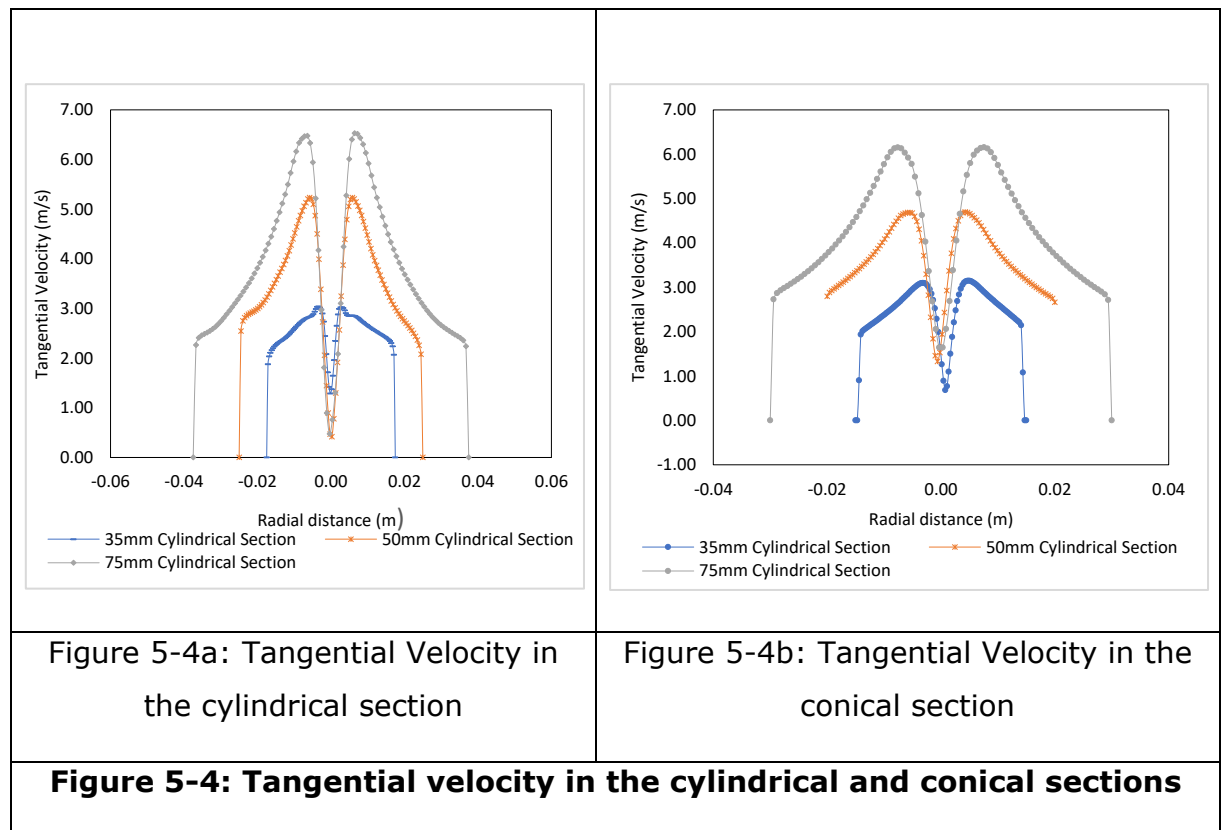
Where

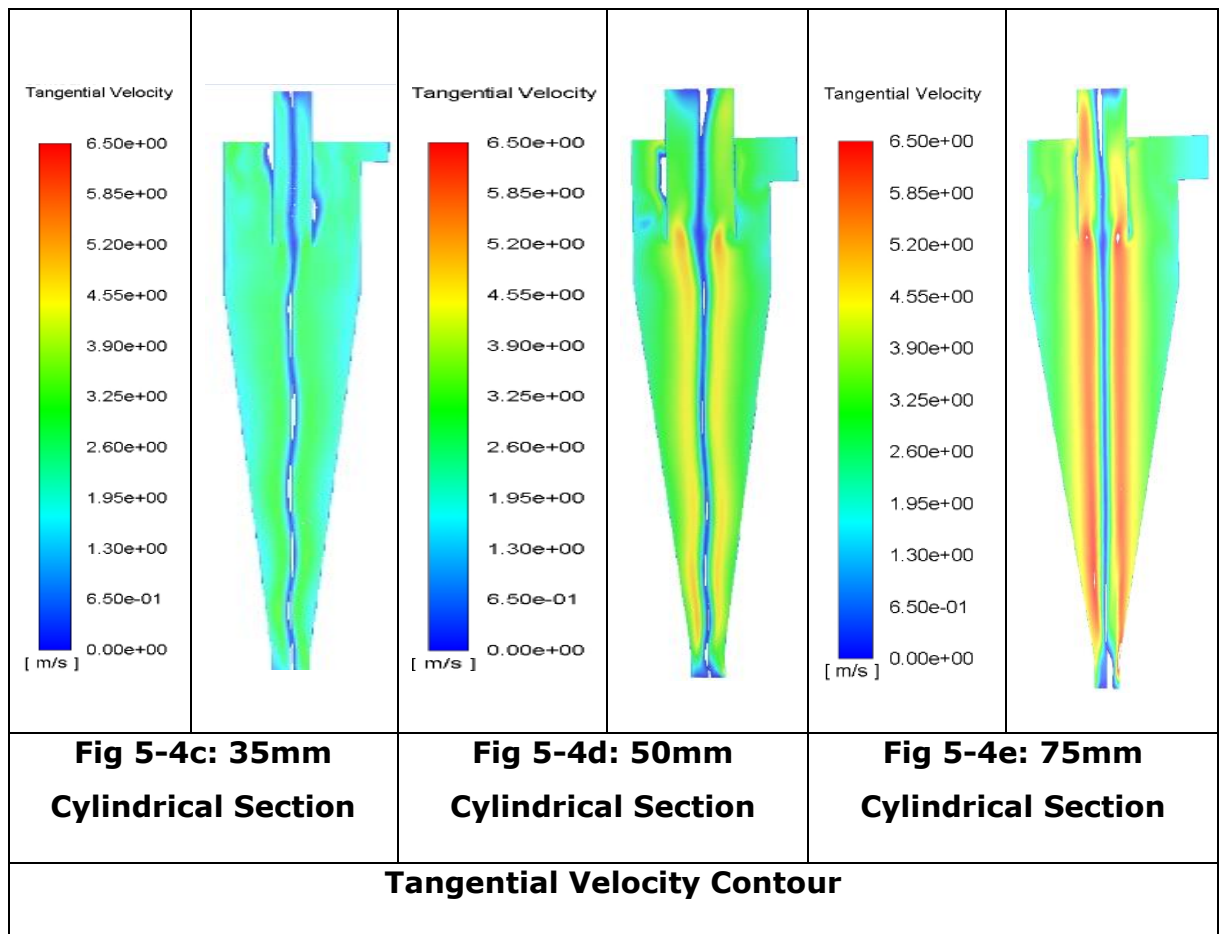
- $\Gamma$  = Swirl Intensity
- $S$  = Cross sectional area
- $\Omega$  = Vorticity Vector
- $n$  = Unit normal vector to  $S$
- $v_t$  = Tangential velocity
- $r$  = Pipe radius

Figure 5-4c to 5-4e shows the contour for the tangential velocity for the cylindrical sections reviewed and it can be seen that tangential velocity increases across the cyclone as the cyclone size increases. This can be attributed to the decreasing radius leading to decrease in tangential velocity (Concha,2007; Lozia, 2007). The tangential velocity below the vortex finder can be related to the radius using equation 2a below given by Kelsall, 1958.  $V$  is the tangential velocity,  $r$  is the radius,  $K$  is a constant and  $0 < n < 1$

$$V_{\theta} r^n = K \tag{3}$$

The maximum tangential velocity within the cyclone is also seen to exceed the cyclone inlet velocity (Lozia, 2007).





### 5.2.3 Axial Velocity

This is the velocity that is responsible for taking particles to the outlets of the hydrocyclone. The particles near the wall, flow axially to the underflow while the material near the centre of the cyclone moves radially towards the overflow. From figure 5-5a and b the smaller the diameter of the cyclone the higher the axial velocity in both the inner and outer regions (Azadi, 2010).

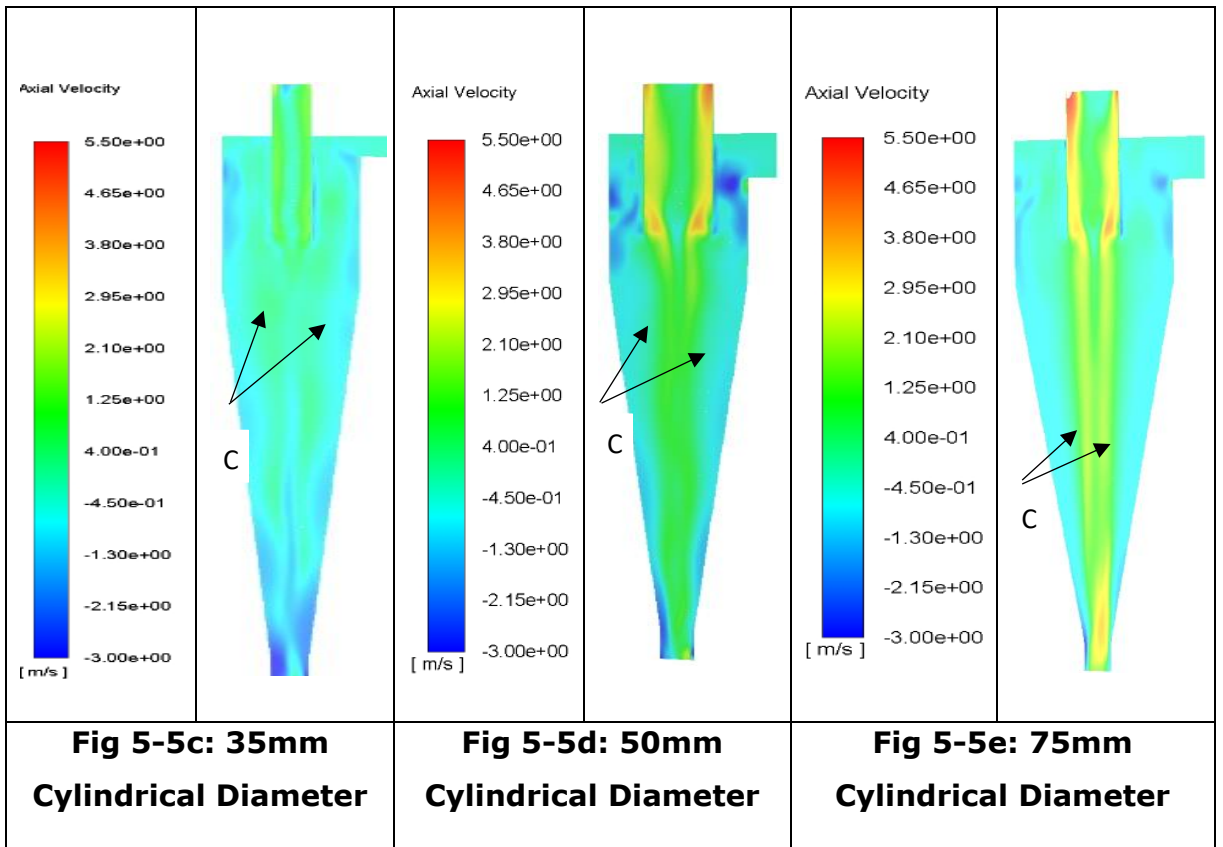
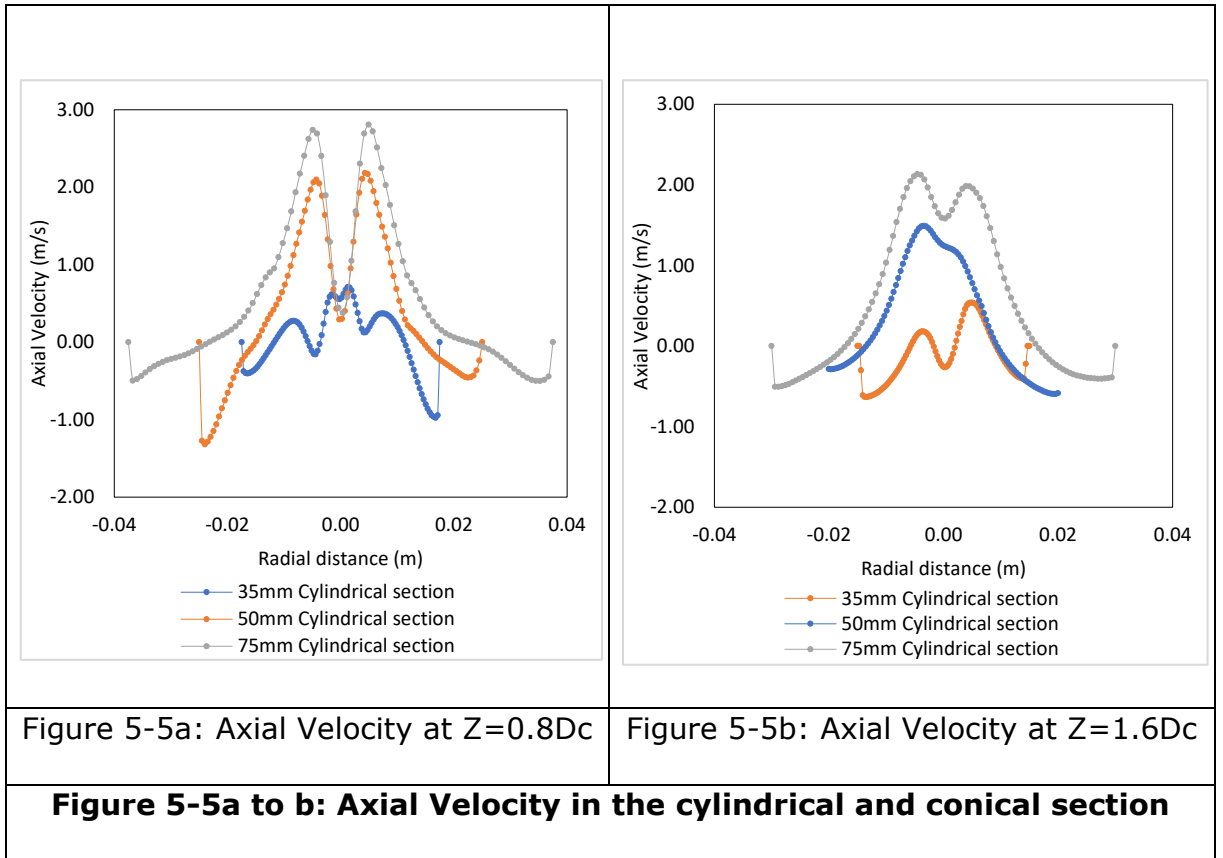
In the cylindrical section, a 75mm hydrocyclone has a high positive axial velocity of up to 2.6m/s while the 50mm result shows a positive axial velocity of about 1.97m/s and the 35mm shows a positive axial velocity of about 0.6m/s. This shows that the secondary vortices in the cylindrical part of the 75mm hydrocyclone are more than the 50mm and 35mm hydrocyclones and more of the particles are likely to move to the overflow in the cylindrical section of a 75mm hydrocyclone than in the other two diameters considered. This can be ascribed to the fact that when the

same fluid velocity that flows into the smaller cyclone comes into the larger cyclone, there is a smaller velocity gradient in the cyclone. Fluid motion at smaller scales eddies is associated with large velocity gradients and correspondingly large shear stress (Doran, 2013).

An increase in shear stress increases the volume of smaller eddies and therefore we have more smaller eddies going towards the overflow in the 75mm cylindrical section of the cyclone than in the 50mm and 35mm cylindrical hydrocyclones. It can be seen that the axial velocity in the conical section is lower than that of the cylindrical section, showing that the speed of movement of fluid to the overflow is higher than cylindrical than in the conical section. This is attributed to the lower fluid separation in the cylindrical section thus lowering drag in the cylindrical section. A reduction in the axial velocity at the core region indicates that the pressure at the central region is lower than the external pressure (Jiang, 2019).

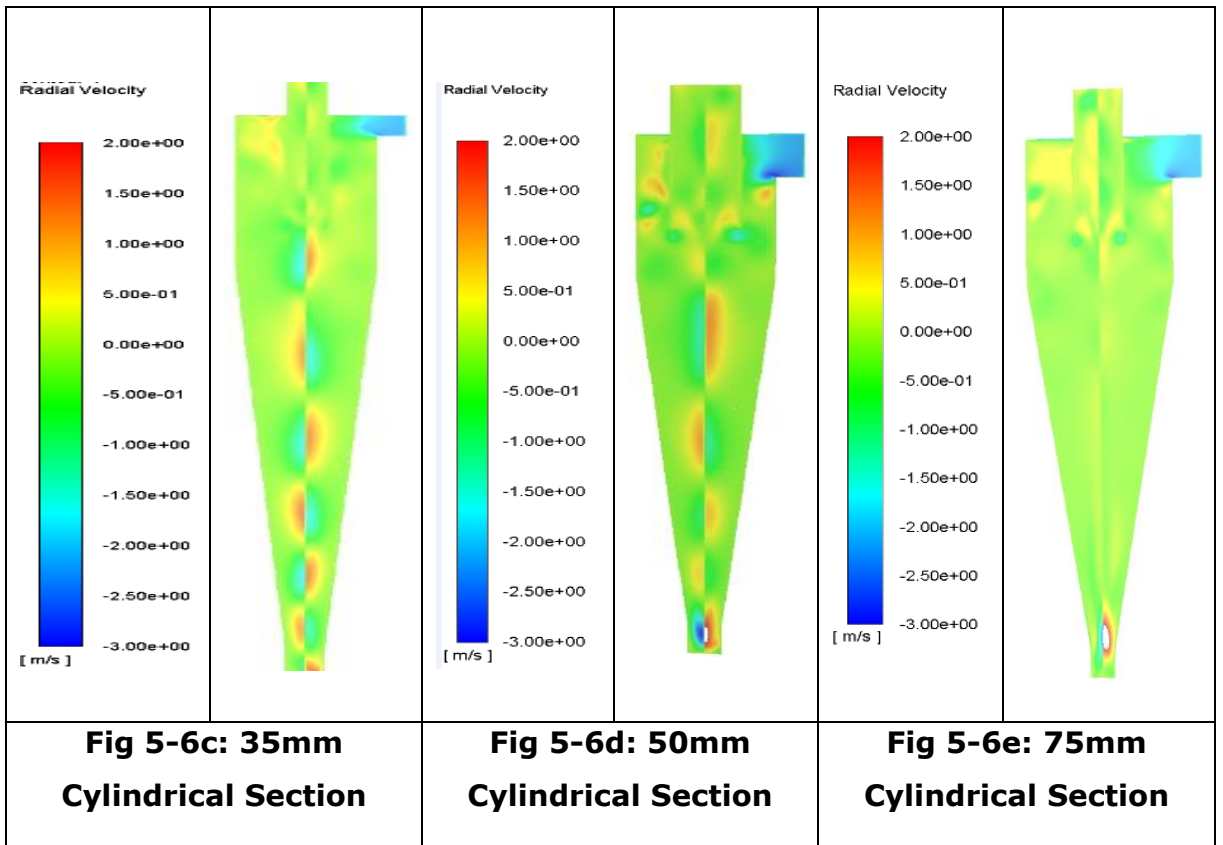
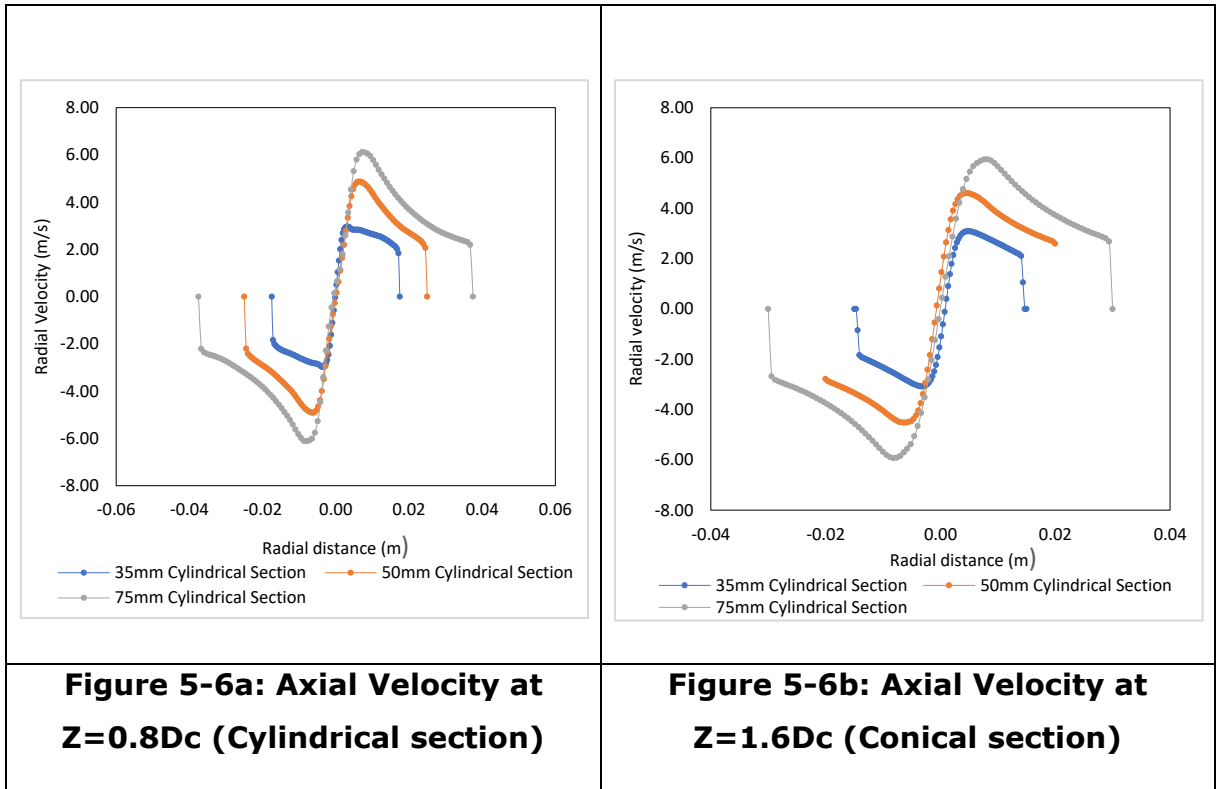
Looking at the axial velocity contour along the vertical section of the cyclone (shown in figure 5-5c to 5-5e), it can be seen that the 35mm cylindrical diameter hydrocyclone has lower axial velocity in the core region compared to the 50mm and the 75mm hydrocyclones. This is because more fluids are separated to the wall of the cyclone and therefore reducing the particles movement to the core region of the cyclone. It also reflects that the locus of zero vertical velocity (point C) spread is larger in the 50mm diameter hydrocyclone showing that more particles have the tendency of moving to the core region and being carried to the overflow when compared with the 35mm and 75mm diameter hydrocyclones.





### 5.1.4

### Radial Velocity



The experimental results of Hsieh, 1998 show that the radial velocity is very small compared to tangential and axial velocity magnitude but from Figure 5-6a and b above the radial velocity seems to be slightly less than the tangential velocity and more than the axial velocity showing that computational fluid dynamics over predict the axial velocity in a hydrocyclone. Other authors like Zhu G (2010) and Utikar (2010) among others have reported this.

What can be seen however is that the radial velocity is positive on one side and negative on the other which can be attributed to the non-symmetrical nature of conventional tangential inlet of the hydrocyclone (Utikar, 2010). In both the cylindrical and the conical sections of the hydrocyclone, the radial velocities increase towards the vortex finder (Muschelknautz, 1972). Outside the vortex finder, the cyclone was seen to have an inward or negative radial velocity. The radial velocity along the central region is zero because of the effect of the centrifugal force around the vortex finder and the formation of the core in the central part of the hydrocyclone. Increasing the cyclone diameter increases the value of the radial velocity.

The radial velocity contour shown in figure 5-6c to 5-6e shows that the radial velocity calculated using computational fluid dynamics have both inward and outward velocities. Below the vortex finder, the radial velocities were inward pointing in the outer region, while the region along the centre line alternates in direction down the axis (Zhu, 2010). The alternation of the radial velocity along the centre line can be attributed to the asymmetric vortex flow inside the hydrocyclones.

#### **5.2.4 Pressure Profile**

Figures 5-7 and 5-8 show that increasing hydrocyclone diameter increases the pressure in the cyclone with the pressure drop in a 75mm cyclone higher than that of the 50mm and 35mm hydrocyclones. This can be explained using the pressure drop equation in hydrocyclones given by Svarosky.

$$\Delta P = Eu. \left( \frac{\rho v^2}{2} \right) \quad (4)$$

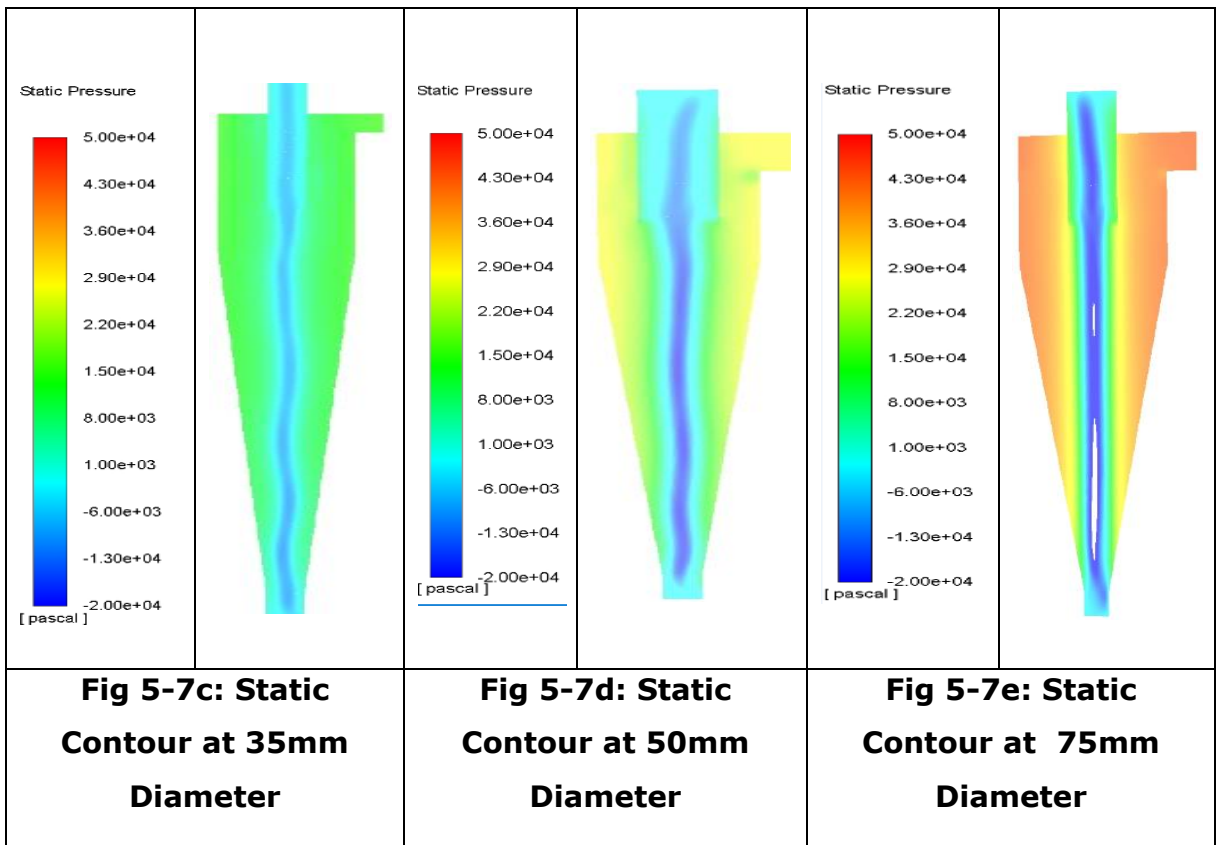
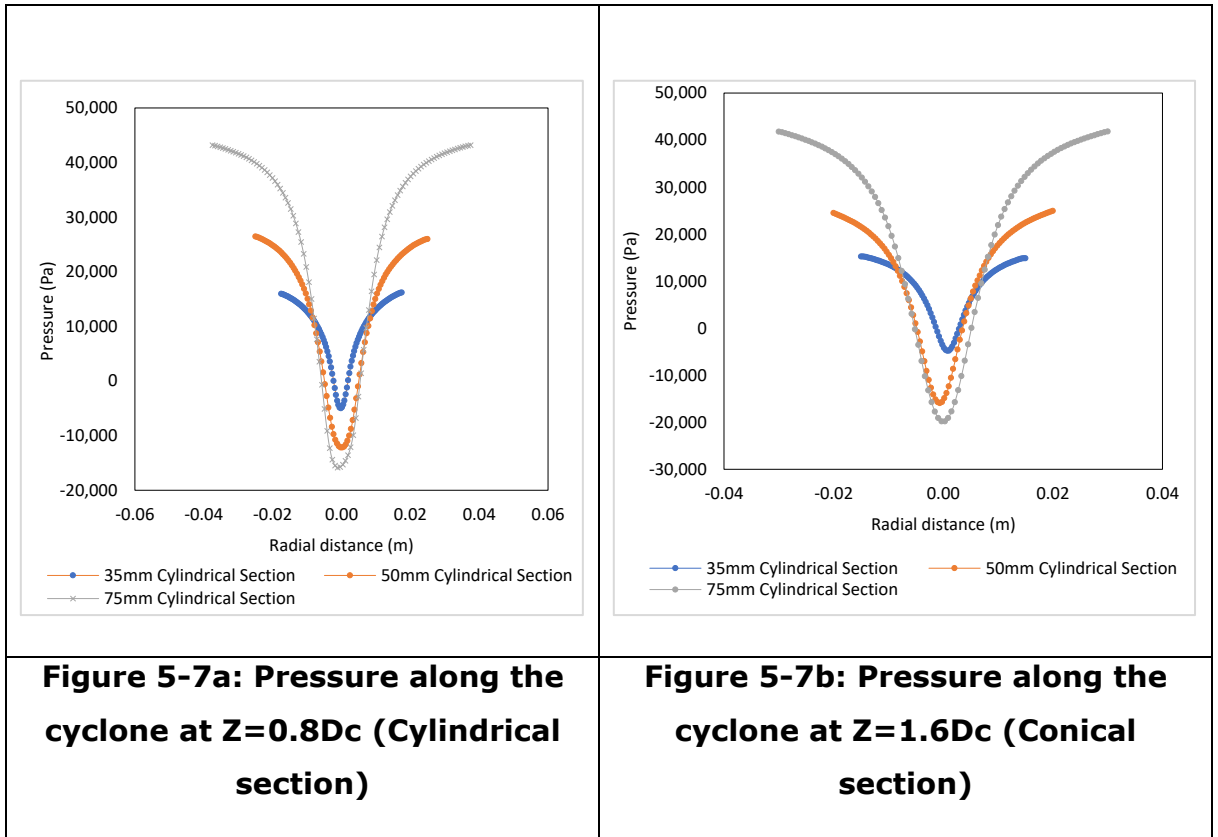
The pressure drop is directly related to the velocity in the fluid and since it has been established that the tangential velocity increases with increasing cyclone diameter, then as expected and based on the equation above, the pressure behaviour in figures 5-7 and 5-8 are in line with the theories.

The static pressure and the pressure chart also show that pressure increases along the radial direction from the cyclone centre with a maximum pressure variation domain seen in the 75mm cyclone (Ghodrat, 2013). A clearly defined air-core can also be seen as the pressure at the centre of the cyclone is 0 barg which is equivalent to the atmospheric pressure and this is clearly visible in the static pressure contours.

### **5.2.5 Pressure Drop**

The pressure drop was evaluated using the pressure at the inlet and the pressure at the overflow of the cyclone, with pressure at the overflow subtracted from the pressure at the inlet. As the hydrocyclone diameter increases, the pressure drop in the hydrocyclone equally increases. From the literature, increase in pressure is expected to increase the separation efficiency although after an optima pressure drop is attained; Svarosky (2000) stated a pressure drop of 0.34 to 24bar, but studies have further shown that 0.34 to 6 bar will give optima separation. The result in figure 5-7f shows that a pressure drop can be related to efficiency for hydrocyclones of the same geometry.

## Pressure Profile



It can also be credited to the influence of the cyclone cylindrical diameter on the velocity; with decreasing diameter, the velocity increases, therefore, increasing the Reynold number which consequently influences the pressure drop in the cyclone. The relationship between the pressure drop in the cyclone and the Reynold number can be evaluated by the equations below.

$$\Delta P = Eu. \left( \frac{\rho v^2}{2} \right) \quad (4)$$

$$Eu = 71 \left( \frac{D_i}{D} \right)^{-1.30} Re^{0.116} \exp^{-2.12c} \quad (4-i)$$

$$Re = \frac{vD\rho}{\mu} \quad (4-ii)$$

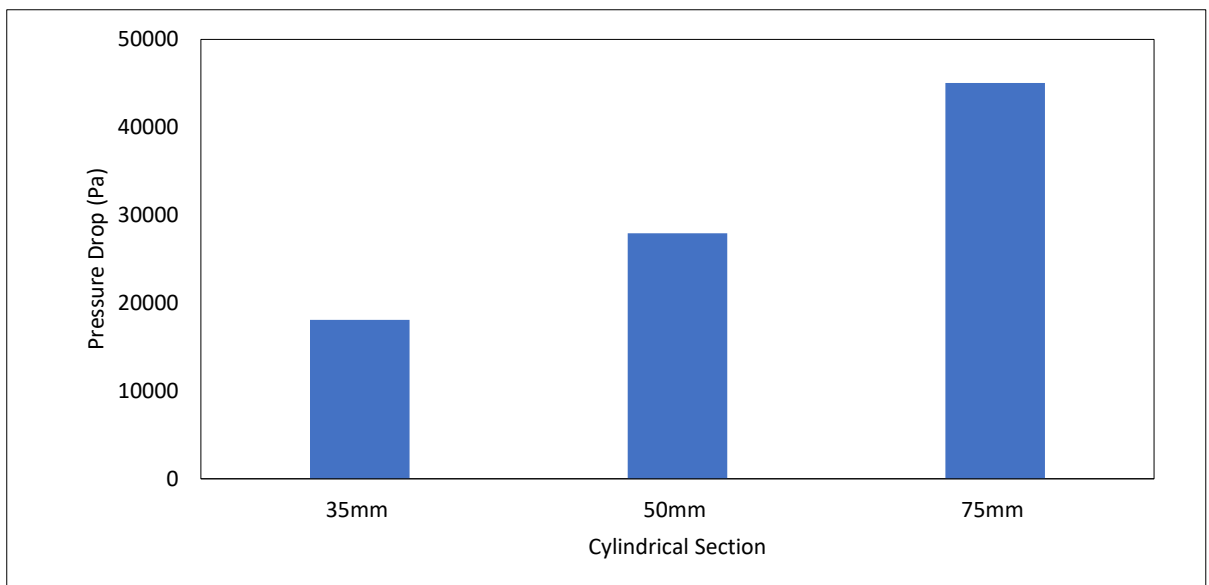


**Figure 5-7f: Pressure drop in hydrocyclone with different cylindrical diameter**

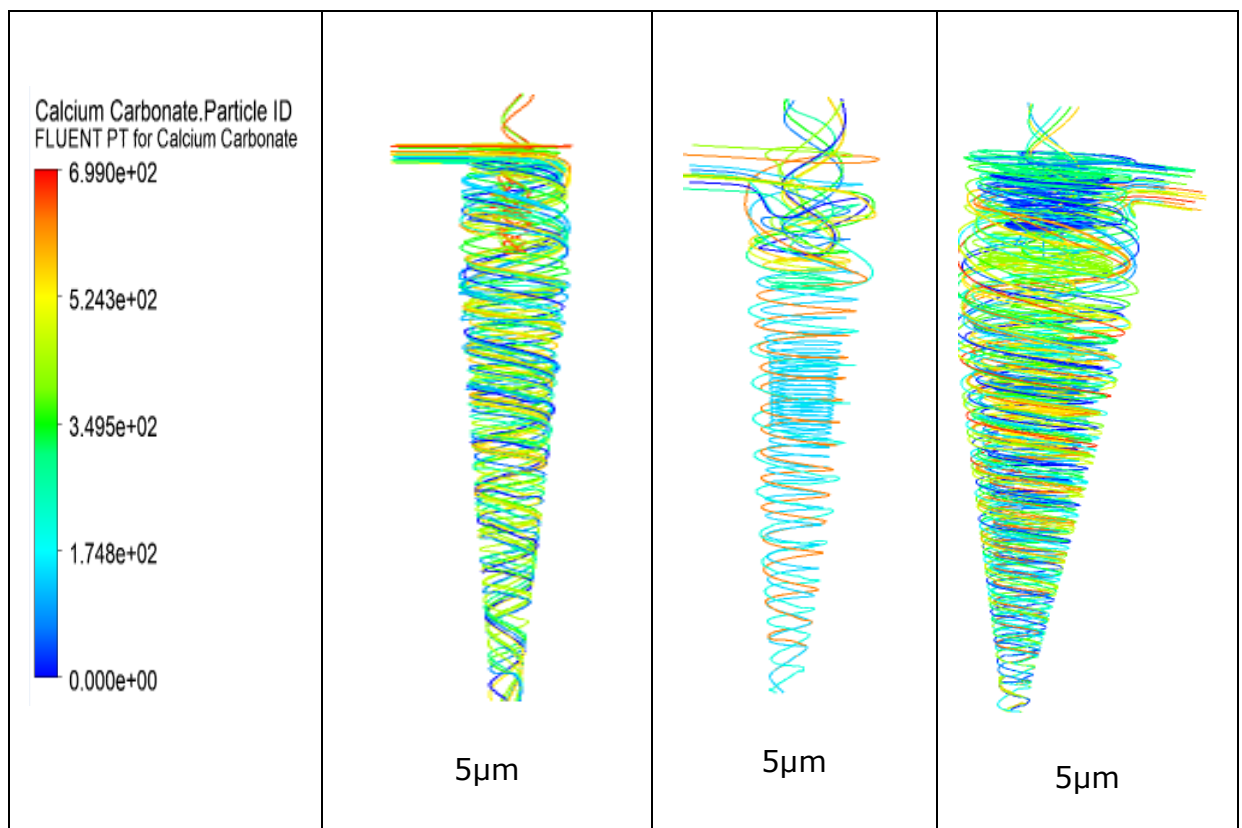
## 5.2.6 Particle Tracking

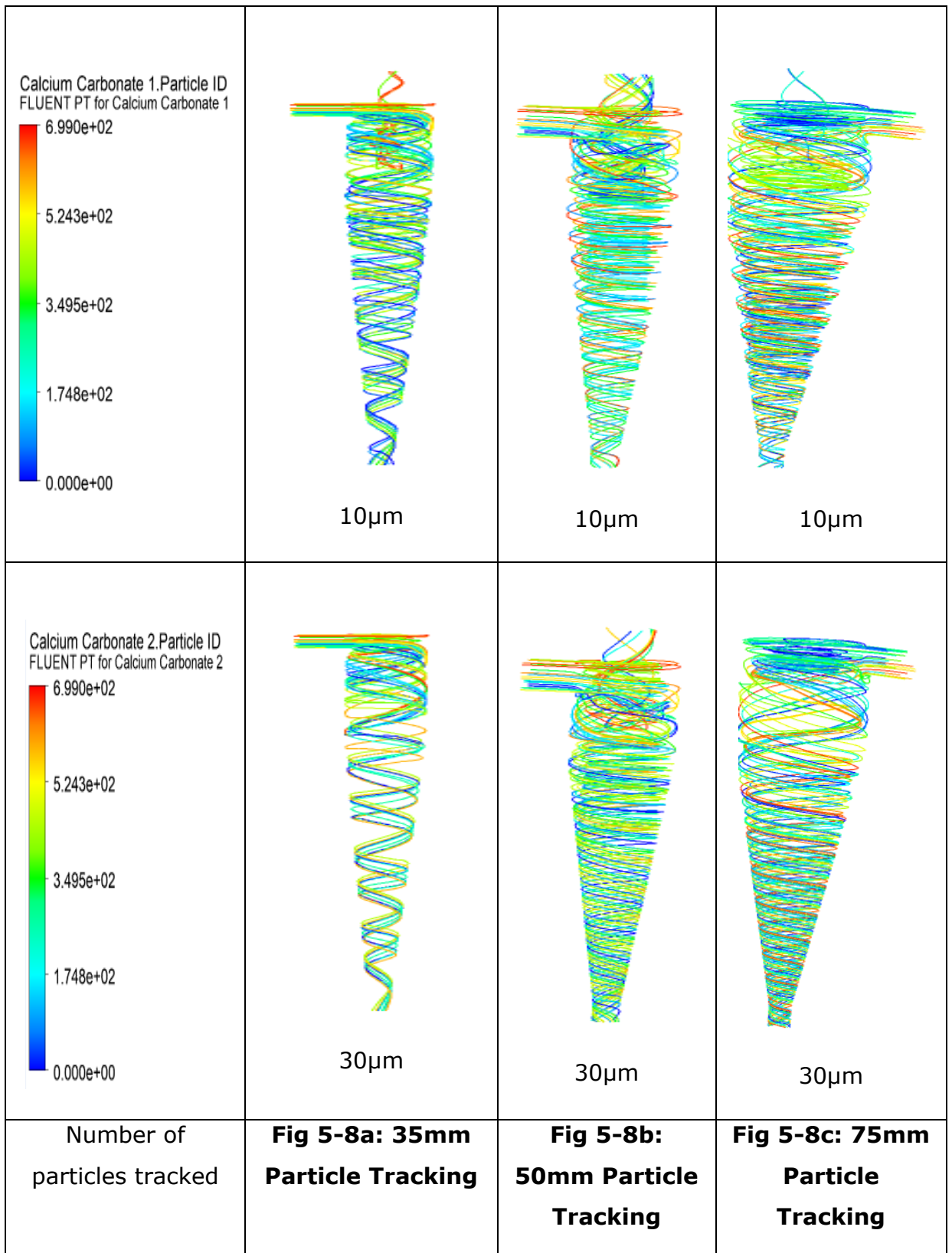
A very important means of evaluating the separation efficiency in a hydrocyclone is by tracking the particles at the overflow of the cyclone (Jiang,2019; Mousavian, 2008). Figures 5-8a to 5-8c tracked 700 particles (but showed 25 particles) at different particle sizes 5 $\mu$ m, 10 $\mu$ m and 30 $\mu$ m to evaluate how hydrocyclone cylindrical size affect the separation efficiency of different particle sizes. It can be seen from figure 5-8 that increasing the particles size decreases the number of particles at the overflow irrespective of the cyclone diameter. Larger particles

produced better separation in a hydrocyclone thus the larger the particle in a hydrocyclone the more the separation/ efficiency (Liu, 2016; Tang, 2018).

However, with increasing cyclone diameter, the number of particles tracked in the 35mm and 75mm hydrocyclone was quite low compared with the 50mm hydrocyclone, showing the 35mm and the 75mm diameter hydrocyclone give better separation than the 50mm hydrocyclone.

The efficiency of the 35mm hydrocyclone can be credited to the overall reduction in the cyclone dimension (inlet and cyclone diameter). With reduction in cyclone diameter alone as seen in the 50mm hydrocyclone, the separation efficiency was seen to be slightly hindered, indicating that changing the hydrocyclone diameter will only improve efficiency if the cyclone diameter is proportional to the other dimensions of the hydrocyclone.







### 5.3 Vortex Finder Depth

Studies (Elsayed, 2013; Bakari, 1998) have shown that the length of the vortex finder can greatly affect the hydrocyclone flow field and strongly affect hydrocyclone performance parameters. The vortex finder length can reduce back mixing losses due to the Bernoulli effect and particle bounce. Use of a vortex finder can also reduce the re-entrainment of particles into the overflow stream and equally prevent "short-circuit" generation at the top section of the hydrocyclone close to the inlet and the overflow upper exit (Martinez 2006)

In this study, three different vortex finder depths in the cyclone were compared to evaluate the effect of vortex finder depth on the fluid flow in the hydrocyclone. The dimension of the hydrocyclone with the vortex finder is as shown in Table 5-3 below. In table 5-3 below, only the vortex finder changed while other geometrical dimensions remain constant.

**Table 5-3: Hydrocyclone with different Vortex Finder Dimension**

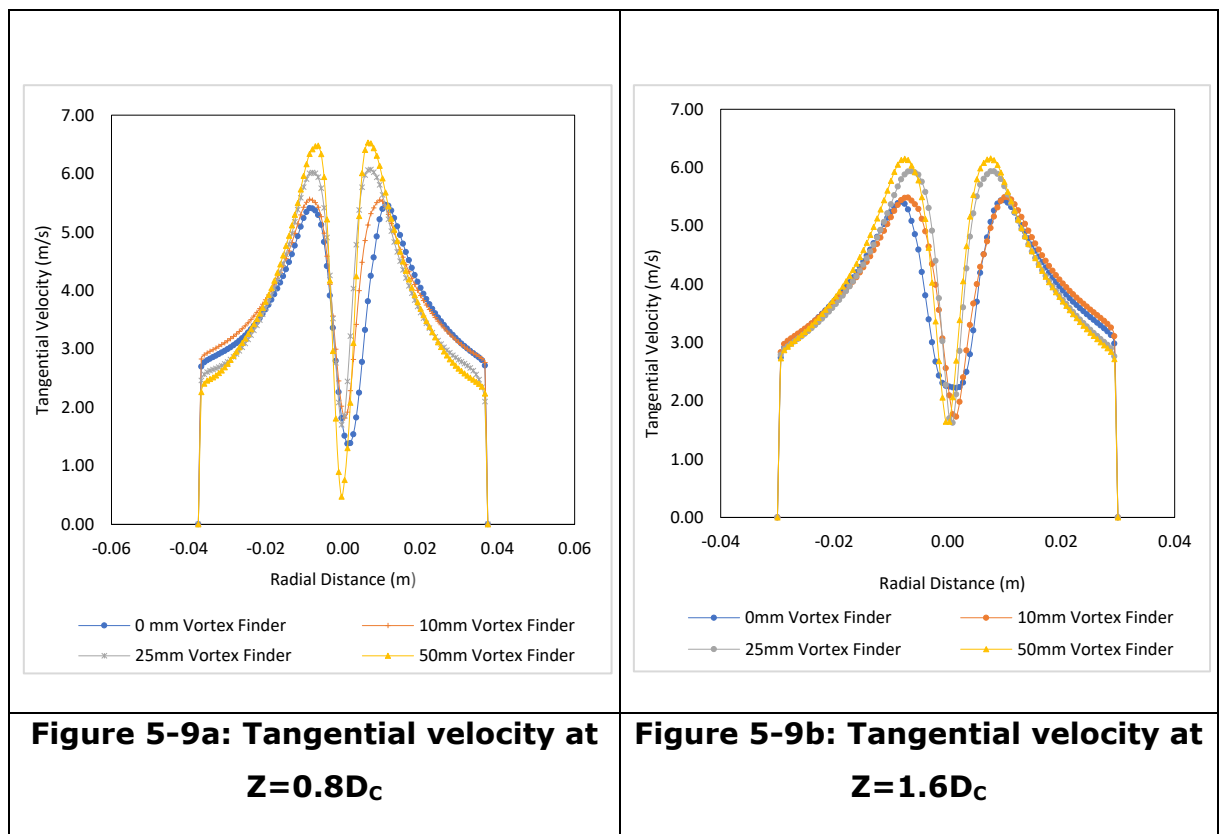
Parameter	Symbol	0mm	10mm	25mm	50mm
Cyclone cylindrical diameter (mm)	$D_c$	75	75	75	75
Size of Inlet (mm)	$D_i$	22.16 x 22.16	22.16 x 22.16	22.16 x 22.16	22.16 x 22.16
Vortex finder diameter (mm)	$D_o$	25	25	25	25
Vortex finder length (mm)	$L_v$	0	10	25	50
Length of the cylindrical part (mm)	$L_c$	75	75	75	75
Cone Angle (°)	$A$	20°	20°	20°	20°
Diameter of the spigot (mm)	$D_u$	12.5	12.5	12.5	12.5

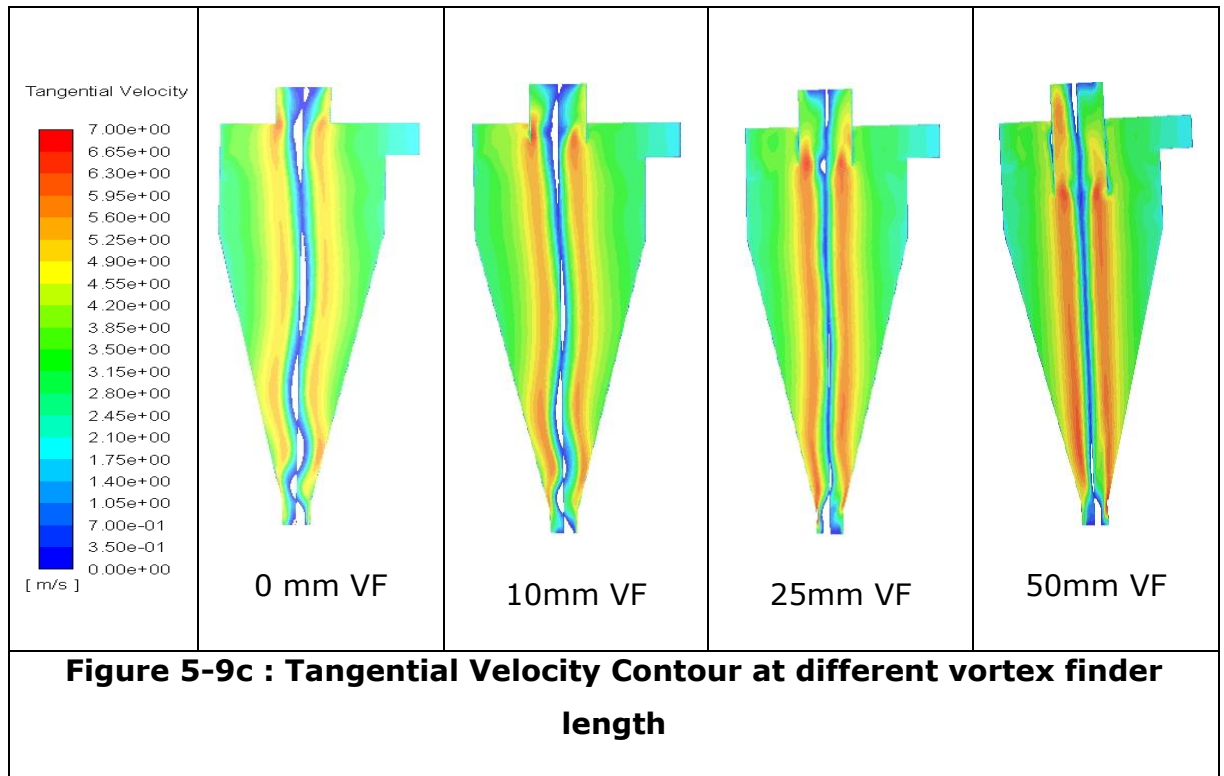
#### 5.3.1 Results and Discussion of Results

Figure 5-9a and figure 5-9b show that increasing the vortex finder length increases the tangential velocity most especially in the cylindrical section of the cyclone

where all the tangential velocities show a typical Rankine profile. Longer vortex finder depth has a higher velocity at the free vortex region than in smaller vortex finder cyclones (50mm>25mm>10mm>0mm) while the forced vortex region of the smaller vortex finder has higher velocity than the longer vortex finder cyclone (50mm<25mm<10mm<0mm). This is because a reduction in the vortex finder length reduces the swirl flow in the hydrocyclone and consequently a reduction in the tangential velocity and the vortices. The vortex core of the cyclone and the corresponding swirling turbulence controls the tangential velocity distribution in the hydrocyclone (Farokhi, 1998). Because of the higher tangential velocity in longer vortex finder, it is expected that the separation efficiency of the longer vortex finder will be higher than the shorter vortex finder.

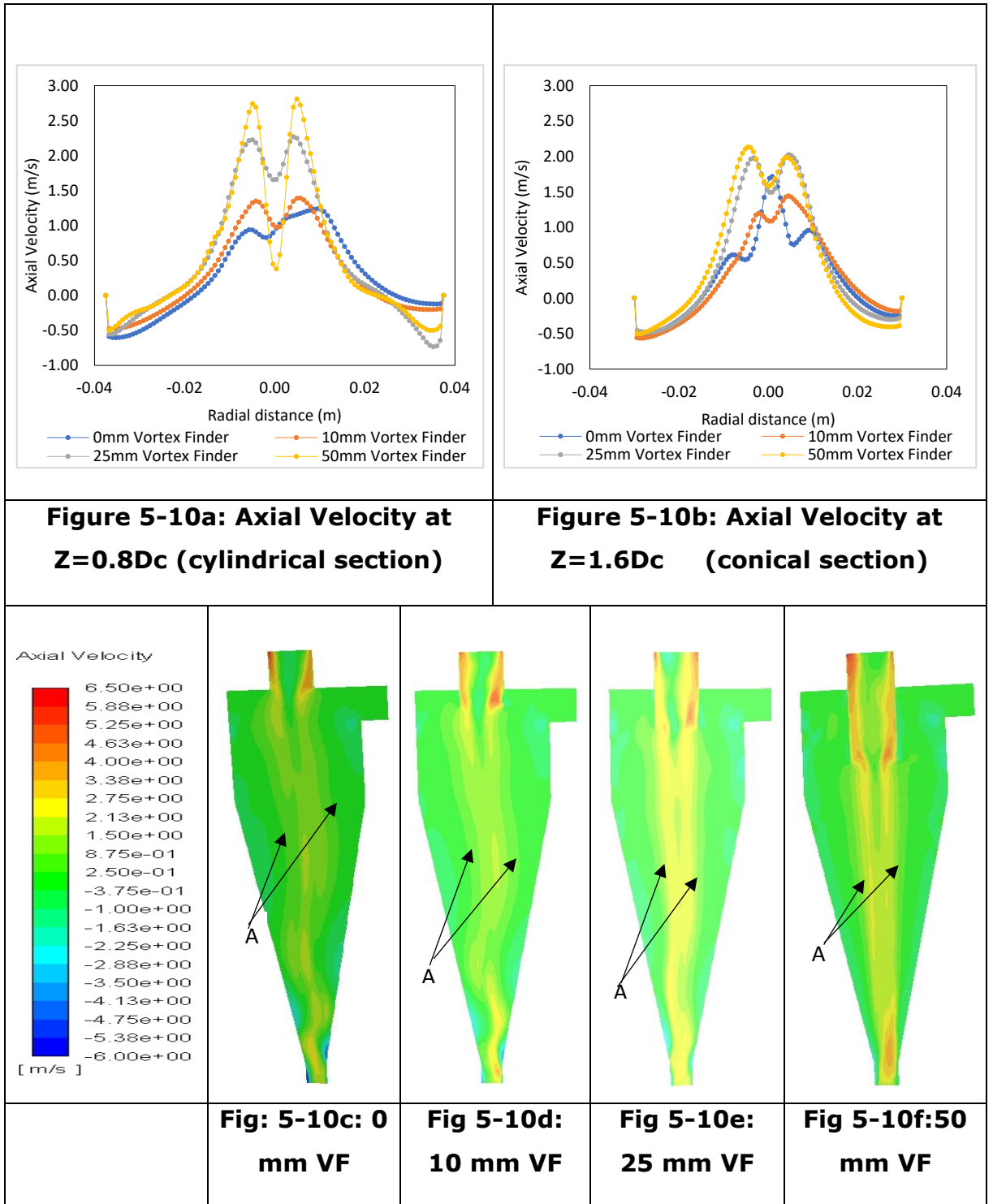
The tangential velocity contour (figure 5-9c) shows that increasing the vortex finder length increases the tangential velocity (Yohana, 2018) most especially around the core / centre of the hydrocyclone. However, the pressure at the centre of the cyclone reduces more with increasing vortex finder. The contour plot also shows that there is a Rankine vortex in the cyclones with the tangential velocity being divided into the inner zone or quasi vortex flow surrounded by an outer zone or quasi-free vortex finder (Yohana, 2018; Hoffman, 2008; Peng 2002).





### 5.3.2 Axial Velocity

Axial velocity is one of the ways in which particle separation can be evaluated as the flow is moved upwards and downwards in the hydrocyclone. Axial velocity has two distinct regions inside the hydrocyclone with net velocity in a different direction; the primary vortex zone flow moves downward towards the underflow while secondary vortex zone flow spins upwards and takes the fluid/particles into the vortex finder.



From figure 5-10a and 5-10b, it can be seen that the axial velocity and the tangential velocity profile in both the conical and cylindrical sections are of similar character (Nemeth, 2011; Kelsall, 1952) with the axial velocity decreasing towards in the core region (from the outer vortex region) of the cyclone and increases from the wall to the core region of the cyclone (inner vortex region). The low axial velocity at the inner vortex region creates circulation flow and induces the particles

to suspend or gather in this zone resulting in reduced efficiency (Zhao, 2019). The direction of the axial velocity profile in figure 5-10a and 5-10b shows that the particle-laden fluid is moving upward, this has a major influence in bringing fluid to the overflow of the cyclone and determines the total residence time of fluid and the split ratio in the hydrocyclone (Jiang, 2019). Therefore, it can be concluded that fluid moves faster above the vortex finder than in the conical section.

It can be seen from the contour plots in figure 5-10c and 5-10e that the maximum and minimum axial velocities were at overflow and underflow respectively. The velocity at the centre changes greatly and is quite small compared to the velocity at the overflow indicating that the cyclone does not have good potential for separating very fine particles (Vakamalla, 2017, Huang, 2017).

From Figure 5-10c and 5-10e, it can also be seen that the locus of particle that can fall into zero vertical velocity (A) is more pronounced as the vortex finder length increases. This indicates that more separation takes place with increasing depth of vortex finder in the hydrocyclone. The locus of zero vertical velocity is the particle imaginary location where underflow and overflow particles are separated; fine particles have an orbit smaller than the locus point and coarse particles have an orbit greater than the locus point.

### **5.3.4 Turbulence Kinetic Energy**

Turbulence flow results in the formation of eddies of different length scale hence viscous force is less important than inertial force. Energy is cascaded from large to small eddies by these inertial forces thus large-scale flow structures have most of the turbulence kinetic energy. The higher the dissipation of the large eddies' energy the lower the turbulence kinetic energy in the flow.

The contour of the turbulence kinetic energy combined with the graphical analysis gives insight into the behaviours of turbulence kinetic energy across the hydrocyclone with different vortex finder depth. Figure 5-12a shows the turbulence kinetic energy in the cylindrical section of the hydrocyclone while 5-12b shows the conical section. The contour plots compare the turbulence across the cyclone for the different vortex finders.

In the cylindrical section, the longer the depth of the vortex finder depth, the narrower the range of the streamline ( the thinner the shape of the turbulence kinetic energy) with the exception of the 0mm vortex finder (depth) that does not fit the profile.

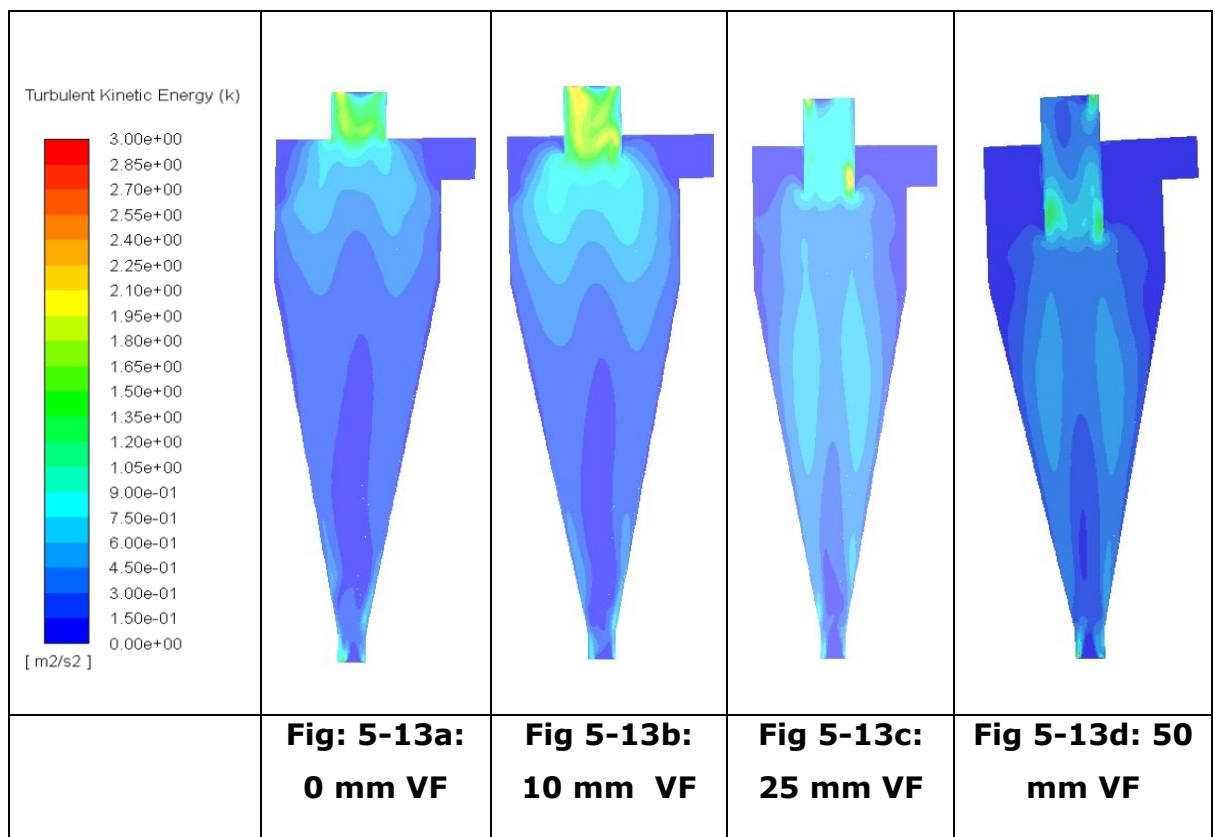
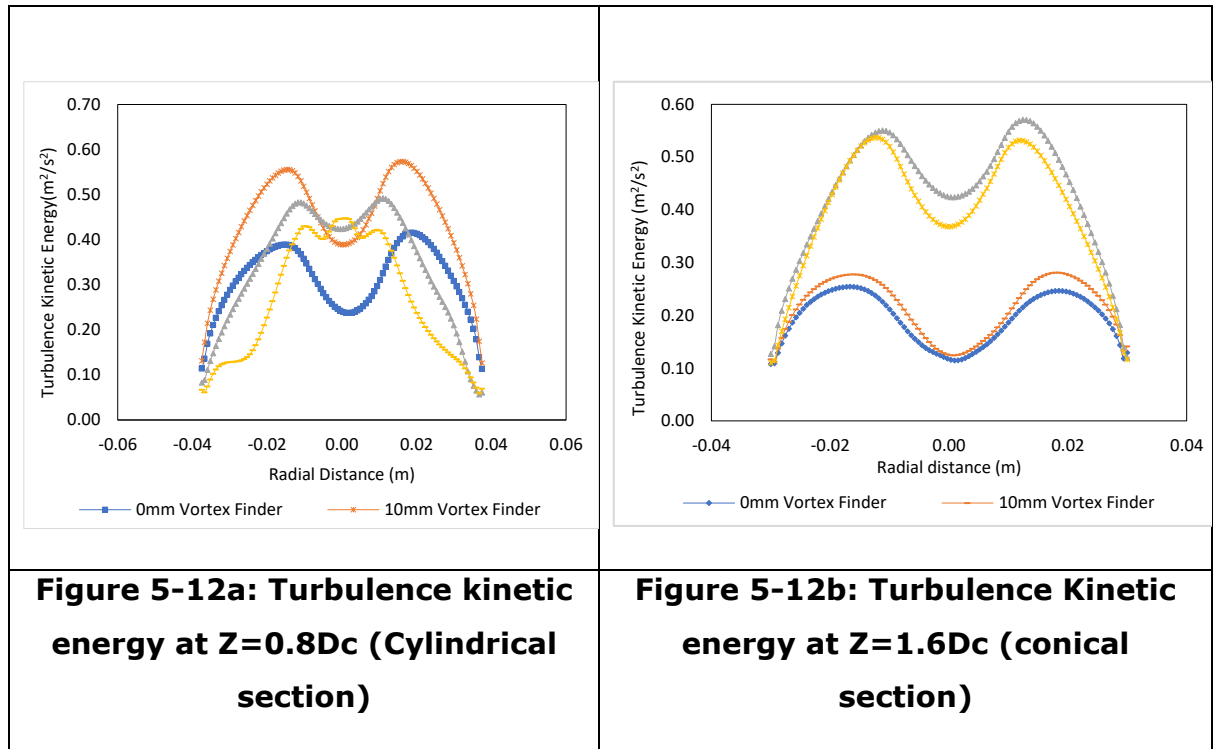
The turbulence kinetic energy at the wall is the lowest because the small eddies destroy themselves while dissipating energy at the wall, therefore, converting the small eddies' kinetic energy into intermolecular energy. As the flow moves away from the wall, free stream energy is converted to large eddies and large eddies to the continuous formation of small eddies (Biferale, 2003).

However, the rate of dissipation of the large eddies into small eddies is affected by the depth of the vortex finder and this is because there is a decrease in the internal diameter of the cylindrical section due to the diameter of the vortex finder. This increases the rate of small eddies production and pressure strain interaction (Torbergsen, 1998) thus there is a rapid conversion of large eddy to small eddy causing a narrower streamline with longer vortex finder. Since high turbulence kinetic energy will mean a reduction in the rate of dissipation, then a cyclone with shorter vortex finder has a lower rate of dissipation and thus higher turbulence kinetic energy.

In the conical section, the longer vortex finder cyclone has higher turbulence kinetic energy. This is because there is a good distribution of kinetic energy across the large and small eddies, starting from the cylindrical to the conical section while the shape and width of the distribution remains the same.

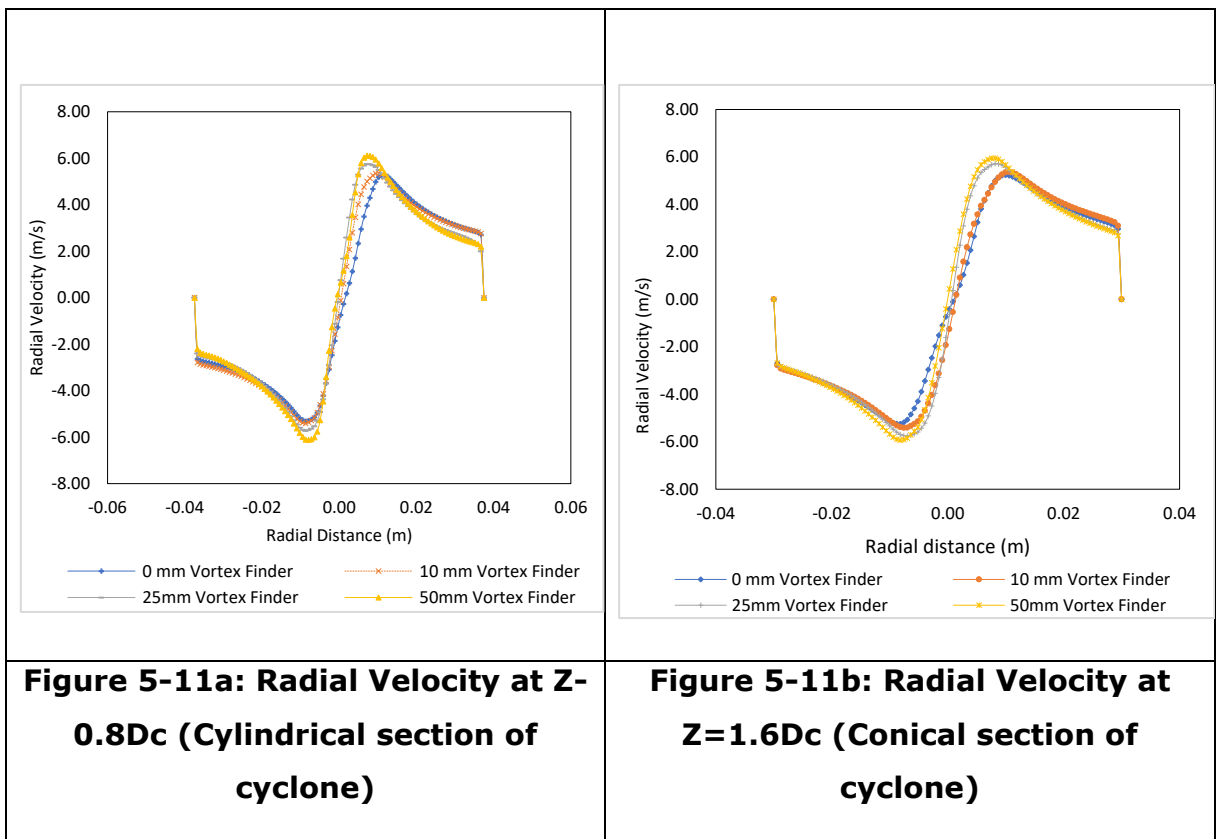
Figure 5-13 shows the turbulence kinetic contours across the cyclone, the turbulence kinetic energy is higher close to the vortex finder while low turbulence kinetic energy is seen near the wall. Across the axis, the turbulence kinetic energy was high and unstable (Valverde 2011, Abdullah, 2003). The distribution of the turbulence kinetic energy in the longer vortex finder cyclone implies that more of the fine particles will be able to pass to the underflow while the shorter vortex finder cyclone will have more of its fine particles moved to the vortex finder (Ficici, 2010). Although the increased vortex finder improves the distribution of the turbulence kinetic energy, when the vortex finder further increases from 25mm to 50mm, a slight reduction in energy distribution was seen across the cyclone

(coupled with decreased TKE energy in the conical section). Thus it can be said that there is a maximum vortex finder depth after which a further increase will deplete the overall effect of the use of a vortex finder (Martinez, 2007).



### 5.3.3 Radial Velocity

For particles to separate in cyclones, radial displacement must occur; the radial velocity varies axially from inward to outward and is directed towards the centre of the cyclone as shown in figure 5-11a and b. It increases towards the apex, therefore, moving lighter density particles to the central region while the larger density particles move to the wall of the cyclone thus causing separation. The negative values in figure 5a represent the inward radial velocity while the positive values show the outward radial velocity showing that the combination of flow source and sink are distributed near the axis of the cyclone.





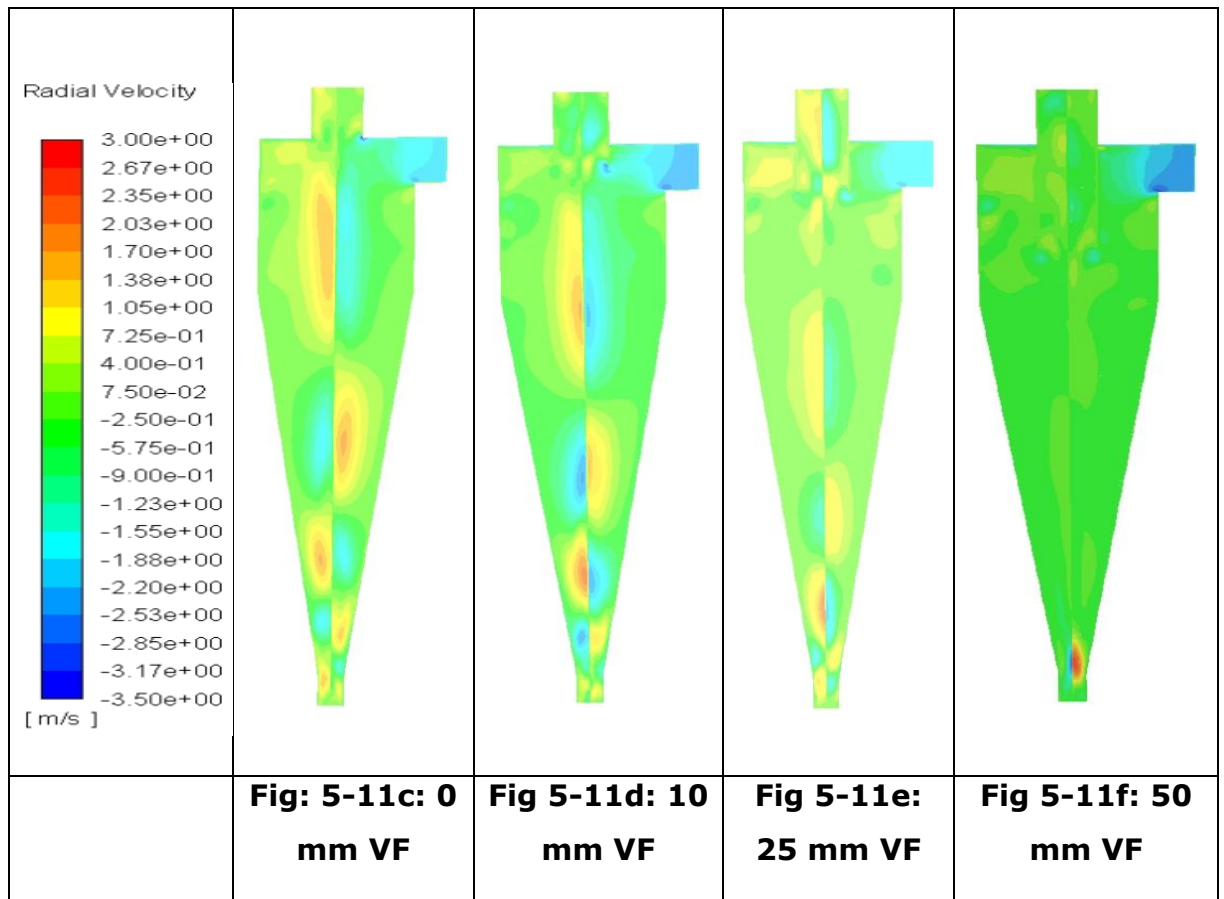


Figure 5-11c to 5-11f show the radial velocity contour plot and it can be seen that as the vortex length increases in the cyclone, the start of the alternation of the radial velocity along the central line lowers showing that the alternation of the radial velocity will be more in the shorter vortex finder than in longer ones (Zhu, 2010).

### 5.3.5 Pressure

The influence of pressure gradient force on hydrocyclone performance has been discussed in many studies (Li Ji, 2016; Salimi, 2011; Chen, 2015; Ciller 2002). The pressure gradient force is an inward force with a negative value whilst the pressure drop in a hydrocyclone is considered a major factor affecting two-phase separation in a hydrocyclone. According to Hoffmann (2002), in the absence of a pressure recovery device at the outlet of the hydrocyclone, the pressure drop across the cyclone is the pressure at the inlet minus the static pressure at the outlet; this is expected to give the true dissipative loss between the inlet and the measurement point.

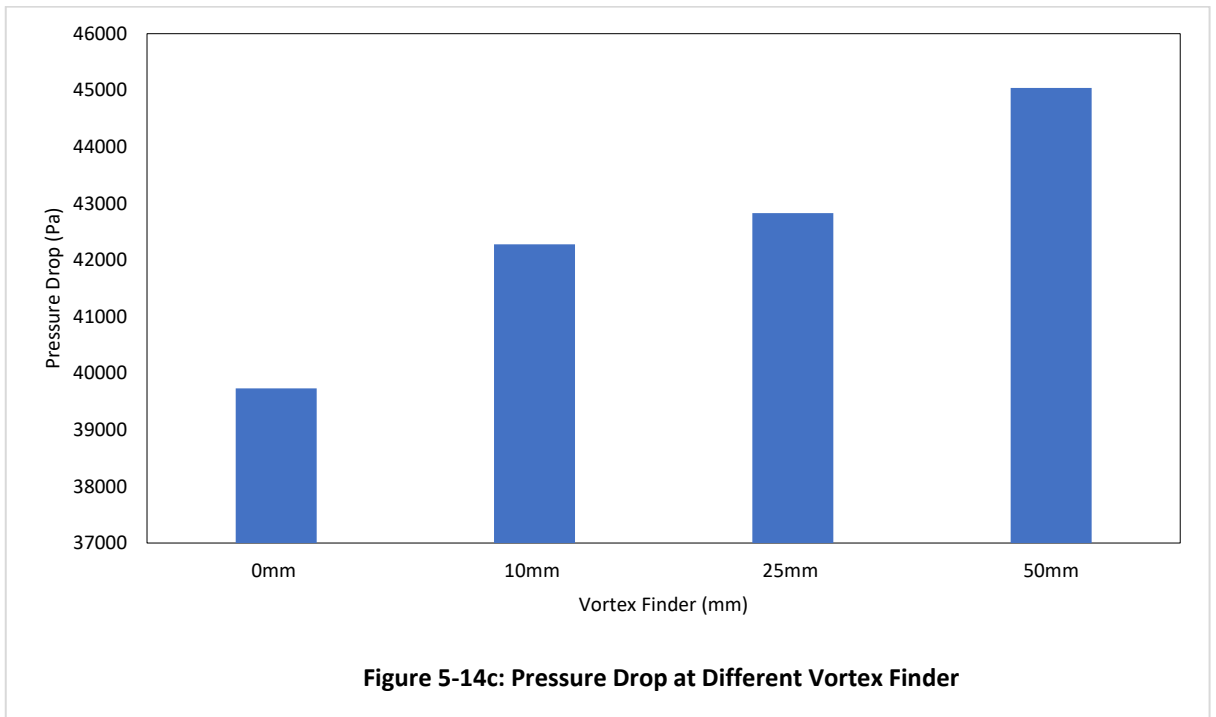
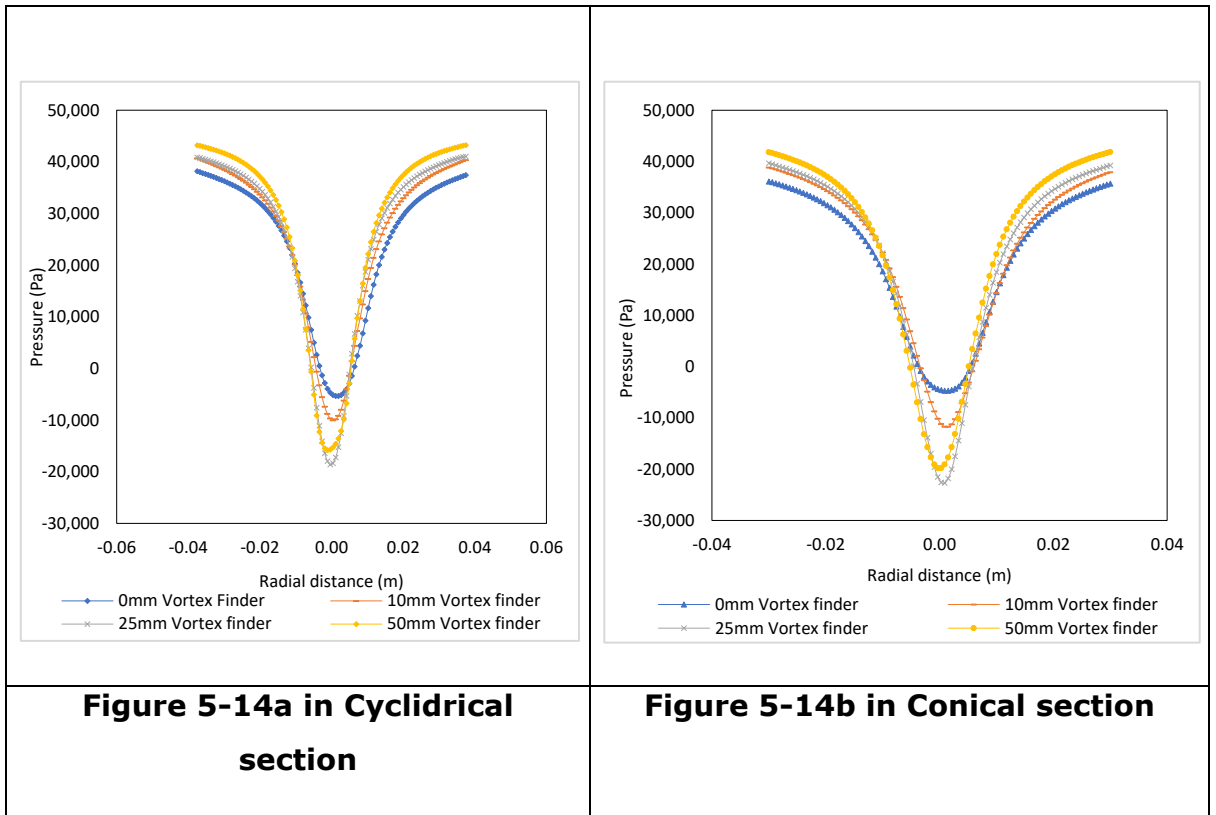
Figure 5-14a and b below show the pressure distribution across the hydrocyclone, the wall pressure increases with the depth of vortex finder, it was also observed that the pressure at centre of the cyclone decreases with an increased vortex finder. This is because the reduction in the cyclone internal diameter due to the vortex finder increases the pressure inside the cyclone hence the higher pressure at the wall of the cyclone. The rate of dissipation in the energy increase is due to the rapid dissipation of kinetic energy across the cyclone, this accounts for the decreased energy at the centre of the cyclone.

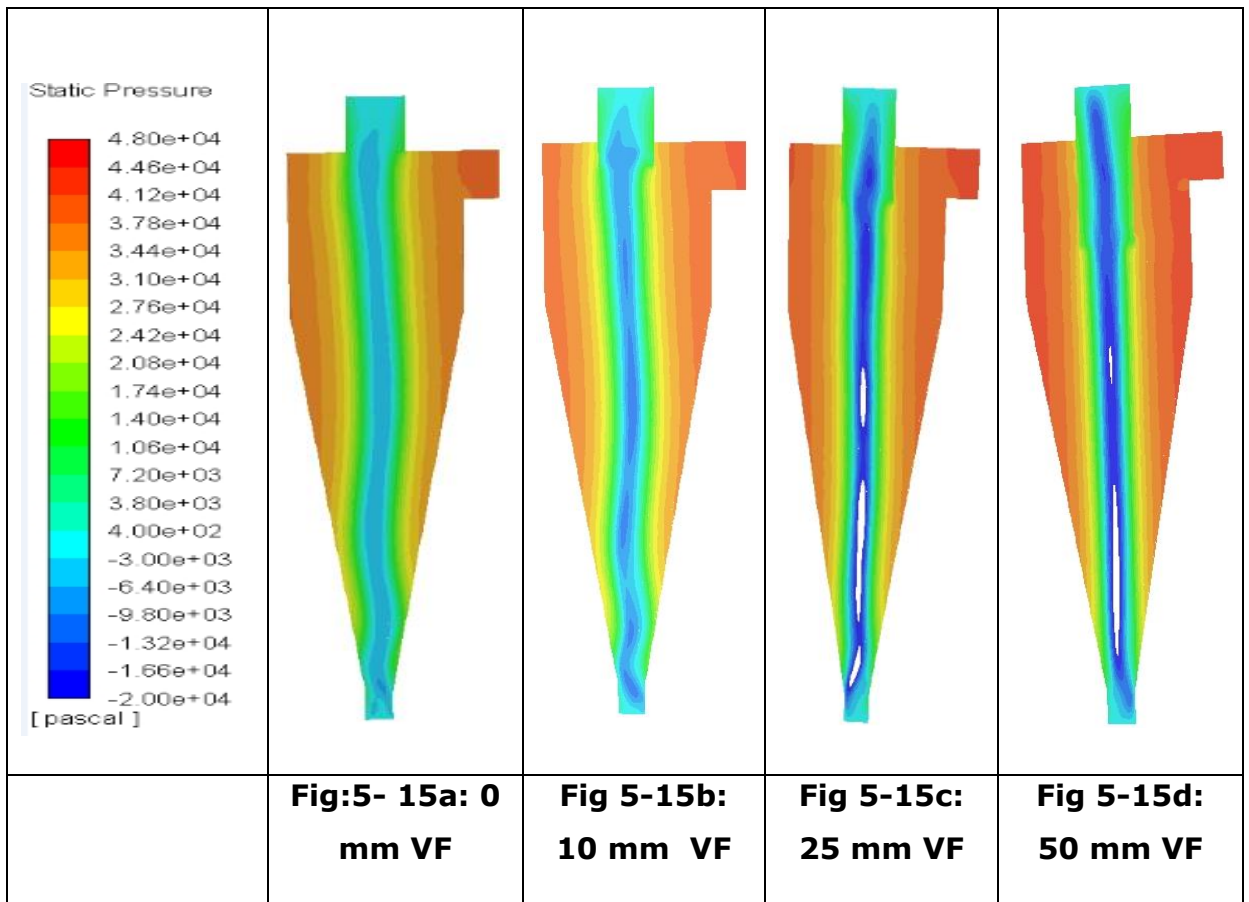
Figure 5-14c is the graph of the pressure drop within the hydrocyclone at different vortex finder length. It was observed that the pressure drop increases with the increasing length of the vortex finder (Patra, 2018; Wang, 2008). According to Svarosky (2000), for separation to take place a minimum of 0.34bar pressure must be dropped in the cyclone. Figure 5-14c shows that not less than 0.34bar (34000Pa) is a drop in all the vortex finder lengths indicating that even with zero insertion of vortex finder into the cyclone cylindrical section, separation will take place. Increasing the vortex finder insertion length in the cyclone is therefore used to improve the performance of the cyclone (Patra, 2018; Martinez, 2008). The pressure drop increases by approximately 5000Pa when the vortex finder length increases from 0mm to a 50mm vortex finder. Therefore, increasing the vortex finder helps to improve the performance of the cyclone provided the length is within the cylindrical section of the cyclone.

Looking at the contour plot in figure 5-15, the static pressure decreases across the radius of the cyclone. Therefore, the pressure drop decreases across the radial length of the cyclone while the gradient of pressure increases across the radial length (Liang-yin Chu, 2007). At the centre of the cyclone, the pressure was very low in the range of negative, indicating that this is the centre core region of the cyclone, this also gives an indication that the cyclone is exposed to the atmosphere.

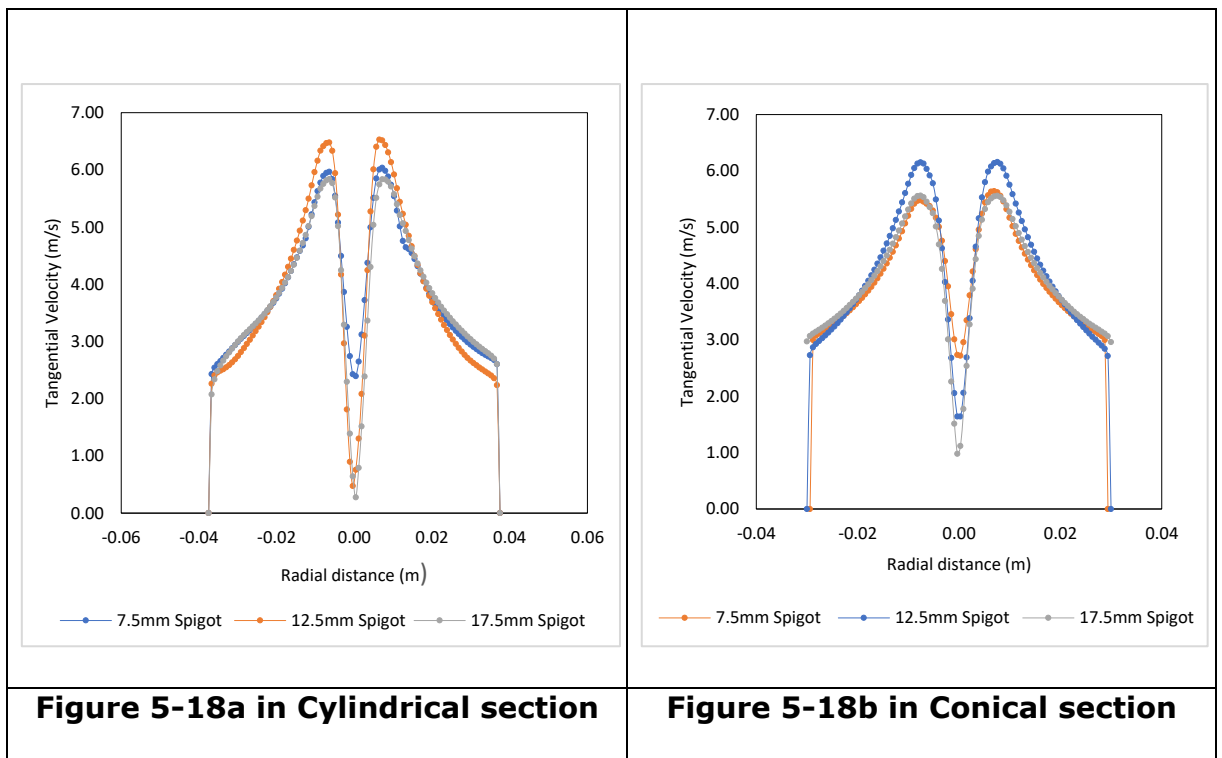
One prominent thing that can be noticed is that although the inlet velocities are the same for all the cyclones; the wall pressure, centre pressure and the overall pressure in the cyclone differ. The pressure increases with increasing vortex finder depth. Based on the inlet pressure and the outlet pressure it can be concluded that

the pressure drop across the cyclone differs and increases with vortex finder depth and this is a result of changes in the rate of energy dissipation in the cyclone.





### 5.3.1 Tangential Velocity



From figure 5-18a and b, the tangential velocity of the 12.5mm spigot diameter is higher than the tangential velocity of the 7.5mm and 17.5mm diameters respectively in the free vortex region, the tangential velocity is at its peak in the free vortex zone. Since tangential velocity is proportional to the centrifugal force then the centrifugal force acting on the cyclone with a 12.5mm spigot section is more than that of 7.5mm and 17.5mm hydrocyclones thus separation efficiency of this cyclone is expected to be more than that of others. Figure 5-18c illustrates how the centrifugal force acts on separating particles to the wall of the cyclone. The increase in tangential velocity increases the centrifugal force which moves more of the solid to the wall and down to the underflow.

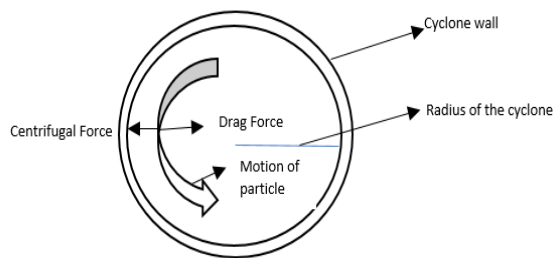


**Figure 5-18c: Forces Acting on Hydrocyclone**

In the forced vortex region, the tangential velocity of the 12.5mm and 17.5mm spigot diameter cyclone were almost the same and the velocity dipped in this zone. It can be said that the depth of the forced vortex is affected by the size of the spigot diameter; the bigger the diameter of the spigot section, the higher the forced vortex. Particles in the centre of the cyclone (a radial distance of 0mm) are moved to the overflow of the cyclone. Finer particles will have a higher chance of either reporting to the overflow in a 17.5mm hydrocyclone rather than the 7.5mm and 12.5mm because the particles are almost lying on the envelope of zero velocity (Wills, 2016).

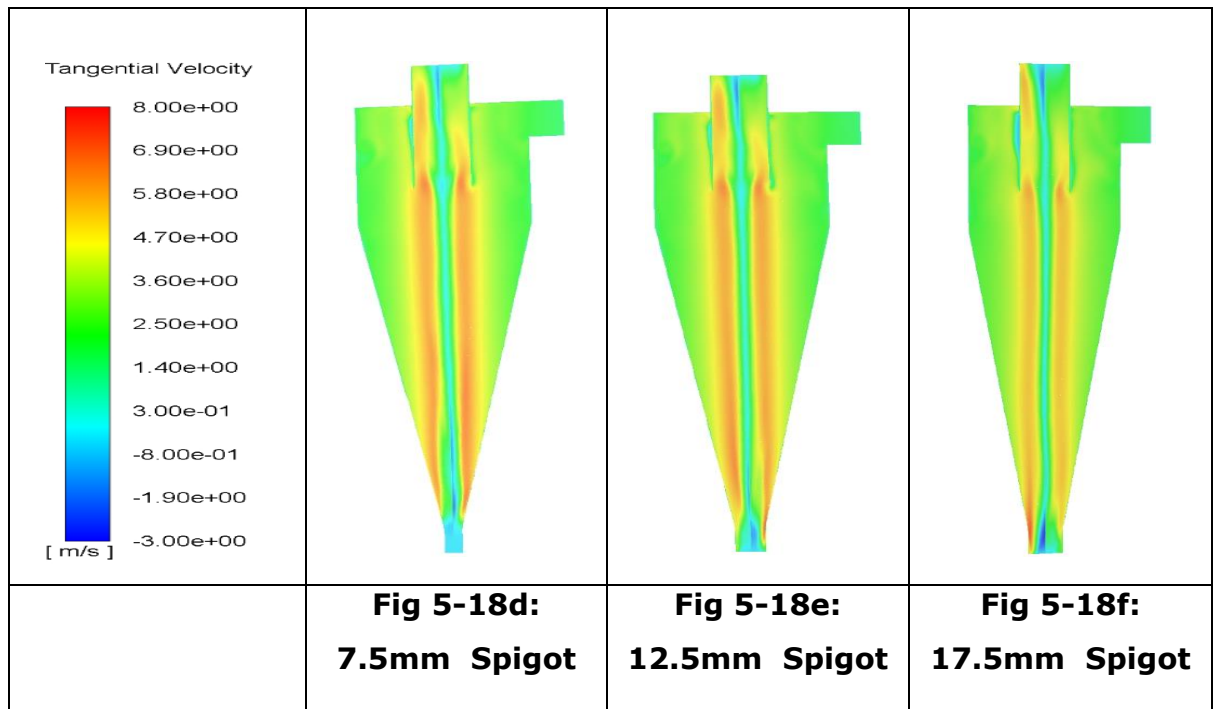


Figure 5-18d to 5-18f are the tangential velocity contour plots at different spigot sizes. It can be seen that the tangential velocity around the core is more intense in the 7.5mm spigot section than the 12.5mm spigot while the 12.5mm spigot section is equally more intense than the 17.5mm spigot section. This is because with a smaller spigot diameter, more of the fluid is expected to be passed to the overflow section of the cyclone thus there is higher velocity around the core of the cyclone. Irrespective of the spigot diameter, the flow shows a Rankine vortex profile.

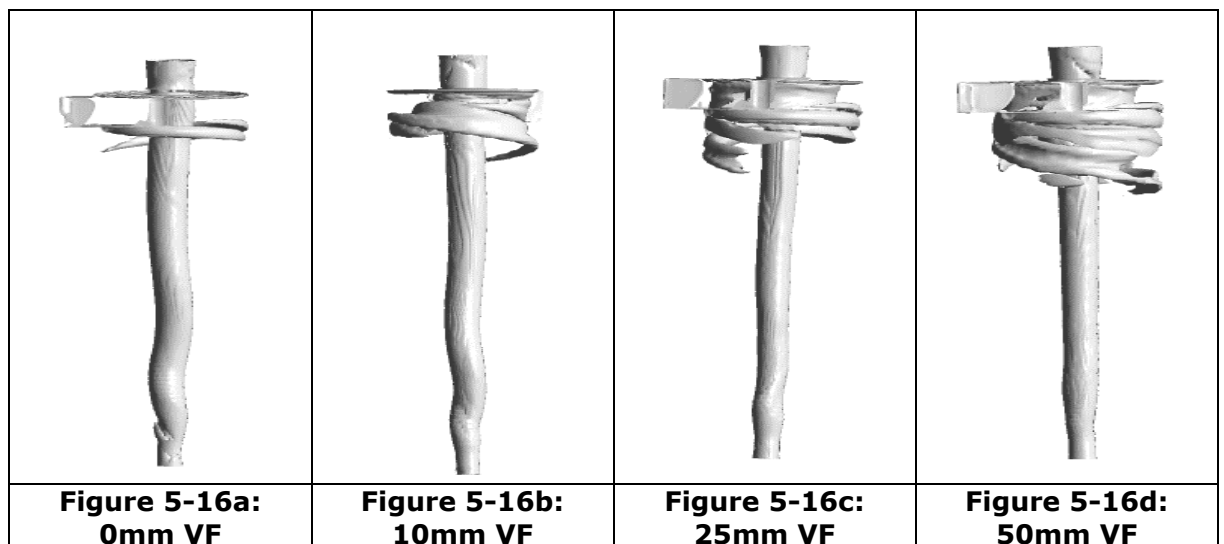
### **5.3.6 Swirling Strength at the Vortex Core Region of the cyclone at level 0.01**

The swirling motion delivers centrifugal force to the particles while turbulence disperses particles therefore the driving force for particle separation in a hydrocyclone is a strong swirl turbulence flow. Swirl plays an important role in increasing the entrainment rate and the velocity decay rate (Tamrin, 2015; Beer and Chigier, 1972). Chigier (1972) and Tamrin (2015) noted in their studies that poor internal circulation is experienced in a weak swirling system due to low axial pressure gradients while strong swirl has an adverse pressure gradient along the flow axis leading to the formation of a recirculation zone in the central region. The re-circulation varies in width and length depending on the swirl strength.

Figure 5-16 (swirl flow at vortex core region;) shows that a swirl flow will form irrespective of the depth of the vortex finder, this is because of the tangential entry of the fluid into the cyclone. It can also be seen from figure 5-16 that increasing the depth of the vortex finder, increases the swirl in the hydrocyclone indicating that more internal recirculation is taking place in the hydrocyclone with a longer vortex finder. The reduction in the cross-sectional area of the geometry is also attributed to this as a decrease in the cross-sectional area will increase the swirl in the hydrocyclone.

The air core diameter was also seen to slightly vary with vortex finder depth with a longer vortex finder having slimmer air-core space than the shorter vortex finder. The result also conveys that the increase in swirl will decrease the air core space and a decrease in swirl increase the air-core space. Another important feature seen on figure 5-16 is that the air-core for the 0mm and 10mm vortex finders were unsteady (a bit wavy at the lower ends), this reflects an unsteady flow field. When a flow field is unsteady the homogeneity and steadiness of the flow will be affected which will lead to lower separation efficiency (Yanxia, 2013).

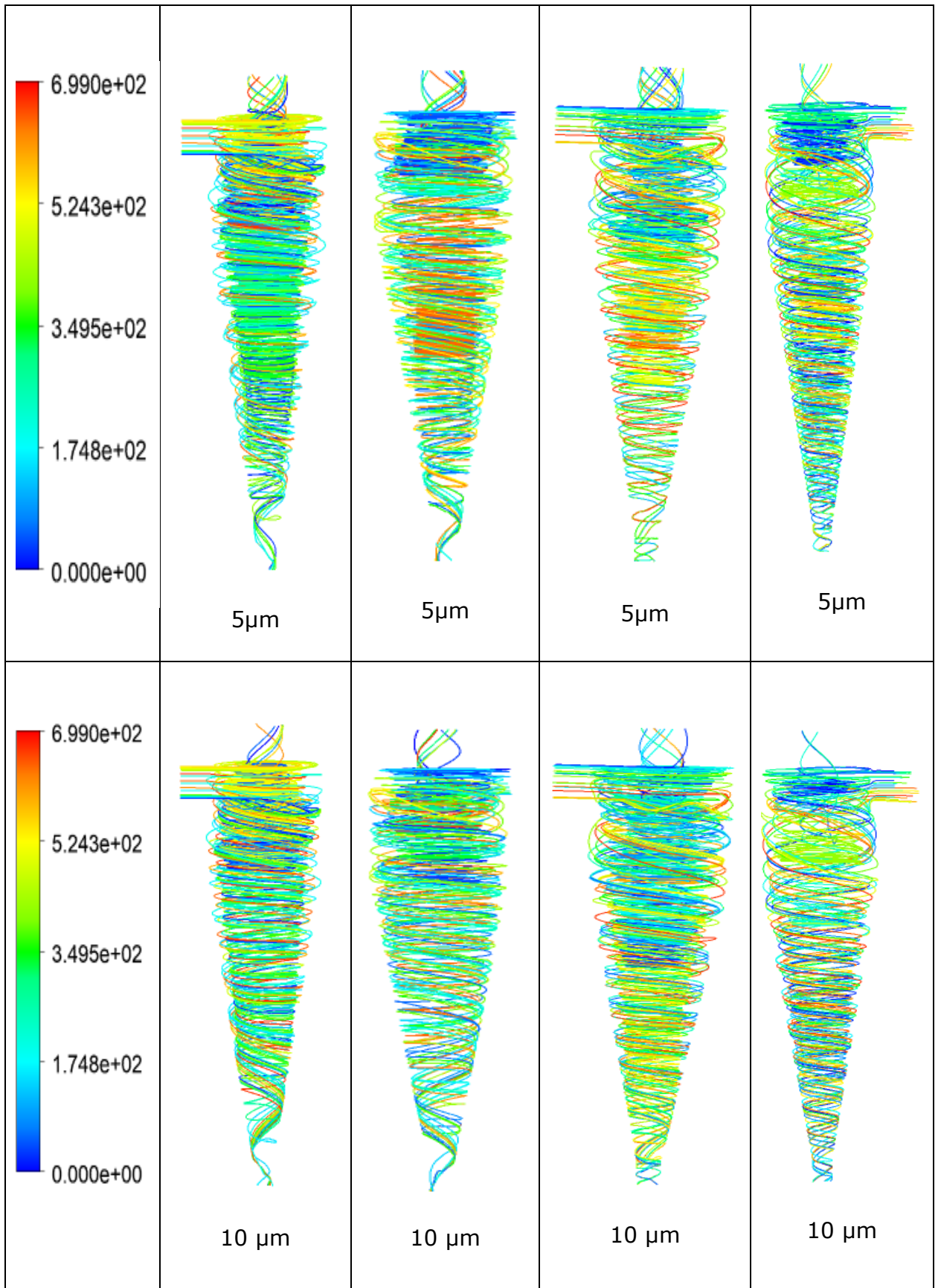
**Swirling Strength of at Vortex core Region of the cyclone at swirl level of 0.01**





## 5.2.8

## Particle Tracking





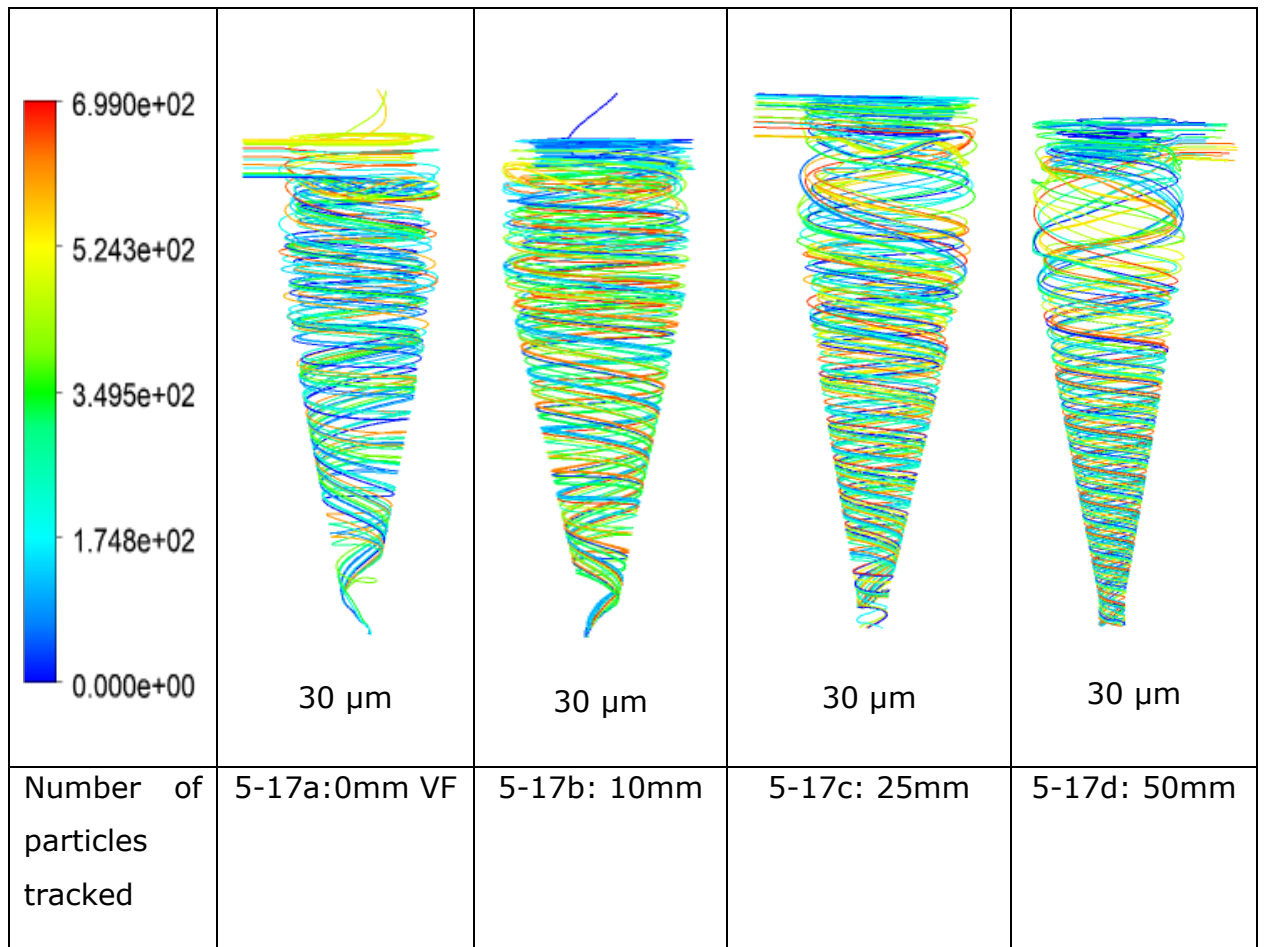


**Figure 5-17: Particle tracking for different vortex finders**

Figure 5-17a to 5-17d show the particle tracking for the different vortex finders considered. It can be seen that the longer the vortex finder, the lower the number of particles seen at the overflow of the hydrocyclone. This shows that the length of the vortex finder improves the separation of particles in the hydrocyclone (Patra, 2018; Martinez, 2008). It can also be observed that as the particle size increases, the number of particles travelling to the overflow section of the cyclone decreases indicating better classification/ separation of the bigger particles (Tang, 2018; Shojaeefard, 2006; Cui, 2017).

### 5.3 Spigot Section

The spigot diameter is an important geometrical parameter used for the adjustment of hydrocyclone operation and efficiency. Research has shown that the optimum spigot diameter depends on the feed concentration (Ghodrat, 2013; Caie, 2019). A large or small spigot diameter smaller than the optimum will lead to reduced or poor performance. Caie, 2019 noted that when the spigot diameter is too small, the separation efficiency and separation sharpness decrease.

**Table 5-4 : The spigot geometries used in Spigot diameter analysis**

Parameter	Symbol	7.5mm	12.5mm	17.5mm
Diameter of the cyclone body (mm)	$D_c$	75	75	75
Size of Inlet (mm)	$D_i$	22.16 x 22.16	22.16 x 22.16	22.16 x 22.16
Diameter of the vortex finder (mm)	$D_o$	25	25	25
Insertion depth of the vortex finder (mm)	$L_v$	50	50	50
Length of the cylindrical part (mm)	$L_c$	75	75	75
Cone Angle (°)	A	20°	20°	20°
Diameter of the spigot (mm)	$D_u$	7.5	12.5	12.5

In this section of the work, the optimum diameter based on the feed mass flowrate of 0.3kg/s was evaluated using the fluid flow parameter. The spigot diameter used in this evaluation were 7.5mm, 12.5mm, and 17.5mm. Air enters the cyclone through the spigot and exits through the vortex finder.

## Result and Discussion of Results

### 5.3.4 Axial Velocity

The axial velocity has been the indicator of the downward and upward movement of fluids to the overflow and underflow of the cyclone, it also determines the water split ratio in the cyclone. The comparison of axial velocity with different spigot diameters is shown in figure 5-19. Just like the tangential velocity, the axial

velocity is of two parts; the outer region and the inner region. The outer region (the region around the wall) occurs when there is a downward movement while the inner region (the region around the centre) occurs when there is upward movement.

It can be seen from figure 5-19 that both the axial velocity at both the outer and inner regions were affected by the size of the spigot diameter. In the cylindrical and conical sections, the 17.5mm spigot diameter cyclone has the lowest axial velocity in both the inner and outer region of the cyclone. This implies that the 17.5mm cyclone particles have a lower residence time in the cyclone than the cyclone with 7.5mm and 12.5mm vortex finder (Jiang, 2019). With reduced residence time, the separation efficiency in the hydrocyclone with 17.5mm spigot diameter decreases (Zhao, 2019). In the conical section, it can be seen that the inner core region of the 7.5mm hydrocyclone was almost non-existent, this implies that most all of the particle-laden fluid is been discharged at the overflow section of the hydrocyclone.

Figure 5-20 shows that the locus of zero vertical velocity of a particle that can fall into the zero velocity region (LZVV), it can be seen that the locus is more pronounced in the 7.5mm hydrocyclone than in the 12.5mm and 17.5mm hydrocyclones, this is because more flow reversal will be experienced in the small spigot section than the larger one.

### **5.3.5 Radial Velocity**

Figure 5-21a and b show similar radial velocity through the length of the hydrocyclone. However, towards the edge of the vortex finder, the radial velocity peaks and these peaks slightly differ with the 12.5mm hydrocyclone having the highest peak. The peak in radial velocity is because of secondary flows in the boundary layer of the cyclone lid which causes slip at the lid and can lead to non-ideal separation of particles (Jafari,2017). Therefore, the secondary flow in the boundary layer of 12.5mm hydrocyclone is more than that of the 7.5mm and 17.5mm diameter hydrocyclones.

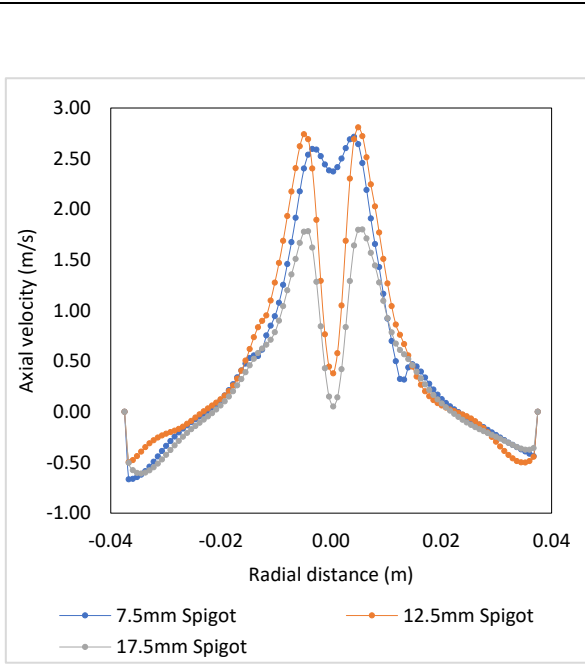


**Figure 5-19a: Axial Velocity at Z=0.8Dc (cylindrical section)**

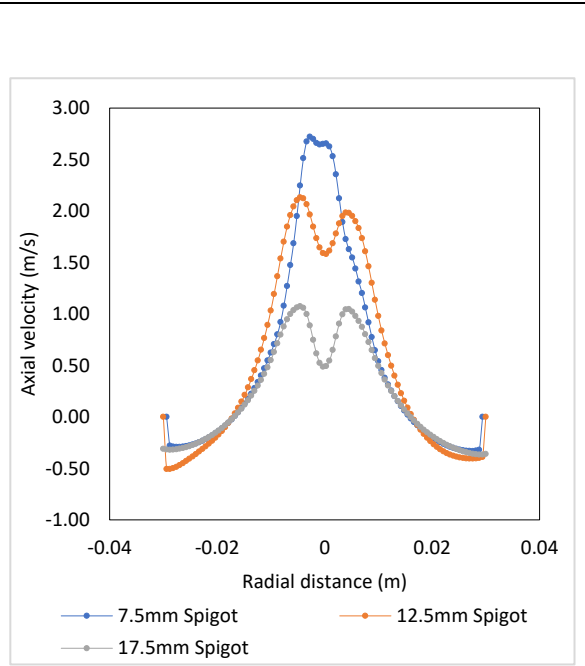


**Figure 5-19b: Axial Velocity at Z=1.6Dc (Conical section)**

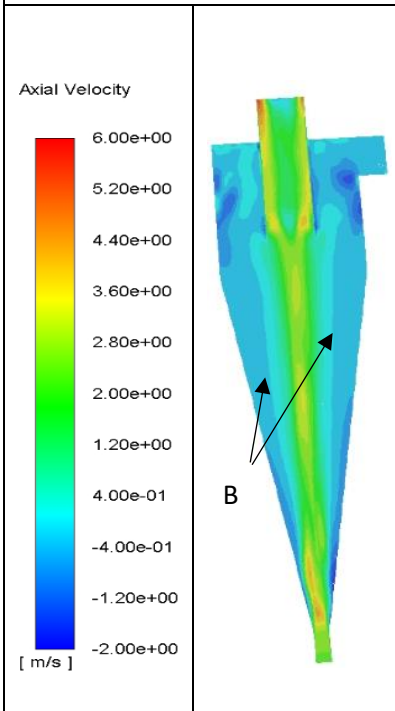


**Figure 5-20a: 7.5mm Spigot**

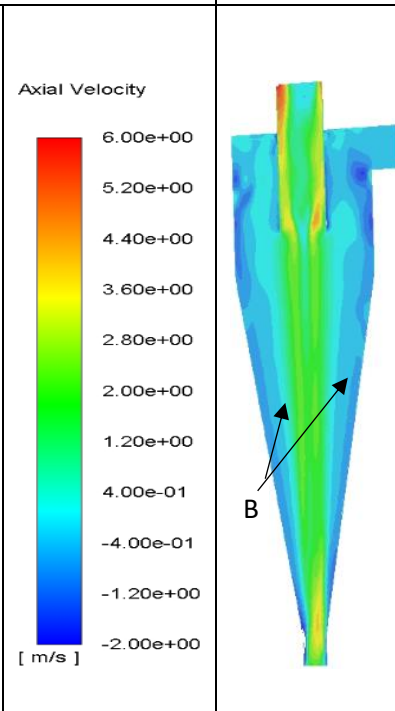


**Figure 5-20b: 12.5mm Spigot**

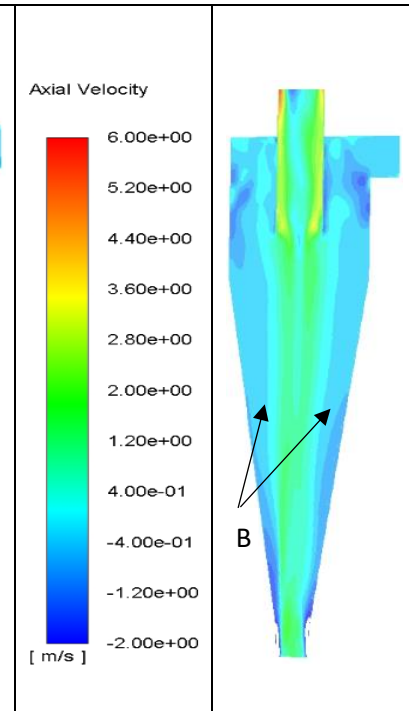
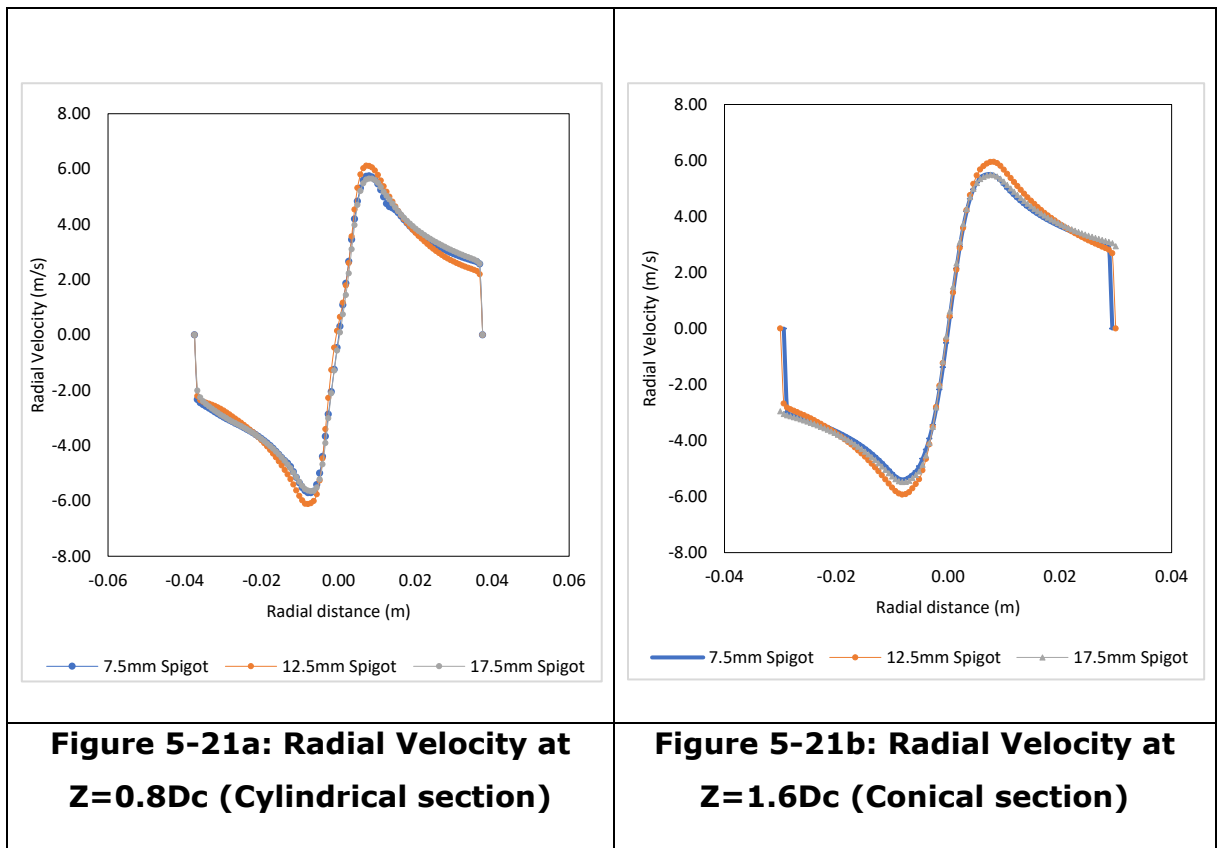


**Figure 5-20c: 17.5mm Spigot**

**Axial Velocity Contour at Different Spigot Diameters**

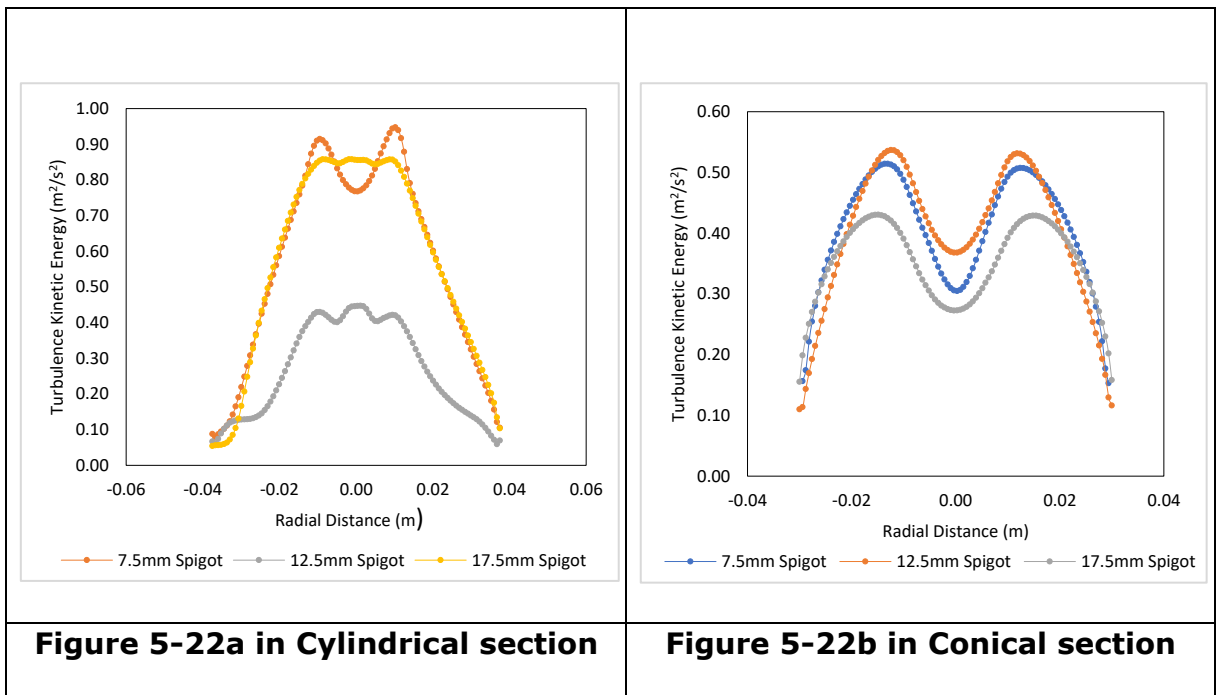


### 5.3.5 Turbulence Kinetic Energy

From figure 5-22a, in the cylindrical section of the cyclone, the turbulence kinetic energy of the 12.5mm hydrocyclone was quite low compared to the 7.5mm and 17.5mm spigot diameters. This implies that the rate of dissipation of energy (transfer of energy from the large to small eddies) is quite high in the 12.5mm hydrocyclone while energy is not properly distributed in the 7.5mm and 17.5mm hydrocyclones.

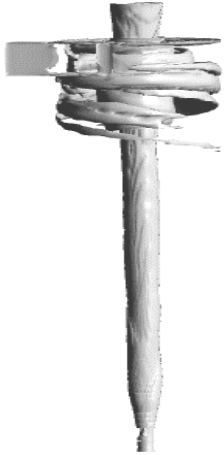


As the flow moves into the conical section of the cyclone, the gap between the turbulence kinetic energy of the three cyclones closes up with the 12.5mm hydrocyclone having the highest turbulence kinetic energy. Comparison of the turbulence kinetic energy of the 12.5mm hydrocyclone in both cylindrical and conical sections shows a slight increase from  $0.4\text{m}^2/\text{s}^2$  to  $0.53\text{m}^2/\text{s}^2$  while the 7.5 to 17.5mm hydrocyclone turbulence kinetic energy drops from  $0.94\text{m}^2/\text{s}^2$  and  $0.86\text{m}^2/\text{s}^2$  to  $0.51\text{m}^2/\text{s}^2$  and  $0.43\text{m}^2/\text{s}^2$  respectively. This shows that more turbulence resolution (more of the large eddies were converted to smaller eddies

in the conical section) takes place in the conical section of the 7.5mm and 17.5mm hydrocyclone than in the cylindrical section.



### 5.3.6 Swirling Strength of the cyclone at Level 0.01

The swirl strength of the flow shows little change in the 7.5mm and 17.5mm and very minimal change in 12.5mm showing that the spigot section of the cyclone has little to no effect on the swirl strength of the cyclone.

7.5mm Spigot	12.5mm Spigot	17.5mm Spigot
		

**Figure 5-23 : Vortex Core Swirl Strength of the cyclone at Level 0.01**

### **5.3.7 Pressure Drop**

The reference point of the pressure drop is very important, in this case the pressure drop was taken by subtracting the overflow pressure from the the inlet pressure. Figure 5-23a is the graph of the effect of the spigot diameter on pressure drop. It can be seen that increasing spigot diameter decreases the pressure drop in the hydrocyclone. This can be attributed to more fluid/particles moving to the overflow section due to flow resistance being increased with a smaller spigot diameter (Silva, 2015) therefore causing more flow reversal in the smaller diameter spigot section compared to the larger spigot diameter hydrocyclone; more pressure/energy is required to move these particles to the overflow section leading to more pressure drop in the smaller diameter spigot hydrocyclone.

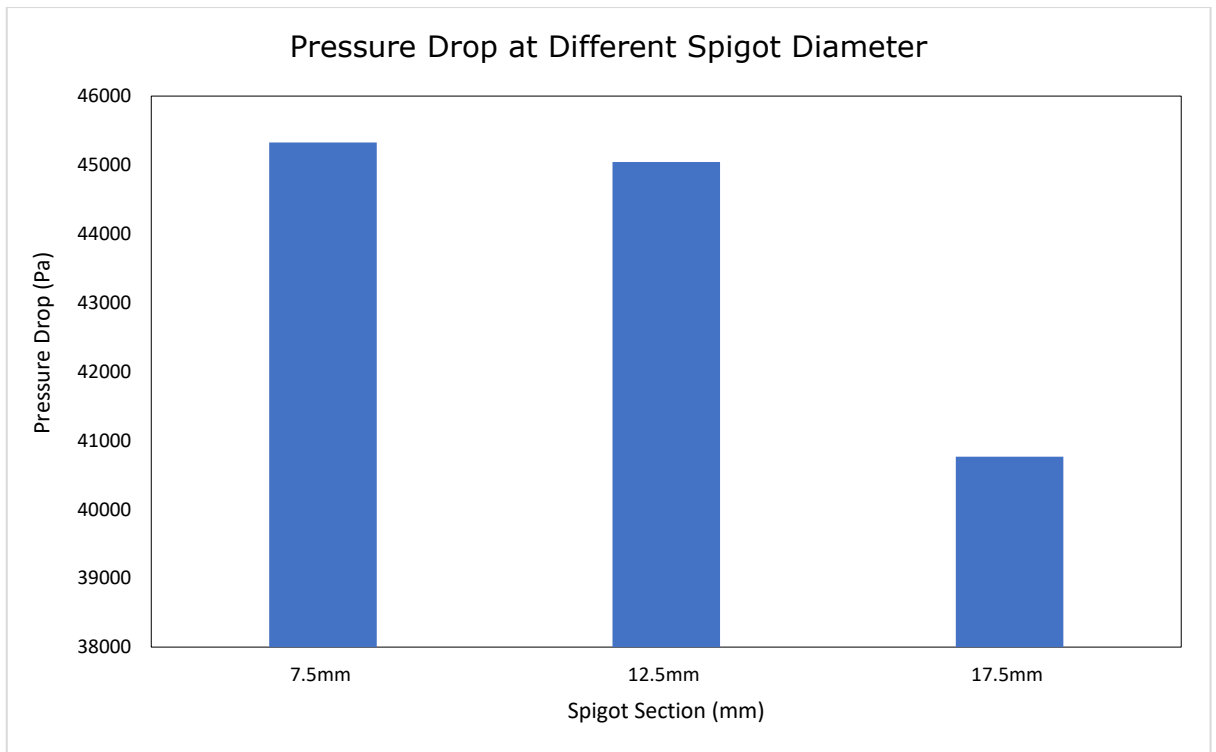


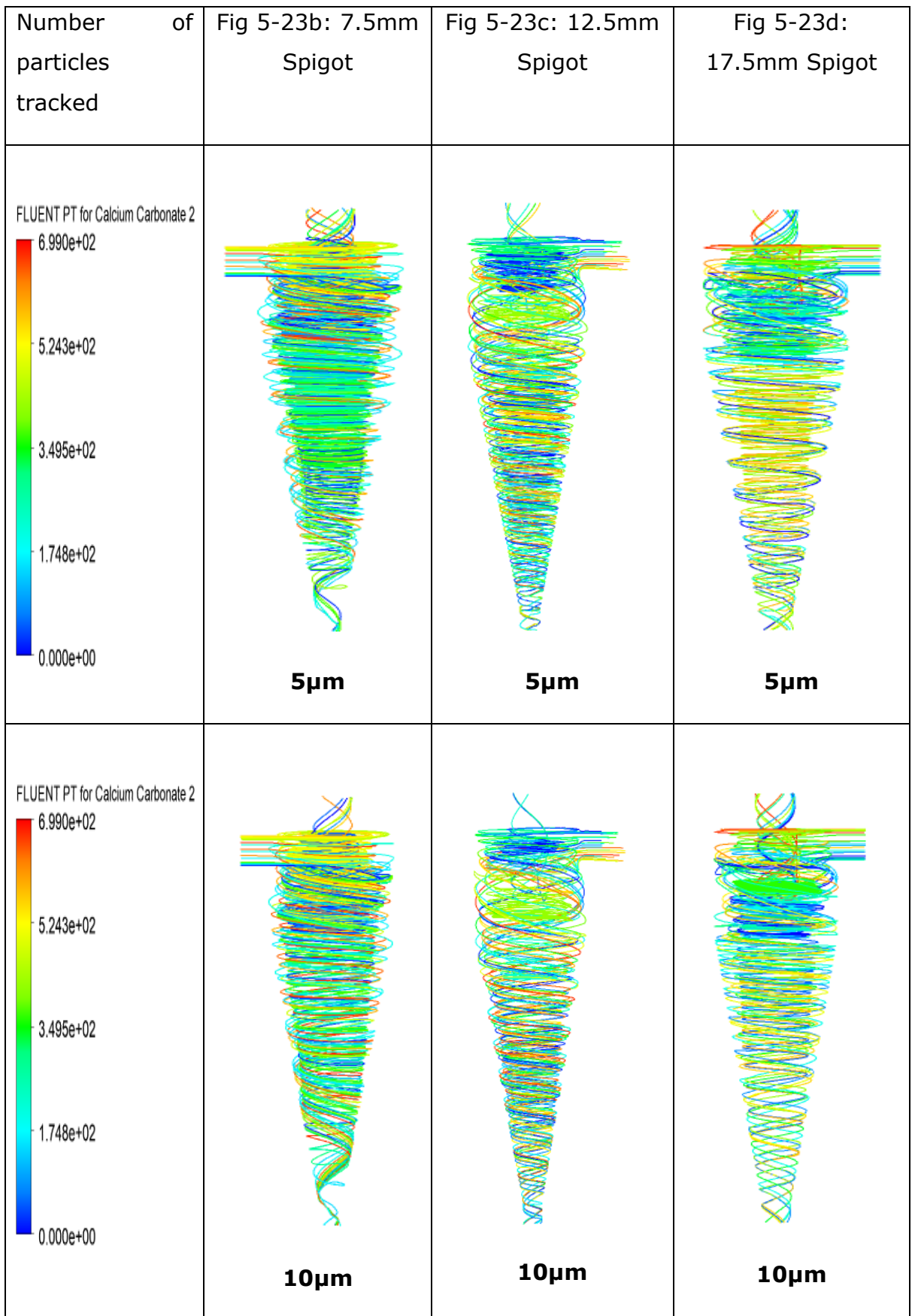
**Figure 5-23a: Effect of Hydrocyclone Spigot Diameter on Pressure drop**

### 5.3.8 Particle Tracking

Studies have shown that when feed concentration is less than 10%; particle separation in a hydrocyclone depends on the size of the spigot section with increasing spigot diameter yielding improved efficiency. However when the optimum spigot diameter is attained a further increase in spigot diameter will decrease the separation efficiency (Ghodrat, 2013 Freitas, 2009; Long, 2016; Mousavian, 2008; Silva, 2015; Saengchan, 2009; Zhang, 2019; Silva, 2015).

Twenty-five particles were tracked in each hydrocyclone to know the quantity of particles which will report to the overflow section of the hydrocyclone. Figure 5-23b to 5-23d as the spigot diameter increases from 7.5mm to 12.5mm, the separation efficiency of the particles increases with a lower number of particles reporting to the overflow section of the cyclone. However, when the spigot diameter was further increased to 17.5mm the separation efficiency decreases. This shows that 12.5mm is the optimum spigot diameter among the spigot diameters evaluated supporting the finding of other researchers.





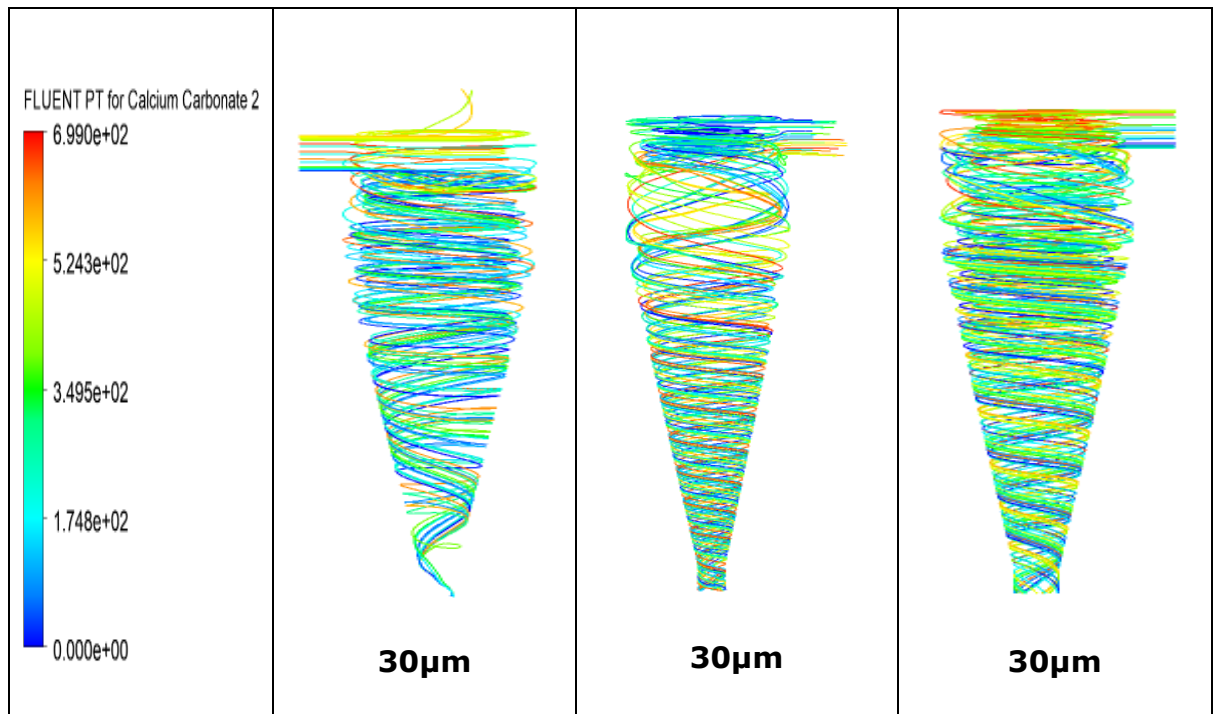


**Figure 5-23b to d: particle tracking for the different spigot sections**

#### **5.4 Comparison of the fluid flow in liquid-liquid and solid-liquid hydrocyclones**

Many researchers have looked at the fluid flow in a liquid-liquid hydrocyclone and solid-liquid hydrocyclone separately but none have compared the flow of fluid in the liquid-liquid and solid-liquid hydrocyclone. This section of the current studies compares the difference in the fluid flow of liquid-liquid and solid-liquid hydrocyclone using the same geometry. The base geometry used in the geometry is given in table 1 above. In addition to the base geometry simulation evaluated, the 50mm cylindrical geometry, 7.5mm spigot geometry, 17.5mm spigot geometry, 0mm vortex finder, 10mm vortex finder and 25mm vortex insertion described above were evaluated to compare the effect of geometry on both the liquid-liquid and solid-liquid hydrocyclone.

Simulation of diesel oil and water was used for the liquid-liquid analysis while calcium carbonate and water simulation represented the solid-liquid simulation. Both simulations were carried using exactly the same process and run for an equal time step of 10000.

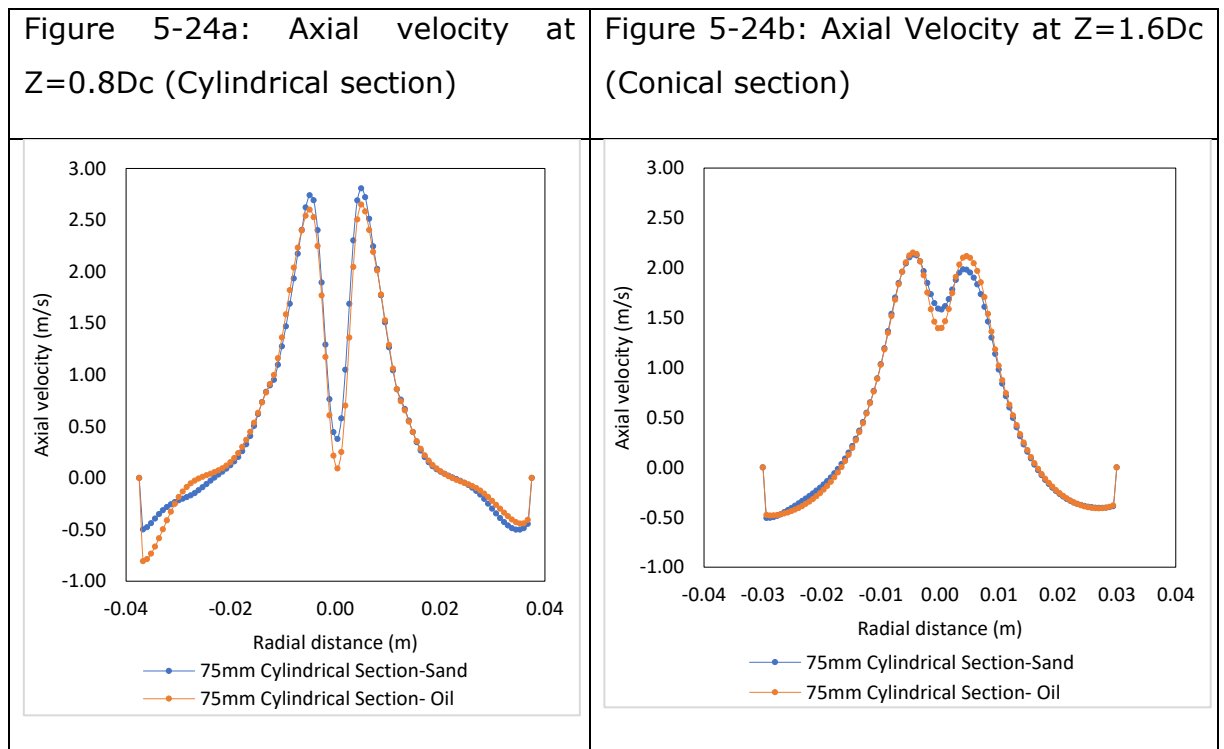
## 5.4.1 Results and Discussion of Results

The results of the geometrical analysis of the spigots, vortex finder depth, and hydrocyclone diameter show that a change in axial velocity and turbulence kinetic energy of the liquid-liquid and solid-liquid hydrocyclone was experienced across the board while other flows of fluid considered (tangential, radial and pressure and swirl) remain relatively the same for both hydrocyclones.

## 5.4.2 The Axial Velocity

Cylindrical section diameter

The axial velocity chart in the cylindrical section of the 75mm hydrocyclone shows that more circulation takes place in liquid-liquid hydrocyclone than in the solid-liquid hydrocyclone. In the 50mm cylindrical diameter, the axial velocity was almost the same in both liquid-liquid and solid-liquid hydrocyclone. From the results of the cylindrical diameter evaluation, it can be seen that increasing the cylindrical diameter increases the difference the axial velocity of liquid-liquid and solid-liquid hydrocyclone. Increasing the diameter also increases the axial velocity of the fluid in the hydrocyclone.



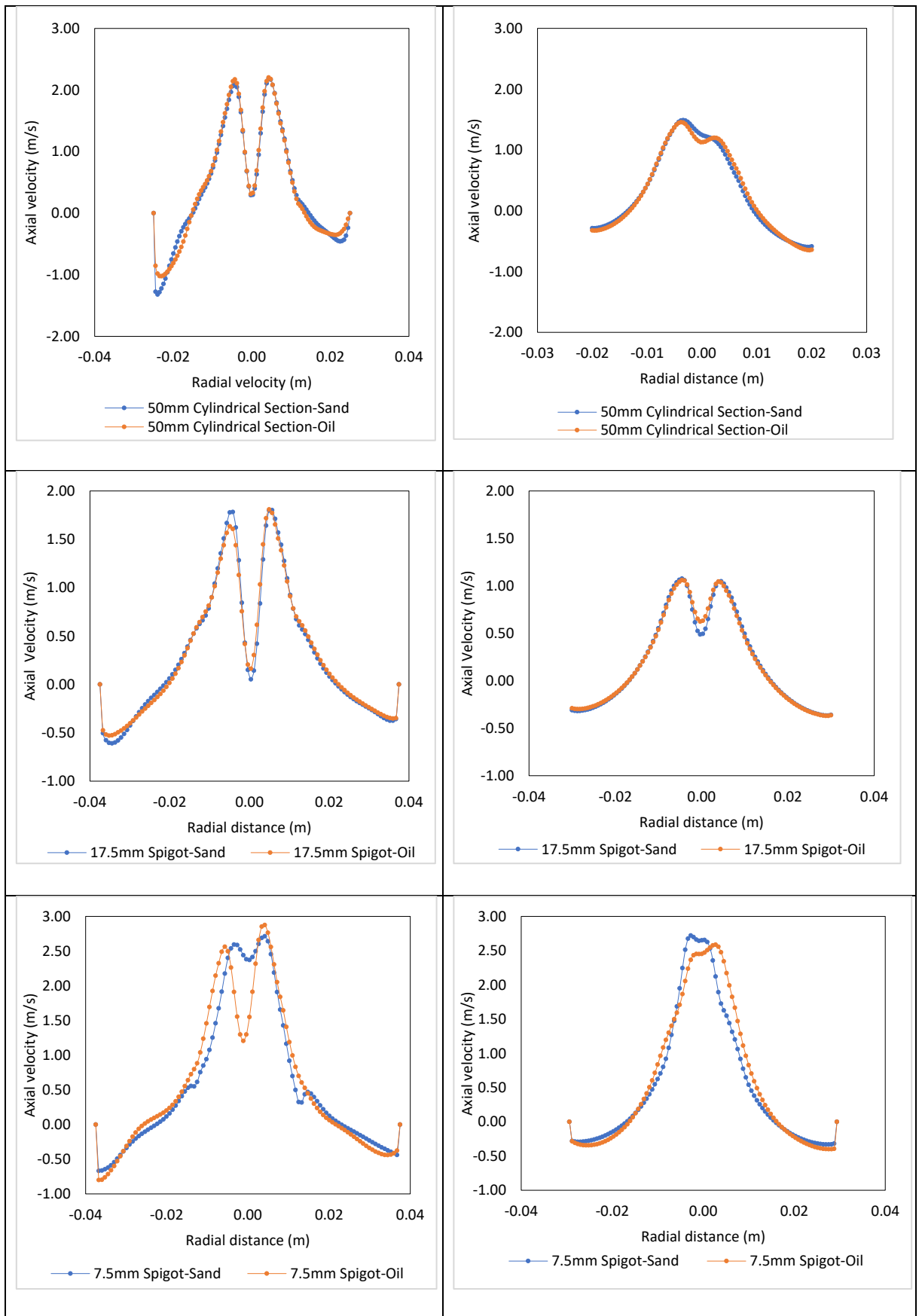


Figure 5-24: Axial Velocity of Base (75mm) cyclone diameter, 50mm cyclone diameter, 7.5mm spigot diameter and 17.5mm Spigot diameter hydrocyclone

### **5.4.3**

### **Spigot Diameter**

In a 17.5mm spigot, the axial velocity of the liquid-liquid hydrocyclone and solid-liquid hydrocyclone were almost the same in both the cylindrical and conical section with flow circulation in both the cylindrical and conical section. However, in a cylindrical section of the 7.5mm spigot cyclone, the axial velocity of the liquid-liquid cyclone and the solid-liquid hydrocyclone were the same in the outer region zone of the cyclone but the difference can be seen in the inner region/ cone of the cyclone. The liquid-liquid hydrocyclone has lower inner region/ dipping core region indicating more revolution (Lee, 2006) of fluid takes place in liquid-liquid hydrocyclone than in solid-liquid hydrocyclone especially in the cylindrical section. Increasing the spigot section also decreases the axial velocity of fluid in the hydrocyclone

### **5.4.4**

### **Vortex Finder**

In a hydrocyclone the inward dipping of the core-annulus region means inflow into the core region and the outward increase of the axial velocity in the outer region indicates radial flow toward the wall (Lee, 2006). However, in the 0mm and 10mm vortex finder, the shape rising of the velocity at the core region means an immediate short circuiting of the inlet flow to the outlet without swirling round the cyclone (Lee, 2006) thus less separation in the 0mm and 10mm vortex finder for the liquid-liquid hydrocyclone compared to that of a solid-liquid hydrocyclone.

The little to no-dipping at the core of the liquid-liquid hydrocyclone at 25mm vortex finder also indicates that the separation in the liquid-liquid hydrocyclone is not as good as that of the solid-liquid hydrocyclone. The improved axial velocity shape of the solid-liquid hydrocyclone can be credited to a higher density differential between the solid particle and water.

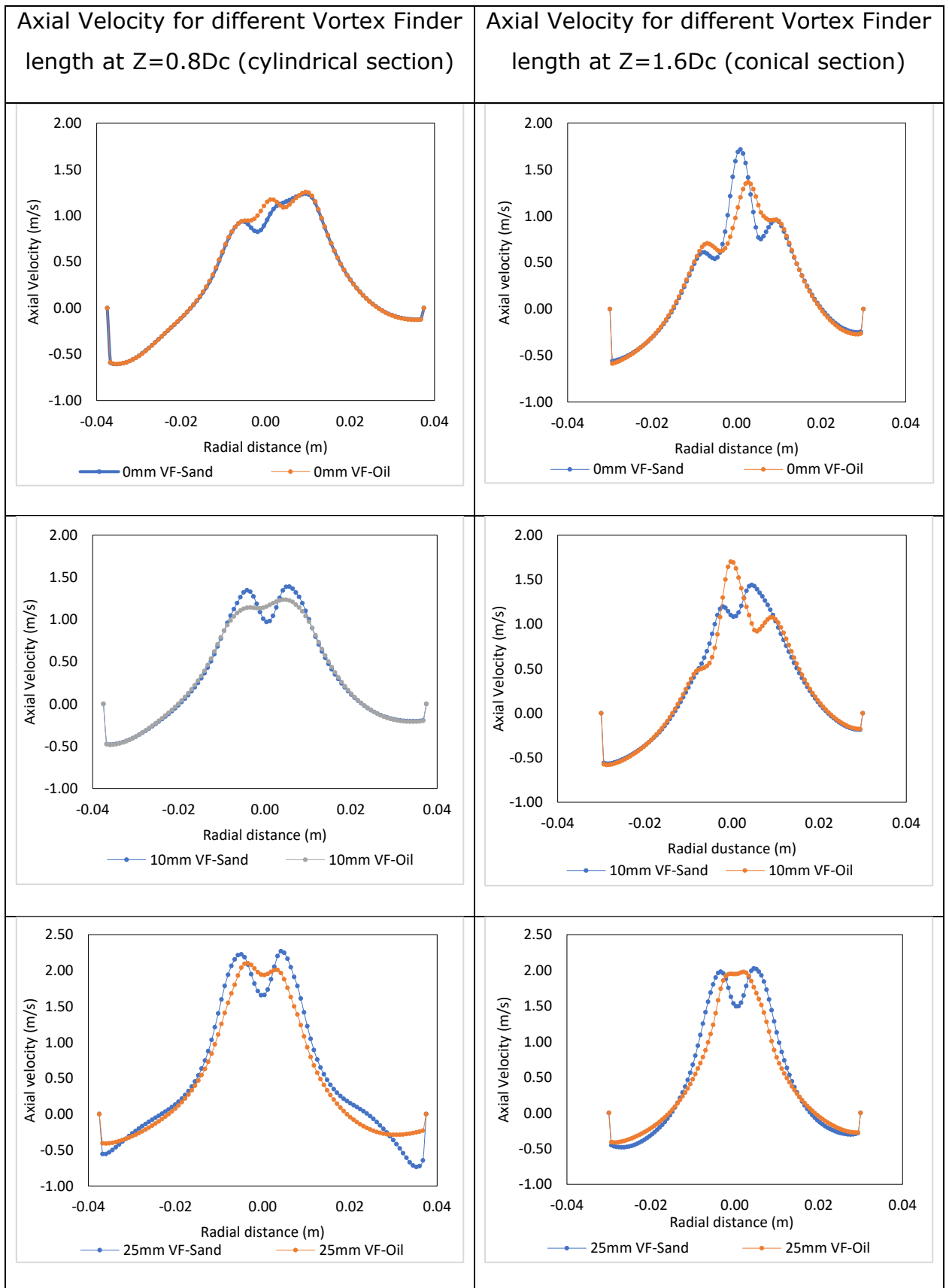


**Figure 5-25 : Axial Velocity in 0mm, 10mm and 25mm Vortex finder for the solid-liquid and liquid-liquid hydrocyclone**

### 5.4.3

### Tangential Velocity

Figure 5-26 compares the tangential velocity profile of the solid-liquid and the liquid-liquid hydrocyclone using the same geometry parameters (same radius) and inlet velocity and mass loading. It can be seen that the tangential velocity for both hydrocyclones remains the same for the cylinder diameters (75mm and 50mm) and spigot section (17.5mm and 7.5mm) considered. This can be ascribed to the way tangential velocity is being calculated by the equation given below, showing that the calculation of the tangential velocity does not consider density which differential is the major difference between the solid-liquid and the liquid-liquid hydrocyclones.

$$V_t = \omega r \quad (5)$$

$$\text{Where } \omega = \frac{2\pi}{T} \quad (6)$$

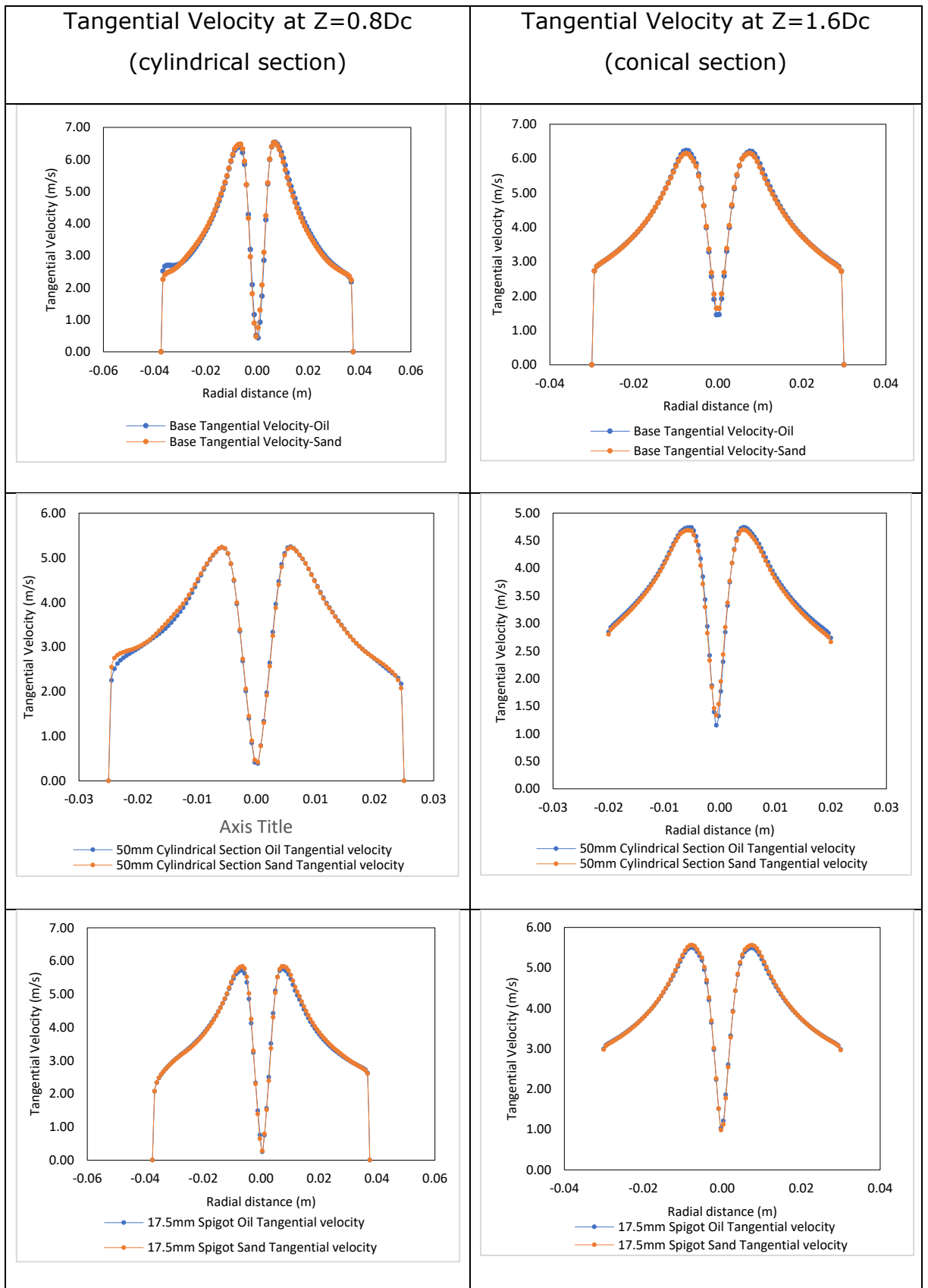
$\omega$  is the angular velocity while T is the period.

The fluid flow in the free vortex region of tangential velocity is given by equation 7 below

$$V_t r^n = C \quad (7)$$

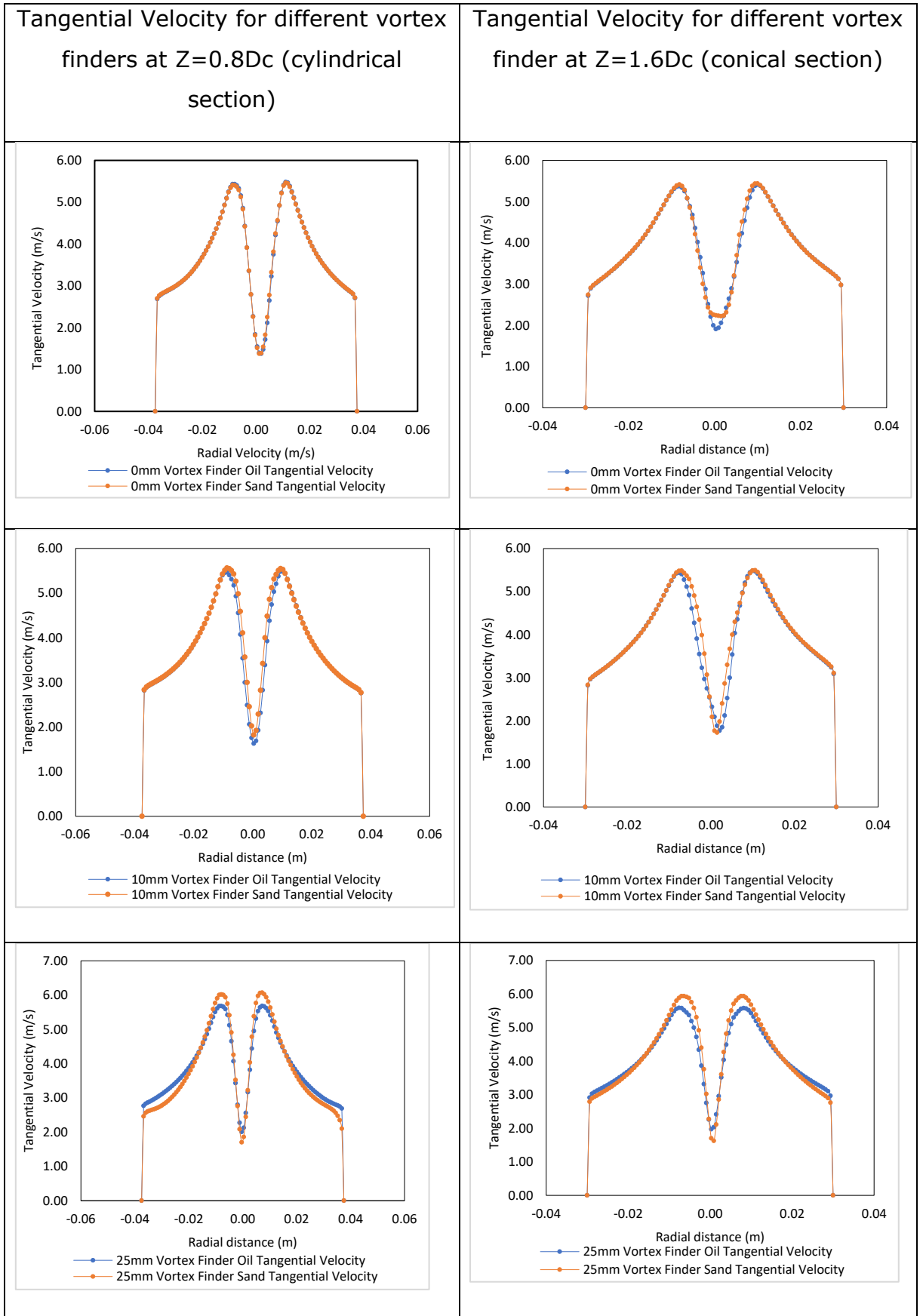
Where  $V_t$  is the tangential velocity,  $r$  is the radius and  $n$  is normally be  $0 < n < 1$  and  $C$  is a constant. The fluid movement equation for the free vortex zone of the tangential velocity is does not include the influence of particle density.

Figure 5-27 is the graph of the comparison between the solid-liquid and liquid-liquid hydrocyclone at different vortex finder lengths. The result of the shorter vortex finder (0mm and 10mm) is almost the same for both hydrocyclones. However, when the vortex finder length was longer, a small change was observed between the tangential velocity of the hydrocyclones with solid-liquid hydrocyclone having a higher tangential velocity. This is because the insertion of the vortex finder influences the tangential velocity gradient by disturbing the flow field (Yang, 2011), a longer vortex finder therefore disturbs the flow field which



**Figure 5-26 : Tangential Velocity in Base cylindrical section (75mm), 50mm cylindrical section, 17.5mm spigot section**





**Figure 5-27 : Tangential Velocity in 0mm, 10mm and 25mm Vortex finder for solid-liquid and liquid-liquid hydrocyclone**

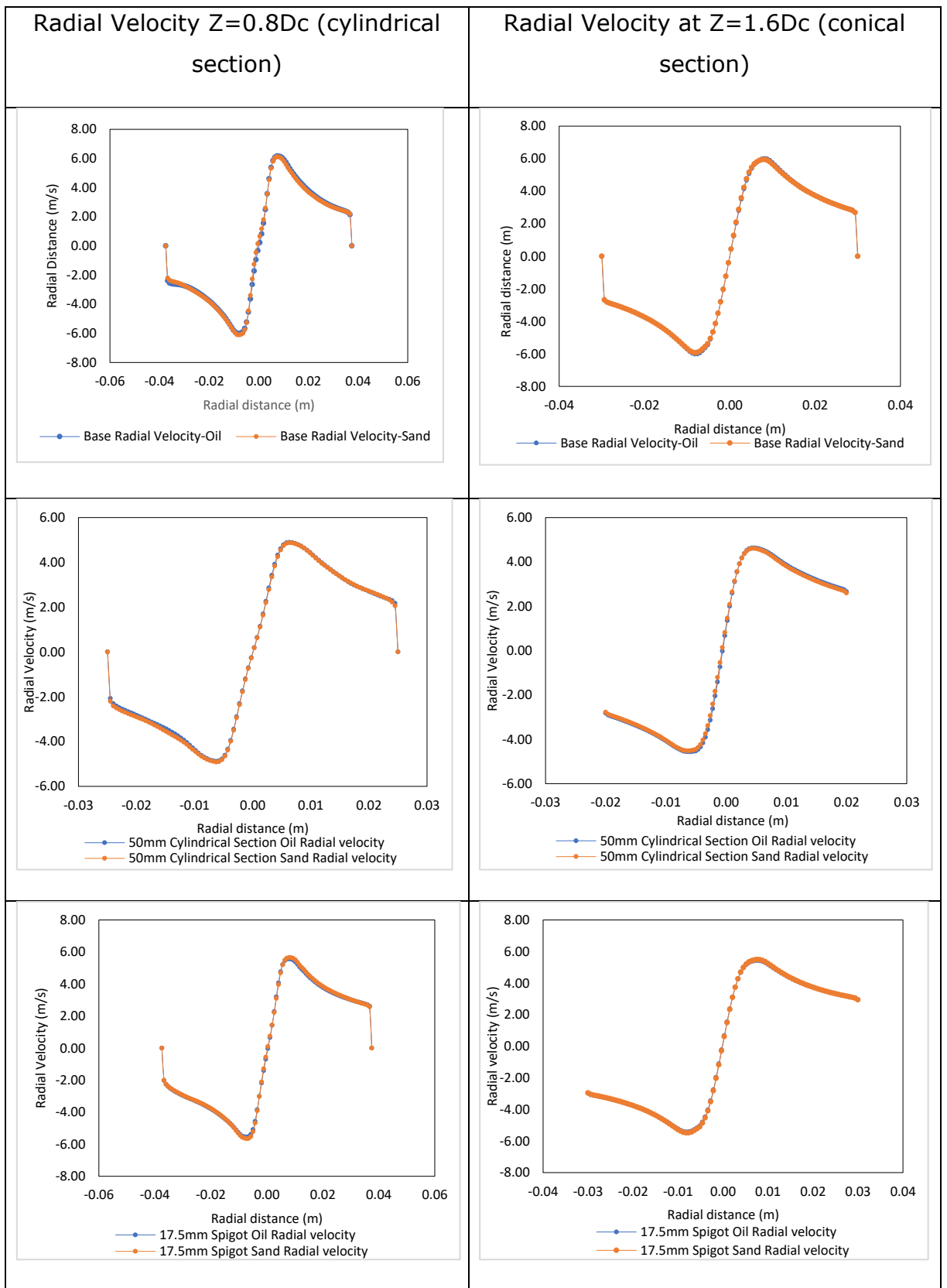


**Figure 5-28 : Radial Velocity in Base cylindrical section (75mm), 50mm cylindrical section, 17.5mm spigot section for the solid and liquid hydrocyclone**

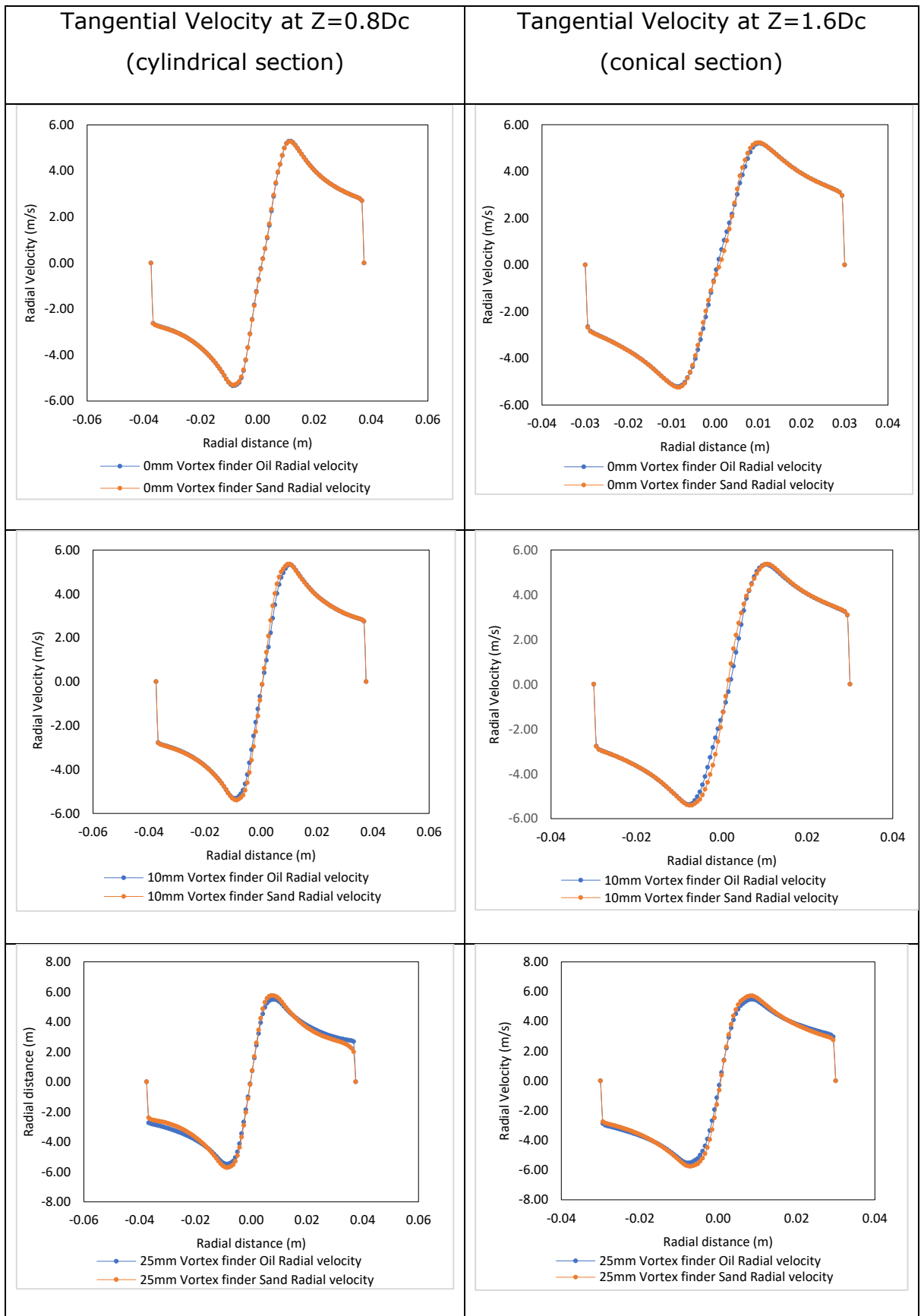


**Figure 5-29 : Radial Velocity in 0mm, 10mm and 25mm Vortex finder for solid-liquid and liquid-liquid hydrocyclone**

helps the swirl flow. A strong fluctuation of the tangential velocity gradient can shear oil droplets thus the optimum vortex finder length for the two hydrocyclones will be slightly different.

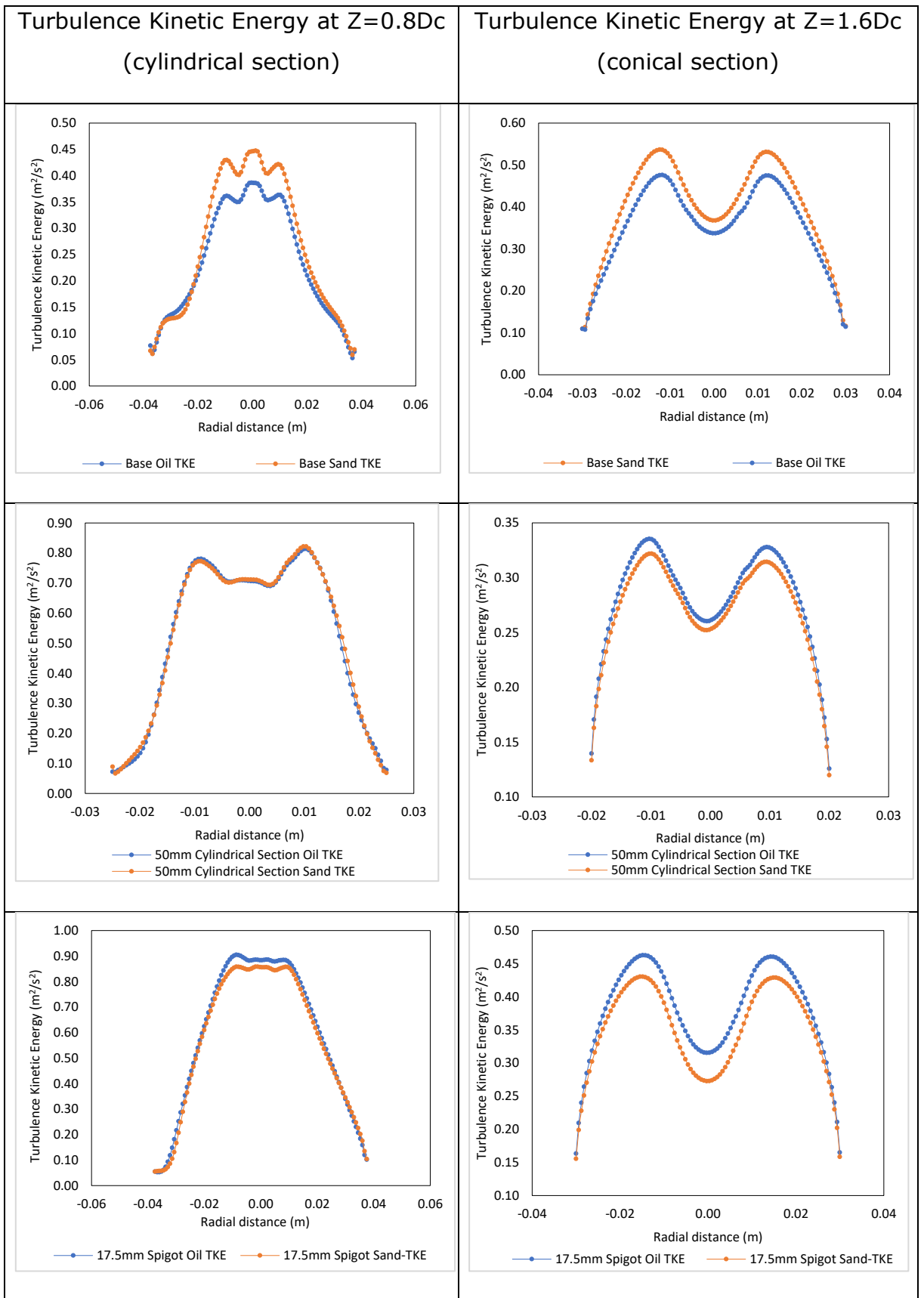
Figures 5-28 and 5-29 are the radial velocity profile of the solid-liquid and liquid-liquid hydrocyclones at different sizes of cylindrical section, vortex finder and 17.5mm spigot section. It can be seen that there is no significant change in the solid-liquid and liquid-liquid hydrocyclones considered. This is because the massflow rate is very small (less than 10%).

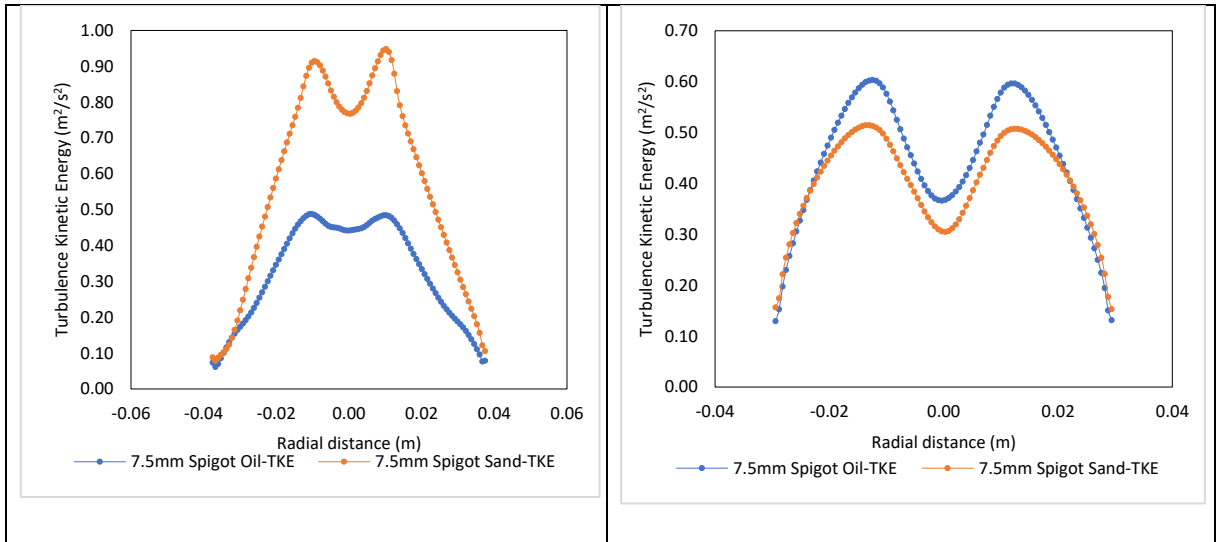
### **5.4.3 Turbulence Kinetic Energy**

For the turbulence kinetic energy of the base cyclone, the upward flow in the cylindrical and conical section of the hydrocyclone with solid-liquid energy is more than the liquid-liquid hydrocyclone and both show flow reversal in the central region of the conical section. This means that the total energy dissipated to the smaller eddies is more in the liquid-liquid hydrocyclone than in the solid-liquid hydrocyclone. In the 50mm cylindrical cyclone, the flow is almost the same in the cylindrical section of the cyclone but in the conical section, the turbulence kinetic energy of the liquid-liquid is more than that of the solid-liquid, indicating that more energy was dissipated in the solid-liquid than in the liquid-liquid hydrocyclone.

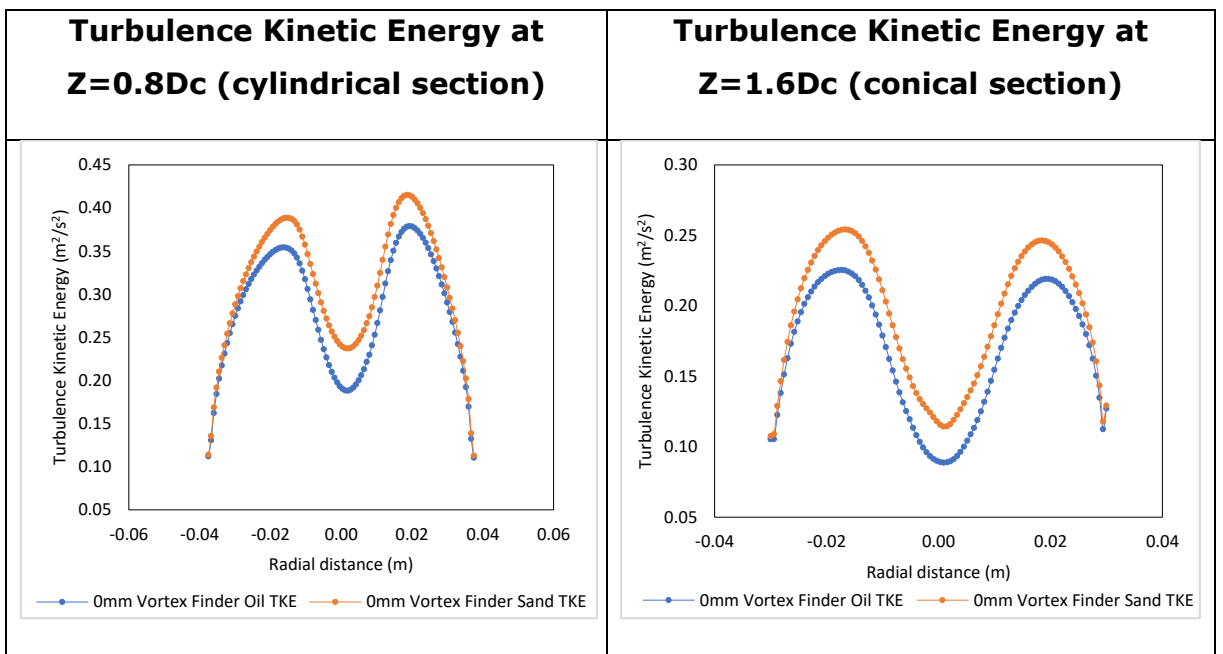
In the 17.5mm and 7.5mm spigot sections (figure 5-30), the conical section charts show that the liquid-liquid hydrocyclone turbulence kinetic energy is more than the solid-liquid hydrocyclone indicating that less energy was transferred to the smaller eddies in the cyclone. In the cylindrical section of the 17.5mm spigot cyclone, the liquid-liquid hydrocyclone turbulence kinetic energy is more than the solid-liquid hydrocyclone though the difference between the two spigots' turbulence kinetic energy was equally small. In the 7.5mm spigot diameter hydrocyclone, the solid-liquid turbulence kinetic energy was more than the liquid-liquid which is due to the different rate at which energy has been dissipated in the two cyclones.

In the vortex finders considered, the turbulence kinetic energy in solid-liquid was higher than the liquid-liquid hydrocyclone. However, in the 25mm hydrocyclone





**Figure 5:30: Turbulence Kinetic Energy of Base, 50mm diameter and 17.5mm Spigot diameter hydrocyclone for solid-liquid and liquid-liquid hydrocyclones**



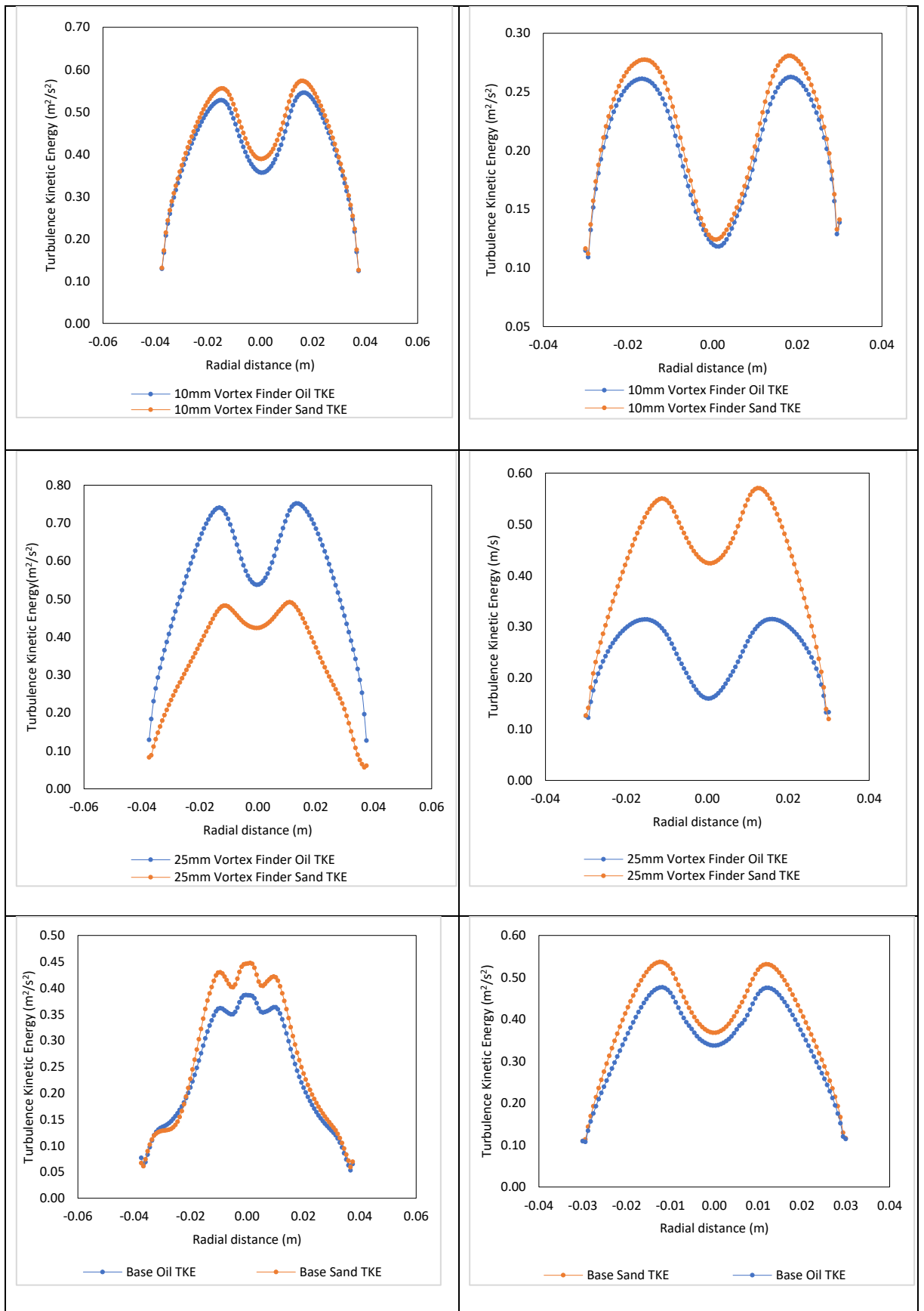


**Figure 5-31 : Turbulence Kinetic Energy in 0mm, 10mm and 25mm Vortex finder for solid-liquid and liquid-liquid hydrocyclones**

there was a huge difference in the turbulence kinetic energy of solid-liquid and the turbulence kinetic energy in the liquid-liquid.

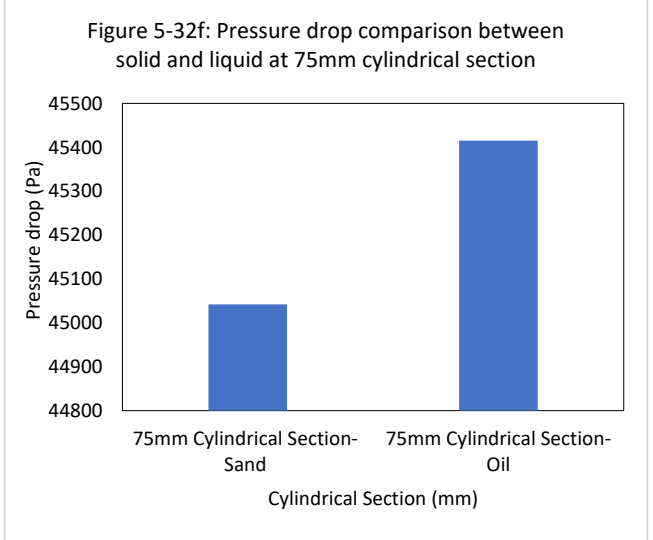
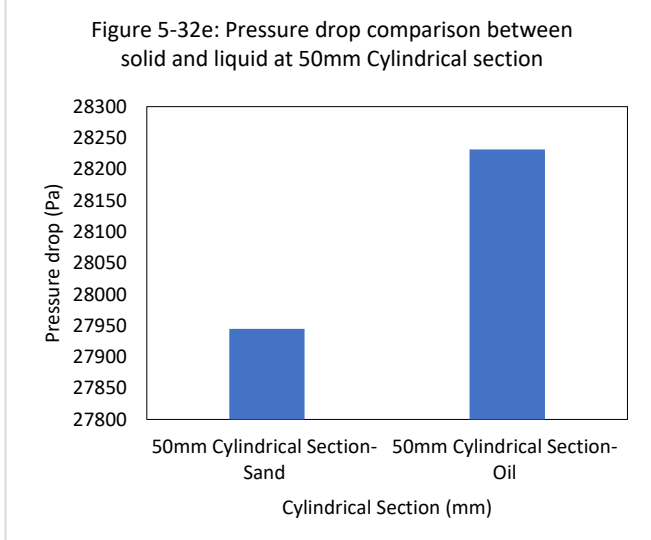
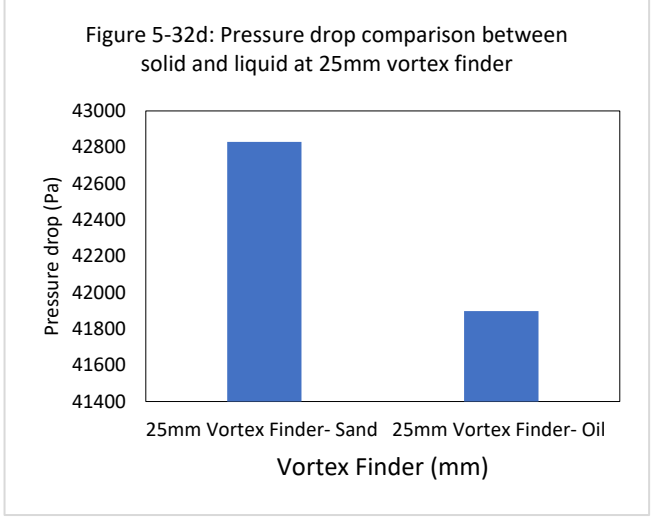
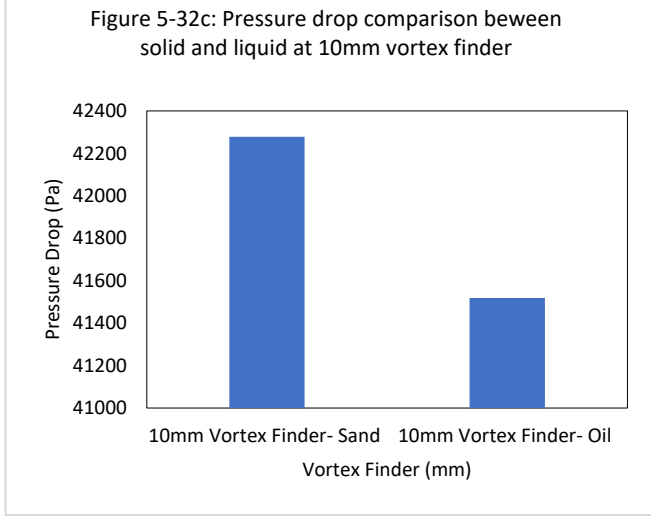
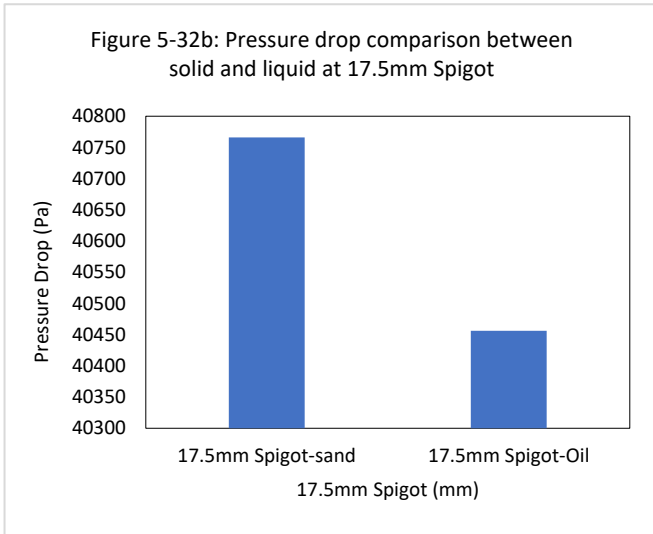
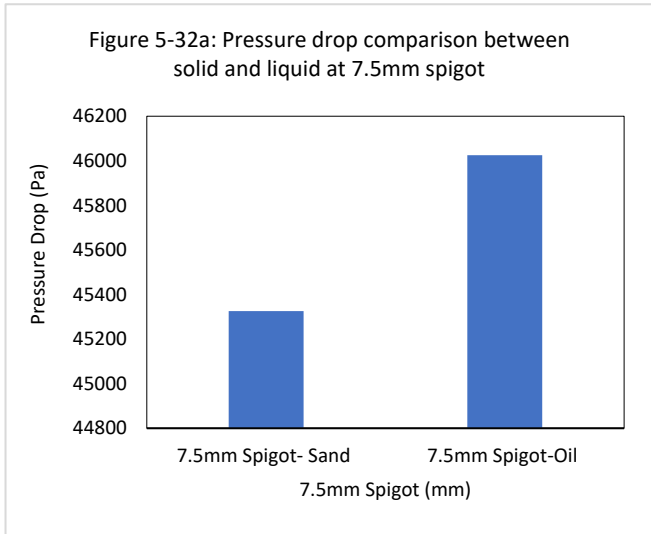
#### **5.4.4 Pressure Drop**

Figure 5-32 shows the pressure drop comparison of the solid-liquid and liquid-liquid hydrocyclone with varying hydrocyclone geometrical parts. Figures 5-32a and 5-32b show the pressure drop at 7.5mm and 17.5mm spigot diameters. It can be seen that the solid-liquid hydrocyclone has a higher pressure than the liquid hydrocyclone when the spigot diameter is small. However, with an increase in the spigot diameter to 17.5mm the reverse was the case (liquid-liquid hydrocyclone having higher pressure drop). This is because flow reversal is forced due to resistance of flow caused by small spigot diameter which makes more of the fluid and particles to be seen in the overflow section of the cyclone. The disparity in the pressure drop between the sand and the oil cyclone occurs as a result of the influence of particle density on pressure in the hydrocyclone. The pressure drop is directly proportional to the fluid density based on equation 4 above (Svarosky, 2000).

There was less resistance to flow when the spigot diameter was 17.5mm, however, the sand cyclone has a higher pressure than the oil cyclone. This is because increasing the spigot section removes the resistance of flow; therefore, density of fluid (which is the blend of the particle and produced water density) will take precedence. Sand with higher density will therefore lead to a higher pressure drop, all other parameters remaining constant.

Figure 5-32c and d is the comparison of the use of 10mm and 25mm vortex finders. It was observed that the solid-liquid hydrocyclone has higher pressure than the liquid-liquid hydrocyclone and this is credited to higher vortex finder length resulting in oil droplet breakage (Yang, 2011) and consequently the hindering of the movement of oil droplets to the underflow resulting in the reduction of the pressure at the overflow section of the cyclone.





### **Figure 5-32: Comparison of the pressure drop for solid-liquid and liquid-liquid hydrocyclones at different geometrical parameters**

Figures 5-32e and 5-32f show that the pressure drop in the solid-liquid hydrocyclone is less than the pressure drop in the liquid-liquid irrespective of the cylindrical section diameter. This centrifugal force pushed sand particles to the wall of the cyclone while the drag force is responsible for the movement of the oil particles (which are less dense than water) to the central/ core region of the hydrocyclone from where it is transferred to the overflow. The pressure resulting from the high drag force causes more pressure to be dropped in the liquid-liquid hydrocyclone than in the solid-liquid hydrocyclone.

#### **5.4.5 Split Ratio**

The two hydrocyclones were simulated using the same geometry, CFD setup, mass loading and inlet velocity. The overflow and underflow pressure of the cyclones were set to 0 barg (atmospheric pressure). Calcium carbonate was used for the solid phase while diesel was used for the oil phase. The split ratio predicts the quantity of the oil or sand phase that will be seen at the overflow or underflow section of the cyclone, this influences the prediction of the size classification curve. The split ratio plotted in figure 5-33 below was evaluated using the ratio of underflow mass flow rate and overflow mass flowrate to the inlet mass flow rate as shown in the equation below. This shows the percentage of the mass flowrate at the overflow and underflow sections respectively. Mass flowrate is used for all split ratio calculations because the quantity of the fluid upstream and downstream of the cyclone are measured

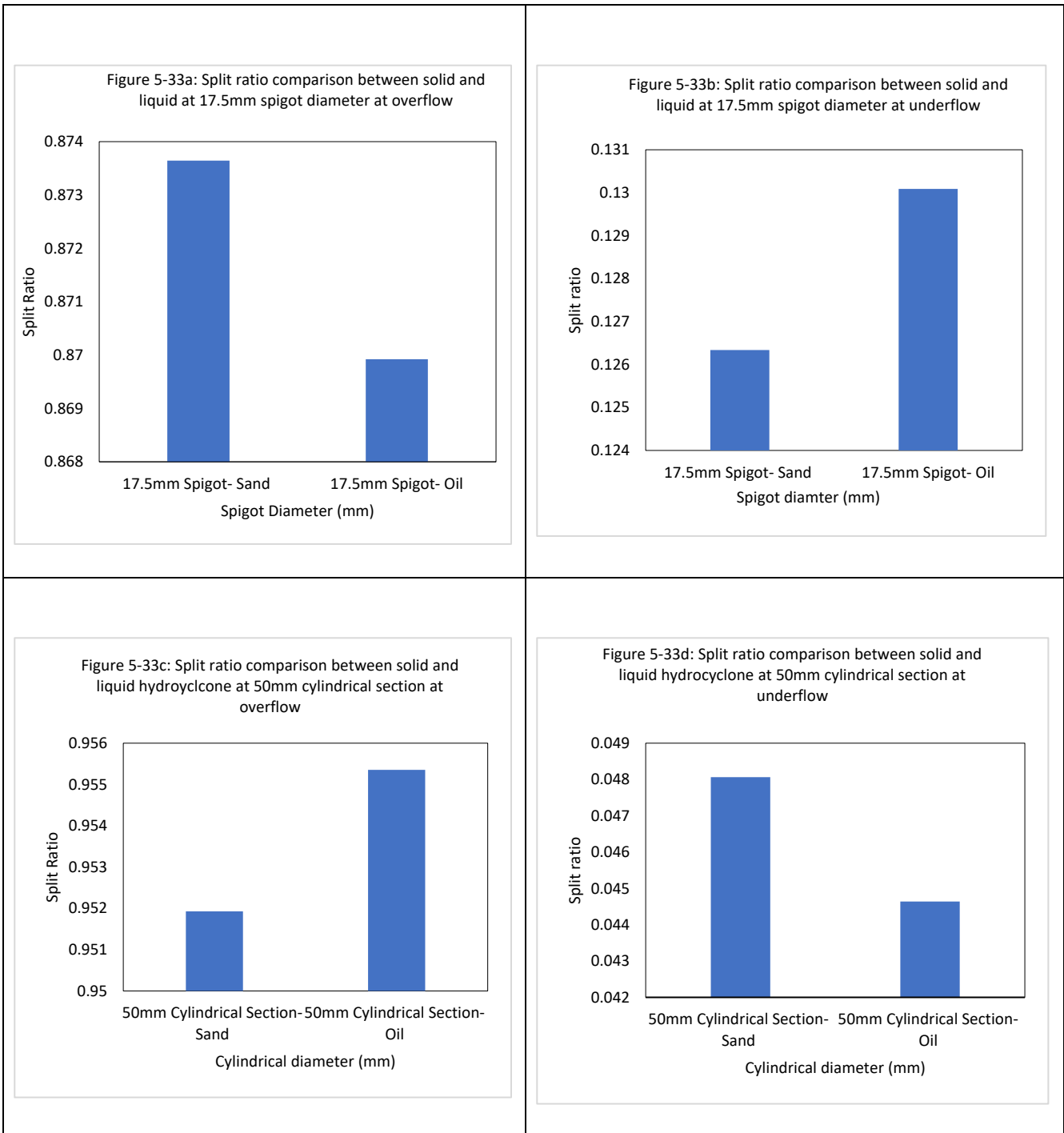
$$Split\ ratio = \frac{U_{underflow}}{U_{inlet}}$$

$$Split\ ratio = \frac{U_{overflow}}{U_{inlet}}$$

The geometrical parts of the hydrocyclone are expected to affect the split ratio in the hydrocyclone. It can be seen that more of the fluid reported to the overflow than to the underflow.

Although the separation of particles in the solid-liquid and liquid-liquid hydrocyclone uses the same principle, the predominant force causing the

separation in the two cyclones are different. In the solid-liquid hydrocyclone, the centrifugal force is the predominant force with the majority of the particles moving to the underflow while the produced water is expected at the overflow which could result in a considerably high split ratio (Jian-Feng 2017). Yuan (2015) has a split ratio of up to 0.47 after which a further increase in split ratio reduced the separation efficiency.



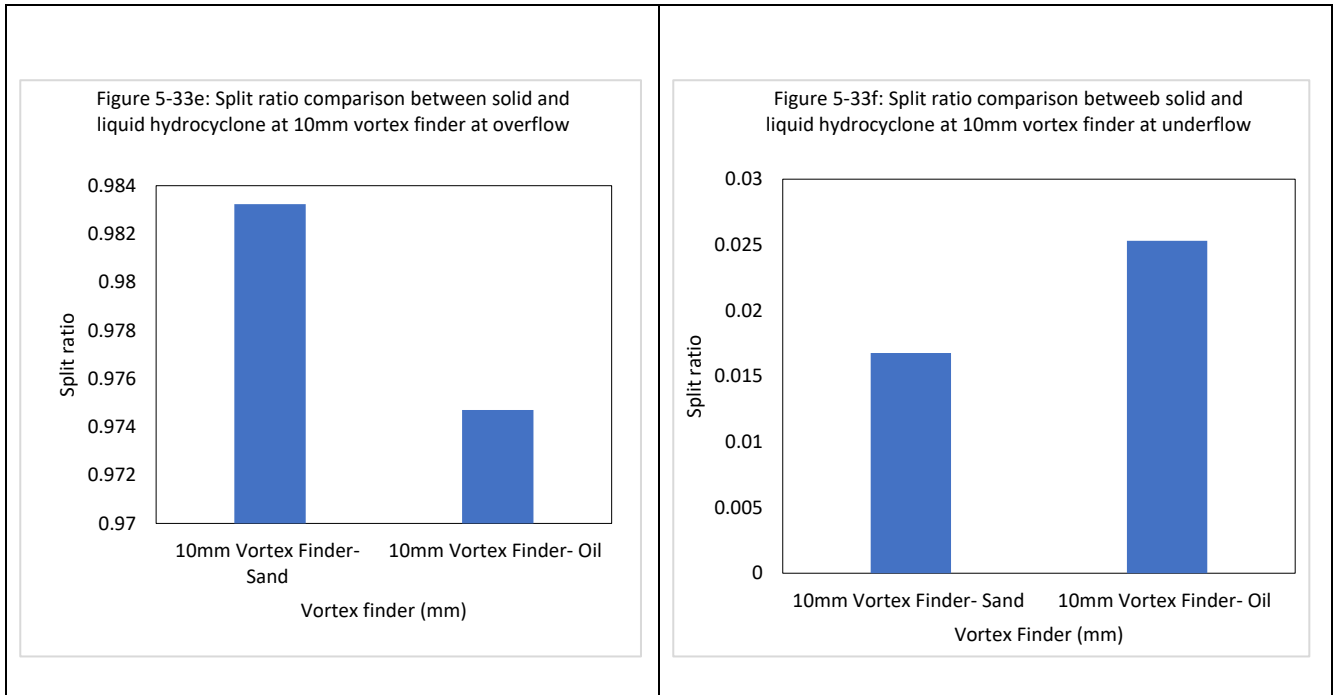


**Figure 5-33: Split ratio comparison for solid-liquid and liquid-liquid hydrocyclone at different geometrical parameters**

However, in the liquid-liquid hydrocyclone in addition to the centrifugal, the drag force is also crucial as this is the force dragging the oil particles to the core region of the cyclone (Song, 2016; Raoufi, 2008; Saidi, 2012) for upward movement to the overflow. Most of the fluid is to be discharged via the underflow while the discrete oil phase is to be discharged via the overflow, therefore a high split ratio (0.87 and above) at the overflow in liquid liquid hydrocyclones translates to poor separation.

## **5.5 Summary of Chapter**

The effect of changing the size of hydrocyclone geometrical parts (spigot, length of vortex finder and cylindrical part) on the fluid flow was reviewed. A comparison of the fluid flow in the liquid-liquid and solid-liquid hydrocyclone was also analysed. The geometrical parameters reviewed are the spigot diameters of 7.5mm, 12.5mm and 17.5mm ; vortex finders of 0mm, 10mm, 25mm and 50mm, and 35mm, 50mm and 75mm cylindrical diameters.

The results analysis revealed that the 75mm cylindrical diameter performs better than the 35mm and 50mm while the 25mm vortex finder and 12.5mm spigot section equally produce better results than other geometrical parameters analysed.

The hydrocyclone geometry used for the simulation was also seen to perform better for the solid-liquid separation than liquid-liquid separation. Most of the fluid flow analysed showed similar results for the solid-liquid and liquid liquid hydrocyclone with the exception of axial velocity and turbulence kinetic energy.

## 6.0 Use of Microparticles and a magnetically induced hydrocyclone in the separation of fine-dispersed oil emulsion

The hydrocyclone operates based on the principle of centrifugal force, the fluid enters into the cyclone tangentially via the inlet into the cylindrical section generating a swirl flow which create the centrifugal force needed to separate the solid particles from produced water by moving particles denser than produced water to the wall of the cyclone and the less dense particles to the centre core region of the cyclone. The denser particles move to the wall of the cyclone and are discharged via the underflow/spigot section while the lighter particles at the core region of the cyclone are discharged via the overflow/vortex finder; the hydrocyclone has two outlets, the spigot/underflow and the overflow/vortex finder.

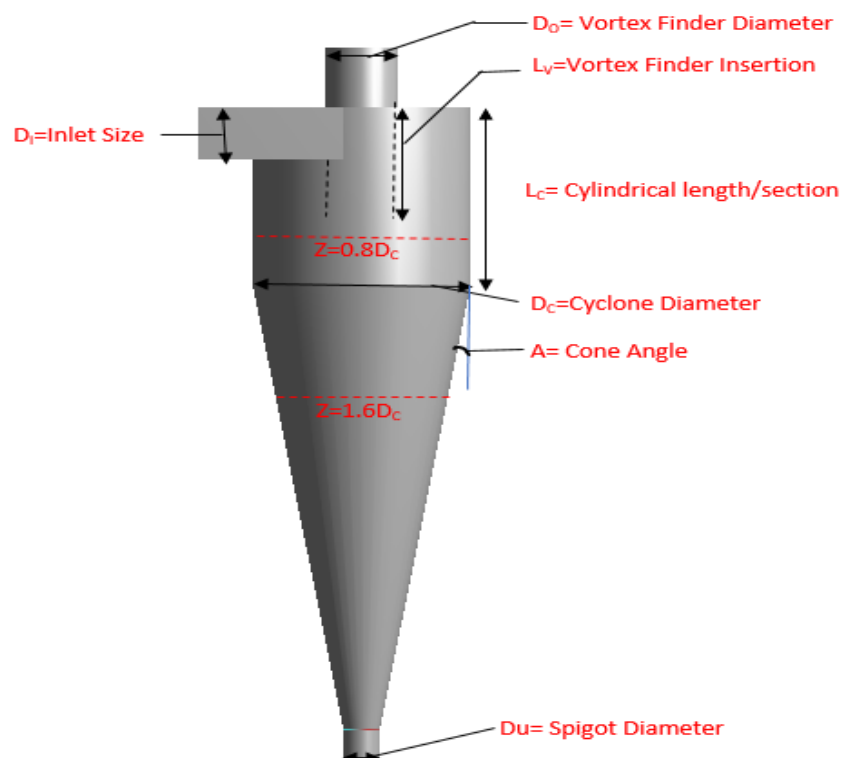


Figure 6-1: Hydrocyclone geometrical parts

The cyclone can be used to separate particles greater than  $10\mu\text{m}$  (Junxiang 2019; Endres,2012; Mokhatab, 2012), however the separation efficiency is greatly reduced when the particle size is less than  $10\mu\text{m}$ . This chapter reviews an innovative way of improving the separation efficiency of oil particles less than  $10\mu\text{m}$  using a hydrocyclone by incorporating microparticles into the oil-water emulsion and inducing magnetism into the hydrocyclone.

The geometry used in evaluating the effect of microparticles and induced magnetism in a hydrocyclone is shown in table 6-1 below

**Table 6-1: Hydrocyclone Geometry**

Parameter	Symbol	Size
Diameter of the cyclone body	Dc	75mm
Size of Inlet	Di	22.16mm x 22.16mm
Diameter of the vortex finder	Do	25mm
Insertion depth of the vortex finder	Lv	50mm
Length of the cylindrical part	Lc	75mm
Cone Angle	A	$20^\circ$
Diameter of the spigot	Du	12.5mm

This chapter reports on the:

- Effect of the use of magnetic particles for oil-water separation in the hydrocyclone
- Introduction of a magnetic field into a micro-doped hydrocyclone (hydrocyclone fed with a polymer-coated magnetic particle with oil doping) and how this affects hydrocyclone efficiency.
- Effect of micro-particle density on oil emulsion separation efficiency in a hydrocyclone
- Influence of microparticle charge density on magnetic hydrocyclone separation
- Effect of micro-particle permeability on magnetic hydrocyclone oil-water separation efficiency.

## **6.1 Solution Technique**

A pressure-based, time-dependent transient solver was used for the calculation of absolute velocity formulation. Gravity was also applied to account for the effect of the gravitational force. To model the turbulence in the hydrocyclone, the Reynolds stress model (RSM) was used. While the discrete phase (oil) was introduced into the continuous phase (water) using the discrete phase model (DPM).

### **6.1.1 RSM Model**

The turbulence was modelled using the Reynold stress model (RSM) with linear pressure strain. In engineering, the wall quantities (velocity gradient, pressure, etc) are very important because flow separation and reattachment are strongly dependent on the correct prediction of the development of turbulence near the wall. In order to accurately predict this near-wall turbulence, the standard wall function was used.

As a result of the high degree of coupling required between the momentum equation and the turbulence stresses in the RSM model, the convergence was deemed achieved when the residual values reach  $10^{-3}$ .

### **6.1.2 Discrete Phase Model**

The discrete phase was enabled and made to interact with the continuous phase to ensure an accurate prediction of the particle movement in the fluid. The particles were treated as steady-state particles.

Diesel was used as the oil particle and injected into the system with the fluid using surface injection via the inlet. Spherical drag law was enabled as the particles were assumed to be spherical in shape. The particle loading, flowrate, and diameter were specified; particle flowrate was considered the same as the produced water (continuous phase) flowrate.

### **6.1.3 Magnetohydrodynamic Model (MhD)**

MHD was enabled in order to induce magnetism into the hydrocyclone carrying micro-doped particles. The magnetic field strength was specified and the MHD



equation was solved with Lorentz force for the analysis. The solution was initialized prior to the running of the simulations

The approach used by Watson (Shen, 1989) was used for the current study where the magnet is placed outside the hydrocyclone for separation to take place. A magnetic strength of 1 Tesla was introduced into the system, 1 Tesla was used because the hydrocyclone is a high intensity (turbulence) device and therefore will require a high intensity magnetic field to penetrate and cause separation, also because the conventional magnetic separator is limited to a magnetic field strength of about 20000 gauss/ 2Tesla (Bannester, 1970); studies of magnetic field strength in magnetic hydrocyclone separation have shown that a strength of magnetic of not more than 2 Tesla has been used (Siadaty, 2017; Premaratne, 2003; Meireles, 2015).

#### **6.1.4 Boundary Conditions and Solution methods**

The vortex finder (overflow) and spigot (underflow) of the cyclone were exposed to the atmosphere, therefore, the gauge pressure was set to 0 atm. The boundary conditions used for the simulations were as follows:

Inlet Section - Velocity Inlet

Outlet Sections- Outlet Vent

Wall - Stationary wall motion, no-slip shear condition, and wall roughness was set at a roughness coefficient of 0.5mm.

To reduce computational time and achieve good results, the hexahedral structured mesh was used. The discretization of continuity and momentum equations for the simulation was solved using a pressure-based solver. The pressure-velocity was coupled using SIMPLE, spatial discretization evaluated using Least Square Cell-Based; pressure, momentum, turbulence kinetic energy, turbulence dissipation rate, and magnetic field in the x,y and z directions all discretized using Quick while the time step used for the simulation was 0.0001 s.

## 6.1.5 Operating Conditions

The oil in water stream fed into a hydrocyclone is typically not more than 5000ppm (Durdevic P, 2018; SAWEA, 2005; Motin, 2015; Veolia, 2019, Eprocess, 2019) this is equivalent to about 0.5% concentration. It is expected that this will be reduced to about 10-40ppm downstream of the hydrocyclone, depending on the regulatory requirement of the area where it is to be disposed.

The mass flowrate of oil particles considered for evaluation were of 0.0007 kg/s, 0.07 kg/s and 0.7 kg/s. With the inlet area of 0.0005527m<sup>2</sup>, inlet velocity of 2.5m/s (for both the continuous and discrete phase). The oil density used was 780 kg/m<sup>3</sup> while the water density used was 1000 kg/m<sup>3</sup>. The equivalent concentration of flowrate was calculated to be 0.00065%, 0.065%, and 0.65%.

The ferromagnetic material used was assumed to have the properties below (Walid, 2017; Zhdanov, 2015; Vella. 2012)

Density 5175kg/m<sup>3</sup>

Magnetic permeability 1.5 h/m

Electrical conductivity 10000 S/m

Charge density 7.02c/m<sup>3</sup>

In the context of this work, conductivity means the ability of the material to conduct current/ charge while permeability is the magnetization capability. Permeability supports the formation of the magnetic field.

The micro-doped oil mass flowrate was assumed to be the same as the undoped oil mass flowrate given above for the evaluation. Since ferromagnetic material has a higher density than oil; the density of ferromagnetic material was assumed to take precedence over oil density in the separation process. The effect of the quantity/ density of ferromagnetic properties is reviewed in the subsequent section. Individual oil droplet sizes were considered, and the ferromagnetic particle was assumed to cover individual oil particles after gentle agitation of the polymer-coated magnetic particle with produced water.

## **Result and Discussion of Results**

### **6.2 *Effect of Magnetic Particle on Oil-Water Separation Efficiency and Velocity Profile***

Doping of the oil emulsion with polymer-coated magnetic particles increases the density of the oil in water therefore an assumption that the oil particles become denser than water was made. This will result in the separation of the oil particles through the spigot section as against the conventional hydrocyclone (conventional hydrocyclone is referring to a hydrocyclone with no magnetic particle or magnetic induction) where separated oil is discharged through the vortex finder.

The results in this section depict the effect of adding microparticles to the oil-water emulsion, and subsequent introduction of an induced magnetic field into the cyclone. A comparison of these two cases was reviewed against the performance of a conventional hydrocyclone. The effects of the use of microparticles and inducing a magnetic field into the micro-doped oil on hydrocyclone efficiency and pressure drop were analysed while looking at the fluid mechanics of the process.

#### **6.2.1 Efficiency**

The electrostatic attraction force bonds the positively charged polymer-coated Magnetic Particles (MP) with negatively charged oil in produced water and controls the attachment of the oil to the Magnetic Particle. The subsequent aggregation of electrically neutral micro-oil droplets plays a significant role in efficient magnetic separation (Saebom Ko, 2016). Figure 6-1 assessed the effect of the magnetic particle on oil-emulsion separation and how the introduction of the magnetic field affects the separation process.

It can be seen that the addition of magnetic particles favours the separation process most especially the smaller droplets rather than the bigger droplets. For the flowrate reviewed ( $0.0007\text{kg/m}^3$ ,  $0.07\text{kg/m}^3$  and  $0.7\text{ kg/m}^3$ ), both the Micro-doped hydrocyclone (hydrocyclone with polymer-coated magnetic particle doped with oil) and the magnetic hydrocyclone (hydrocyclone with micro-doped oil plus magnetic induction) improve the separation of particles by up to 30% or more when compared with the conventional hydrocyclone (hydrocyclone without

microparticles or magnetic induction) for very fine particles, that is a particle size ranging from 0-30 $\mu\text{m}$  depending on the mass flowrate/ concentration.

The magnetic hydrocyclone shows greater separation efficiency than a Micro-doped hydrocyclone for a particle size less than 10 $\mu\text{m}$  in all the cases reviewed. As the mass flowrate increases the effect of the magnetic hydrocyclone on the separation efficiency of small particles decreases when compared to the micro-doped hydrocyclone. Therefore, it can be seen that the magnetic hydrocyclone has greater efficiency on the particle size of up to 15 $\mu\text{m}$  than the micro-doped hydrocyclone when the mass flowrate was 0.0007kg/s. Magnetic hydrocyclone efficiency only outperforms the micro-doped hydrocyclone when the particle size is less than or equal to 10 $\mu\text{m}$  at a mass flowrate of 0.07kg/s.

Further increase of the mass flowrate to 0.7kg/s decreases the particle size at which magnetic hydrocyclone efficiency can outperform micro-doped hydrocyclone to less than 10 $\mu\text{m}$ . This is similar to the finding of Saebom (2016) where the smaller particles are greatly affected by the magnetic field when compared with the larger particles. This also shows that the influence of the magnetic hydrocyclone on separation efficiency is dependent on the particle size and concentration/ particle loading.

When the particle size was greater than 10 $\mu\text{m}$  but less than 30 $\mu\text{m}$ , the micro-doped hydrocyclone was seen to outperform the magnetic hydrocyclone with both hydrocyclones (micro-doped and magnetic) having higher efficiency when compared to the conventional hydrocyclone. This can be attributed to the external magnetic field strength and the magnetic field gradient (Svoboda, 2005). However, because it was assumed that the same magnetic materials were used, the magnetic field gradient will be similar or almost the same. Therefore, this makes the effect of the magnetic force on smaller particles (<10 $\mu\text{m}$ ) and higher concentration the most liable cause of the change in the separation seen in the micro-doped hydrocyclone and magnetic hydrocyclones (Sambom, 2015).

The result also shows that the density differential has a more significant effect on the improvement seen in the separation efficiency than the induced magnetism with a micro-doped hydrocyclone having a similar separation efficiency for smaller

particles and outrightly outperforming the magnetic hydrocyclone for larger particles (particles larger than  $10\mu\text{m}$ ).

Boosting the density of oil in water with the introduction of MPs is therefore considered a major contributor to the improved separation of oil from water in this hydrocyclone analysis. This is in accordance with the findings of Svarosky (2000) and Medronho's (1998) design analysis and calculations where the hydrocyclone separation efficiency factor is directly proportional to the density differential between the particles and water and inversely proportional to the particle size.

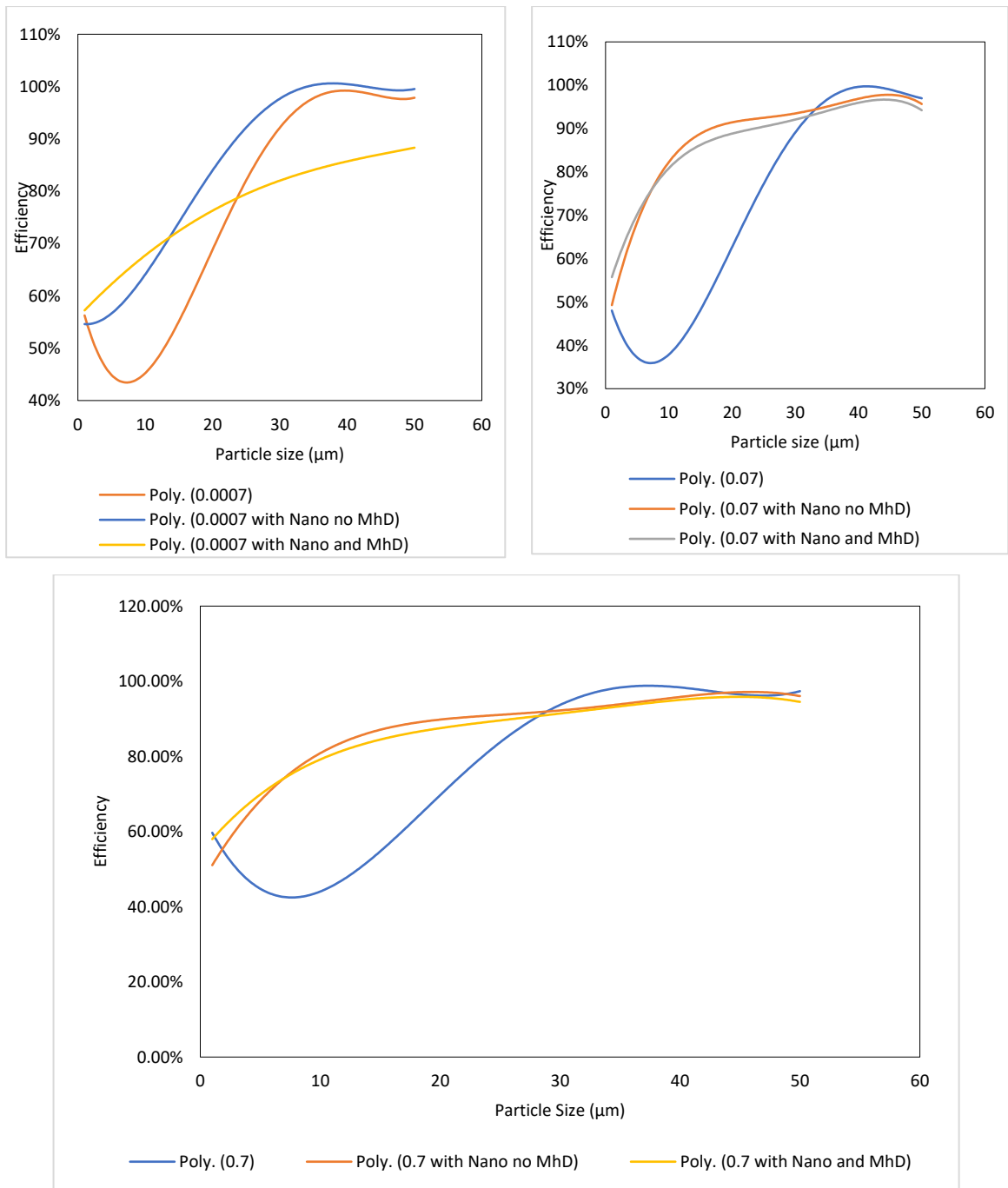
## **6.2.2 Pressure Drop**

The pressure inside the cyclone drops as a result of the friction in the cyclone body (Kharoua, 2011). Some of the factors responsible for this are density differential, particle size, and cyclone geometry (Stewart 2009). With the use of the same geometry and particle size in the simulations, the contribution of the density difference is expected to take dominance in the simulation.

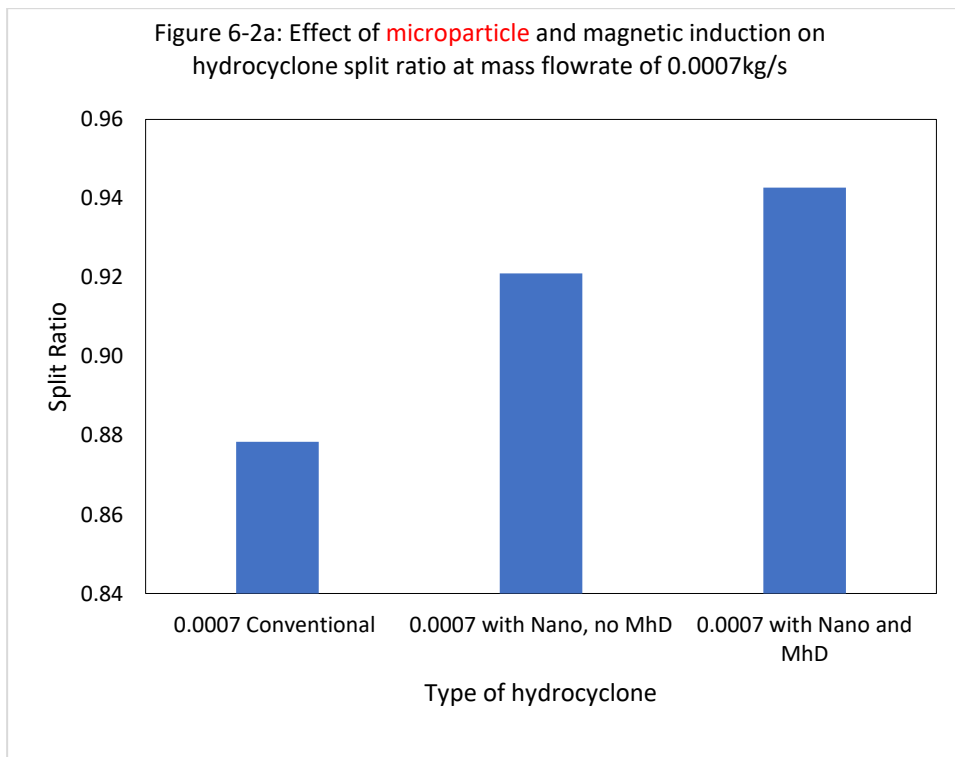
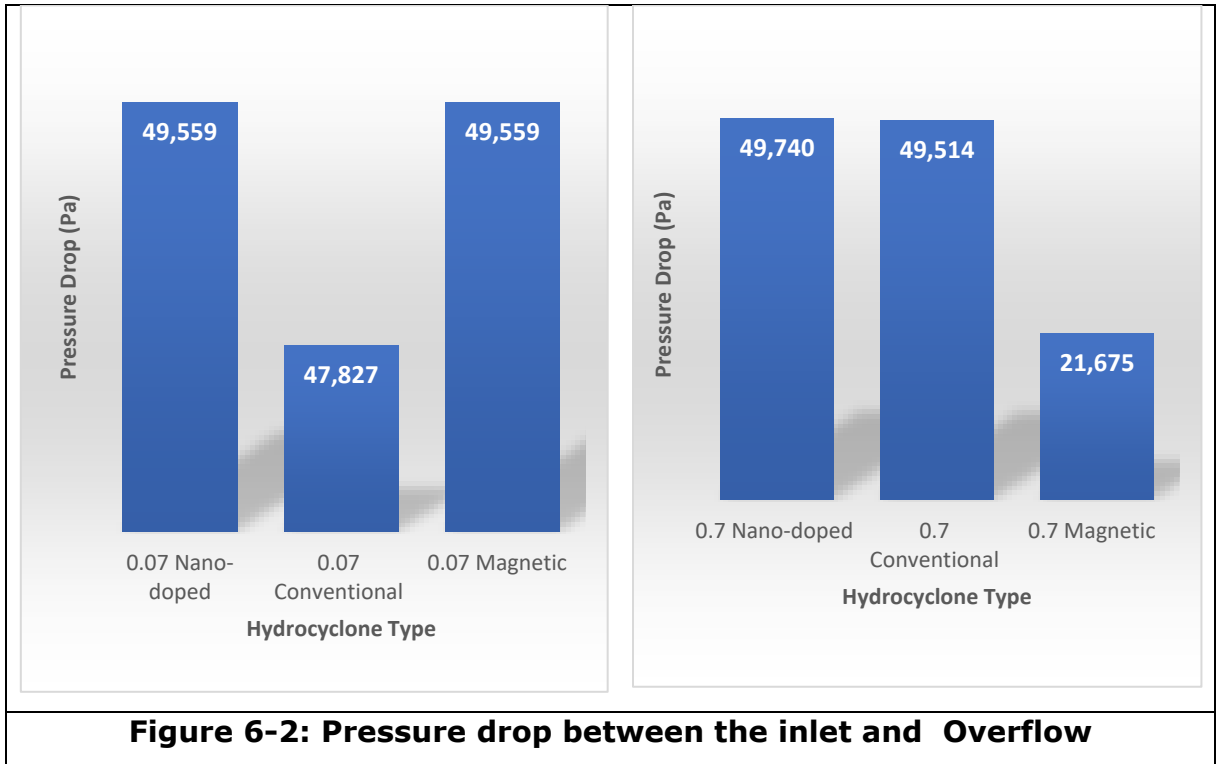
The result shows that in both conventional and micro-doped hydrocyclones, an increase in particle concentration increases pressure drop. Also increasing the particle density from  $780\text{kg/m}^3$  to  $5175\text{kg/m}^3$  increases the pressure drop (Kharoua, 2011; Stewart 2009) in conventional and micro-doped hydrocyclones for all the mass flowrates considered in figure 6-2 above (figure 6-2 is the pressure drop between the inlet and overflow). However, in the magnetic hydrocyclone, the reverse was the case as the pressure drop decreases with an increasing flowrate (Bhuyan, 2008).

A comparison of micro-doped and magnetic hydrocyclones show that at a lower mass flowrate, the pressure drop was almost the same but a huge disparity was seen in higher concentrations. This is because the motion of microparticles in the magnetic field generates a current. The interaction of this current with the imposed magnetic field produces a Lorentz force affecting the motion (Bhuyan, 2008); this force modifies the velocity and opposes the MHD pressure drop. With increasing concentration, more particles will be at the wall of the cyclone resulting in a decrease in pressure caused by the reduction of hydrocyclone wall conductivity. The wall conductivity reduces because of blockage imposed on the wall as a result

of particle deposition; since eddy current due to the motion of magnetic particles closes their current at the wall.



**Figure 6-1a: Effect of Use of MicroParticles and Induction of Magnetic field on Deoiling Hydrocyclone efficiency**



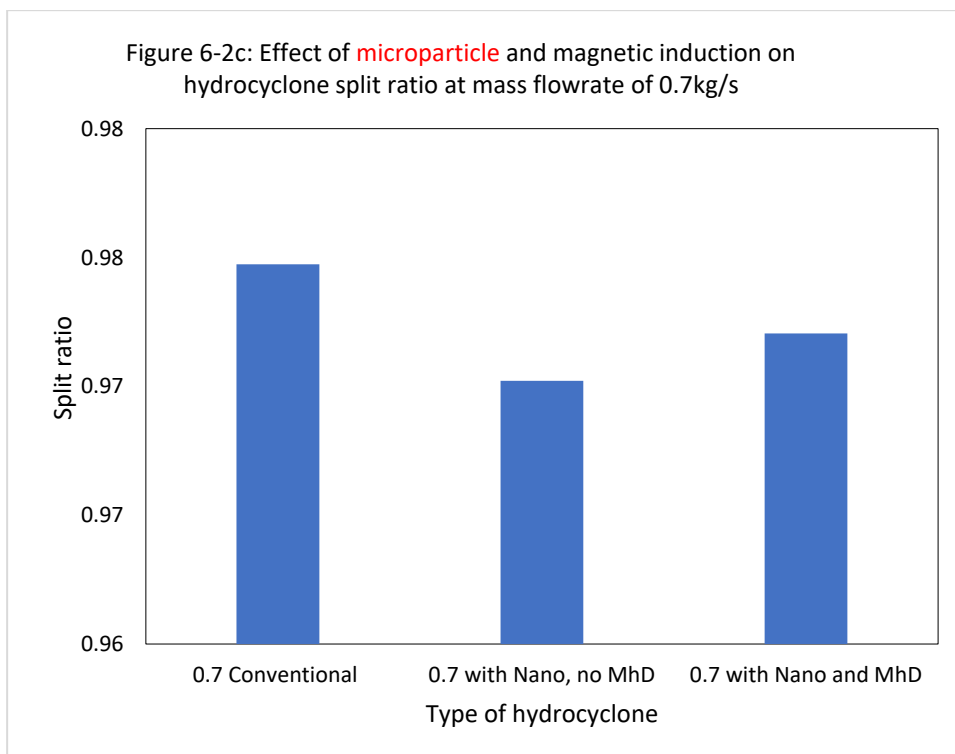
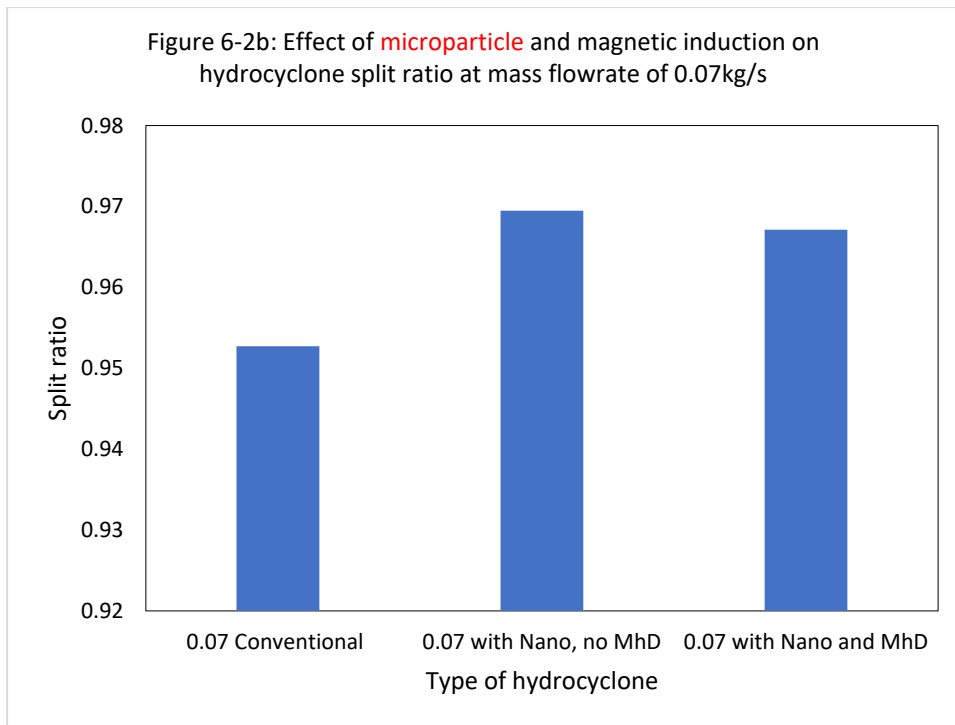
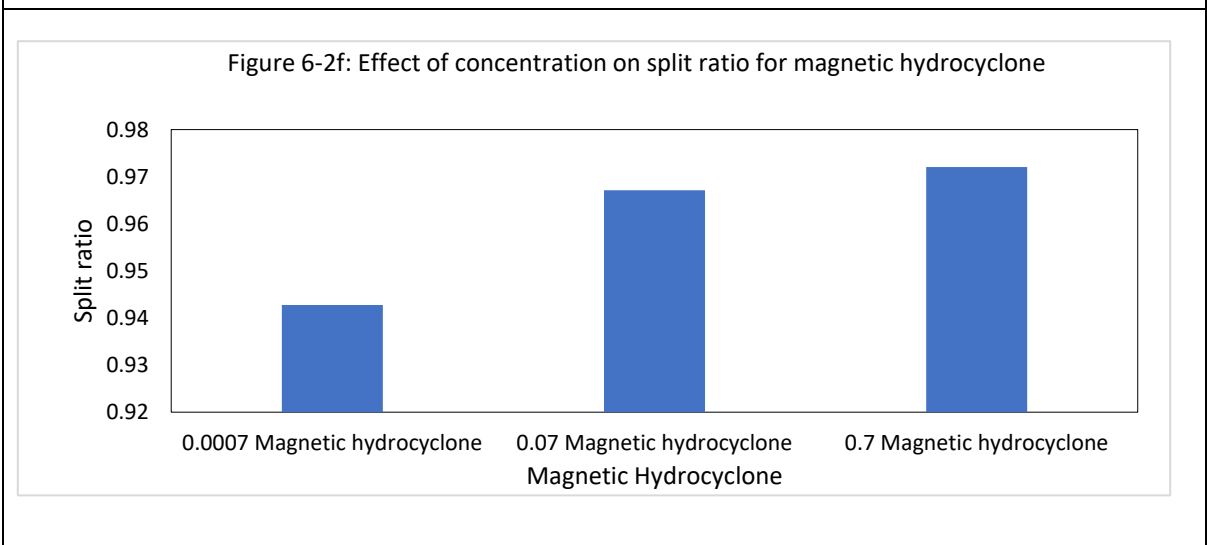
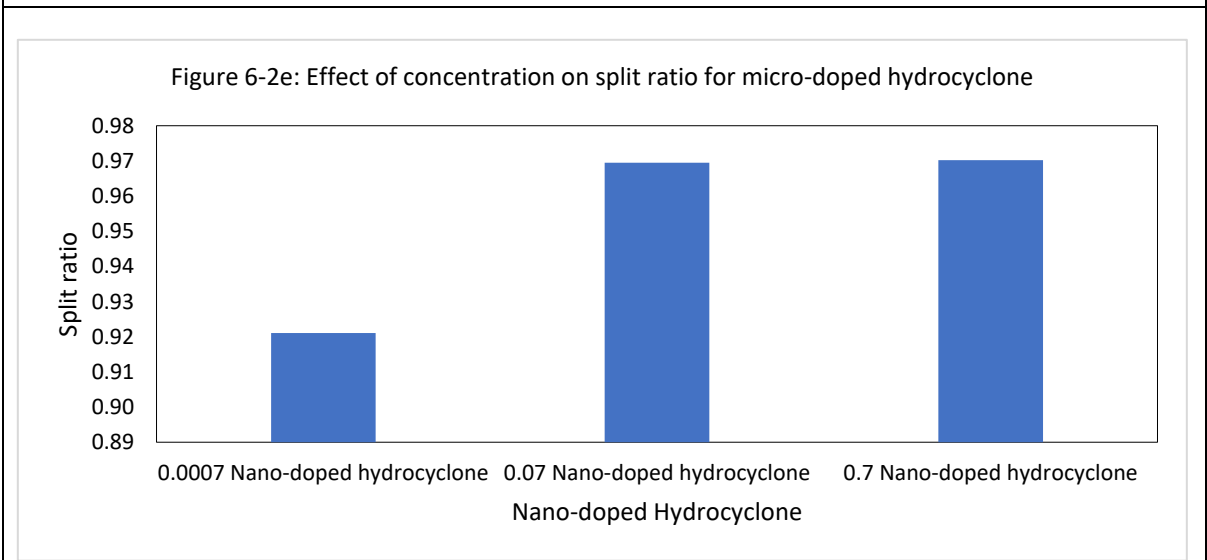
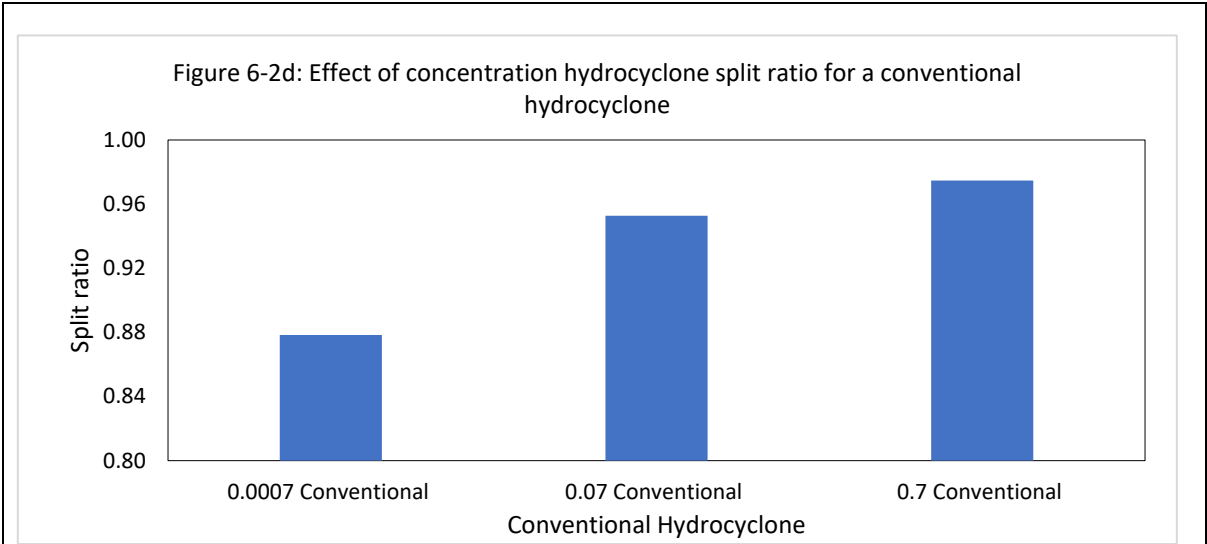


**Figure 6-2a to c: Effect of microparticle and magnetic induction on hydrocyclone split ratio at different mass flowrate**





### 6.2.3

### Split Ratio

Figure 6-2a to 6-2c compared the split ratio of the conventional, micro-doped and magnetic hydrocyclone at different concentrations. The split ratio was calculated with respect to the mass flowrate of the underflow section to the mass flowrate of the inlet flowrate

$$\text{Split ratio} = \frac{U_{\text{underflow}}}{U_{\text{inlet}}}$$

The result shows that the concentration increases from conventional to magnetic hydrocyclone at mass loading of 0.0007kg/s. In mass loading of 0.07kg/s, the conventional hydrocyclone has the lowest split ratio while the micro-doped hydrocyclone has the highest. While in the 0.7kg/s, the conventional hydrocyclone has the highest split ratio while the magnetic hydrocyclone has the lowest split ratio.

According to Yuan (2015) and Jian-Feng (2016), the separation efficiency of a hydrocyclone increases with an increase in split ratio. Although the magnetic hydrocyclone has the lowest overall efficiency in 0.0007kg/s mass loading, with separation efficiency of particles above 30 $\mu\text{m}$  lower than both the conventional and micro-doped hydrocyclone; the split ratio was higher. This shows that comparison of the split ratio of the conventional, micro-doped and magnetic hydrocyclone cannot be related to the separation efficiency. This can be ascribed to the mode of separation of the conventional liquid-liquid hydrocyclone where oil is discharged via the overflow, therefore the split ratio is expected to be lower. However, in the magnetic and micro-doped hydrocyclone, the particles are discharged in the underflow section of the cyclone, therefore the split ratio of the conventional hydrocyclone is expected to be lower than the magnetic and micro-doped hydrocyclone.

Figure 6-2d to figure 6-2f are the graphs of the effect of concentration on conventional, micro-doped and magnetic hydrocyclones. The three types of hydrocyclone show that an increase in concentration increases the split ratio; according to previous work (Jiang, 2018), at low inlet velocity, increasing the feed concentration increases the split ratio. It can also be seen that the rate of the feed mass loading affects the split ratio which is higher in the conventional hydrocyclone

with an increment of about 10% from the split ratio of 0.0007kg/s mass loading to a split ratio of 0.7kg/s mass loading. While in the micro-doped and magnetic hydrocyclone the rate of increase from 0.0007kg/s to 0.7kg/s was 5% and 3% respectively.

#### **6.2.4 Tangential Velocity**

The strength of the primary separating force in a hydrocyclone (centrifugal force) is determined by tangential velocity. The higher the tangential velocity, the higher the centrifugal force. Tangential velocity is equally an important factor in evaluating the classification and separation performance of the conventional hydrocyclone. Most of the factors used to improve the separation performance of hydrocyclone influence the tangential velocity (inlet flowrate/ velocity, geometrical factor-like inlet size, cylindrical size, cone angle, spigot size among others) with increasing tangential velocity leading to better separation performance.

Figure 6-3a shows that increasing the mass flowrate of the particle changes the way the magnetic field influences the separation of particles in the magnetic hydrocyclone. When the concentration was low i.e. at a mass flowrate of 0.0007 kg/s, the conventional hydrocyclone was seen to have a low tangential velocity profile compared with the micro-doped and magnetic hydrocyclone. This reflects that the influence of the density differential on the tangential velocity is more pronounced at a very low mass flowrate when compared to higher mass flowrates. At the same mass flowrate of 0.0007kg/s, the tangential velocity of the magnetic hydrocyclone was seen to be higher than that of the micro-doped hydrocyclone. This can be attributed to the influence of the strength of the magnetic field strength on microparticles at a lower mass flowrate. Higher magnetic field strength is felt at lower concentrations.

At higher concentrations with mass flowrates of 0.07 kg/s and 0.7 kg/s, the tangential velocity profile of the micro-doped and magnetic hydrocyclones were almost the same. Showing that the magnetic field strength does not have a significant effect on particle movement and therefore little effect on the tangential velocity as the concentration of the microparticles increases. This can be credited to increasing the particle aggregation as the mass flowrate of the microparticle increases (Rosicka, 2013). The aggregation occurs as a result of increase in the

force between particle-particle due to the close proximity of the particles. Increasing aggregation decreases the rate of magnetic field intensity penetrating into the aggregated particles leading to reduction in the movement of particles to the wall of the cyclone and therefore reduced tangential velocity which can lead to a lower pressure drop.

Figure 6-3b is the contour plot for the tangential velocity of the three types of hydrocyclone under review (conventional hydrocyclone, micro-doped hydrocyclone, and magnetic hydrocyclone) at mass flowrates of 0.0007kg/s, 0.07kg/s, and 0.7kg/s.

For the three types of hydrocyclone under review at different concentrations, all the tangential velocities are similarly shaped with the tangential velocity increasing with decreasing radius from the wall. All the tangential velocity contour plots show the characteristic of Rankine flow with forced vortex at the centre of the cyclone and free vortex towards the wall of the cyclone.

Increasing the concentration of the cyclone affects the tangential velocity of the cyclones in various ways. From the contour plot, it can be seen that increasing the concentration of the micro-doped hydrocyclone increases the tangential velocity. In a conventional hydrocyclone, the tangential velocity is affected by very low concentration (mass flowrate). However, as the mass flowrate increases, changes in the tangential velocity become insignificant (Bai, 2008).

The magnetic hydrocyclone behaves differently from the other two types of hydrocyclones. An increase in mass flowrate from 0.0007 kg/s to 0.07 kg/s was seen to increase the spread of high velocity around the core area and a further increase in mass flowrate from 0.07 kg/s to 0.7 kg/s increases the intensity along the core area of the cyclone.

This indicates that higher speed is required to move fluid along the core and less time is required for separation as the mass flowrate increases in the magnetic hydrocyclone.

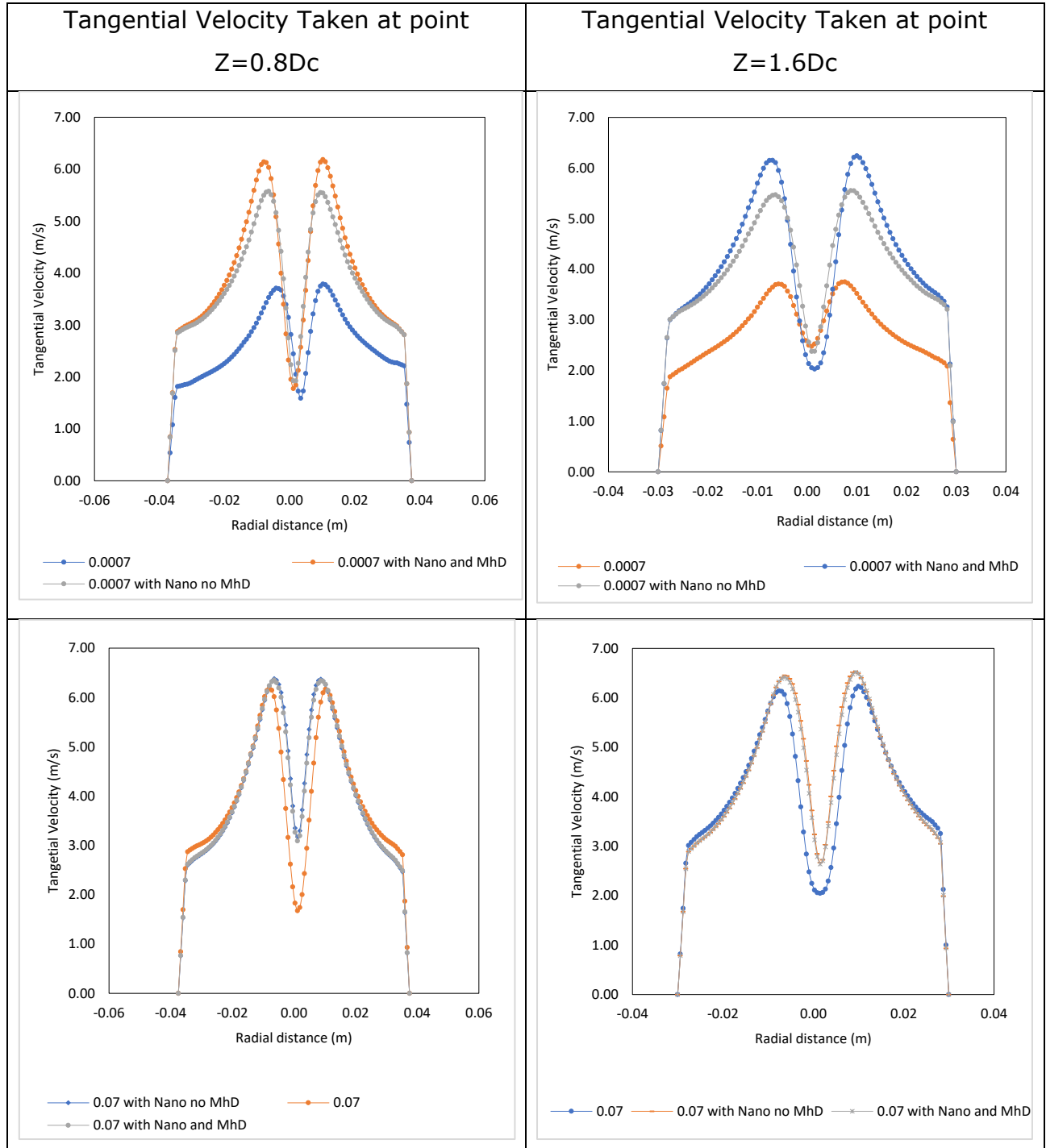
From basic physics, tangential velocity ( $V_{\theta}$ ) is given by equation 6a below

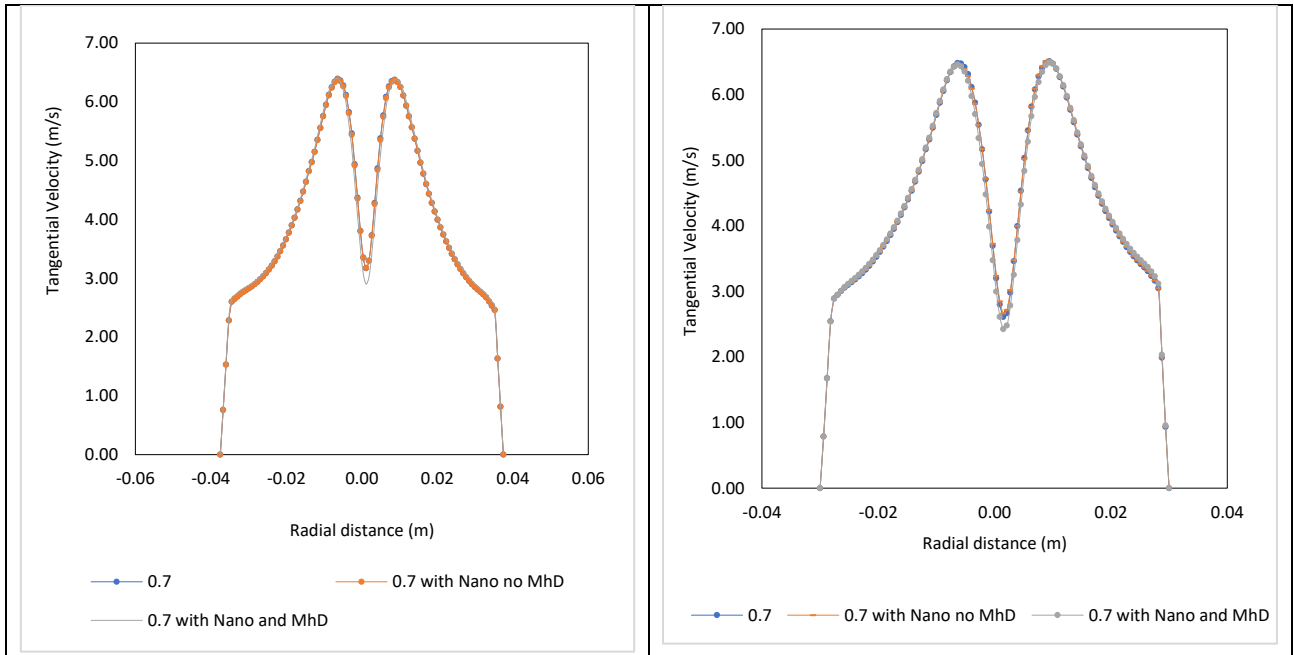
$$V_{\theta} = \omega r$$

6-a

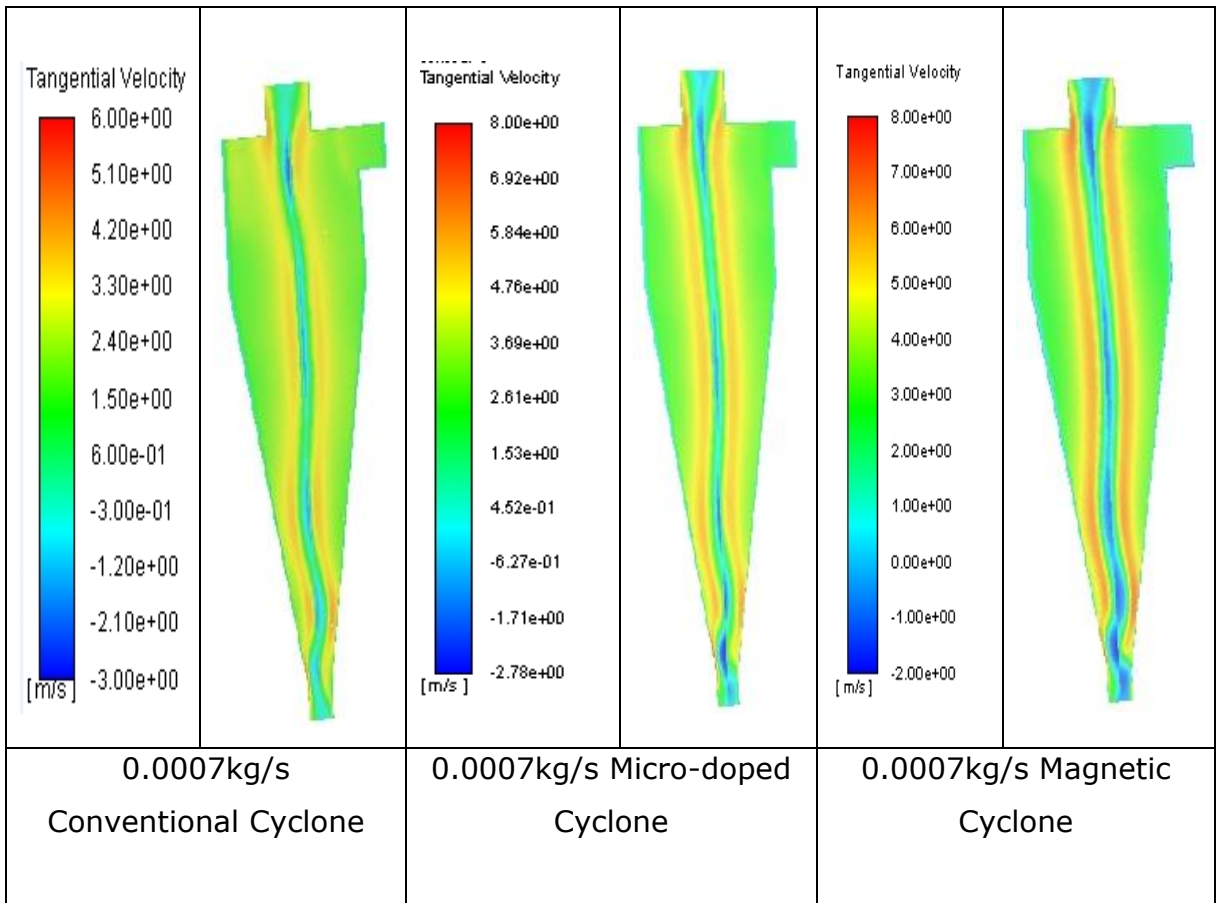
$$\text{where } \omega = \frac{2\pi}{T}$$

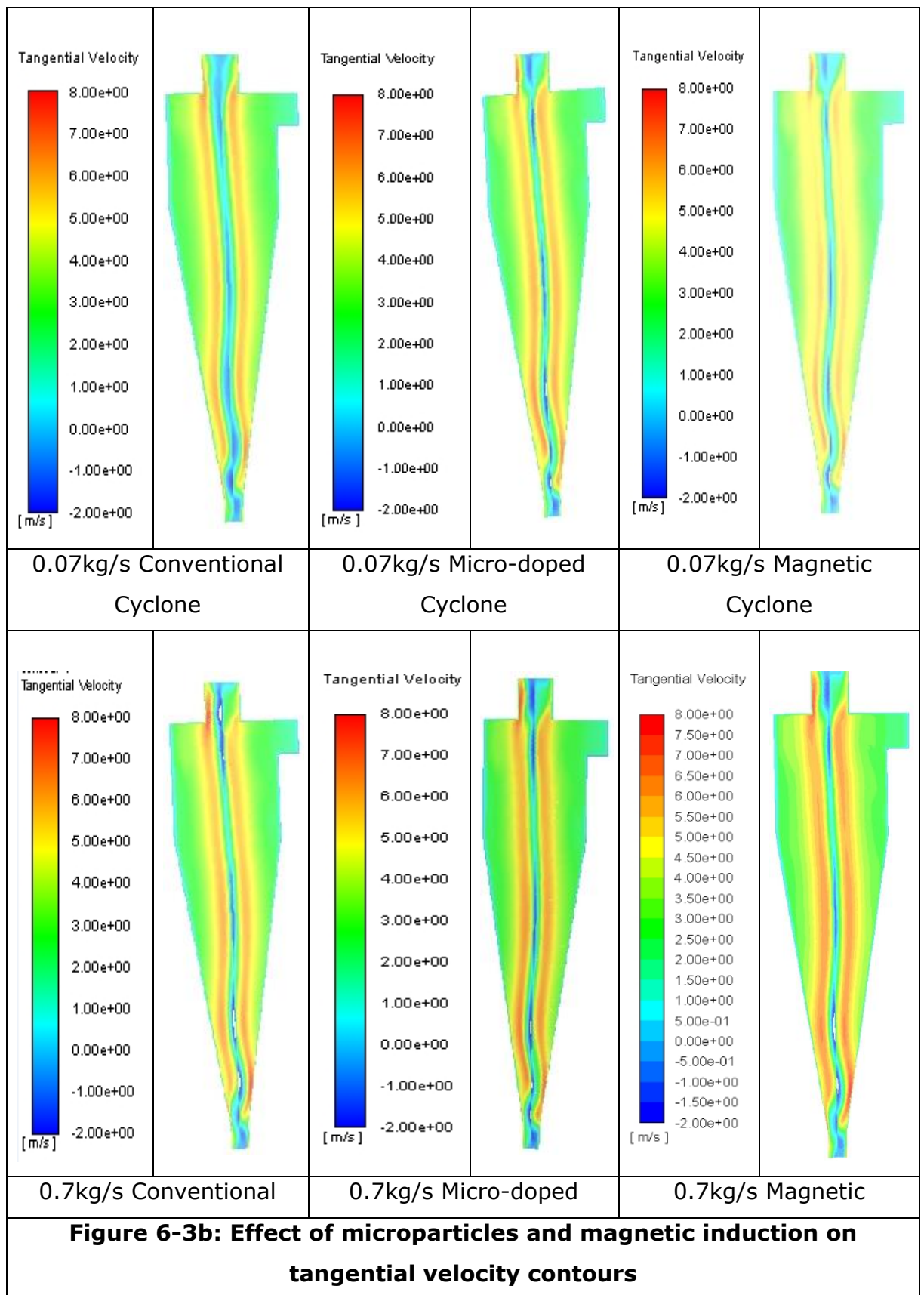
$\omega$  is the angular velocity while T is the period





**Figure 6-3a: Effect of microparticles and magnetic induction on the tangential velocity of hydrocyclone**





## 6.2.4

### Axial Velocity

The axial velocity determines the separation zone or space, it is of two parts and acts towards the longitudinal axis of the hydrocyclone with directions opposite to each other. It is an important part of the cyclone flow field as it also determines the residence time (total time from entry to exit of the fluid) and the split ratio. The axial velocity has two types of flow movement, the outer flow which moves high-density fluid to the underflow and the inner flow which moves lower density fluid to overflow (Siadaty, 2017).

The axial velocities were taken in the cylindrical section at  $Z=0.8D_c$  (above the vortex finder in the cyclone) and in the conical section at  $Z=1.6D_c$  (below the vortex finder in the cyclone). Figure 6-3ci and 6-3civ show that at a low concentration of  $0.0007\text{kg/s}$ , the axial velocity of the conventional hydrocyclone is higher than the axial velocity on the magnetic and the micro-doped hydrocyclone, indicating that the particle-laden fluid in the conventional hydrocyclone will have a higher residence time in the conventional hydrocyclone (Jiang, 2019) than in the magnetic and micro-doped hydrocyclones. The shape of the magnetic hydrocyclone in the conical section at a mass flowrate of  $0.0007\text{kg/s}$  also indicates that there is a short circuiting /revolution of flow in the cyclone (Lee, 2006). This can be associated with the magnetic force induced into the cyclone causing attraction of the magnetic-doped oil to the wall of the cyclone thus magnetic force reducing the swirl movement.

At increasing mass flowrate, the axial velocity of the conventional hydrocyclone was seen to decrease in the cylindrical and conical sections of the hydrocyclone. However, when compared with the micro-doped hydrocyclone and magnetic hydrocyclone, the conventional hydrocyclone has a higher axial velocity than the magnetic and micro-doped hydrocyclone at  $0.0007\text{kg/s}$  and higher than magnetic hydrocyclone at  $0.7\text{kg/s}$  while having approximately the same value as the micro-doped hydrocyclone. However, at  $0.07\text{kg/s}$ , the micro-doped and magnetic hydrocyclones have approximately the same value.

Increasing the mass flowrate from  $0.0007\text{kg/s}$  to  $0.07\text{kg/s}$ , the magnetic and micro-doped hydrocyclones have approximately the same axial velocity, indicating the fluid flow in both cyclones have the same residence time. In all of figures 6-



3c, the axial velocity of the micro-doped hydrocyclone is larger than that of the magnetic and conventional hydrocyclones or of approximate size indicating an overall better performance of the micro-doped cyclone.

### **Axial Contour Plots**

The effect of the concentration is more pronounced in the axial velocity as can be seen from figure 6-3d in that the locus of zero vertical velocity, LZVV (A) becomes more pronounced with increasing concentration in all the hydrocyclones. This shows that the maximum concentration is not at the wall of the hydrocyclone but rather near the LZVV lines of the particles (Dai, 1999). According to equilibrium orbit theory, particles outside the LZVV go to the underflow while particles inside the LZVV report to the overflow (Kelsell, 1952). A particle on this LZVV has zero velocity, therefore, has a 50% chance of moving either to the overflow or underflow section of the cyclone. In other words, LZVV is not an absolute boundary for solids or separation (Dai, 1999).

The magnetic hydrocyclone LZVV is more pronounced than that of conventional and micro-doped hydrocyclones, indicating that the induced magnetism has an effect on the concentration of the hydrocyclone.

### **6.2.6 Radial Velocity**

The radial velocity reflects the motion of the fluid along the radial direction. For particles to separate in cyclones, radial displacement must occur; figure 6-3e shows that radial velocity increases along the radial length, and near the wall becomes zero due to the need for the total flow to pass through the smaller area as it leaves the cyclone. The negative value in radial velocity denotes inward radial velocity, this denotes the passage of fluid through to the vortex finder which then becomes zero. The positive value is due to centrifugal force, (Wang B, et al, 2007).

Figure 6-3ci-iii: Axial Velocity Taken at point Z=0.8Dc

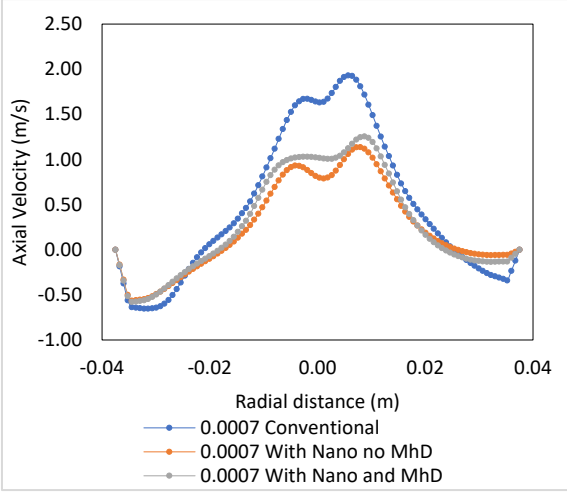
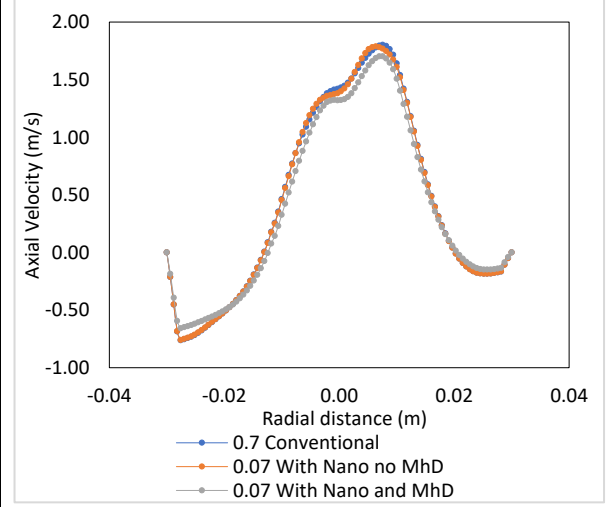
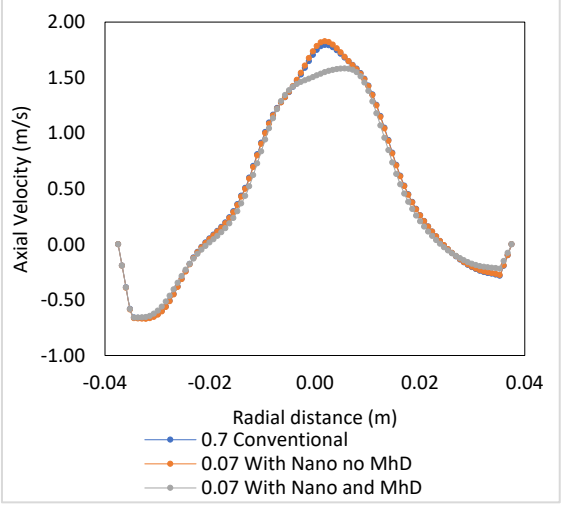
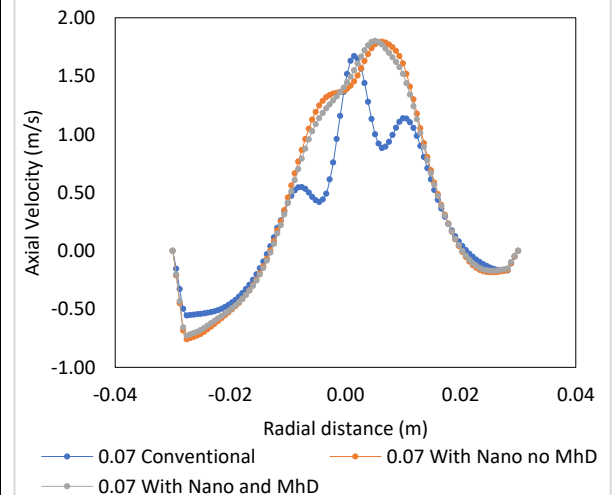
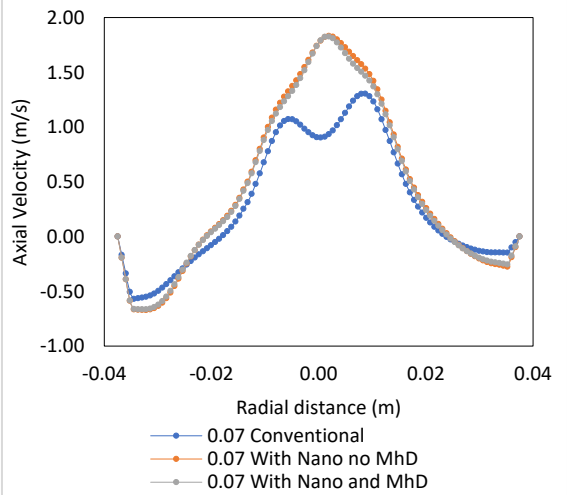
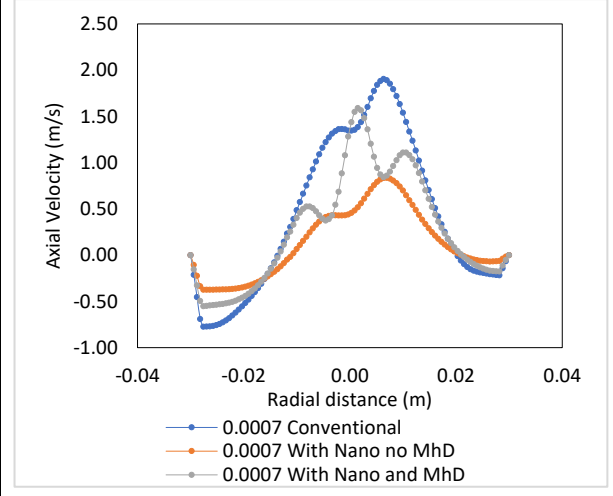
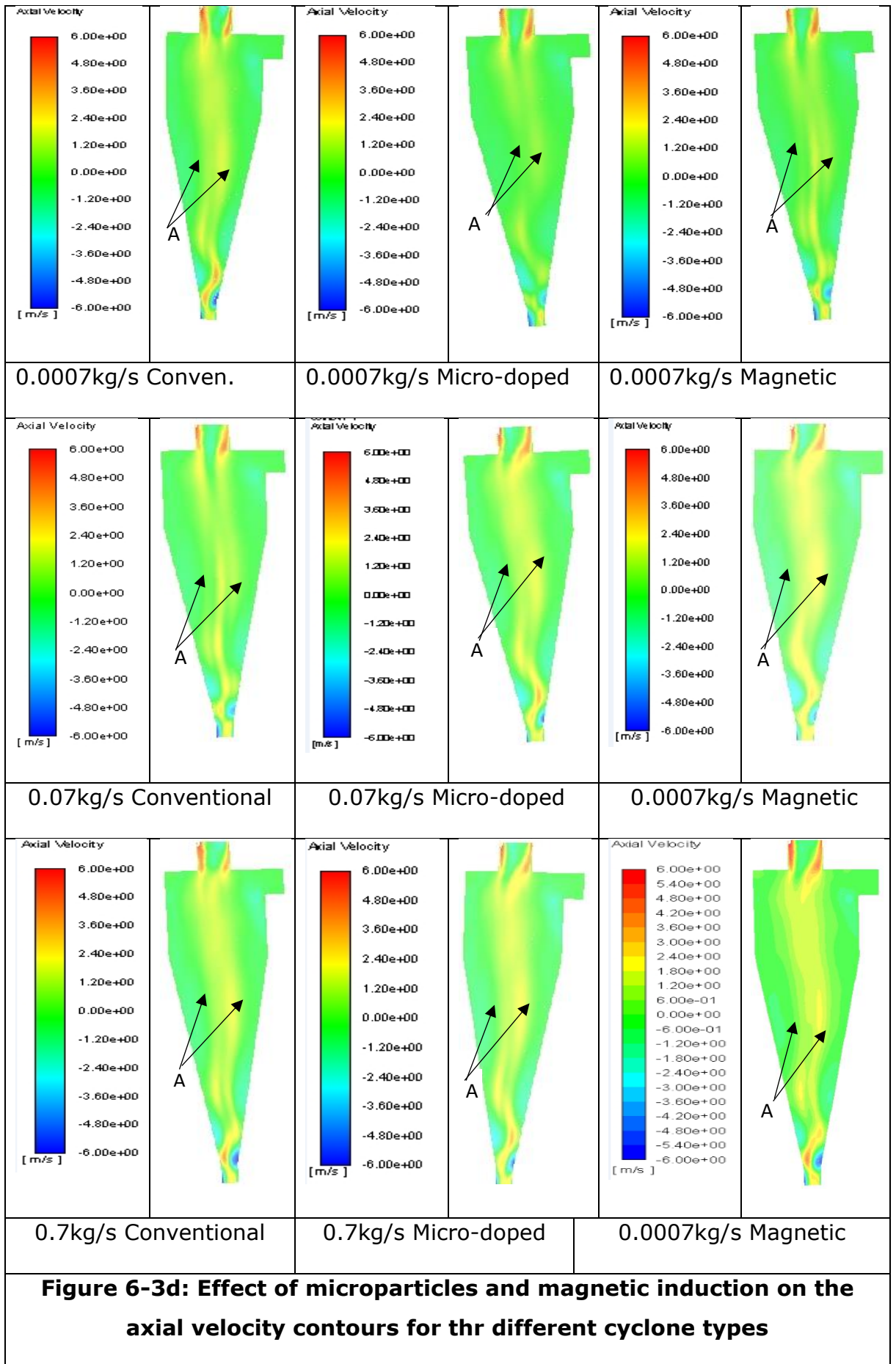
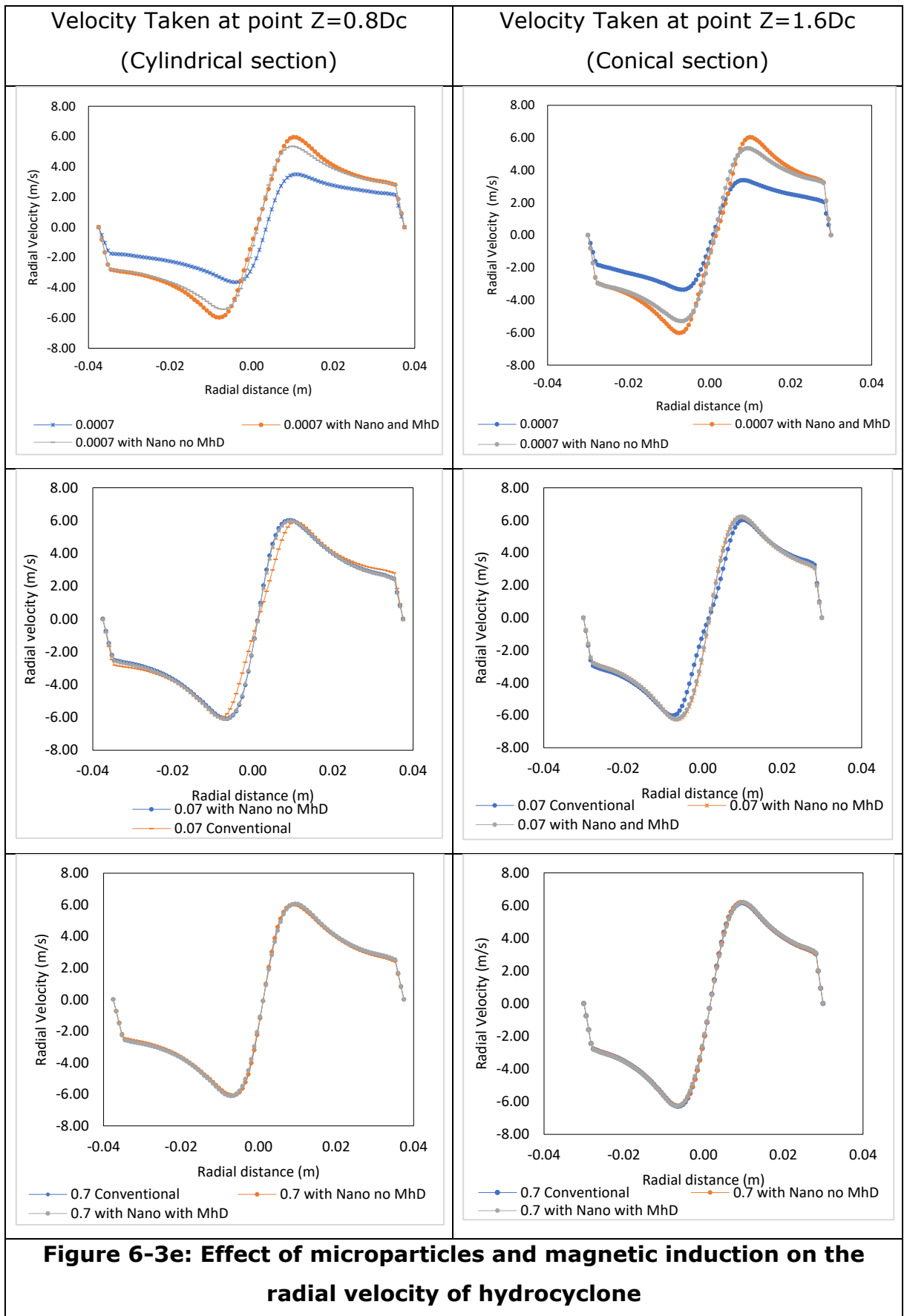


Figure 6-3civ-vi Axial Velocity Taken at point Z=1.6Dc



**Figure 6-3c: Effect of microparticles and magnetic induction on axial velocity of hydrocyclone**





**Figure 6-3e: Effect of microparticles and magnetic induction on the radial velocity of hydrocyclone**

The radial velocity at a mass flowrate of 0.0007kg/s in the conventional and micro-doped hydrocyclone was smaller than that of the magnetic hydrocyclone. This can be attributed to the additional force due to the magnetic field strength in the hydrocyclone. It is also an indication of the magnetic force having a greater effect on the lower concentration than the higher concentration. This can be linked to enhanced aggregation caused in the modified confinement owing to the magnetic field (Couedel, 2019).

### **6.3 Effect of Micro-Particle Permeability on Hydrocyclone Separation efficiency of Oil-Emulsion**

Permeability is the measure of the resistance of a material against the formation of a magnetic field, therefore it is the ratio of magnetic induction to the magnetic field strength within a material. Magnetic materials can be classified by permeability; the permeability of a diamagnetic material is slightly less than 1 while the permeability of paramagnetic material is slightly more than one. Ferromagnetic material, however, has varying magnetic permeability depending on the magnetic field with purified iron and many magnetic alloys have up to 100,000 or more permeability. The value of the magnetic permeability of some of the ferromagnetic material are listed below

Table 6-2: Magnetic permeability of different ferromagnetic materials

Mineral	Magnetic Permeability (Static)
Magnetite	2.5-16
Sidente	1.0035
Hematite	1.0004-1.001
Ankente	1.00025
Pyrite	1.000045
Magnesite	1.000250-1.000500
Graphite	0.9999990

$$\mu = \frac{B}{H}$$

6-b

Where B is the magnetic flux density, it is also known as the magnetic induction while H is magnetic field strength.  $\mu$  is the magnetic permeability.

From table 1 above, it can be seen that the permeability of ferromagnetic material is much higher; at higher magnetic field strength the magnetic material shows saturation and hysteresis (magnetic induction lagging behind the magnetic force). The influence of magnetic permeability on hydrocyclone separation efficiency and fluid flow was reviewed in this section. The same geometry of the magnetic hydrocyclone used in section 6.1 above was also used in this section. The permeability evaluated in this section was 0.5h/m, 1.5h/m, 3.0h/m and 4.5h/m. A constant magnetic induction of 1 tesla was used for the introduction of magnetism into the hydrocyclone. With a magnetic field of 1 tesla and above (Fengyu Xu, 2016), this system can be classified as a high gradient magnetic separator. A high gradient magnetic field is used to separate ferromagnetic particles less than 50 $\mu$ m

### 6.3.1 Efficiency

The influence of a magnetic field on separation depends largely on the behaviour of the particles to be separated when exposed to the magnetic field. Generally, it can be seen from the result in figure 6-4 below that at lower permeability, more of the micro-doped particles were separated leading to higher efficiency of oil-water separation irrespective of the oil particle size considered. This is because higher permeability increases the eddy current induced into the first layer of the atoms of the material, this eddy current generates a magnetic field in an opposite direction to the induced magnetic field and therefore reduces the magnetic field strength going into the other layers of the magnetic material's atoms. This result in less separation as there is an opposing force hindering the separation of the micro-doped oil droplet from water (Sato,1990). With lower permeability, less eddy current is induced therefore, the magnetic field penetrates longer, and separation of oil droplets increases. It can also be seen that the change between the permeability of 1.5h/m and 3.0h/m as it relates to efficiency is a little wide, this is because the behaviour of ferromagnetic permeability is not linear with respect to the strength of the external field (Demirel, 2009).

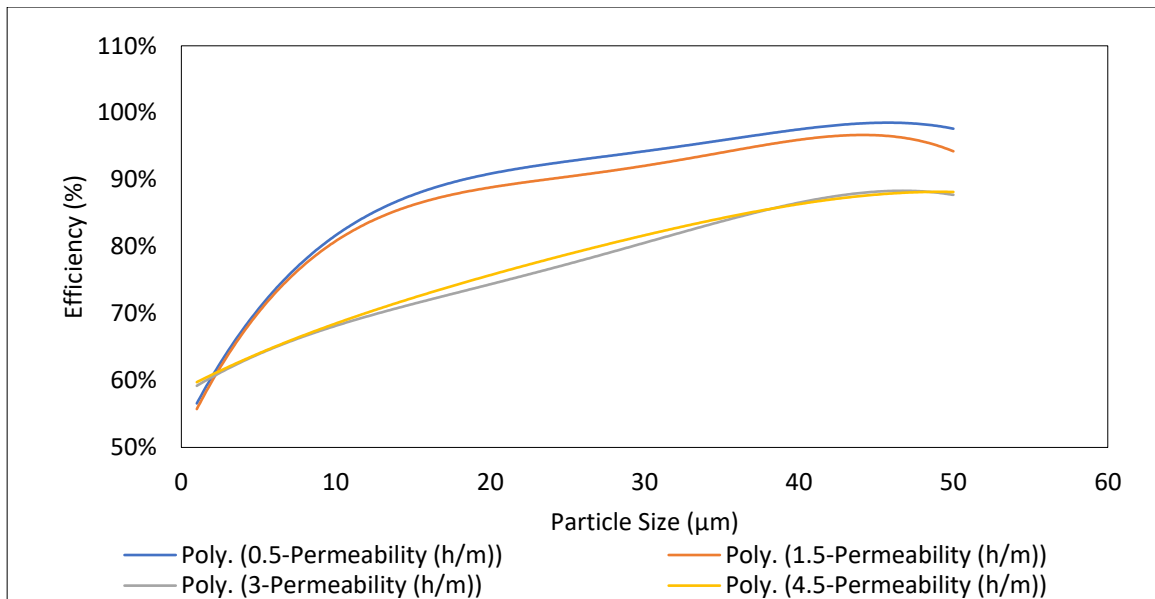


**Figure 6-4 Effect of magnet particle permeability on the efficiency of the magnetic hydrocyclone**

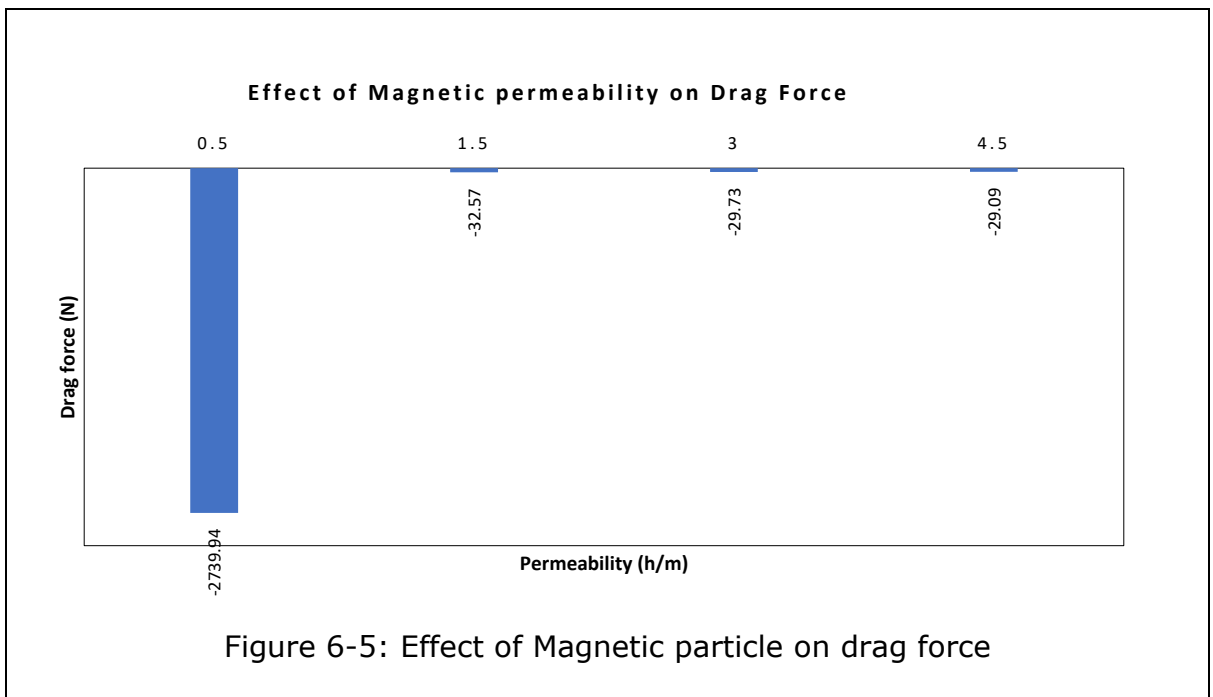
### 6.3.2 Forces in the Hydrocyclone

Simulation of the motion of particles in a hydrocyclone is governed by drag force, Saffman lift force, Brownian force, Basset force, Magnus force, thermophoretic force, pressure gradient force, and mass force. In this analysis the Magnus force will be neglected because of the very small micron particles considered (spinning effects are ignored); thermophoretic force is not considered because the temperature gradient is considered negligible and both the fluid and particles are assumed to have the same temperature. Pressure gradient, Brownian, and Basset forces were also assumed to be negligible because of the particle size being considered (1-50μm). In this section, the drag force, lift force and moment of the particles will be considered to analyse the movement of the micro-doped particles in relation to the stream under the influence of a magnet.

#### 6.3.2.1 Drag Force

Figure 6-5 below also shows the effects of magnetic permeability on drag force. The drag force can be seen to reduce with increasing permeability, this is because increasing magnetic permeability increases eddy currents within the hydrocyclone thus causing ohmic dissipation and consequently generating greater drag force, the retarding nature of this drag force is a display of Lenz's law (Hosseini, 2008).

As drag force decreases with increasing microparticle permeability, it will be safe to conclude that increasing the magnetic permeability reduces the rate at which magnetism is induced into the micro-doped oil in the hydrocyclone. The negative drag indicates that the micro-doped oil particles with lower permeability move faster to the wall than micro-doped oil droplets with higher magnetic permeability; since radial movement is obstructed by drag force as the particles move through the carrying fluids (Premaratne, 2003).



### 6.3.2.2 Lift Force

Lift force is generally known to be perpendicular to the flow direction. From the literature (Svarosky, 2000; Medronho, 1998; Dai, 1999; Siadaty, 2017) higher density particles move to the wall of the hydrocyclone while lower density particles to the central part of the cyclone, therefore, lift force will give an indication of the force available to move lower particles to the overflow of the cyclone.

Figure 6-6 shows that the lift force decreases with increasing magnetic permeability, this reveals that the influence of permeability on the lift force is not significant when the permeability is high but sizable when the permeability is low as is the case of 0.5h/m permeability. This also means that particles in the central



region of the cyclone have a higher force to move to the overflow section in a 0.5h/m permeability hydrocyclone than in other hydrocyclones.

### 6.3.2.3 Moment

The moment measures the tendency of a particle to rotate around an axis, this will typically occur when the force applied to the particle is not equal to the opposing force. Figure 6-7 shows that a hydrocyclone with a micro-doped particle of 0.5h/m permeability produces a higher moment than other hydrocyclones. This means that when permeability was 0.5h/m, magnetization was easier thus 0.5h/m permeability resulted in highly magnetizable particles than other permeabilities considered; highly magnetizable material produces higher net magnetic moment (Hermann A., 1989). In other words, the induced field (strength) in 0.5h/m permeability is higher. The product of the magnetic strength and the distance between the magnetic poles gives the moment and the magnitude of the moment per unit volume of material is magnetization (Denis Yan, 2016).

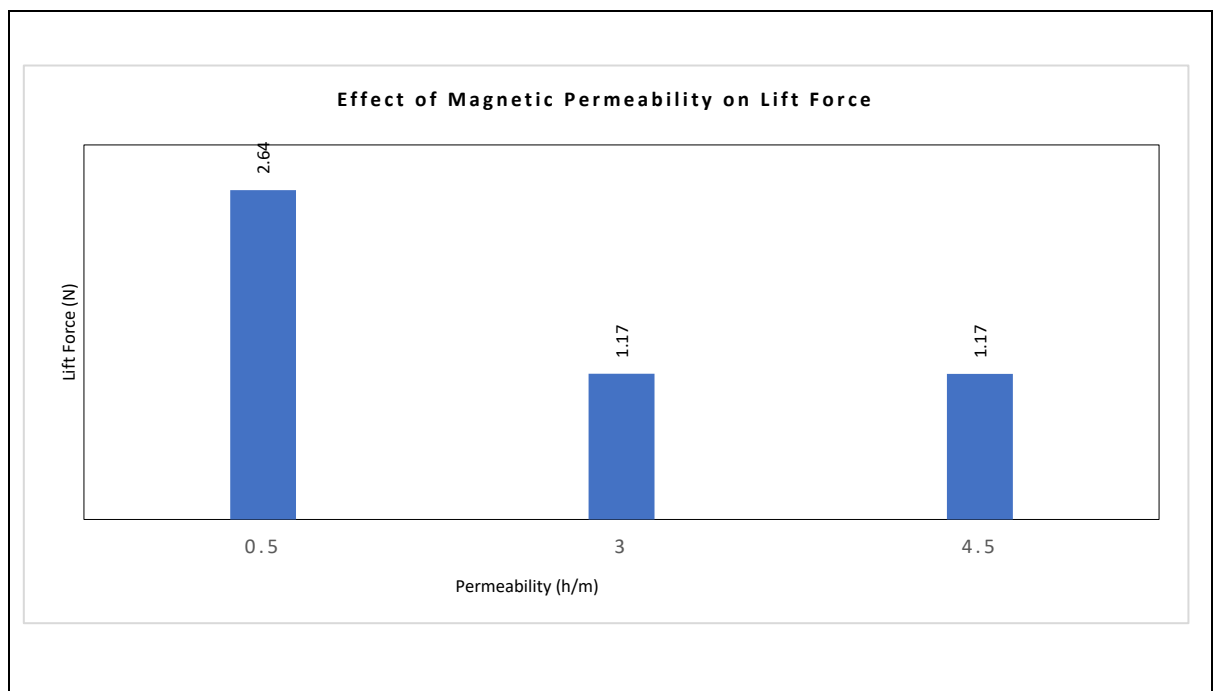


Figure 6-6: Effect of magnetic permeability on lift force

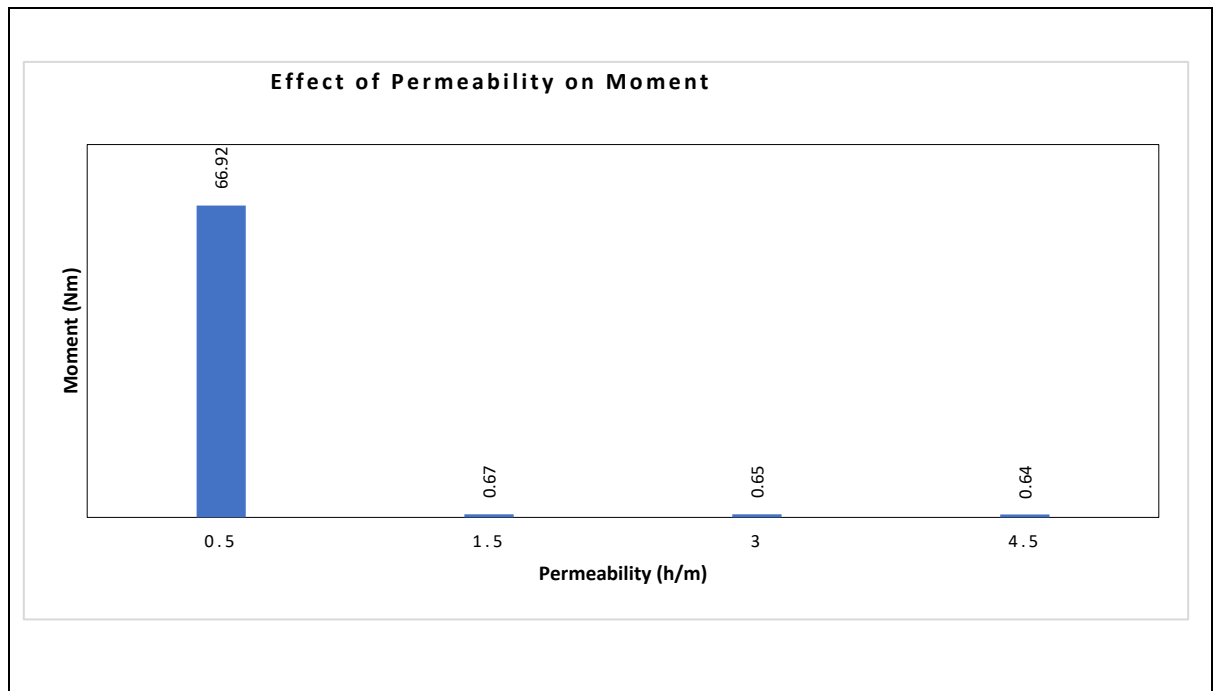


Figure 6-7: Effect of magnetic permeability on moment

### 6.3.3 Velocity profiles at different magnetic permeability

The velocity profiles were taken at two different points in the hydrocyclone, the first velocity reading was taken at  $Z=0.8D_c$  which falls above the vortex finder in the cylindrical section of the cyclone. The second velocity was taken at  $Z=1.6D_c$  which is below the vortex finder and falls in the conical section of the cyclone.

#### 6.3.3.1 Tangential Velocity

It can be seen that the tangential velocity (figure 6-8) of the hydrocyclones irrespective of permeability all show the characteristics of free and forced vortex towards the wall and the centre of the cyclone (Rankine flow). In the cylindrical section of the hydrocyclone; at the free vortex region, the tangential velocity of  $0.5h/m$  and  $1.5h/m$  were almost the same and higher than the tangential velocity of  $3.0h/m$  and  $4.5h/m$  permeability. However, in the forced zone, it was observed that that the tangential velocity of the  $3.0h/m$  and  $4.5h/m$  hydrocyclone was lower than  $0.5h/m$  and  $1.5h/m$  permeabilities.

In a hydrocyclone the centrifugal force is the dominant force for separating higher density particles from lower density particles. However, in a magnetic hydrocyclone, the centrifugal force is complemented by external magnetic force

due to the induction of a magnetic field into the cyclone (Premaratne, 2003). This magnetic force is given by the equation below

$$F_m = \mu_o k V H \bar{v} H$$

6-c

Where  $F_m$  is magnetic force

$\mu_o$  is permeability of vacuum

$k$  is volumetric magnetic susceptibility

$V$  is particle volume

$H$  is field strength

$\bar{v}H$  is the magnetic field gradient.

Since  $\mu = B / H$ , is at constant magnetic force, increasing permeability will reduce the magnetic field strength. A reduction in magnetic field strength also leads to a reduction in the magnetic field gradient, therefore a reduction in the overall velocity of particles moving to the wall of the cyclone. This means a reduction in the overall forces (centrifugal force and magnetic force) attracting/ moving particles to the wall of the cyclone.

The tangential velocity contour (figure 6-8a) along the longitudinal section of the cyclone shows that while the velocity for the higher permeability hydrocyclone (3.0 and 4.5h/m) looks fairly the same, the lower permeability hydrocyclone (0.5 and 1.5h/m) is approximately same too. This can be linked to the different flow resistances that were experienced in the cyclone at different permeability constants (Bram, 2018).

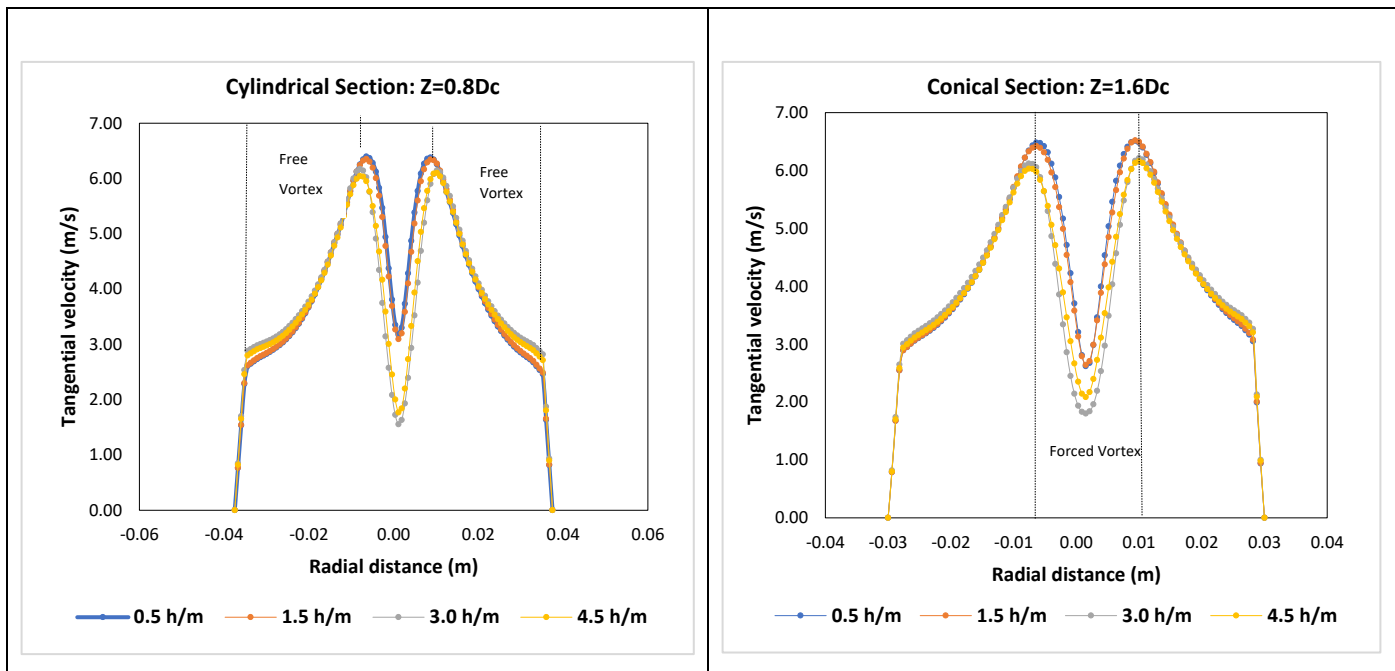


**Figure 6-8: Effect of magnetic permeability on hydrocyclone tangential velocity**

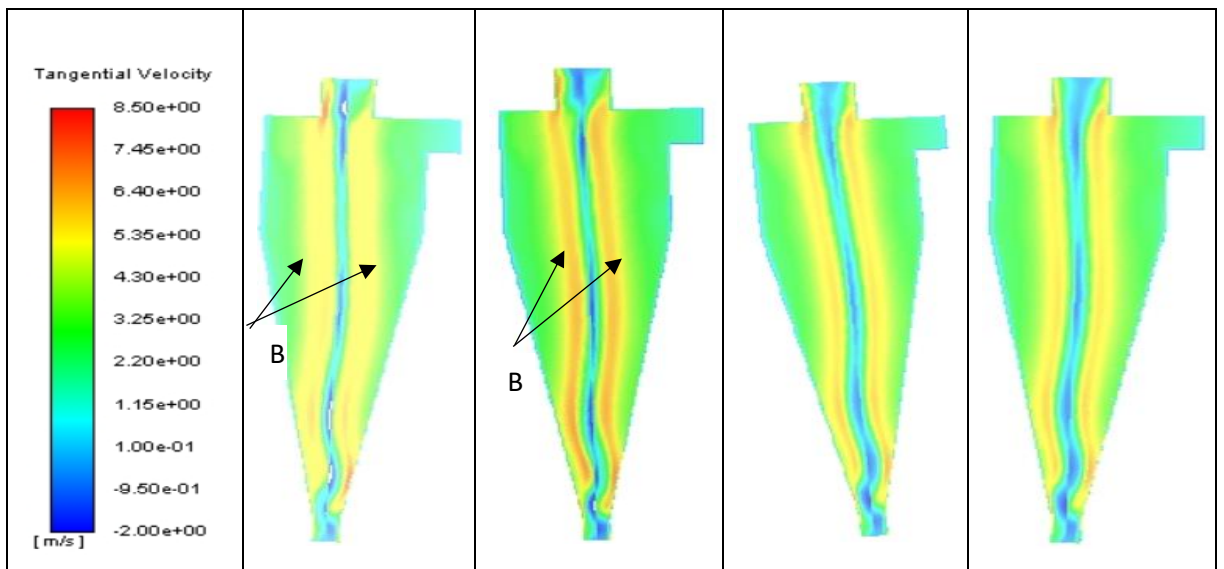


**Figure 6-8a: Effect of magnetic permeability on hydrocyclone tangential velocity- Contour plots**

### 6.3.3.2 Axial velocity

The axial velocity is responsible for moving particles along the longitudinal axis of the cyclone. From figure 6-9, the maximum axial velocity was seen in the 0.5h/m and 1.5h/m permeability hydrocyclone. This means the residence time of the lower permeable micro-doped fluid is more than that of the high permeable micro-doped fluid (Jiang, 2019)

The shape of the axial velocity at 0.5h/m and 1.5h/m shows no dipping at the core of the cyclone. In a conventional hydrocyclone, this shape means that the revolution in the cyclone is small thus poor separation (Lee, 2006). However, this study has shown that in the magnetic hydrocyclone, the revolution of fluid can be reduced due to the influence of the magnetic force introduced into the system which helps to improve the separation efficiency.

The axial velocities of the high permeability (3.0h/m and 4.5h/m) cyclones were also seen to be lower than 0.5h/m and 1.5h/m permeability. This is because the increase in permeability increases the resistance of flow in the cyclone which leads to the overall decrease in the axial velocity of the cyclone (Demirel, 2009). The shape of the high permeability hydrocyclone shows flow reversal with the dipping at the core region of the cyclone and higher swirl/ revolution of the fluid which is typical of the hydrocyclone. The magnetic hydrocyclone axial shape reflects a typical hydrocyclone axial velocity because as the microparticle permeability increases the magnetic field has lesser influence on the microparticle due the generation of larger magnetic force opposing called eddy current (García-Martín, 2011).

It can therefore be concluded to improve the efficiency of oil-water separation in the magnetic hydrocyclone, the permeability of the microparticle fluid should be relatively low.

From the contour chart in figure 6-9a below (the legend applies to all contours), the locus of zero vertical velocity (C) in the 0.5h/m hydrocyclone is more pronounced than 1.5h/m permeability while the higher permeability hydrocyclone shows less intensity and smaller width of LZVV. This shows that the locus of zero velocity can be influenced by the permeability of the micro-doped particles in a hydrocyclone. This also reveals that fluids/ particles within the region of LZVV will move faster to the overflow in a cyclone with more pronounced (high intensity) LZVV than in the less pronounced or intense LZVV.

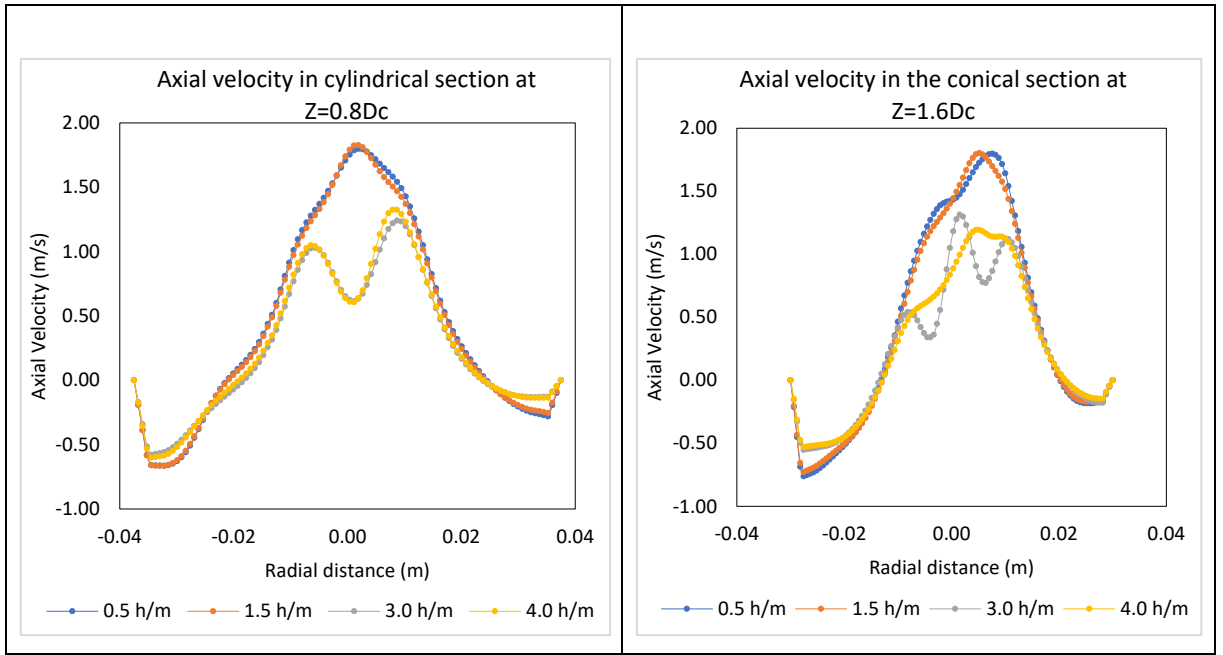


**Figure 6-9: Effect of magnetic permeability on hydrocyclone Axial Velocity**

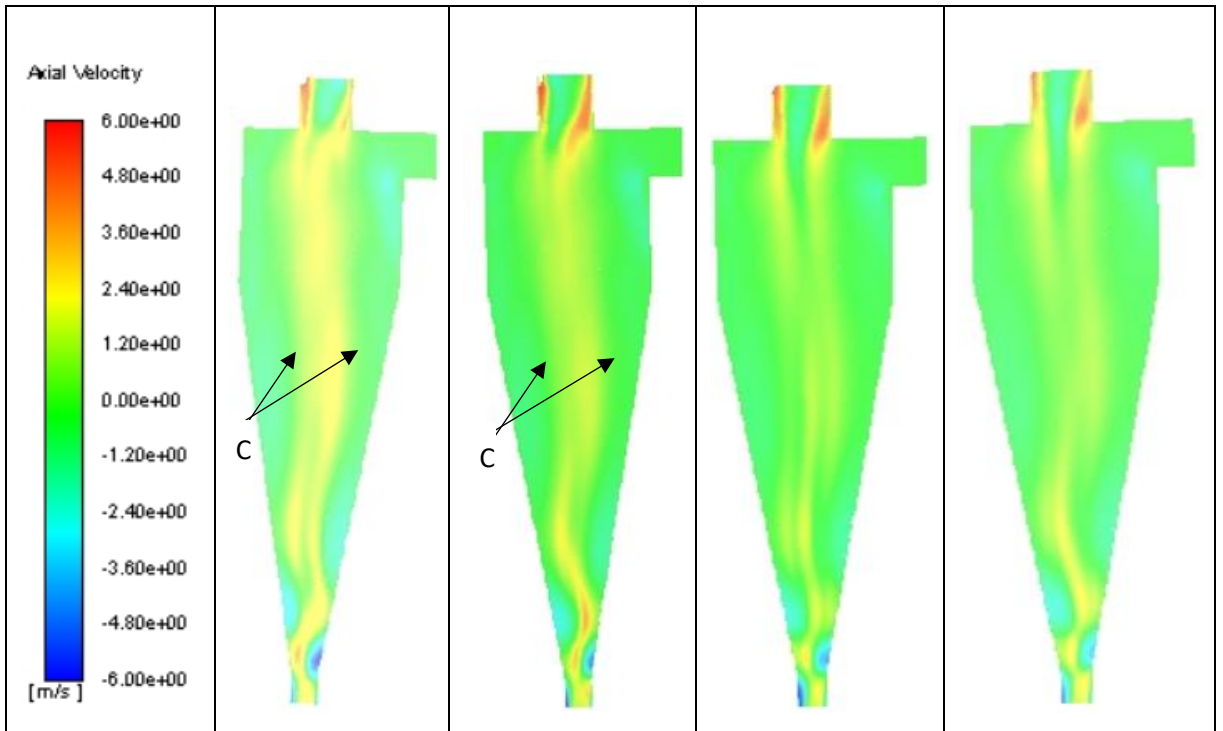
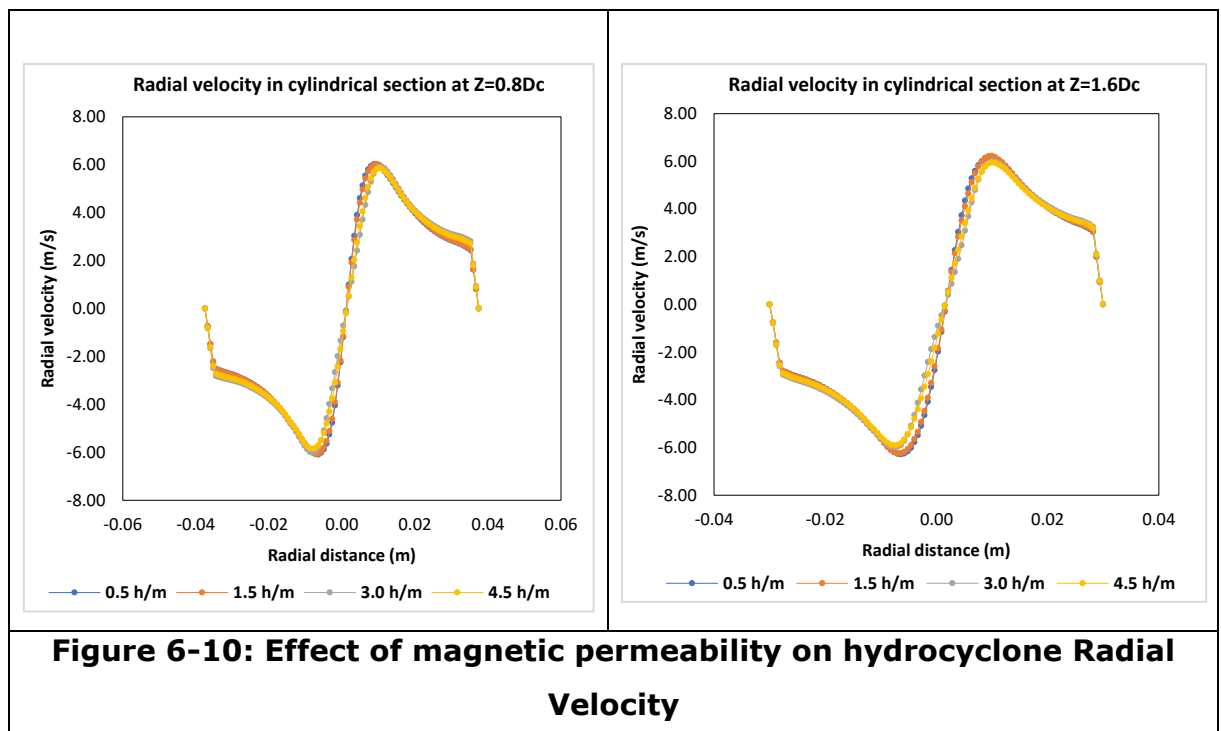


**Figure 6-9a: Effect of magnetic permeability on hydrocyclone Axial Velocity-Contour Plots**

### 6.3.3.3 Radial Velocity

The radial velocity for different permeability considered all produce almost the same value indicating that increasing permeability does not significantly change the radial velocity when compared to other velocities. The negative values of radial velocity indicate that the direction of flow is from the wall to the centre (Vieira, 2011) while the positive value indicates movement from the centre to the wall. This result shows that the radial dragging of the particles towards the centre of the cyclone is not significantly affected by permeability.



### 6.3.4 Turbulence Kinetic Energy

The turbulence kinetic energy (fig 6-11) is seen to be quite small in the cylindrical section of the cyclone (at Z=0.8Dc) for 0.5h/m and 1.5h/m permeability with a turbulence kinetic energy of less than  $0.2\text{m}^2/\text{s}^2$  while the turbulence kinetic energy of higher permeable particles was more than  $0.4\text{m}^2/\text{s}^2$ . This is because there is a suppression of turbulence kinetic energy at lower permeabilities (Chan, 2005).

This means the rate of energy dissipation of large eddies to smaller eddies in the lower permeability hydrocyclone is larger than the rate of energy dissipation in the higher permeability hydrocyclone. This can be linked to the influence of magnetic

permeability on eddy current as magnetic permeability greatly affects the eddy current (García-Martín, 2011). This eddy current does play a minor role in energy dissipation (Beatrice, 2008). Therefore, it can be concluded that the influence of the eddy current on the dissipation of energy is more prominent in the cylindrical part of the hydrocyclone (where the turbulence is not fully developed) as particles with higher permeability (which result in increased eddy current) have a lower dissipation of energy from large eddies to low eddies, therefore, high kinetic energy. However, in the conical section when the flow is fully turbulence, the impact of the eddy current was very low and therefore the disparity in the turbulence kinetic energy of the different permeabilities was minimal in the conical section.

### 6.3.5 Pressure Drop

Figure 6-12 shows the graph of pressure drop against permeability, the pressure drop is seen to increase with decreasing permeability (Klaentschi, 1998; You L., 2020). According to the literature (Svarosky, 2000), the higher the pressure drop, the greater the separation efficiency and this is what was recorded on the efficiency graph (figure 6-4) above. Although the change in pressure drop is not significant between 0.5h/m and 1.5h/m, a significant change was seen when the permeability increases from 1.5h/m to 3.0h/m permeability.

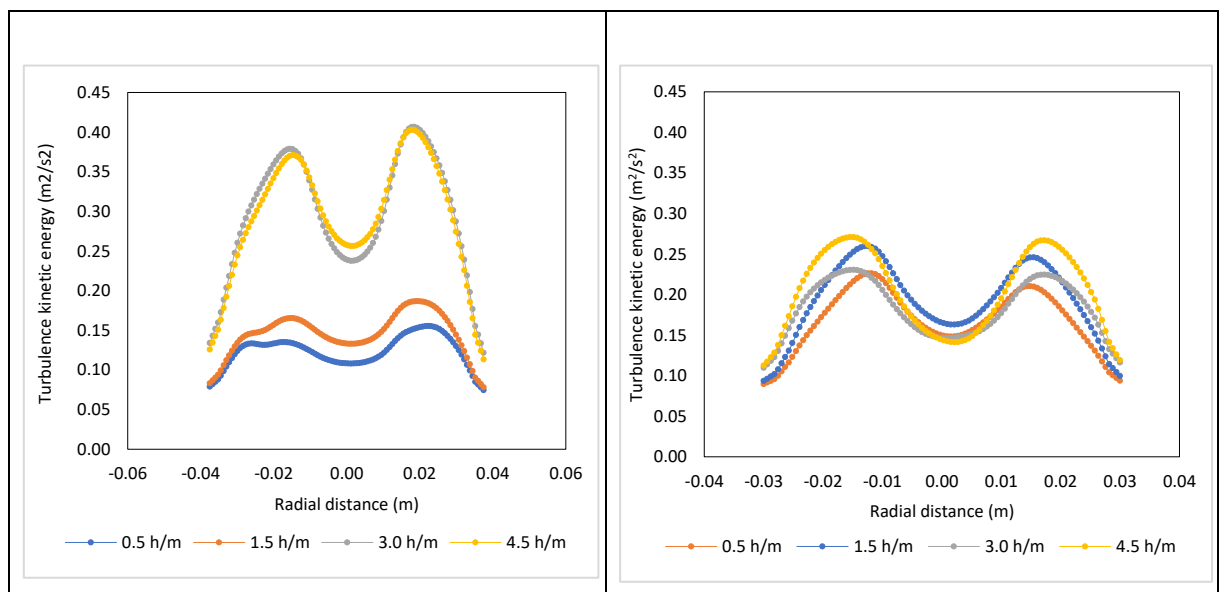


**Figure 6-11: Effect of magnetic permeability on hydrocyclone Turbulence Kinetic Energy**



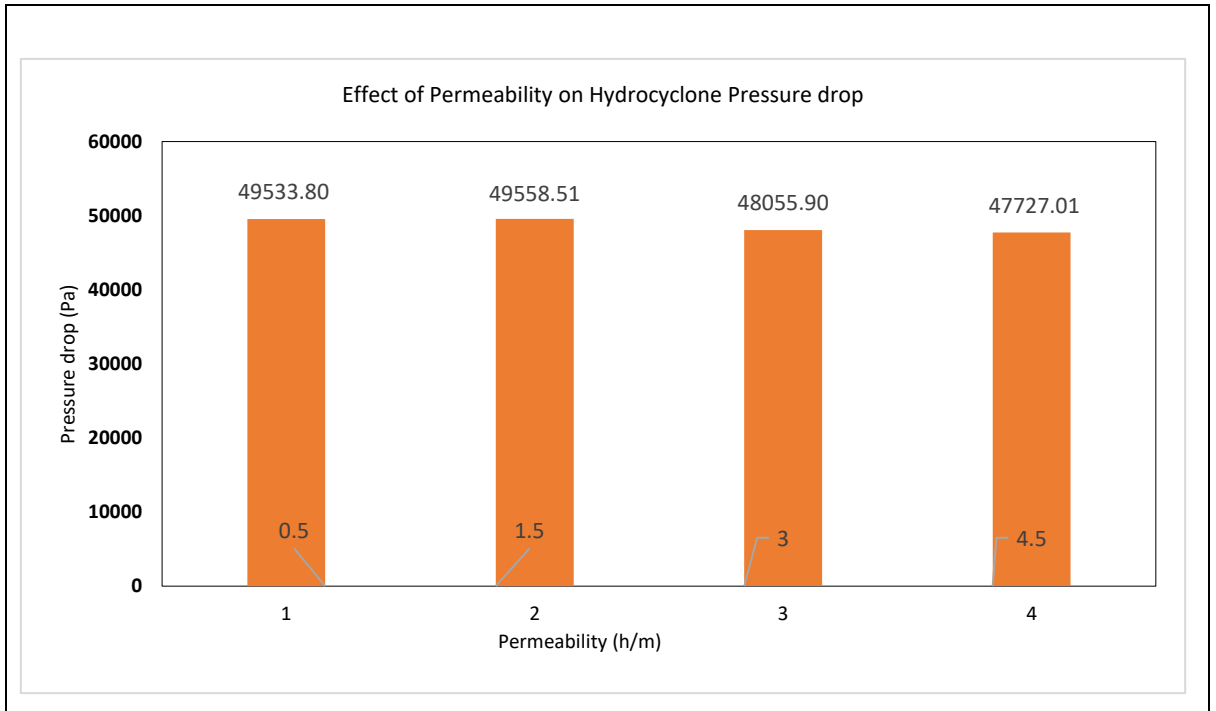
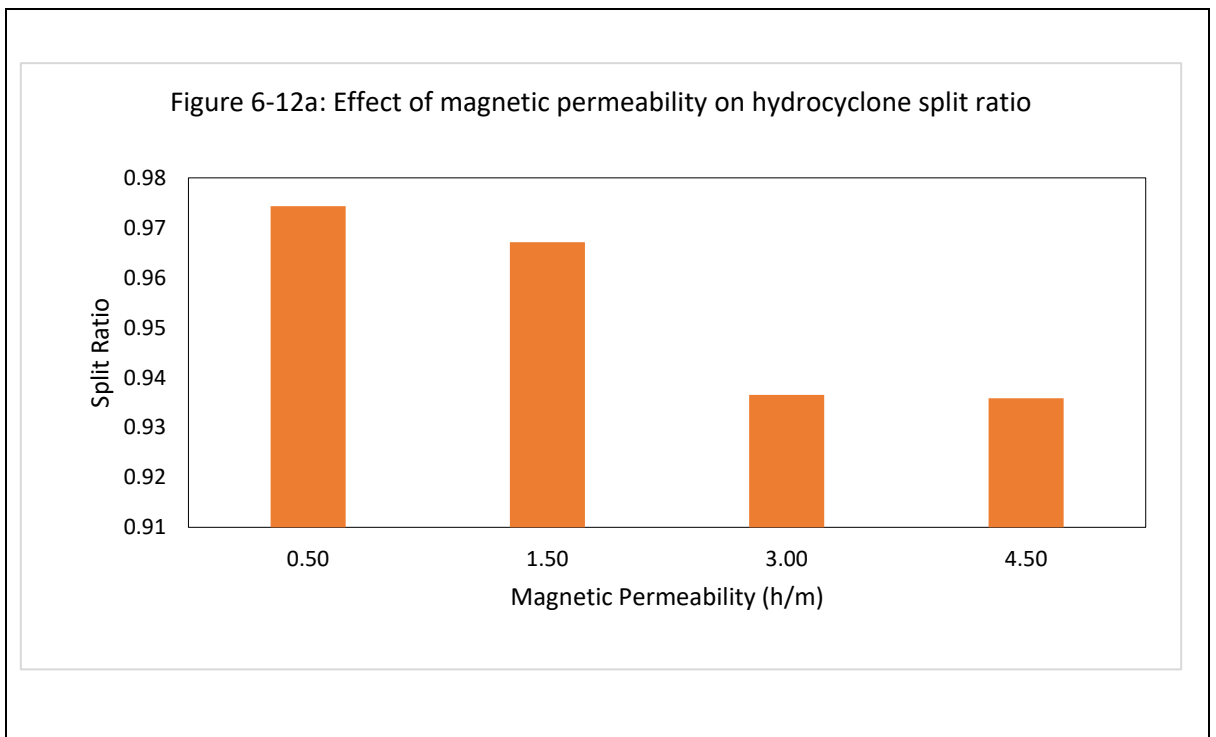


Figure 6-12: Effect of magnetic permeability on hydrocyclone Static Pressure



### **6.3.6 Split Ratio at different magnetic permeability**

The split ratio between the inlet and the overflow was examined and figure 6-12a reflects the result of this.

$$\text{Split ratio} = \frac{U_{\text{underflow}}}{U_{\text{inlet}}}$$

Figure 6-12a shows the effect of magnetic permeability on the split ratio in a magnetic hydrocyclone. The split ratio reduces with increasing magnetic permeability and this suggests that the efficiency of the hydrocyclone with higher permeability will be lower than the efficiency of a hydrocyclone with lower permeability. From the separation efficiency results above, it can be concluded that the higher split ratio the more the quantity of fluid that will be seen in the overflow section of the hydrocyclone and also the particles that will be discharged are larger at the underflow section of the hydrocyclone.

### **6.4 Effect of Micro-Particle Density on Hydrocyclone Separation efficiency of Oil-Emulsion Without the Use of MhD**

The density of microparticle changes as a result of changes in the size of the microparticle or the material used for the microparticles. The higher the density of the magnetic particle the smaller the size of particles (Kar Nanda, 2019). In this section, the effects of changing the density of this micro-doped particle on the efficiency, pressure, and the fluid flow of the cyclone will be analysed.

The geometry used for the simulation is the same used in the hydrocyclone above, the microparticle density was varied. The properties of the microparticles used for the different simulations are shown in the table below.

**Table 6-3: Properties of Microparticles used for Density Analysis simulations**

Density (kg/m <sup>3</sup> )	2175	3175	5175
Magnetic permeability (h/m)	1.5	1.5	1.5
Electrical conductivity (siemens/m)	2000000	2000000	2000000
Charge density	7.02	7.02	7.02

### 6.4.1 Efficiency

In a hydrocyclone, the separation efficiency increases with increasing particle density (Cilliers, 2000; Ji Li, 2017). This same principle was seen to be applicable when microparticles of various densities were reviewed. The increasing density of the microparticle was seen to improve the efficiency of the cyclone.

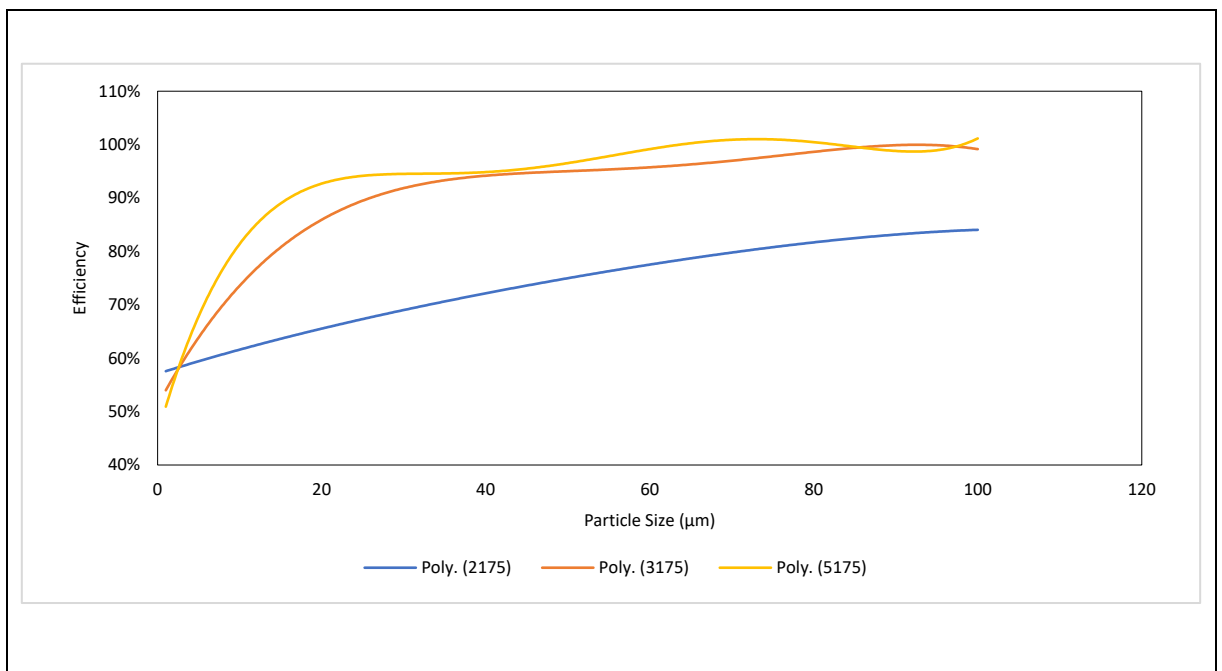


**Figure 6-13: Effect of magnetic density on hydrocyclone efficiency**

### 6.4.2 Split Ratio

The split ratio reflects the flow distribution of compounds in a hydrocyclone, the inlet velocity, and the rotating speed have a great effect on the split ratio (Jiang, 2018) since the inlet velocity, in this case, is the same for all the cyclones, the rotating speed will be responsible for significant change in the split ratio.

From figure 6-14, it can be seen that the split ratio increases with increasing particle density from 2175 kg/m<sup>3</sup> and 3175 kg/m<sup>3</sup>; and the split ratio of both magnetic particle density of 3175kg/m<sup>3</sup> and 5175kg/m<sup>3</sup> were approximately 0.97 showing that there is a maximum density after which further increase in density will not significantly affect the split ratio in the hydrocyclone

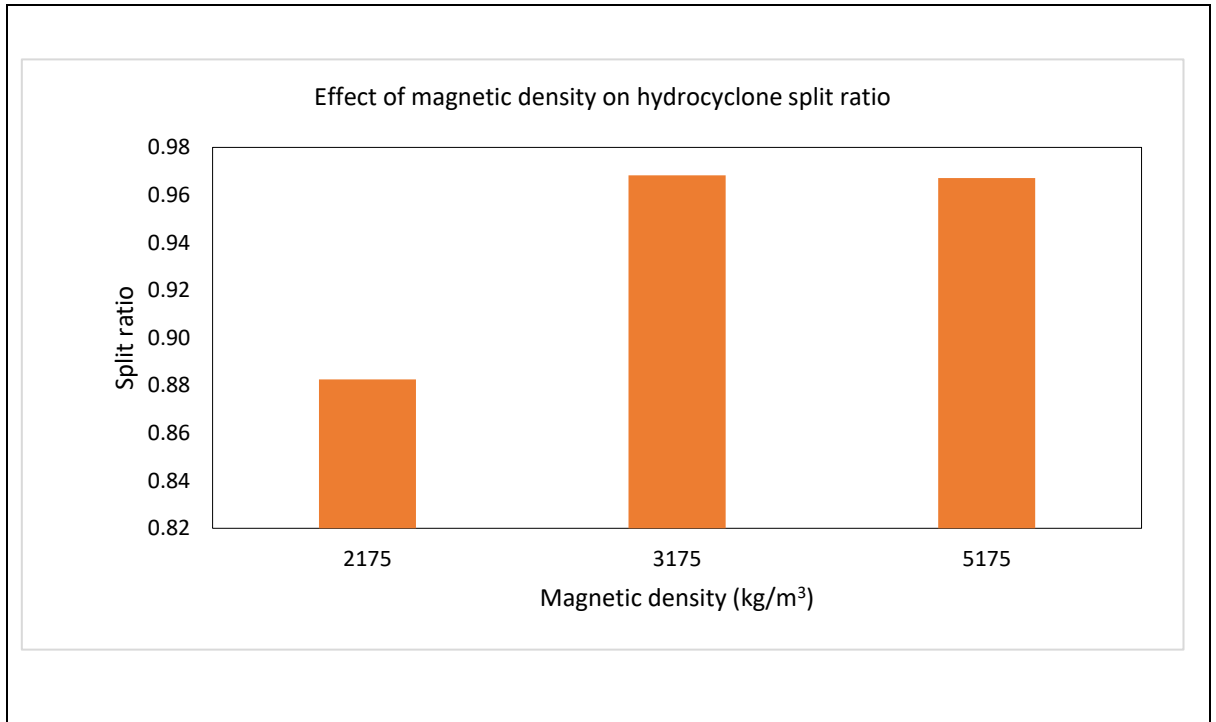


**Figure 6-14: Effect of magnetic density on hydrocyclone split ratio**

### 6.4.3 Pressure

The pressure drop in the higher density hydrocyclone was also seen in figure 6-15 to be higher than the pressure in the lower density hydrocyclone and this can be explained with the pressure calculation equation given by Svarosky L, 2000. The pressure drop is directly proportional to the fluid density, therefore increase in density increases the pressure drop in the cyclone since the overall density of the fluid increases with increasing density of the microparticle.

$$\Delta P = Eu. \left( \frac{\rho v^2}{2} \right) \quad 6d$$

$\Delta P$  is the pressure drop

$Eu$  is Euler number

$\rho$  is the density of the fluid

$v$  is the flow velocity

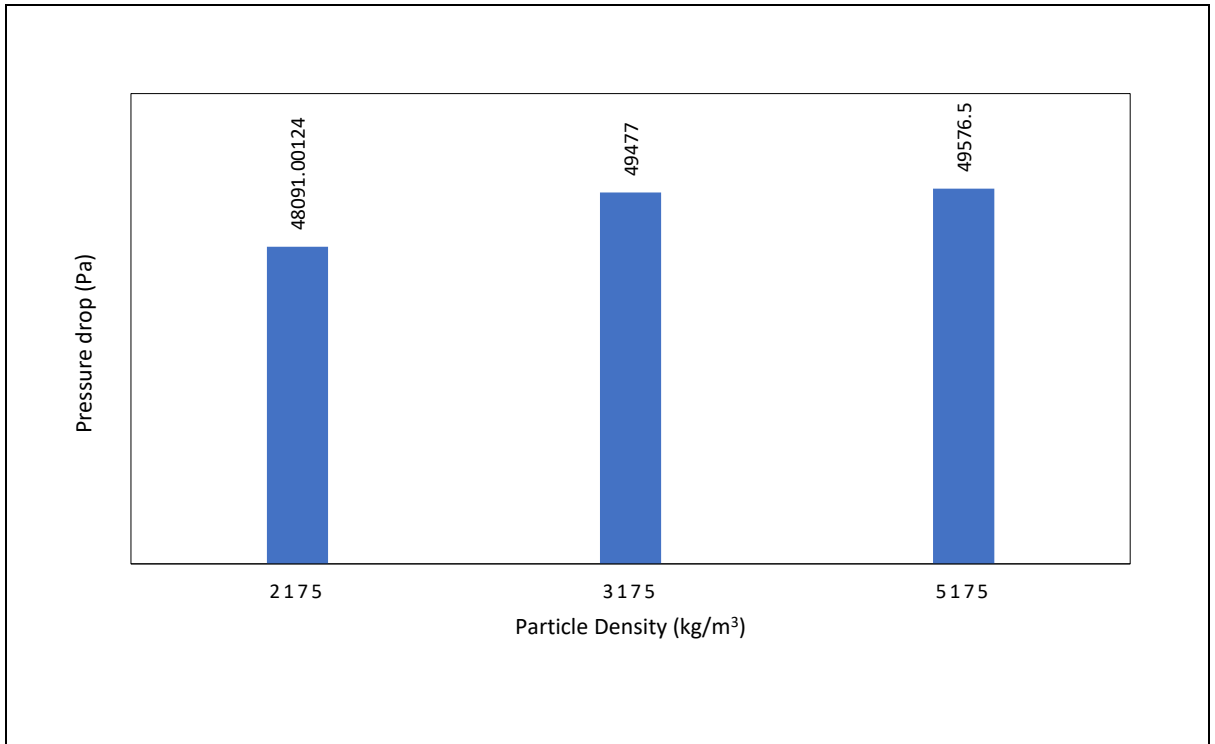


**Figure 6-15: Effect of magnetic density on hydrocyclone split ratio**

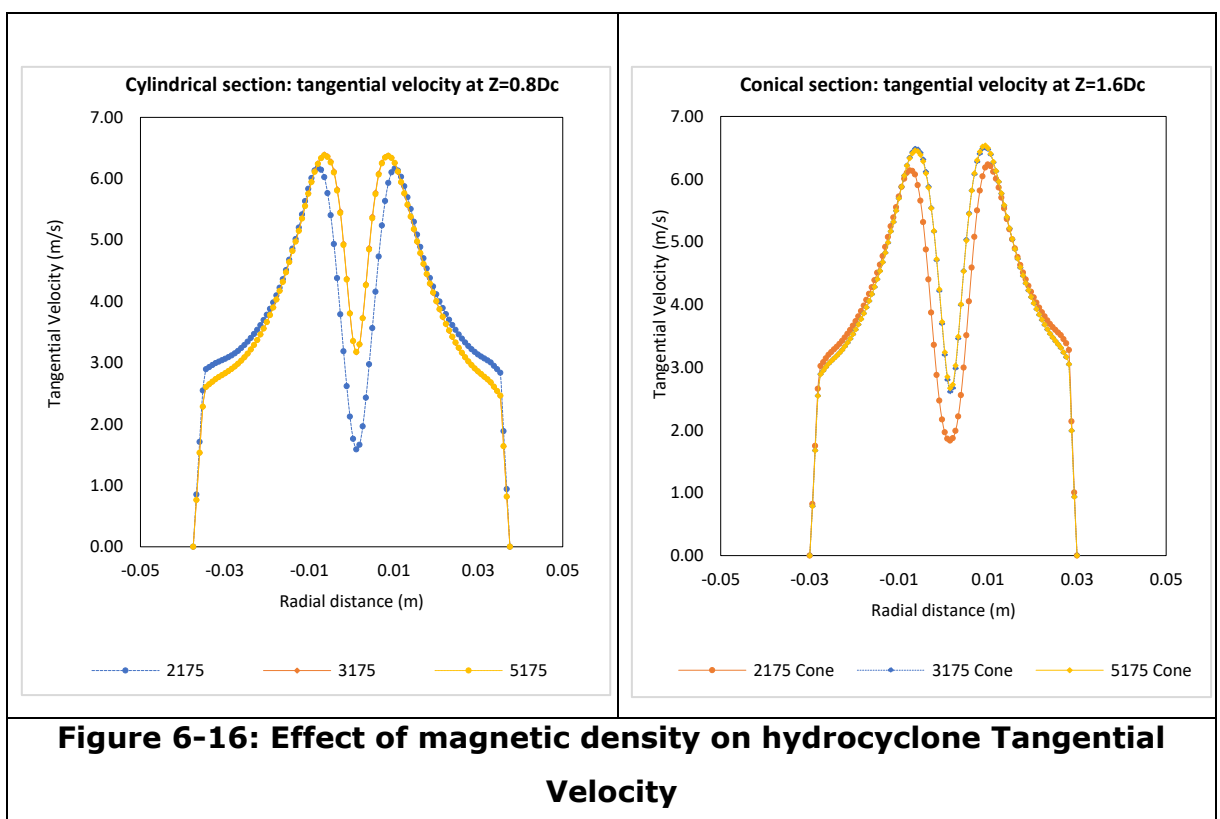
## 6.4.4 Velocity Distribution

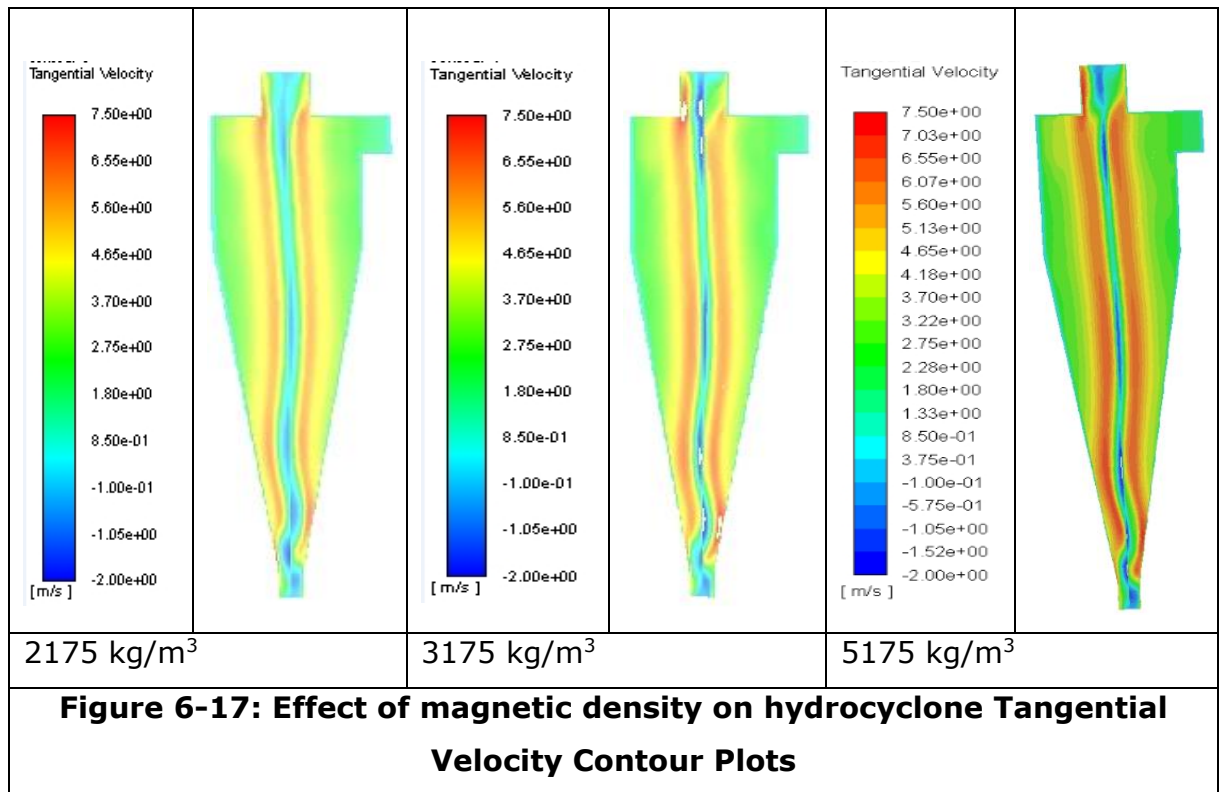
The velocity profile of a hydrocyclone can effectively predict the flow pattern in the cyclone. The three-dimensional nature of the flow produces an anisotropic flow near the inlet region and axial-symmetric flow is possible without losing the main features of the vortex motion (Concha, 2007)

### 6.4.4.1 Tangential Velocity

From the tangential velocity profile in figure 6-16 below, it can be seen that the tangential velocity distribution in micro-doped particles increases as density increases. The tangential velocity profile also reflects a typical hydrocyclone tangential velocity profile with the free and forced vortex. The increasing density increases the tangential velocity in both the free and the forced vortex zone. The tangential velocity in the cylindrical and conical sections is similar for the 2175kg/m<sup>3</sup> with the peak of the free and forced soon almost the same. However, in higher densities (3175 kg/m<sup>3</sup> and 5175 kg/m<sup>3</sup>) the tangential velocities in the forced vortex zone were lower in the conical section than in the cylindrical section.

The strength of the centrifugal force used in the cyclone separation is determined by the tangential velocity Jiang L. (2019). The high tangential velocity in a higher density hydrocyclone, therefore, means that greater centrifugal force will be experienced in the 3175 kg/m<sup>3</sup> and 5175 kg/m<sup>3</sup> hydrocyclone than 2175 kg/m<sup>3</sup>. Therefore, higher density particles move faster in the proximity of the walls (Fornari, 2018). It is also not surprising that the tangential velocity of 3175 kg/m<sup>3</sup> to 5175 kg/m<sup>3</sup> are almost equal, indicating that increasing the density from 3175 kg/m<sup>3</sup> to 5175 kg/m<sup>3</sup> will not have a huge impact on the separation of the particles in the hydrocyclone.





As can be seen, the velocity distribution is affected by the density of the fluid with 3175kg/m<sup>3</sup> and 5175kg/m<sup>3</sup> having a higher velocity than the 2175kg/m<sup>3</sup> hydrocyclone. This can be credited to microparticle aggregation that takes place at higher density. This aggregation results in a decrease in friction (Bao 2019) between the fluid-particle and the particle-wall in the cyclone which therefore can contribute to increasing velocity. When microparticles are evenly distributed, the influence of viscosity on velocity profiles is dominant, otherwise, aggregation, aggregation-configuration and distribution of microparticles have a dominant impact on the flow characteristics of fluid (Bao, 2019).

From the tangential velocity contour plots (figure: 6-17), it can be seen that the tangential velocity around the core region increases with increasing density while away from the core towards the wall the tangential velocity decreases with almost zero showing the no-slip condition used in the simulation. This shows mass conservation, as the speed close to the wall reduces to zero, the speed in the central region of the pipe increases.

#### **6.4.4.2 Axial Velocity**

The axial velocity is a function of the radial position in which the measurement was taken (Chiné, 2000). In this section, the axial velocity was taken at a point  $Z=0.8D_c$  which falls above the vortex finder in the cylindrical section and at point  $Z=1.6D_c$  which falls below the vortex finder and also in the conical section.

Figure 6-18 shows that the lower density micro-doped fluid hydrocyclone has lower axial velocity than the higher density fluid. The upward shape is an indication that flow reversal is taking place and consequently separation is taking place (Cullivan 2003). Figure 6-18 also indicates that the rate of fluid movement to the overflow increases with increasing density. The reduction of axial velocity in  $2175 \text{ kg/m}^3$  means more of the fluid mixture (magnetic particle and water) is being drained into the spigot section of the cyclone (Bing Liu, 2019) when compared to the higher density hydrocyclones.

The axial velocity contour plot in figure 6-19 above shows that the mean axial velocities for the cyclone vary with densities. The noticeable difference in the axial velocities is at the core of the cyclone. The contour plot is seen to be more pronounced as the density of the fluid increases most especially at the overflow section of the cyclone where the axial velocities were seen to be at a peak for all the cyclones. The increase of axial velocities at the overflow can be attributed to the increase in the quantity of fluid going out of the vortex finder which can also be associated with the pronounced core centre in the higher density hydrocyclone.



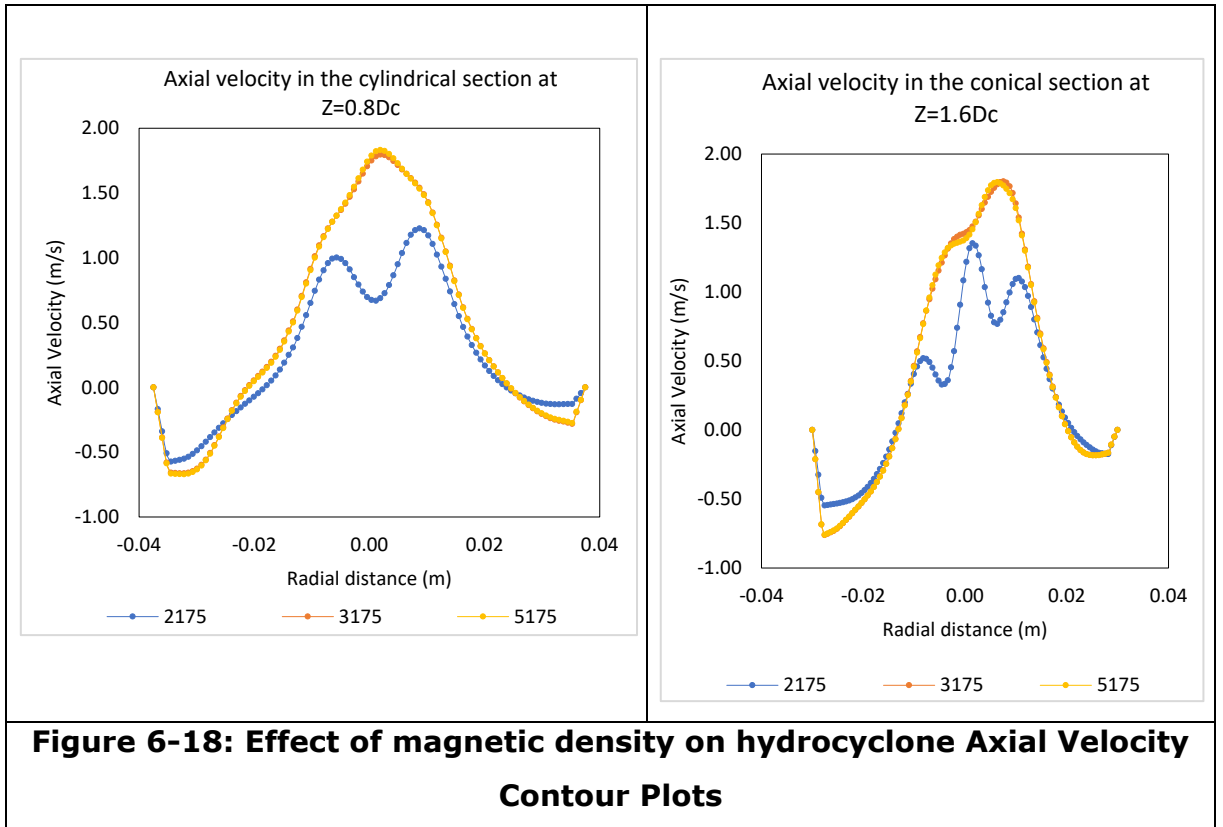


**Figure 6-18: Effect of magnetic density on hydrocyclone Axial Velocity Contour Plots**

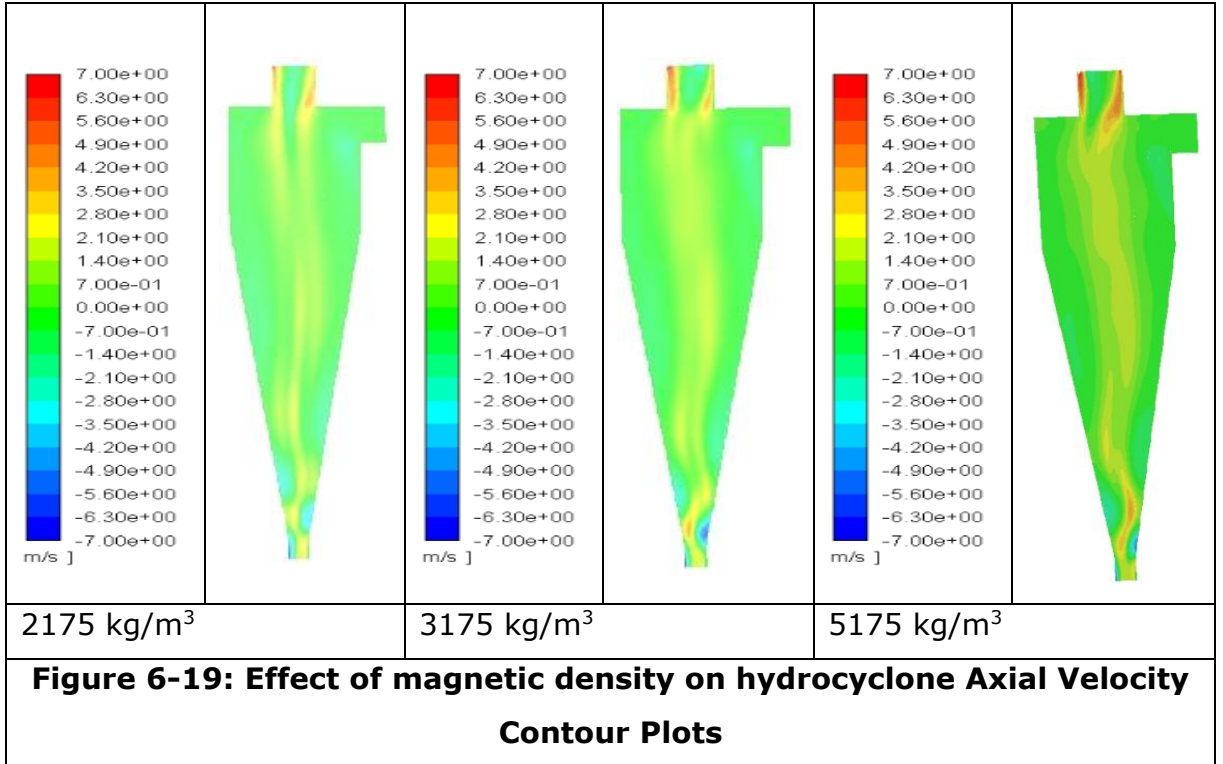
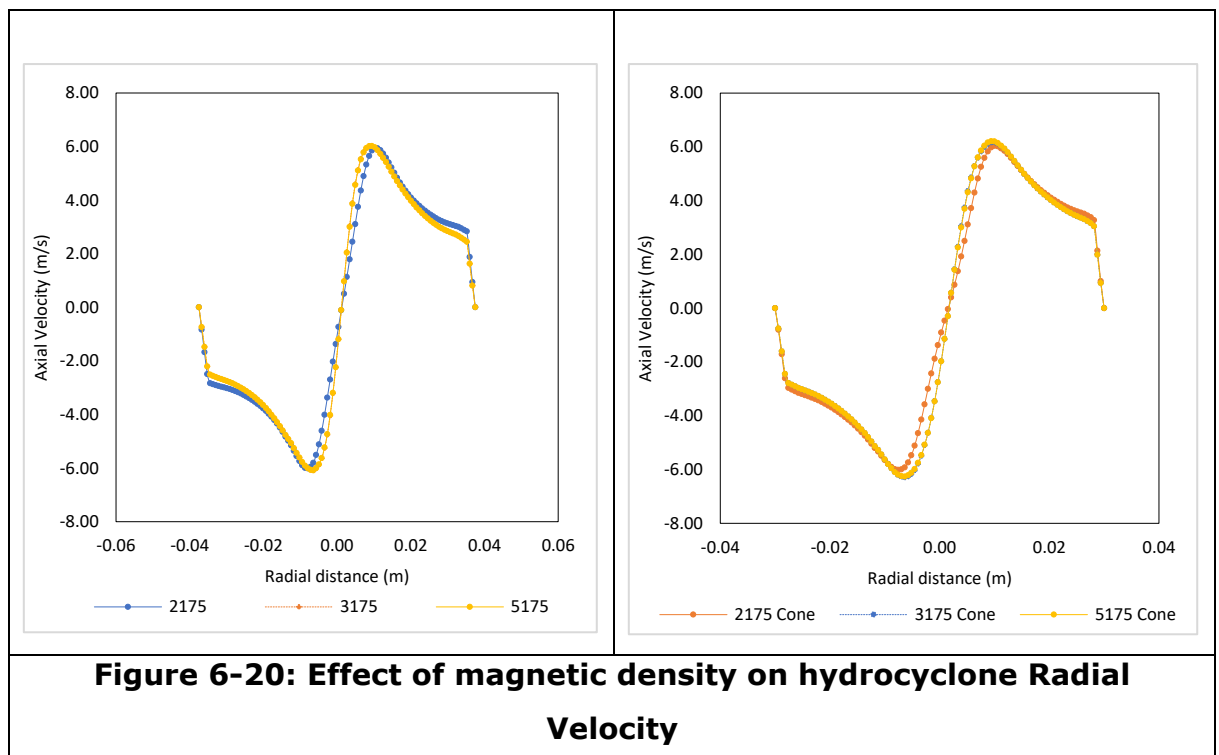


**Figure 6-19: Effect of magnetic density on hydrocyclone Axial Velocity Contour Plots**

### 6.4.4.3 Radial Velocity

The radial velocity profiles in both the cylindrical and conical section of the cyclone are similar for the densities considered. Although a slight shift was noticed for the 5175 kg/m<sup>3</sup> hydrocyclone. The slight change can be credited to a slight change in the movement of fluid/particles from the wall to the centre of the cyclone, and from this centre to the wall. Changes like this can affect the velocity stochastic turbulent transport of particles between the wall and the core of the cyclone (Cullivan 2003).



### 6.4.5 Turbulence Kinetic Energy

According to Zhou (2014), magnetic nanoparticles properties have no effect on fully developed turbulence, therefore the changes in the turbulence kinetic evaluation below are mostly due to the density differential. Turbulence kinetic energy is formed by friction or buoyancy, fluid shear under and in unstable conditions (Yue, 2015)

The graph of the turbulence kinetic energy below shows that the turbulence kinetic energy of the 2175 kg/m<sup>3</sup> is higher than 3175 kg/m<sup>3</sup> and 5175 kg/m<sup>3</sup> both in the cylindrical and conical sections. This shows that the 2175kg/m<sup>3</sup> hydrocyclone has

more large-scale eddies than the 3175kg/m<sup>3</sup> and 5175kg/m<sup>3</sup> density hydrocyclones especially in the cylindrical section of the cyclone where turbulence is formed. In the Reynold stress model, the turbulence kinetic energy is proportional to the rate of kinetic energy dissipation from the mean flow to the velocity field. The production term of the RSM model accounts for the transfer of kinetic energy in the turbulence flow. The higher the production rate, the higher the transfer of kinetic energy from the mean flow to the velocity and also the greater the rate of energy dissipation. The relationship is represented by the equation provided by Menter, 2012

$$\frac{P_k}{\varepsilon} = \sqrt{2C_\mu II_S} \quad 6e$$

Therefore, an increase in turbulence kinetic energy will mean that less kinetic energy is transferred from the mean flow to the velocity field and a decrease in turbulence kinetic energy will mean more energy is transferred from the mean flow to the velocity field.

Where  $II_S$  is the tensor invariants,  $C_\mu$  is the constant,  $P_k$  is the production of kinetic energy,  $\varepsilon$  is the dissipation.

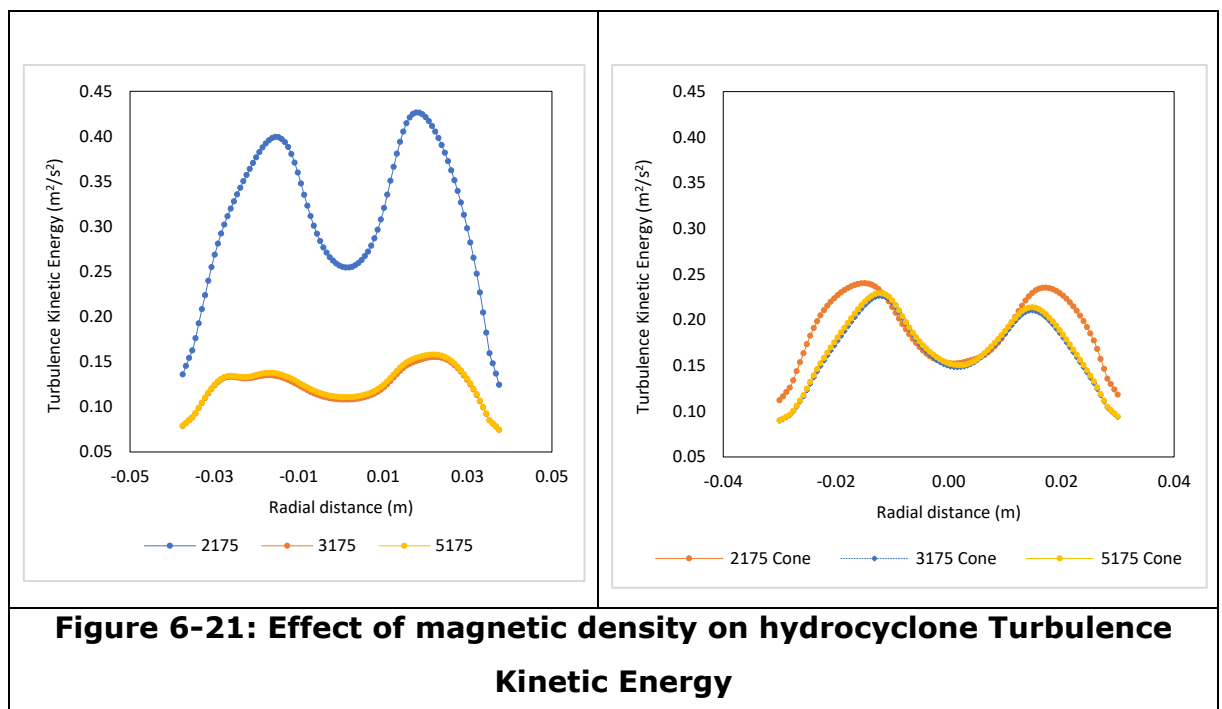
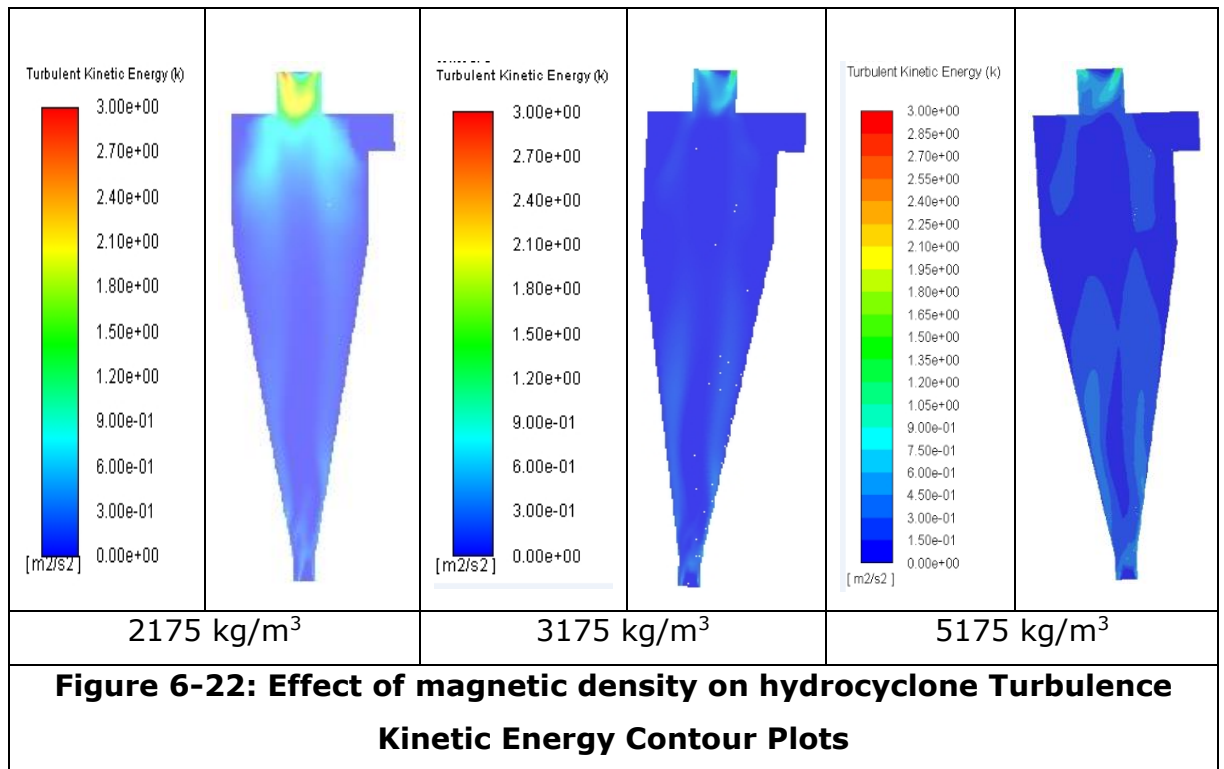


**Figure 6-21: Effect of magnetic density on hydrocyclone Turbulence Kinetic Energy**

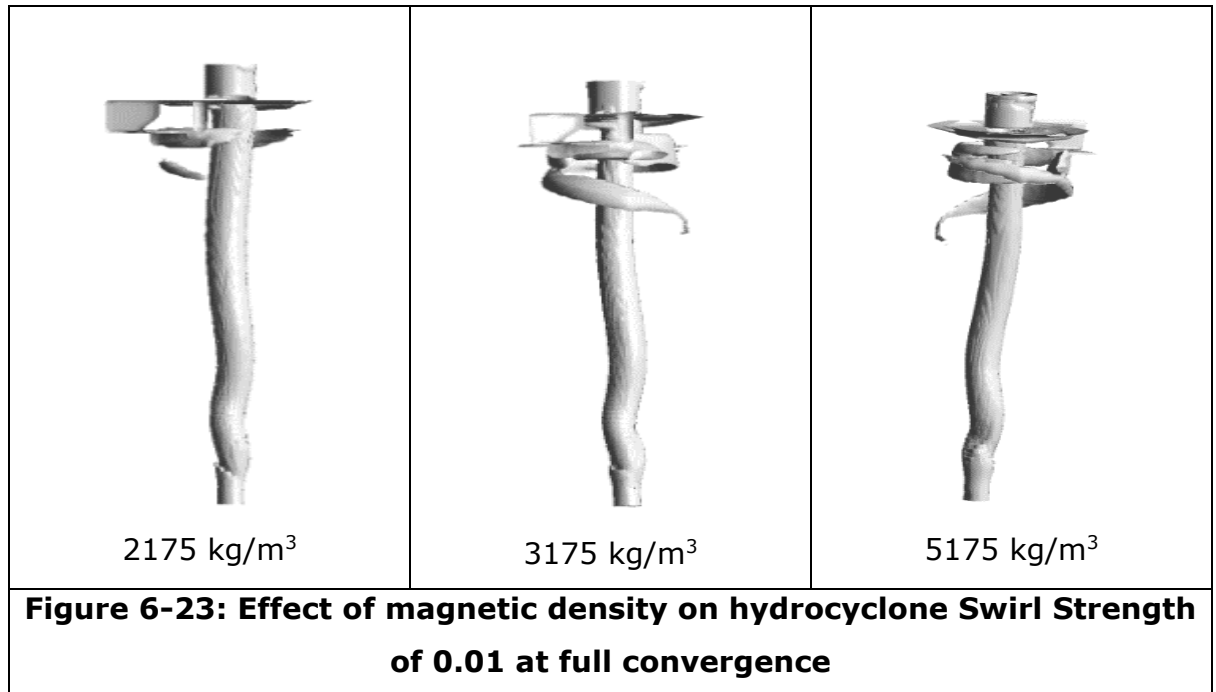
The turbulence kinetic energy contour shown in figure 6-22 below shows the 2175kg/m<sup>3</sup> hydrocyclone having the highest turbulence kinetic energy and that the highest turbulence kinetic energy was seen around the top of the vortex finder for all the hydrocyclones indicating that the swirl effect is very low around this area and consequently the rate of dissipation energy is low, with 2175kg/m<sup>3</sup> having the lowest dissipation energy.



#### 6.4.6 Swirl Strength at Vortex Core Region

From figure 6-23 below, the swirl strength increases with the magnetic particle density with 2175kg/m<sup>3</sup> having a lower swirl strength than 3175 kg/m<sup>3</sup> and 5175 kg/m<sup>3</sup>. The swirl strengths of the 3175kg/m<sup>3</sup> and 5175kg/m<sup>3</sup> were almost the same. Swirl strength is an effective vortex indicator in wall turbulence (Chen 2018) therefore the vortex formation in the higher density microparticle hydrocyclone can be interpreted as being more than vortex formation in the low-density hydrocyclone. Since a highly unsteady turbulent swirling flow is affected by a strong pressure gradient (Mulu, 2014), we can equally conclude that the pressure

gradient in hydrocyclones with 3175 kg/m<sup>3</sup> and 5175 kg/m<sup>3</sup> is more than the pressure gradient in a 2175 kg/m<sup>3</sup> hydrocyclone.



## **6.5 Effect of Charge Density of Micro-particles in Magnetic Hydrocyclone Separation**

Volume charge density is the quantity of the charge per unit volume at any point on a surface charge distribution in a three-dimensional surface. It is measured in coulombs per cubic metre. The effect the surface charge will have on the microparticle performance has been looked at in different fields, results from previous work have shown that the effect of the surface charge depends on the type of microparticle used, the degree of positivity or negativity of the charge, the particle size and on the type of operation that is being reviewed (Daniel, 2010; Kai Xiao, 2011; He, 2010; Li, 2019; Abbas, 2007). Higher charge density has been linked to smaller particle size (Li, 2019; Abbas, 2007) in microparticles, most especially when particles are of the size range of 10nm or smaller, a large particle is expected to have a lower charge density.

Although in this section of the study, we have considered the use of relatively large magnetic particles, the effect the surface charge of the magnetic particle will have on the separation of oil from water will be reviewed. A positive charge was used in

the simulation because positively charged particles naturally move downward while negative charge particles move upward. Since Watson's style of magnetic hydrocyclone was simulated, particles will be attracted to the wall and move down to the spigot; the positive charge is expected to enhance the separation in comparison to the negative charge magnetic particles.

The same geometry used for the other simulations above was modeled with all parameters remaining the same except for the microparticle charge density that was varied. The properties of the microparticles used for the different simulations are shown in the table below.

**Table- 6-4: Magnetic particle properties at varying charge density**

Density (kg/m <sup>3</sup> )	5175	5175	5175	5175
Magnetic permeability (h/m)	1.5	1.5	1.5	1.5
Electrical conductivity (siemens/m)	2000000	2000000	2000000	2000000
Charge density (c/m <sup>3</sup> )	3.0	4.0	6.0	7.02

## Results and Discussion of results

### 6.5.1. Efficiency

From figure 6-24 below, it can be seen that the charge density has minimal effect on the separation efficiency with particles having higher charge density yielding the highest efficiency while the lower surface charge particle has slightly lower efficiency. This can be attributed to the electrostatic repulsion between the particles of the produced water and the micro-doped oil, as the higher the charge density the larger the electrostatic repulsion (Li, 2019, Bossa 2016) and therefore better separation.

An increase in charge density leads to decrease in interfacial assembly (Luo, 2012) between particles and produced water. The repulsive force has a long-range dipolar and short ranges exponentially decaying components, the magnitude of this long-range dipolar interaction is largely determined by the residual charges that remain attached to the oil exposed region of the microparticle (Bossa, 2016).

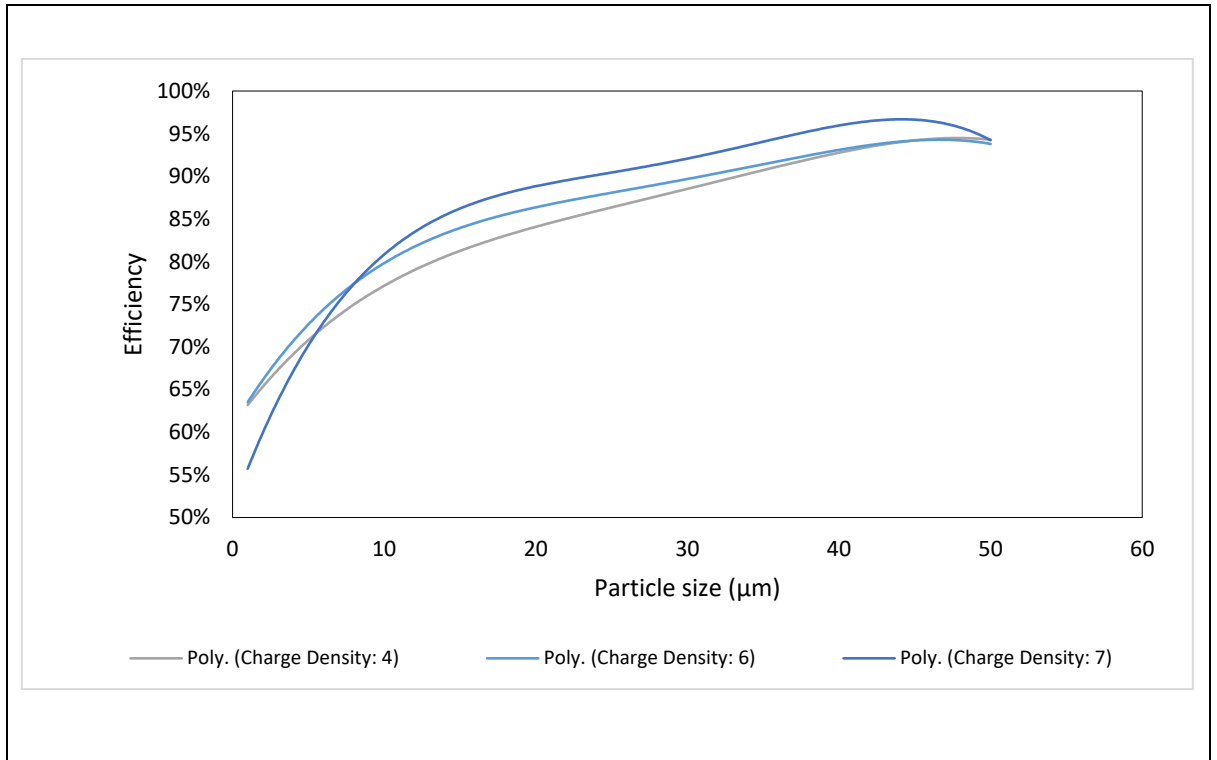


**Figure 6-24: Effect of charge density on hydrocyclone efficiency**

## 6.5.2 Split Ratio

From figure 6-25 below, it can be seen that the pressure drop decreases with increasing split ratio with  $3\text{c/m}^3$  having the highest split ratio of about 96.8% while  $7\text{c/m}^3$  have the lowest split ratio of about 95.3%

Since this type of magnetic hydrocyclone behaves like a typical solid-liquid hydrocyclone, more water is expected at the overflow when the charge density is higher (lowest split ratio) than when the charge density is lower. An increase in the water at the overflow shows better separation and an improved separation will mean more of the magnetic particles will be discharged via the underflow (Yuan, 2015; Jian-Feng Yu, 2016).

Finally, changes in the split ratio are minimal, with the difference in split ratio between  $3.0\text{c/m}^3$  and  $7.0\text{c/m}^3$  less than 2%.

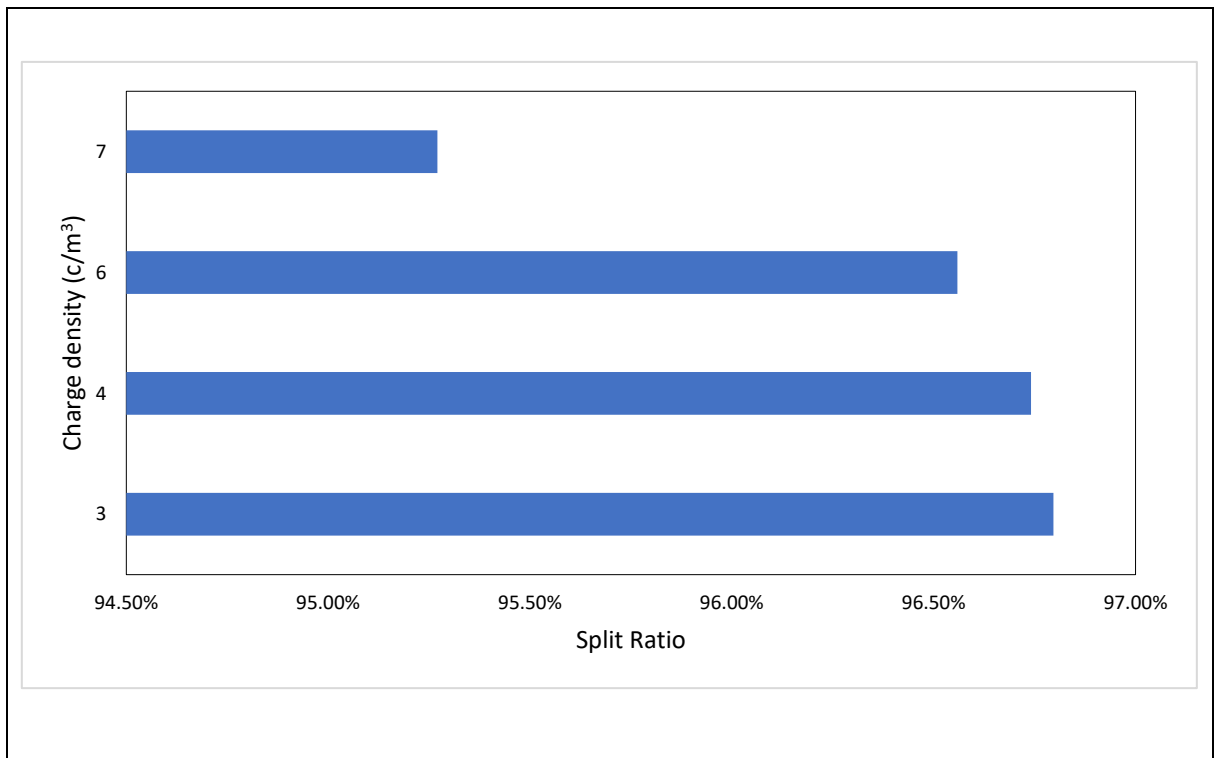


**Figure 6-25: Effect of charge density on hydrocyclone Split Ratio**

### 6.5.3 Velocity Profile

Figure 6-26 below reveals that the velocity profile is weakly affected by the charge densities considered with  $7\text{c/m}^3$  having the highest tangential and axial velocity profile and no change was observed in the radial velocity profile for the varied charge densities.

In the tangential velocities, both the cylindrical and conical sections show the attributes of Rankine vortex with a forced and free vortex at the core and towards the wall respectively. In the free vortex zone, the  $7\text{c/m}^3$  charge density was slightly higher than the other charge densities in both the cylindrical and conical sections. According to Daniel 2007, the velocity of a free particle is directly proportional to the surface charge density on the particle meaning there is a direct relationship between charge density and tangential velocity and consequently the effective force acting on magnetic hydrocyclones (since tangential velocity is a measure of centrifugal force).

Although changes in the axial velocities with varying velocities were minimal, the axial velocities were in accordance with typical hydrocyclone axial velocity. The



conical section also follows the typical hydrocyclone profile with flow reversal towards the overflow of the cyclone.

The radial velocity is the same for all the charge densities showing that radial movement of the fluids and particles are all at the same rate. The radial velocity shows all the attributes of a typical hydrocyclone radial velocity; positive on one side and negative on the other. The positive and negative values are a result of the non-symmetrical nature tangential inlet (Utikar 2010). In accordance with Muschelknautz (1972), the velocity increases towards the vortex finder and decreases away from the vortex finder.

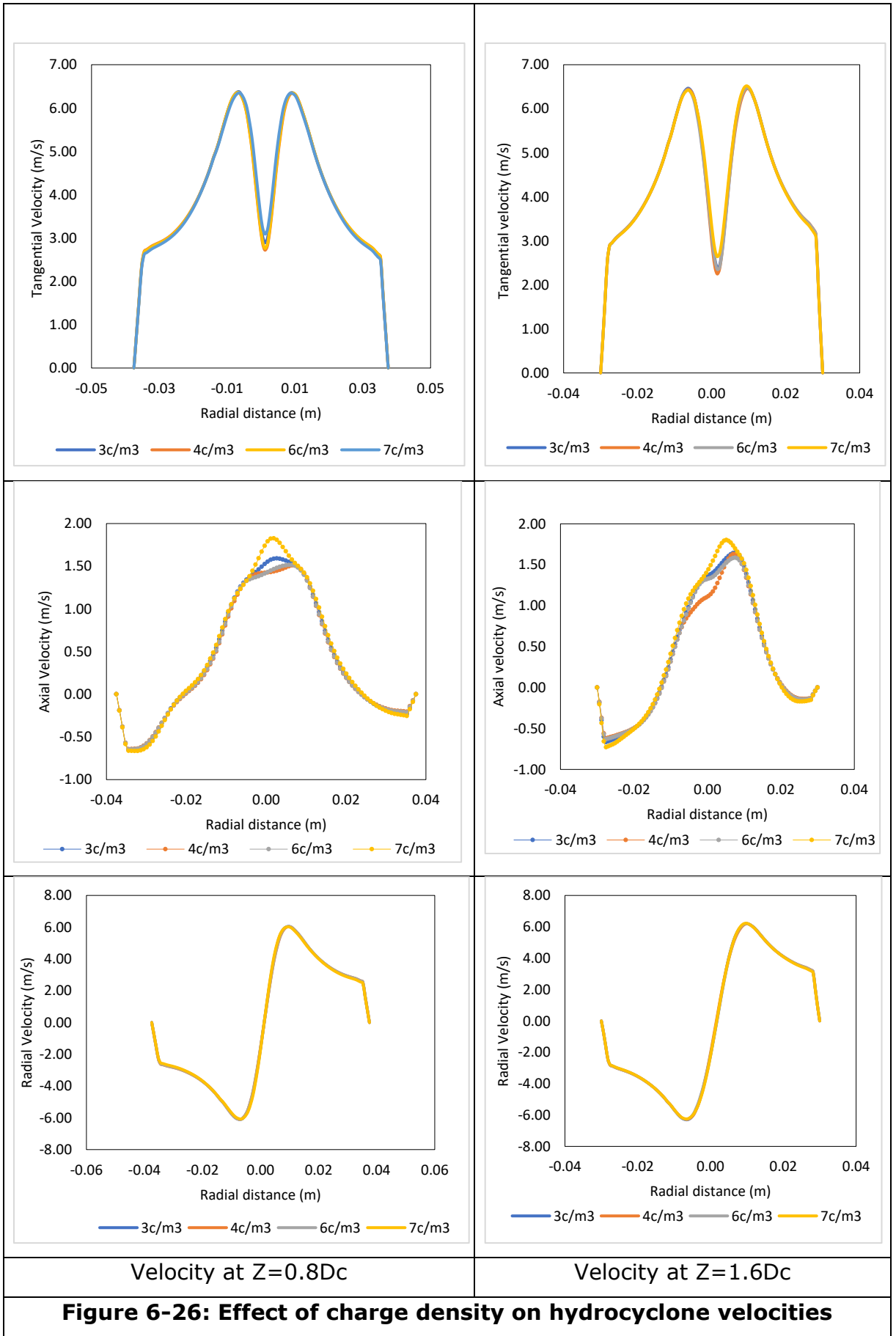
#### **6.5.4 Turbulence Kinetic Energy**

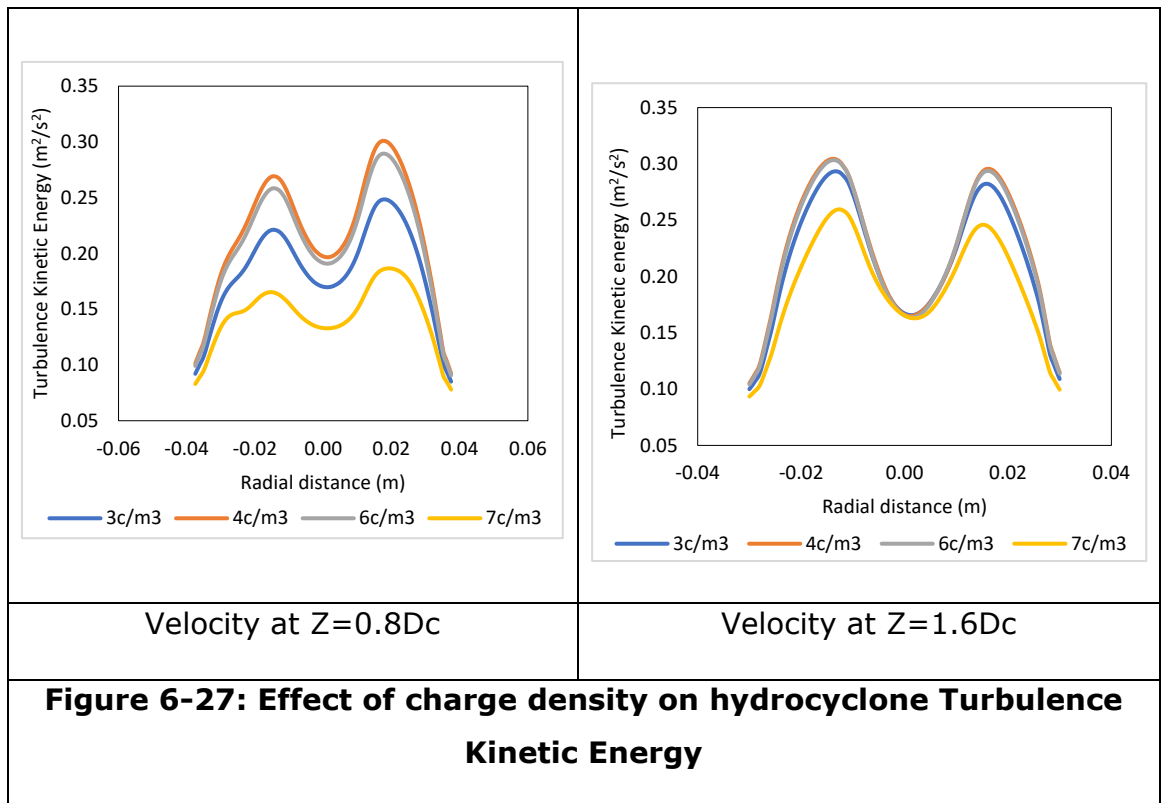
The turbulence kinetic energy determines the mean kinetic energy per unit mass associated with eddy inflow. From figure 6-27 below, it can be seen that with increasing particle charge density, a decrease in turbulence kinetic energy was seen. At small charge density, high turbulence is experienced and this is associated with low dissipation of energy from large eddies to small eddies; this reduces the rate of small eddies production and pressure strain interaction (Torbergsen, 1998) therefore there is a reduction in the conversion of large eddies into small eddies.

Just as in other hydrocyclones, the turbulence kinetic energy at the wall is lowest and as expected the eddies at the centre of the cyclone are highest. At the wall, the small eddies kinetic energy is converted into intermolecular energy but the movement of flow is from the wall to the centre of the fluid, the free stream energy is transferred large eddies and large eddies to smaller eddies (Biferale, 2003).

#### **6.5.5 Swirl Strength at Vortex Core Region**

The result of the swirl shows almost similar strength with increasing charge density. The intensity of the swirl is characterized by the swirl number which is the ratio of the axial flux of the angular momentum to the axial momentum flux times the equivalent radius (Mulu, 2015). The equation for the swirl strength is given in equation 6-f below.





$$S_w = \frac{\int_0^R UVr^2 dr}{R \int_0^R U^2 r dr}$$

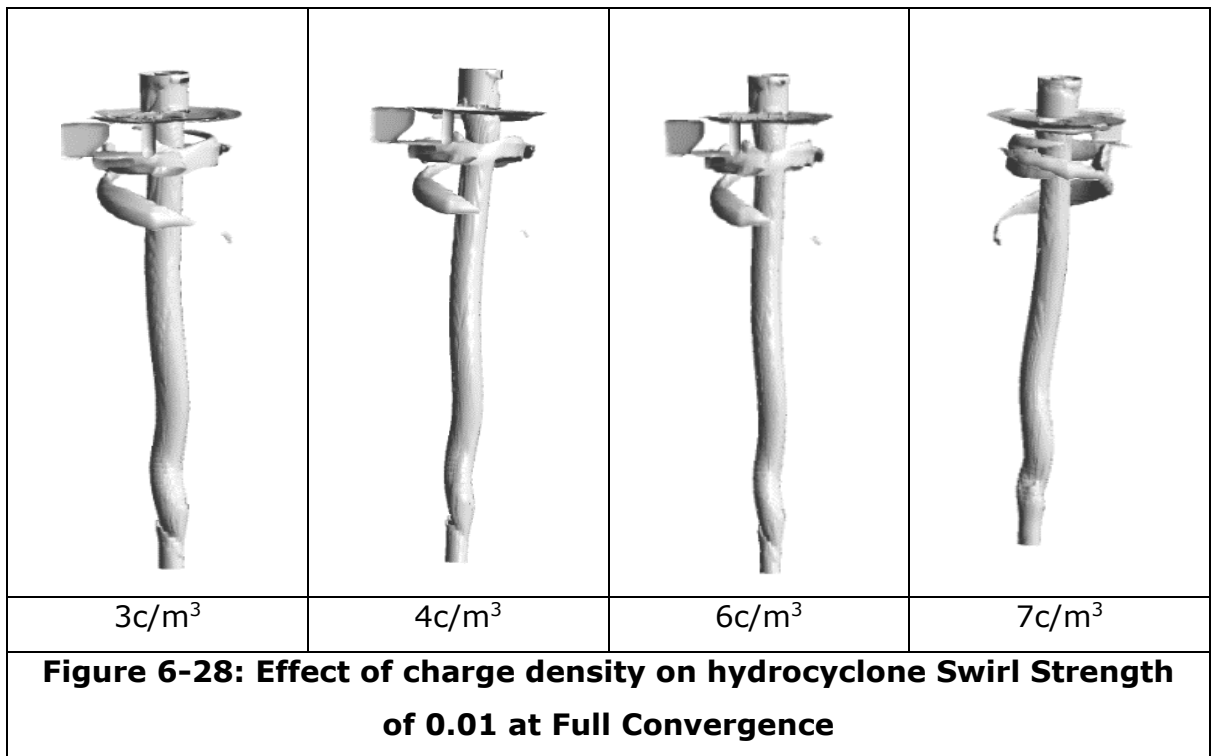
6-f

U= Axial velocity component

V= Tangential velocity component

R= Exit Radius

Since the tangential and the axial velocity are not strongly affected by the particle charge density, the swirl cannot be strongly affected as shown below. The similarity in swirl strength also means the entrainment in the flow is almost the same for all the charge densities considered (Tamrin, 2015; Beer and Chigier, 1972), thus the velocity decay' rate is almost the same.



## 6.6 *Summary of Chapter*

This chapter looks at the effect of the use of a micro-doped hydrocyclone and a magnetic hydrocyclone on the separation of oil from produced water. The micro-doped hydrocyclone evaluates the separation of micro-doped oil without inducing magnetism while the magnetic hydrocyclone evaluates the separation of micro-doped oil with induction of magnetism into the hydrocyclone. The effect the magnetic density, charge density and microparticle permeability will have on the separation efficiency and fluid flow was also evaluated.

The flowrate analysis result shows that the magnetic hydrocyclone yields better separation for particles less than 10µm for all the mass flowrate considered while the micro-doped hydrocyclone performs better to improve the efficiency of particles between 10µm and 30µm. The pressure drop in magnetic hydrocyclone decreases with increasing flowrate; the difference between the pressure drop of micro-doped and magnetic hydrocyclones was in the generation of eddy current due to the introduction of magnetic field. Increasing the concentration of particles was also seen to increase the split ratio in the three types of hydrocyclone examined. The influence of the use of micro-particles and inducing magnetic was more pronounced on the velocity profile when the concentration was lower.

Analysis of the effect of magnetic permeability was seen to show that decreasing magnetic permeability increases drag force, lift force and moment while the velocity profile (tangential, axial and radial) of a lower permeability microparticle hydrocyclone was to have a higher velocity profile than the highly permeable microparticle hydrocyclone. The pressure and split ratio were also seen to decrease with increasing permeability.

The microparticle density result analysis shows that increasing the density of the microparticle increases the separation efficiency; the split ratio, however, increases from a density of  $2175\text{kg/m}^3$  to  $3175\text{kg/m}^3$  after which a further increase of density from  $3175\text{kg/m}^3$  to  $5175\text{kg/m}^3$  did not significantly affect the split ratio. The difference in pressure drop was also not significant but with increasing density yielding a slightly higher pressure drop. The tangential and axial velocity were affected by the change in density with a hydrocyclone with microparticles of  $2175\text{kg/m}^3$  density having lower velocity compared to the  $3175\text{kg/m}^3$  and  $5175\text{kg/m}^3$  hydrocyclone. The turbulence kinetic energy and the swirl strength were also seen to increase with increasing microparticle density.

The final analysis evaluated in this chapter was the effect of charge density of the microparticle on hydrocyclone separation and the result reflects that increasing charge density increases separation, however, it decreases the split ratio although the difference was really small. Changes in the microparticle charge density did not significantly affect the velocity profile but did affect the distribution of the turbulence kinetic energy in the hydrocyclone while the swirl strength remains the same.

## **7.0 Conclusion, Future Work and Recommendation**

### **7.1 Conclusion**

A hydrocyclone is an equipment that can be used for separating liquid or solid separation from produced water. The hydrocyclone has a proven record of efficiently separating particles more than 10-20 $\mu\text{m}$  from produced water. However, when the particle size is less than 10 $\mu\text{m}$ , the separation efficiency of the hydrocyclone greatly reduced. Thus, the research objective is to improve the separation efficiency of the hydrocyclone for fine oil droplets/ particle from produced water in the oil and gas industry. To achieve this aim, the use of microparticles was employed.

The effect of doping the oil in oil emulsion with magnetic particles and using the hydrocyclone to separate the micro doped oil emulsion was analysed. The hydrocyclone used for this was called micro-doped hydrocyclone, the effect of inducing magnetism into the micro-doped hydrocyclone was reviewed using a magnetic hydrocyclone. Computational fluid dynamics (CFD) was used to investigate the influence of microparticles and magnetic induction in hydrocyclone separation. The simulation predicted the performance of a conventional hydrocyclone, micro-doped hydrocyclone and magnetic hydrocyclone. The analysis of the effect of the microparticle charge density, permeability, density was also reviewed in the process to ascertain the influence of this microparticle properties on the separation of the micro-doped oil from water and also the influence on the fluid flow of the hydrocyclones.

The first set of analysis established the efficacy of the use of computational fluid dynamics in analysing fluid flow in a hydrocyclone and confirms the mesh independency of the model. A review of the appropriate RANS turbulence model

was also done using eddy viscosity models (standard  $k-\epsilon$  models, realizable  $k-\epsilon$  models, renormalisation  $k-\epsilon$  models and transition SST model hydrocyclone) with and without curvature correction terms and the RSM model and comparing the model results to Hsieh's experimental results.

The next set of analyses investigates the effect of changing inlet/overflow dimension, outlet/spigot dimension and hydrocyclone cylindrical dimension on hydrocyclone separation and fluid flow. Comparison of liquid-liquid and solid-liquid separation and fluid flow was also reviewed using the same geometry and fluid properties.

From the result of the conventional eddy viscosity models (without curvature correction terms), it was concluded that these models cannot predict the anisotropy flow in a hydrocyclone. It was concluded that for a good accurate prediction of fluid flow in a hydrocyclone, the RSM is the best model to use among the models analysed. However, for a preliminary analysis, any of the eddy viscosity models can be used with the incorporation of curvature correction terms with emphasis on the SST and RNG models which produce better results than standard and realizable  $k-\epsilon$  models.

The geometrical analysis results show that a 75mm cylindrical diameter performs better than the 35mm and 50mm cylindrical diameter hydrocyclone while the 25mm vortex finder and 12.5mm spigot section equally produce better results than other geometrical parameters analysed. Comparison of the liquid-liquid and the solid-liquid hydrocyclone simulation using the same geometry also shows that the solid-liquid hydrocyclone produces a better performance than liquid-liquid separation. Though, most of the fluid flow parameters analysed showed similar result for the solid-liquid and liquid-liquid hydrocyclone with the exception of axial velocity and turbulence kinetic energy where significant changes were seen.

The result of the use of a microparticle and magnetic hydrocyclone shows that a magnetic hydrocyclone can improve the efficiency of particles less than  $10\mu\text{m}$  by more than 30%, therefore it was concluded a magnetic hydrocyclone is better used for particle sizes less than  $10\mu\text{m}$ . The micro-doped hydrocyclone is better to be used to improve the efficiency of particles between  $10-30\mu\text{m}$  while the conventional hydrocyclone is better used for a particle size greater than  $30\mu\text{m}$ . It

can also be concluded that the density difference as a result of the use of microparticle is the most important factor influencing separation.

The influence of microparticle density on magnetic hydrocyclone separation was also reviewed and it was concluded that increasing the density of the microparticle increases the separation efficiency. The split ratio increases from a density of 2175 kg/m<sup>3</sup> to 3175 kg/m<sup>3</sup> after which a further increase of density from 3175 kg/m<sup>3</sup> to 5175 kg/m<sup>3</sup> did not significantly affect the split ratio. The difference in the pressure drop was also not significant but with increasing density yielding a slightly higher pressure drop.

Decreasing magnetic permeability increases the drag force, lift force and moment while a hydrocyclone with lower permeability has higher velocity profile than hydrocyclone with high permeability. The pressure and split ratio also decrease with increasing permeability. Finally increasing the microparticle charge density increases separation, however, it decreases the split ratio although the difference is really small.

Changes in the microparticle charge density did not significantly affect the velocity profile but did affect the distribution of the turbulence kinetic energy in the hydrocyclone while the swirl strength remains the same.

## **7.2 Future Work and Recommendations**

Comprehensive work was done on the use of micro and nano particles and the induction of magnetism into a micro and nano-doped hydrocyclone, analysis of the influence of magnetic particle concentration, charge density, permeability and density on hydrocyclone separation has also been reviewed. However, a good understanding of the type of magnetic particle and the improvement/ development of microparticles that can better improve the efficiency should be looked at in future work.

A mathematical model on the use of the magnetic hydrocyclone is also an important analysis to better understand magnetic and micro-doped hydrocyclone performance. I would also strongly recommend an experimental analysis of this work as a future study and research.



The influence of microparticles on the separation of clay and other fine solid particles should also be reviewed in future work plus the improvement to polymer used in micro-doping.

The use of an electric field instead of magnetic field should be reviewed to reduce the size and weight of the hydrocyclone skid for an industrial setting.

Although the RSM model provides acceptable results, for industrial hydrocyclone analysis LES should be used to carry out any computational analysis on the hydrocyclone.

## References

ABBAS, Z., LABBEZ, C., NORDHOLM, S. and AHLBERG, E., 2008. Size-dependent surface charging of nanoparticles. *The Journal of Physical Chemistry C*, **112**(15), pp. 5715-5723.

ALAHMADI, Y.H. and NOWAKOWSKI, A.F., 2016. Modified shear stress transport model with curvature correction for the prediction of swirling flow in a cyclone separator. *Chemical Engineering Science*, **147**, pp. 150-165.

AL-KAYIEM, H., OSEI, H., YIN, K. and HASHIM, F., 2014. A comparative study on the hydrodynamics of liquid–liquid hydrocyclonic separation. *WIT Transactions on Engineering Sciences*, **82**, pp. 361-370.

AL-KAYIEM, H.H., OSEI, H., HASHIM, F.M. and HAMZA, J.E., 2019. Flow structures and their impact on single and dual inlets hydrocyclone performance for oil–water separation. *Journal of Petroleum Exploration and Production Technology*, **9**(4), pp. 2943-2952.

AROLLA, S.K. and DURBIN, P.A., 2014. A rotation/curvature correction for turbulence models for applied CFD. *Progress in Computational Fluid Dynamics, an International Journal*, **14**(6), pp. 341-351.

ARTERBURN, R.A., 1982. The sizing and selection of hydrocyclones. *Design and Installation of Comminution Circuits*, **1**, pp. 597-607.

ATTA, A.M., EZZAT, A.O. and HASHEM, A.I., 2017. Synthesis and application of monodisperse hydrophobic magnetite nanoparticles as an oil spill collector using an ionic liquid. *RSC advances*, **7**(27), pp. 16524-16530.

AZADI, M., AZADI, M. and MOHEBBI, A., 2010. A CFD study of the effect of cyclone size on its performance parameters. *Journal of hazardous materials*, **182**(1-3), pp. 835-841.

BAI, Z., WANG, H. and TU, S., 2009. Experimental study of flow patterns in deoiling hydrocyclone. *Minerals Engineering*, **22**(4), pp. 319-323.

BANNISTER, J.D., 1970. *Superconductive magnetic separator*, .

- BAO, L., ZHONG, C., JIE, P. and HOU, Y., 2019. The effect of nanoparticle size and nanoparticle aggregation on the flow characteristics of nanofluids by molecular dynamics simulation. *Advances in Mechanical Engineering*, **11**(11), pp. 1687814019889486.
- BEATRICE, C., FIORILLO, F., LANDGRAF, F., LAZARO-COLAN, V., JANASI, S. and LEICHT, J., 2008. Magnetic loss, permeability dispersion, and role of eddy currents in Mn–Zn sintered ferrites. *Journal of Magnetism and Magnetic Materials*, **320**(20), pp. e865-e868.
- BHASKAR, K.U., MURTHY, Y.R., RAJU, M.R., TIWARI, S., SRIVASTAVA, J. and RAMAKRISHNAN, N., 2007. CFD simulation and experimental validation studies on hydrocyclone. *Minerals Engineering*, **20**(1), pp. 60-71.
- BHUYAN, P.J. and GOSWAMI, K.S., 2008. Effect of magnetic field on MHD pressure drop inside a rectangular conducting duct. *IEEE Transactions on Plasma Science*, **36**(4), pp. 1955-1959.
- BIANCO, V., KHAIT, A., NOSKOV, A. and ALEKHIN, V., 2016. A comparison of the application of RSM and LES turbulence models in the numerical simulation of thermal and flow patterns in a double-circuit Ranque-Hilsch vortex tube. *Applied Thermal Engineering*, **106**, pp. 1244-1256.
- BICALHO, I.C., MOGNON, J.L., SHIMOYAMA, J., ATAÍDE, C.H. and DUARTE, C.R., 2012. Separation of yeast from alcoholic fermentation in small hydrocyclones. *Separation and purification technology*, **87**, pp. 62-70.
- BO, T., XU, Y., SONG, X., ZE, S. and YU, J., 2017. Effect of inlet configuration on hydrocyclone performance. *Transactions of Nonferrous Metals Society of China*, **27**(7), pp. 1645-1655.
- BRAR, L.S., SHARMA, R. and ELSAYED, K., 2015. The effect of the cyclone length on the performance of Stairmand high-efficiency cyclone. *Powder Technology*, **286**, pp. 668-677.
- BREN~ A DE LA ROSA, A, WANG, G. and BACHALO, W., 1992. The effect of swirl on the velocity and turbulence fields of a liquid spray.
- BRENNAN, M.S., NARASIMHA, M. and HOLTHAM, P.N., 2007. Multiphase modelling of hydrocyclones–prediction of cut-size. *Minerals Engineering*, **20**(4), pp. 395-406.

- BRITO-PARADA, P.R., DEWES, R.M., VEGA-GARCIA, D. and CILLIERS, J.J., 2018. Influence of Design Parameters on Biomass Separation in Mini-hydrocyclones. *Chemical Engineering & Technology*, **41**(12), pp. 2323-2330.
- CHAN, E.C. and LIEN, F., 2005. Permeability effects of turbulent flow through a porous insert in a backward-facing-step channel. *Transport in Porous Media*, **59**(1), pp. 47-71.
- CHAWARE, P. and SEWATKAR, C., 2017. Effects of tangential and radial velocity on the heat transfer for flow through pipe with twisted tape insert-turbulent flow. *International Journal of Heat and Technology*, **35**(4), pp. 811-820.
- CHEN, H., LI, D., BAI, R. and WANG, X., 2018. Comparison of swirling strengths derived from two-and three-dimensional velocity fields in channel flow. *AIP Advances*, **8**(5), pp. 055302.
- CHEN, J., YANG, B., JIANG, Z. and WANG, Y., 2019. Effect of External Cyclone Diameter on Performance of a Two-Stage Cyclone Separator. *ACS omega*, **4**(8), pp. 13603-13616.
- CHENG, G., NICHOLS, R., NEROORKAR, K. and RADHAMONY, P., 2009. Validation and assessment of turbulence transition models, *47th AIAA Aerospace Sciences Meeting including The New Horizons Forum and Aerospace Exposition 2009*, pp. 1141.
- CHINÉ, B. and CONCHA, F., 2000. Flow patterns in conical and cylindrical hydrocyclones. *Chemical Engineering Journal*, **80**(1-3), pp. 267-273.
- CHU, L., QIN, J., CHEN, W. and LEE, X., 2000. Energy consumption and its reduction in the hydrocyclone separation process. II. Time-averaged and fluctuating characteristics of the turbulent pressure in a hydrocyclone. *Separation Science and Technology*, **35**(15), pp. 2543-2560.
- CILLIERS, J., 2000. Hydrocyclones for particle size separation. *UMIST: Manchester, UK*, .
- CONCHA, F., BARRIENTOS, A., MONTERO, J. and SAMPAIO, R., 1996. Air core and roping in hydrocyclones. *International Journal of Mineral Processing*, **44**, pp. 743-749.

- COUËDEL, L., ARTIS, D., KHANAL, M., PARDANAUD, C., COUSSAN, S., LEBLANC, S., HALL, T., THOMAS JR, E., KONOPKA, U. and PARK, M., 2019. Influence of magnetic field strength on nanoparticle growth in a capacitively-coupled radio-frequency Ar/C<sub>2</sub>H<sub>2</sub> discharge. *Plasma Research Express*, **1**(1), pp. 015012.
- CUI, B., ZHANG, C., WEI, D., LU, S. and FENG, Y., 2017. Effects of feed size distribution on separation performance of hydrocyclones with different vortex finder diameters. *Powder Technology*, **322**, pp. 114-123.
- CULLIVAN, J., WILLIAMS, R.A. and CROSS, R., 2003. Understanding the hydrocyclone separator through computational fluid dynamics. *Chemical Engineering Research and Design*, **81**(4), pp. 455-466.
- DANIEL, M., TSVETKOVA, I.B., QUINKERT, Z.T., MURALI, A., DE, M., ROTELLO, V.M., KAO, C.C. and DRAGNEA, B., 2010. Role of surface charge density in nanoparticle-templated assembly of bromovirus protein cages. *ACS nano*, **4**(7), pp. 3853-3860.
- DAOUSH, W., 2017. Co-precipitation and magnetic properties of magnetite nanoparticles for potential biomedical applications. *J.Nanomed.Res*, **5**(3), pp. 00118.
- DAS, B., DHARA, S. and RASTOGI, A., 1995. Magnetic study above the curie temperature of  $\gamma$ -Fe<sub>2</sub>O<sub>3</sub> in determining the dispersion nature of Co<sup>2+</sup> ions in Co-modified  $\gamma$ -Fe<sub>2</sub>O<sub>3</sub> thin films. *Bulletin of Materials Science*, **18**(8), pp. 989-996.
- DAVIS, P., RINEHIMER, A. and UDDIN, M., 2012. A comparison of RANS-based turbulence modeling for flow over a wall-mounted square cylinder, *20th Annual Conference of the CFD Society of Canada 2012*.
- DE NIJS, M.A. and PIETRZAK, J.D., 2012. On total turbulent energy and the passive and active role of buoyancy in turbulent momentum and mass transfer. *Ocean dynamics*, **62**(6), pp. 849-865.
- DEJOAN, A., SANTIAGO, J.L., PINELLI, A. and MARTILLI, A., 2007. Comparison between LES and RANS computations for the study of contaminant dispersion in the MUST field experiment, 2007, AMS.

DELGADILLO, J.A. and RAJAMANI, R.K., 2005. A comparative study of three turbulence-closure models for the hydrocyclone problem. *International Journal of Mineral Processing*, **77**(4), pp. 217-230.

DLAMINI, N.G., BASSON, A.K. and PULLABHOTLA, V.S.R., 2019. Optimization and Application of Bioflocculant Passivated Copper Nanoparticles in the Wastewater Treatment. *International journal of environmental research and public health*, **16**(12), pp. 2185.

DORIS, M., AZIZ, F., ALHUMMIANY, H., BAWAZEER, T., ALSENANY, N., MAHMOUD, A., ZAKARIA, R., SULAIMAN, K. and SUPANGAT, A., 2017. Determining the effect of centrifugal force on the desired growth and properties of PCPDTBT as p-type nanowires. *Nanoscale research letters*, **12**(1), pp. 67.

DURDEVIC, P., PEDERSEN, S. and YANG, Z., 2017. Challenges in modelling and control of offshore de-oiling hydrocyclone systems, *Journal of Physics: Conference Series* 2017, IOP Publishing, pp. 012048.

DURDEVIC, P. and YANG, Z., 2018. Dynamic Efficiency Analysis of an Off-Shore Hydrocyclone System, Subjected to a Conventional PID-and Robust-Control-Solution. *Energies*, **11**(9), pp. 2379.

ELLIOTT, K., SAVORY, E., MARTINUZZI, R. and LIN, W., 2012. Analysis of a curvature corrected turbulence model using a 90 degree curved geometry modelled after a centrifugal compressor impeller. *Computational Fluid Dynamics (CFD) Society of Canada (CFDSC)*, .

ELSAYED, K. and LACOR, C., 2013. The effect of cyclone vortex finder dimensions on the flow pattern and performance using LES. *Computers & Fluids*, **71**, pp. 224-239.

ELSAYED, K. and LACOR, C., 2011. The effect of cyclone inlet dimensions on the flow pattern and performance. *Applied Mathematical Modelling*, **35**(4), pp. 1952-1968.

ENDRES, E., DUECK, J. and NEESSE, T., 2012. Hydrocyclone classification of particles in the micron range. *Minerals Engineering*, **31**, pp. 42-45.

- ERIKLI, Ş. and OLCAY, A., 2015. Inlet Diameter and Flow Volume Effects on Separation and Energy Efficiency of Hydrocyclones, *IOP Conference Series: Materials Science and Engineering* 2015, IOP Publishing, pp. 012074.
- ESAKKIMUTHU, T., SIVAKUMAR, D. and AKILA, S., 2014. Application of nanoparticles in wastewater treatment. *Pollut.Res*, **33**(03), pp. 567-571.
- EZZAIER, H., MARINS, J.A., CLAUDET, C., HEMERY, G., SANDRE, O. and KUZHIR, P., 2018. Kinetics of aggregation and magnetic separation of multicore iron oxide nanoparticles: effect of the grafted layer thickness. *Nanomaterials*, **8**(8), pp. 623.
- FAKHRU'L-RAZI, A., PENDASHTEH, A., ABDULLAH, L.C., BIAK, D.R.A., MADAENI, S.S. and ABIDIN, Z.Z., 2009. Review of technologies for oil and gas produced water treatment. *Journal of hazardous materials*, **170**(2-3), pp. 530-551.
- FAN, X., 2016. Oil-water separation efficiency and fluid mechanics of a hydrocyclone, *2016 7th International Conference on Mechatronics, Control and Materials (ICMCM 2016)* 2016, Atlantis Press.
- FARIAS, F., SOUZA, J., LIMA, W., MACÊDO, A., NETO, S. and LIMA, A., 2016. Influence of Geometric Parameters of the hydrocyclone and sand concentration on the water/sand/heavy-oil separation process: Modeling and Simulation. *The International Journal of Multiphysics*, **5**(3),.
- FAROKHI, S., TAGHAVI, R. and RICE, E., 1988. Effect of initial tangential velocity distribution on the mean evolution of a swirling turbulent free jet, *1st National Fluid Dynamics Conference* 1988, pp. 3592.
- FASSANI, F.L. and GOLDSTEIN JR, L., 2000. A study of the effect of high inlet solids loading on a cyclone separator pressure drop and collection efficiency. *Powder Technology*, **107**(1-2), pp. 60-65.
- FICICI, F., ARI, V. and KAPSIZ, M., 2010. The effects of vortex finder on the pressure drop in cyclone separators. *Int J Phys Sci*, **5**(6), pp. 804-813.
- FISHER, M. and FLACK, R., 2002. Velocity distributions in a hydrocyclone separator. *Experiments in Fluids*, **32**(3), pp. 302-312.

FORNARI, W., FORMENTI, A., PICANO, F. and BRANDT, L., 2016. The effect of particle density in turbulent channel flow laden with finite size particles in semi-dilute conditions. *Physics of Fluids*, **28**(3), pp. 033301.

FU, S., HUA, W., YUAN, H., LING, J. and SHI, Q., 2019. Study on the light medium separation of waste plastics with hydrocyclones. *Waste Management*, **91**, pp. 54-61.

GANDHI, A., PAUL, A., SEN, S.O. and SEN, K.K., 2015. Studies on thermoresponsive polymers: Phase behaviour, drug delivery and biomedical applications. *asian journal of pharmaceutical sciences*, **10**(2), pp. 99-107.

GARCÍA-MARTÍN, J., GÓMEZ-GIL, J. and VÁZQUEZ-SÁNCHEZ, E., 2011. Non-destructive techniques based on eddy current testing. *Sensors*, **11**(3), pp. 2525-2565.

GARG, R.P., FERZIGER, J.H., MONISMITH, S.G. and KOSEFF, J.R., 2000. Stably stratified turbulent channel flows. I. Stratification regimes and turbulence suppression mechanism. *Physics of Fluids*, **12**(10), pp. 2569-2594.

GHODRAT, M., KUANG, S., YU, A., VINCE, A., BARNETT, G. and BARNETT, P.J., 2014. Numerical analysis of hydrocyclones with different vortex finder configurations. *Minerals Engineering*, **63**, pp. 125-138.

GHODRAT, M., KUANG, S., YU, A., VINCE, A., BARNETT, G.D. and BARNETT, P.J., 2013. Computational study of the multiphase flow and performance of hydrocyclones: effects of cyclone size and spigot diameter. *Industrial & Engineering Chemistry Research*, **52**(45), pp. 16019-16031.

GHODRAT, M., QI, Z., KUANG, S., JI, L. and YU, A., 2016. Computational investigation of the effect of particle density on the multiphase flows and performance of hydrocyclone. *Minerals Engineering*, **90**, pp. 55-69.

GRADY, S., WESSON, G., ABDULLAH, M. and KALU, E., 2003. Prediction of 10-mm hydrocyclone separation efficiency using computational fluid dynamics. *Filtration & Separation*, **40**(9), pp. 41-46.

GUMFEKAR, S.P., VAJIHINEJAD, V. and SOARES, J.B., 2019. Advanced Polymer Flocculants for Solid–Liquid Separation in Oil Sands Tailings. *Macromolecular rapid communications*, **40**(1), pp. 1800644.



GUTIERREZ, A.M., DZIUBLA, T.D. and HILT, J.Z., 2017. Recent advances on iron oxide magnetic nanoparticles as sorbents of organic pollutants in water and wastewater treatment. *Reviews on environmental health*, **32**(1-2), pp. 111-117.

HANJALIC, K., 2004. Closure models for incompressible turbulent flows. *Lecture Notes at Von Kármán Institute*, **75**.

HATAMIE, A., PARHAM, H., ZARGAR, B. and HEIDARI, Z., 2016. Evaluating magnetic nano-ferrofluid as a novel coagulant for surface water treatment. *Journal of Molecular Liquids*, **219**, pp. 694-702.

HE, C., HU, Y., YIN, L., TANG, C. and YIN, C., 2010. Effects of particle size and surface charge on cellular uptake and biodistribution of polymeric nanoparticles. *Biomaterials*, **31**(13), pp. 3657-3666.

HE, F., ZHANG, Y., WANG, J., YANG, Q., WANG, H. and TAN, Y., 2013. Flow Patterns in Mini-Hydrocyclones with Different Vortex Finder Depths. *Chemical Engineering & Technology*, **36**(11), pp. 1935-1942.

HLONGWANE, G.N., SEKOAI, P.T., MEYYAPPAN, M. and MOOTHI, K., 2019. Simultaneous removal of pollutants from water using nanoparticles: A shift from single pollutant control to multiple pollutant control. *Science of the Total Environment*, **656**, pp. 808-833.

HONDA, R.J., KEENE, V., DANIELS, L. and WALKER, S.L., 2014. Removal of TiO<sub>2</sub> nanoparticles during primary water treatment: role of coagulant type, dose, and nanoparticle concentration. *Environmental Engineering Science*, **31**(3), pp. 127-134.

HOSOKAWA, S. and TOMIYAMA, A., 2003. Turbulence modification in gas-liquid and solid-liquid dispersed two-phase pipe flows, *Third Symposium on Turbulence and Shear Flow Phenomena 2003*, Begel House Inc.

HSU, C. and WU, R., 2010. Effect of overflow depth of a hydrocyclone on particle separation. *Drying Technology*, **28**(7), pp. 916-921.

HUANG, L., DENG, S., GUAN, J., HUA, W. and CHEN, M., 2018. Separation performance of a novel liquid-liquid dynamic hydrocyclone. *Industrial & Engineering Chemistry Research*, **57**(22), pp. 7613-7623.

HWANG, K., WU, W., QIAN\*, S. and NAGASE, Y., 2008. CFD study on the effect of hydrocyclone structure on the separation efficiency of fine particles. *Separation Science and Technology*, **43**(15), pp. 3777-3797.

IGUNNU, E.T. and CHEN, G.Z., 2014. Produced water treatment technologies. *International Journal of Low-Carbon Technologies*, **9**(3), pp. 157-177.

IOZIA, D.L. and LEITH, D., 1989. Effect of cyclone dimensions on gas flow pattern and collection efficiency. *Aerosol Science and Technology*, **10**(3), pp. 491-500.

ITO, S., OGAWA, K. and KURODA, C., 1980. Turbulent swirling flow in a circular pipe. *Journal of Chemical Engineering of Japan*, **13**(1), pp. 6-10.

JAKOBSEN, H.A., 2008. Chemical reactor modeling. *Multiphase Reactive Flows*, .

JI, L., KUANG, S., QI, Z., WANG, Y., CHEN, J. and YU, A., 2017. Computational analysis and optimization of hydrocyclone size to mitigate adverse effect of particle density. *Separation and Purification Technology*, **174**, pp. 251-263.

JI, Z., XIONG, Z., WU, X., CHEN, H. and WU, H., 2009. Experimental investigations on a cyclone separator performance at an extremely low particle concentration. *Powder Technology*, **191**(3), pp. 254-259.

JIANG, J., YING, R., FENG, J. and WANG, W., 2018. Computational and Experimental Study of the Effect of Operating Parameters on Classification Performance of Compound Hydrocyclone. *Mathematical Problems in Engineering*, **2018**.

JIANG, L., LIU, P., YANG, X., ZHANG, Y., WANG, H. and XU, C., 2019. Numerical analysis of flow field and separation characteristics in hydrocyclones with adjustable apex. *Powder Technology*, **356**, pp. 941-956.

JIANG, L., LIU, P., ZHANG, Y., YANG, X. and WANG, H., 2019. The Effect of Inlet Velocity on the Separation Performance of a Two-Stage Hydrocyclone. *Minerals*, **9**(4), pp. 209.

JIMÉNEZ, S., MICÓ, M., ARNALDOS, M., MEDINA, F. and CONTRERAS, S., 2018. State of the art of produced water treatment. *Chemosphere*, **192**, pp. 186-208.

KAUSHAL, D., SATO, K., TOYOTA, T., FUNATSU, K. and TOMITA, Y., 2005. Effect of particle size distribution on pressure drop and concentration profile in pipeline

flow of highly concentrated slurry. *International Journal of Multiphase Flow*, **31**(7), pp. 809-823.

KAYA, F. and KARAGOZ, I., 2012. Experimental and numerical investigation of pressure drop coefficient and static pressure difference in a tangential inlet cyclone separator. *Chemical Papers*, **66**(11), pp. 1019-1025.

KHAROUA, N., KHEZZAR, L. and NEMOUCHI, Z., 2010. Computational fluid dynamics study of the parameters affecting oil–water hydrocyclone performance. *Proceedings of the Institution of Mechanical Engineers, Part E: Journal of Process Mechanical Engineering*, **224**(2), pp. 119-128.

KHAROUA, N., KHEZZAR, L. and NEMOUCHI, Z., 2010. Hydrocyclones for de-oiling applications—A review. *Petroleum Science and Technology*, **28**(7), pp. 738-755.

KHAROUA, N., KHEZZAR, L. and NEMOUCHI, Z., 2011. Study of the pressure drop and flow field in standard gas cyclone models using the granular model. *International Journal of Chemical Engineering*, **2011**.

KLAENTSCHI, K., BROWN, J.A., NIBLETT, P.G., SHORE, A.C. and TOOKE, J.E., 1998. Pressure-permeability relationships in basement membrane: effects of static and dynamic pressures. *American Journal of Physiology-Heart and Circulatory Physiology*, **274**(4), pp. H1327-H1334.

KO, J., ZAHRAI, S., MACCHION, O. and VOMHOFF, H., 2006. Numerical modeling of highly swirling flows in a through-flow cylindrical hydrocyclone. *AIChE Journal*, **52**(10), pp. 3334-3344.

KÖNÖZSY, L., 2019. *A new hypothesis on the anisotropic Reynolds stress tensor for turbulent flows*. Springer.

KUHN, S.J., HALLAHAN, D.E. and GIORGIO, T.D., 2006. Characterization of superparamagnetic nanoparticle interactions with extracellular matrix in an in vitro system. *Annals of Biomedical Engineering*, **34**(1), pp. 51-58.

KUMAR, S., AHLAWAT, W., BHANJANA, G., HEYDARIFARD, S., NAZHAD, M.M. and DILBAGHI, N., 2014. Nanotechnology-based water treatment strategies. *Journal of nanoscience and nanotechnology*, **14**(2), pp. 1838-1858.

LAUNDER, B.E. and SPALDING, D.B., 1983. The numerical computation of turbulent flows. *Numerical prediction of flow, heat transfer, turbulence and combustion*. Elsevier, pp. 96-116.

LEE, J.W., YANG, H.J. and LEE, D.Y., 2006. Effect of the cylinder shape of a long-coned cyclone on the stable flow-field establishment. *Powder Technology*, **165**(1), pp. 30-38.

LI, S., TORSÆTER, O., LAU, H.C., HADIA, N.J. and STUBBS, L.P., 2019. The Impact of Nanoparticle Adsorption on Transport and Wettability Alteration in Water-Wet Berea Sandstone: An Experimental Study. *Frontiers in Physics*, **7**, pp. 74.

LIANG, Y., NING, Y., LIAO, L. and YUAN, B., 2018. Special focus on produced water in oil and gas fields: origin, management, and reinjection practice. *Formation Damage During Improved Oil Recovery*. Elsevier, pp. 515-586.

LIM, K., KWON, S. and LEE, K., 2003. Characteristics of the collection efficiency for a double inlet cyclone with clean air. *Journal of Aerosol Science*, **34**(8), pp. 1085-1095.

LIU, B., WANG, H., LI, L., ZHAO, Z., XU, L. and XUE, J., 2019. Study of GLR and Inlet Velocity on Hydrocyclone for Fracturing Flow-Back Fluids. *Mathematical Problems in Engineering*, **2019**.

LIU, H., XU, J., ZHANG, J., SUN, H., ZHANG, J. and WU, Y., 2012. Oil/water separation in a liquid-liquid cylindrical cyclone. *Journal of Hydrodynamics, Ser.B*, **24**(1), pp. 116-123.

LIU, M., CHEN, J., CAI, X., HAN, Y. and XIONG, S., 2018. Oil-water pre-separation with a novel axial hydrocyclone. *Chinese Journal of Chemical Engineering*, **26**(1), pp. 60-66.

LU, Y., ZHOU, L. and SHEN, X., 2000. Numerical simulation of strongly swirling turbulent flows in a liquid-liquid hydrocyclone using the Reynolds stress transport equation model. *Science in China Series E: Technological Sciences*, **43**(1), pp. 86.

LUO, M., OLIVIER, G.K. and FRECHETTE, J., 2012. Electrostatic interactions to modulate the reflective assembly of nanoparticles at the oil-water interface. *Soft Matter*, **8**(47), pp. 11923-11932.

- LUTZ, J., AKDEMIR, Ö. and HOTH, A., 2006. Point by point comparison of two thermosensitive polymers exhibiting a similar LCST: is the age of poly (NIPAM) over? *Journal of the American Chemical Society*, **128**(40), pp. 13046-13047.
- MARGHUSSIAN, V. and MARGHUSSIAN, V., 2015. Magnetic properties of nano-glass ceramics. *Nano-Glass Ceramics*, , pp. 181-223.
- MARTÍNEZ, L.F., LAVÍN, A.G., MAHAMUD, M.M. and BUENO, J.L., 2008. Vortex finder optimum length in hydrocyclone separation. *Chemical Engineering and Processing: Process Intensification*, **47**(2), pp. 192-199.
- MARTINS, N.M., CARRIÇO, N.J., COVAS, D. and RAMOS, H., 2014. Velocity-distribution in pressurized pipe flow using cfd: mesh independence analysis, *Third IAHR Europe Congress 2014*, pp. 145-156.
- MATEI, E., PREDESCU, A. and VASILE, E., 2011. Properties of magnetic iron oxides used as materials for wastewater treatment, *Journal of Physics: Conference Series* 2011, IOP Publishing, pp. 012022.
- MATEUS, G.A.P., PALUDO, M.P., DOS SANTOS, TÁSSIA RHUNA TONIAL, SILVA, M.F., NISHI, L., FAGUNDES-KLEN, M.R., GOMES, R.G. and BERGAMASCO, R., 2018. Obtaining drinking water using a magnetic coagulant composed of magnetite nanoparticles functionalized with Moringa oleifera seed extract. *Journal of environmental chemical engineering*, **6**(4), pp. 4084-4092.
- MATVIENKO, O., 2004. Analysis of turbulence models and investigation of the structure of the flow in a hydrocyclone. *Journal of Engineering Physics and Thermophysics*, **77**(2), pp. 316-323.
- MAZHAR, Z., 2016. *Fully Implicit, Coupled Procedures in Computational Fluid Dynamics*. Springer.
- MEIRELES, M., BOURGEOIS, F., TOURBIN, M., GUIRAUD, P. and FRANCES, C., 2010. Removal of oversize & recovery of particles from suspensions in the nano size range.
- MENG, S., LI, X., YAN, X., WANG, L., ZHANG, H. and CAO, Y., 2019. Turbulence Models for Single Phase Flow Simulation of Cyclonic Flotation Columns. *Minerals*, **9**(8), pp. 464.

- MENTER, F.R., 2009. Review of the shear-stress transport turbulence model experience from an industrial perspective. *International journal of computational fluid dynamics*, **23**(4), pp. 305-316.
- MENTER, F.R., 1994. Two-equation eddy-viscosity turbulence models for engineering applications. *AIAA Journal*, **32**(8), pp. 1598-1605.
- MENTER, F.R., LANGTRY, R.B., LIKKI, S., SUZEN, Y., HUANG, P. and VÖLKER, S., 2006. A correlation-based transition model using local variables—part I: model formulation.
- MENTER, F., GARBARUK, A. and EGOROV, Y., 2012. Explicit algebraic Reynolds stress models for anisotropic wall-bounded flows. *Progress in Flight Physics*, **3**, pp. 89-104.
- MENTER, F., LANGTRY, R. and VÖLKER, S., 2006. Transition modelling for general purpose CFD codes. *Flow, turbulence and combustion*, **77**(1-4), pp. 277-303.
- MOKNI, I., DHAOUADI, H., BOURNOT, P. and MHIRI, H., 2015. Numerical investigation of the effect of the cylindrical height on separation performances of uniflow hydrocyclone. *Chemical Engineering Science*, **122**, pp. 500-513.
- MOROZOVA, A. and ESKIN, A., 2017. Centrifugal Pump Effect on Average Particle Diameter of Oil-Water Emulsion, *Materials Science and Engineering Conference Series 2017*, pp. 012215.
- MOTIN, A. and BÉNARD, A., 2017. Design of liquid–liquid separation hydrocyclones using parabolic and hyperbolic swirl chambers for efficiency enhancement. *Chemical Engineering Research and Design*, **122**, pp. 184-197.
- MOTSAMAI, O.S., 2010. Investigation of the influence of hydrocyclone geometric and flow parameters on its performance using CFD. *Advances in Mechanical Engineering*, **2**, pp. 593689.
- MOUSAVIAN, S. and NAJAFI, A., 2009. Influence of geometry on separation efficiency in a hydrocyclone. *Archive of Applied Mechanics*, **79**(11), pp. 1033-1050.
- MUKHERJEE, A., SRIPRIYA, R., RAO, P. and DAS, P., 2003. Effect of increase in feed inlet pressure on feed rate of dense media cyclone. *International Journal of Mineral Processing*, **69**(1-4), pp. 259-274.

- MULU, B., CERVANTES, M., DEVALS, C., VU, T. and GUIBAULT, F., 2015. Simulation-based investigation of unsteady flow in near-hub region of a Kaplan Turbine with experimental comparison. *Engineering Applications of Computational Fluid Mechanics*, **9**(1), pp. 139-156.
- MURPHY, S., DELFOS, R., POURQUIE, M., OLUJIĆ, Ž., JANSENS, P. and NIEUWSTADT, F., 2007. Prediction of strongly swirling flow within an axial hydrocyclone using two commercial CFD codes. *Chemical engineering science*, **62**(6), pp. 1619-1635.
- MUSA, O., XIONG, C., CHANGSHENG, Z. and LUNKUN, G., 2016. Assessment of the modified rotation/curvature correction SST turbulence model for simulating swirling reacting unsteady flows in a solid-fuel ramjet engine. *Acta Astronautica*, **129**, pp. 241-252.
- NANDA, K.K., 2012. Size-dependent density of nanoparticles and nanostructured materials. *Physics Letters A*, **376**(45), pp. 3301-3302.
- NASIRI-LOHESARA, M., 2015. Heat transfer enhancement and hydrodynamic characteristics of nanofluid in turbulent flow regime. *Journal of Energy*, **2015**.
- NEESSE, T. and DUECK, J., 2007. Dynamic modelling of the hydrocyclone. *Minerals Engineering*, **20**(4), pp. 380-386.
- NÉMETH, J. and VERDES, S., 2011. Flow pattern within hydrocyclone. *Hungarian Journal of Industry and Chemistry*, **39**(3), pp. 437-445.
- NG, S., PRIESTMAN, G. and ALLEN, R., 2006. Investigation of flooding, re-entrainment and grade efficiency in axial flow cyclones. *Chemical Engineering Research and Design*, **84**(10), pp. 884-894.
- NI, L., TIAN, J., SONG, T., JONG, Y. and ZHAO, J., 2019. Optimizing geometric parameters in hydrocyclones for enhanced separations: a review and perspective. *Separation & Purification Reviews*, **48**(1), pp. 30-51.
- NI, L., TIAN, J. and ZHAO, J., 2016. Experimental study of the effect of underflow pipe diameter on separation performance of a novel de-foulant hydrocyclone with continuous underflow and reflux function. *Separation and Purification Technology*, **171**, pp. 270-279.

NOROOZI, S., HASHEMABADI, S. and CHAMKHA, A., 2013. Numerical analysis of drops coalescence and breakage effects on de-oiling hydrocyclone performance. *Separation Science and Technology*, **48**(7), pp. 991-1002.

NOROOZI, S. and HASHEMABADI, S.H., 2009. CFD simulation of inlet design effect on deoiling hydrocyclone separation efficiency. *Chemical Engineering & Technology: Industrial Chemistry-Plant Equipment-Process Engineering-Biotechnology*, **32**(12), pp. 1885-1893.

OPOKU, F., KIARII, E.M., GOVENDER, P.P. and MAMO, M.A., 2017. Metal Oxide Polymer Nanocomposites in Water Treatments. *Descriptive Inorganic Chemistry Researches of Metal Compounds*. IntechOpen, .

OSEI, H., AL-KAYIEM, H. and HASHIM, F., 2015. Numerical studies on the separation performance of liquid-liquid Hydrocyclone for higher water-cut wells, *IOP Conference Series: Materials Science and Engineering 2015*, IOP Publishing, pp. 012014.

OSEI, H., AL-KAYIEM, H. and OSMAN, A., 2016. Flow dynamics behaviour of a novel liquid-liquid hydrocyclone with varying upper cylindrical lengths and number of inlets. *ARPN J Eng Appl Sci*, **11**, pp. 12159-12164.

PADHI, M., MANGADODDY, N., SREENIVAS, T., VAKAMALLA, T.R. and MAINZA, A., 2019. Study on multi-component particle behaviour in a hydrocyclone classifier using experimental and computational fluid dynamics techniques. *Separation and Purification Technology*, **229**, pp. 115698.

PANDEY, N., SHUKLA, S. and SINGH, N., 2017. Water purification by polymer nanocomposites: an overview. *Nanocomposites*, **3**(2), pp. 47-66.

PANTEA, H.J., HELLSTRÖM, G. and GEBART, R., 2017. Turbulence Modelling of a Single-Phase Flow Cyclone Gasifier. *Engineering*, **9**(9), pp. 779-799.

PARK, S.J. and KIM, S.S., 1998. Effects of particle space charge and turbulent diffusion on performance of plate-plate electrostatic precipitators. *Journal of Electrostatics*, **45**(2), pp. 121-137.

PATEL, V. and SOTIROPOULOS, F., 1997. Longitudinal curvature effects in turbulent boundary layers. *Progress in Aerospace Sciences*, **33**(1-2), pp. 1-70.



PATRA, G., CHAKRABORTY, S. and MEIKAP, B., 2018. Role of vortex finder depth on pressure drop and performance efficiency in a ribbed hydrocyclone. *South African Journal of Chemical Engineering*, **25**, pp. 103-109.

PATRO, B., MURUGAN, S. and PATRO, P., 2012. NUMERICAL MODELING OF GAS-SOLID FLOW IN A HORIZONTAL PIPE. *Multiphase Science and Technology*, **24**(4),.

PELLEGRINO, T., MANNA, L., KUDERA, S., LIEDL, T., KOKTYSH, D., ROGACH, A.L., KELLER, S., RÄDLER, J., NATILE, G. and PARAK, W.J., 2004. Hydrophobic nanocrystals coated with an amphiphilic polymer shell: a general route to water soluble nanocrystals. *Nano letters*, **4**(4), pp. 703-707.

PERICLEOUS, K. and RHODES, N., 1986. The hydrocyclone classifier—a numerical approach. *International Journal of Mineral Processing*, **17**(1-2), pp. 23-43.

QIAN, F., ZHANG, J. and ZHANG, M., 2006. Effects of the prolonged vertical tube on the separation performance of a cyclone. *Journal of hazardous materials*, **136**(3), pp. 822-829.

RAKESH, A., KUMAR REDDY, VAKAMALLA TS R and NARASIMHA, M., 2014. Air-Core Size Measurement of Operating Hydrocyclone by Electrical Resistance Tomography. *Chemical Engineering & Technology*, **37**(5), pp. 795-805.

RAOUFI, A., SHAMS, M., FARZANEH, M. and EBRAHIMI, R., 2008. Numerical simulation and optimization of fluid flow in cyclone vortex finder. *Chemical Engineering and Processing: Process Intensification*, **47**(1), pp. 128-137.

ROSICKÁ, D. and ŠEMBERA, J., 2013. Changes in the nanoparticle aggregation rate due to the additional effect of electrostatic and magnetic forces on mass transport coefficients. *Nanoscale research letters*, **8**(1), pp. 20.

RYTWO, G., 2012. The use of clay-polymer nanocomposites in wastewater pretreatment. *The scientific world journal*, **2012**.

SAENGCHAN, K., NOPHARATANA, A. and SONGKASIRI, W., 2019. New hydrocyclone design for high starch yield: Effect of cylindrical-conical length proportion on the starch, sulfur and protein separation efficiencies. *Powder Technology*, **346**, pp. 1-8.

- SAENGCHAN, K., NOPHARATANA, A. and SONGKASIRI, W., 2009. Enhancement of tapioca starch separation with a hydrocyclone: effects of apex diameter, feed concentration, and pressure drop on tapioca starch separation with a hydrocyclone. *Chemical Engineering and Processing: Process Intensification*, **48**(1), pp. 195-202.
- SAIDI, M., MADDAHIAN, R. and FARHANIEH, B., 2013. Numerical investigation of cone angle effect on the flow field and separation efficiency of deoiling hydrocyclones. *Heat and Mass Transfer*, **49**(2), pp. 247-260.
- SAIDI, M., MADDAHIAN, R., FARHANIEH, B. and AFSHIN, H., 2012. Modeling of flow field and separation efficiency of a deoiling hydrocyclone using large eddy simulation. *International Journal of Mineral Processing*, **112**, pp. 84-93.
- SALIMI, A., 2015. *The effect of fluid viscosity and geometry on hydrocyclone performance*, .
- SALMANIZADE, F., GHAZANFARI MOGHADDAM, A. and MOHEBBI, A., 2020. Improvement hydrocyclone separation of biodiesel impurities prepared from waste cooking oil using CFD simulation. *Separation Science and Technology*, , pp. 1-16.
- SAMPAIO, L.E.B., REZENDE, A.L.T. and NIECKELE, A.O., 2014. The challenging case of the turbulent flow around a thin plate wind deflector, and its numerical prediction by LES and RANS models. *Journal of Wind Engineering and Industrial Aerodynamics*, **133**, pp. 52-64.
- SCHALIN, A. and NIELSEN, P.V., 2004. Impact of turbulence anisotropy near walls in room airflow. *Indoor air*, **14**(3), pp. 159-168.
- SCHWARZKOPF, J.D., CROWE, C.T. and DUTTA, P., 2009. A turbulence dissipation model for particle laden flow. *AIChE Journal*, **55**(6), pp. 1416-1425.
- SHAH, H., MAJUMDER, A. and BARNWAL, J., 2006. Development of water split model for a 76 mm hydrocyclone. *Minerals Engineering*, **19**(1), pp. 102-104.
- SHAO, S., LI, Y., LÜ, T., QI, D., ZHANG, D. and ZHAO, H., 2019. Removal of emulsified oil from aqueous environment by using polyvinylpyrrolidone-coated magnetic nanoparticles. *Water*, **11**(10), pp. 1993.

- SILVA, N.K., SILVA, D.O., VIEIRA, L.G. and BARROZO, M.A., 2015. Effects of underflow diameter and vortex finder length on the performance of a newly designed filtering hydrocyclone. *Powder Technology*, **286**, pp. 305-310.
- SMITH, L.M. and WOODRUFF, S.L., 1998. Renormalization-group analysis of turbulence. *Annual Review of Fluid Mechanics*, **30**(1), pp. 275-310.
- SONG, C., PEI, B., JIANG, M., WANG, B., XU, D. and CHEN, Y., 2016. Numerical analysis of forces exerted on particles in cyclone separators. *Powder Technology*, **294**, pp. 437-448.
- SUKORIANSKY, S., GALPERIN, B. and STAROSELSKY, I., 2003. Cross-term and  $\epsilon$ -expansion in RNG theory of turbulence. *Fluid Dynamics Research*, **33**(4), pp. 319.
- SUZEN, Y.B., HUANG, P., HULTGREN, L.S. and ASHPIS, D.E., 2003. Predictions of separated and transitional boundary layers under low-pressure turbine airfoil conditions using an intermittency transport equation. *J.Turbomach.*, **125**(3), pp. 455-464.
- SVAROVSKY, L., 1984. *Hydrocyclones*. Technomic Pub Co.
- SVOBODA, J., 2005. Magnetic separation.
- SVOBODA, J., 1994. The effect of magnetic field strength on the efficiency of magnetic separation. *Minerals Engineering*, **7**(5-6), pp. 747-757.
- TANG, Z., YU, L., WANG, F., LI, N., CHANG, L. and CUI, N., 2019. Effect of particle size and shape on separation in a hydrocyclone. *Water*, **11**(1), pp. 16.
- TAVARES, L., SOUZA, L., LIMA, JOSÉ RENATO BAPTISTA DE and POSSA, M.V., 2002. Modeling classification in small-diameter hydrocyclones under variable rheological conditions. *Minerals Engineering*, **15**(8), pp. 613-622.
- TENO, J., BROGAN, T.R. and PETTY, S., 1970. *Research studies and the development of mhd generators and accelerators*, .
- TEOTIA, A., SAMI, H. and KUMAR, A., 2015. Thermo-responsive polymers: structure and design of smart materials. *Switchable and responsive surfaces and materials for biomedical applications*. Elsevier, pp. 3-43.

- TIAN, J., NI, L., SONG, T. and ZHAO, J., 2020. CFD simulation of hydrocyclone-separation performance influenced by reflux device and different vortex-finder lengths. *Separation and Purification Technology*, **233**, pp. 116013.
- TORBERGSEN, L., 1998. *Experiments in turbulent pipe flow*, .
- UTIKAR, R., DARMAWAN, N., TADE, M., LI, Q., EVANS, G., GLENNY, M. and PAREEK, V., 2010. Hydrodynamic simulation of cyclone separators. *Computational Fluid Dynamics*. InTech, pp. 241-266.
- VAKAMALLA, T.R., KORUPROLU, V.B.R., ARUGONDA, R. and MANGADODDY, N., 2017. Development of novel hydrocyclone designs for improved fines classification using multiphase CFD model. *Separation and Purification Technology*, **175**, pp. 481-497.
- VAKAMALLA, T.R. and MANGADODDY, N., 2019. The dynamic behaviour of a large-scale 250-mm hydrocyclone: A CFD study. *Asia-Pacific Journal of Chemical Engineering*, **14**(2), pp. e2287.
- VALVERDE, M.R., COURY, J.R. and GONCALVE, J., 2011. Modeling the effects of the vortex finder height on pressure drop in the cyclone using computational fluid dynamics. *Asociacion Argentina de Mecanica Computacional*, **30**, pp. 525-533.
- VATTA, L., KEKANA, R., RADEBE, B., MYBURGH, I. and SVOBODA, J., 2003. The effect of magnetic field on the performance of a dense medium separator. *Physical Separation in Science and Engineering*, **12**(3), pp. 167-178.
- VELLA, L. and EMERSON, D., 2012. Electrical Properties of Magnetite-and Hematite-Rich Rocks and Ores. *ASEG Extended Abstracts*, **2012**(1), pp. 1-4.
- VIEIRA, L.G. and BARROZO, M.A., 2014. Effect of vortex finder diameter on the performance of a novel hydrocyclone separator. *Minerals Engineering*, **57**, pp. 50-56.
- VIGUERAS-ZUÑIGA, M., VALERA-MEDINA, A. and SYRED, N., 2012. Studies of the precessing vortex core in swirling flows. *Journal of applied research and technology*, **10**(5), pp. 755-765.

- WAN, G., SUN, G., XUE, X. and SHI, M., 2008. Solids concentration simulation of different size particles in a cyclone separator. *Powder Technology*, **183**(1), pp. 94-104.
- WANG, B. and YU, A., 2006. Numerical study of particle–fluid flow in hydrocyclones with different body dimensions. *Minerals Engineering*, **19**(10), pp. 1022-1033.
- WANG, F., HE, J., LIANG, Y., LUO, Y., LIAO, Z. and LI, L., 2018. Study on the permeability characteristics of coal containing coalbed methane under different loading paths. *Energy Science & Engineering*, **6**(5), pp. 475-483.
- WANG, L. and FU, S., 2011. Development of an intermittency equation for the modeling of the supersonic/hypersonic boundary layer flow transition. *Flow, turbulence and combustion*, **87**(1), pp. 165-187.
- WOODFIELD, D. and BICKERT, G., 2004. Separation of flocs in hydrocyclones—significance of floc breakage and floc hydrodynamics. *International Journal of Mineral Processing*, **73**(2-4), pp. 239-249.
- WU, J., ZHANG, Y. and WANG, H., 2014. Numerical study on tangential velocity indicator of free vortex in the cyclone. *Separation and Purification Technology*, **132**, pp. 541-551.
- WU, S., HWANG, K., CHENG, T., HUNG, T. and TUNG, K., 2017. Effectiveness of a hydrocyclone in separating particles suspended in power law fluids. *Powder Technology*, **320**, pp. 546-554.
- YAKHOT, V. and ORSZAG, S.A., 1986. Renormalization group analysis of turbulence. I. Basic theory. *Journal of Scientific Computing*, **1**(1), pp. 3-51.
- YANG, Q., WANG, H., WANG, J., LI, Z. and LIU, Y., 2011. The coordinated relationship between vortex finder parameters and performance of hydrocyclones for separating light dispersed phase. *Separation and purification technology*, **79**(3), pp. 310-320.
- YANG, X., SIMMONS, M.J., LIU, P., ZHANG, Y. and JIANG, L., 2019. Effect of feed body geometry on separation performance of hydrocyclone. *Separation Science and Technology*, **54**(17), pp. 2959-2970.

- YANG, X., SIMMONS, M.J., LIU, P., ZHANG, Y. and JIANG, L., 2019. Effect of feed body geometry on separation performance of hydrocyclone. *Separation Science and Technology*, **54**(17), pp. 2959-2970.
- YANHONG, Z., PENG, Q., YI, L. and HUALIN, W., 2011. Experimental Study of Hydrocyclone Flow Field with Different Feed Concentration [J]. *Industrial and Engineering Chemistry Research*, **50**(13), pp. 8176-8184.
- YARJIABADI, H., SHOJAEEFARD, A., YARJIABADI, H., HABIBIAN, M. and NOORPOOR, A., 2006. Particle size effects on hydro-cyclone performance. *International Journal of Industrial Engineering & Production Research*, **17**(3), pp. 9-19.
- YE, J., XU, Y., SONG, X. and YU, J., 2019. Novel conical section design for ultra-fine particles classification by a hydrocyclone. *Chemical Engineering Research and Design*, **144**, pp. 135-149.
- YOHANA, E., TAUVIQIRRAHMAN, M., PUTRA, A.R., DIANA, A.E. and CHOI, K., 2018. Numerical analysis on the effect of the vortex finder diameter and the length of vortex limiter on the flow field and particle collection in a new cyclone separator. *Cogent Engineering*, **5**(1), pp. 1562319.
- YOSHIDA, H., HAYASE, Y., FUKUI, K. and YAMAMOTO, T., 2012. Effect of conical length on separation performance of sub-micron particles by electrical hydrocyclone. *Powder Technology*, **219**, pp. 29-36.
- YU, J., FU, J., CHENG, H. and CUI, Z., 2017. Recycling of rare earth particle by mini-hydrocyclones. *Waste Management*, **61**, pp. 362-371.
- YUAN, H., FU, S., TAN, W., HE, J. and WU, K., 2015. Study on the hydrocyclonic separation of waste plastics with different density. *Waste Management*, **45**, pp. 108-111.
- YUAN, H., 1992. A Cylindrical Hydrocyclone. *Hydrocyclones*. Springer, pp. 177-189.
- YUAN, Q., FU, Y., SUN, Q. and LI, X., 2010. A new method of showing magnetic field based on ferrofluid. *Physics Procedia*, **9**, pp. 210-215.

- YUE, P., ZHANG, Q., WANG, R., LI, Y. and WANG, S., 2015. Turbulence intensity and turbulent kinetic energy parameters over a heterogeneous terrain of Loess Plateau. *Advances in Atmospheric Sciences*, **32**(9), pp. 1291-1302.
- ZAMAN, E., 2017. *Hydrodynamics of the hydrocyclone flow field: effects of turbulence modelling, geometrical and design parameters*, .
- ZANK, G. and MATTHAEUS, W., 1992. The equations of reduced magnetohydrodynamics. *Journal of plasma physics*, **48**(1), pp. 85-100.
- ZHANG, C., CUI, B., WEI, D. and LU, S., 2019. Effects of underflow orifice diameter on the hydrocyclone separation performance with different feed size distributions. *Powder Technology*, **355**, pp. 481-494.
- ZHANG, Y., QIAN, P., LIU, Y. and WANG, H., 2011. Experimental study of hydrocyclone flow field with different feed concentration. *Industrial & Engineering Chemistry Research*, **50**(13), pp. 8176-8184.
- ZHANG, Y., LIU, P., JIANG, L. and YANG, X., 2019. The Study on Numerical Simulation and Experiments of Four Product Hydrocyclone with Double Vortex Finders. *Minerals*, **9**(1), pp. 23.
- ZHANG, Y., LIU, P., JIANG, L., YANG, X. and YANG, J., 2019. Numerical Simulation of Flow Field Characteristics and Separation Performance Test of Multi-Product Hydrocyclone. *Minerals*, **9**(5), pp. 300.
- ZHANG, Y., LIU, P., XIAO, L., YANG, X. and YANG, J., Computational simulation of the effects of vortex finder diameter on the air core in a hydrocyclone separator.
- ZHANG, Y., CAI, P., JIANG, F., DONG, K., JIANG, Y. and WANG, B., 2017. Understanding the separation of particles in a hydrocyclone by force analysis. *Powder Technology*, **322**, pp. 471-489.
- ZHAO, Q., CUI, B., WEI, D., SONG, T. and FENG, Y., 2019. Numerical analysis of the flow field and separation performance in hydrocyclones with different vortex finder wall thickness. *Powder Technology*, **345**, pp. 478-491.
- ZHDANOV, M.S., 2009. Electromagnetic properties of rocks and minerals. *Methods in Geochemistry and Geophysics*. Elsevier, pp. 395-447.

ZHOU, D., ABDEL-FATTAH, A.I. and KELLER, A.A., 2012. Clay particles destabilize engineered nanoparticles in aqueous environments. *Environmental science & technology*, **46**(14), pp. 7520-7526.

ZHOU, N., GAO, Y., AN, W. and YANG, M., 2010. Investigation of velocity field and oil distribution in an oil–water hydrocyclone using a particle dynamics analyzer. *Chemical Engineering Journal*, **157**(1), pp. 73-79.

ZHU, G., LIOW, J. and NEELY, A., 2010. Computational Study of Flow in a Micro-Sized Hydrocyclone, *Proc. 17th Australasian Fluid Mechanics Conference, Auckland, New Zealand 2010*, pp. 1-4.